Theses and Dissertations

2018

Hydrothermal Synthesis: A Gateway To Metastable Crystals With Unusual Properties

Justin B. Felder
University of South Carolina

Follow this and additional works at: https://scholarcommons.sc.edu/etd

Part of the Chemistry Commons

HYDROTHERMAL SYNTHESIS: A GATEWAY TO METASTABLE CRYSTALS WITH
UNUSUAL PROPERTIES

by

Justin B. Felder

Bachelor of Science
Lander University, 2013

Submitted in Partial Fulfillment of the Requirements

For the Degree of Doctor of Philosophy in

Chemistry

College of Arts and Sciences

University of South Carolina

2018

Accepted by:

Hans-Conrad zur Loye, Major Professor

Dmitry Peryshkov, Committee Member

Donna Chen, Committee Member

John Weidner, Committee Member

Cheryl L. Addy, Vice Provost and Dean of the Graduate School

DEDICATION

For Amanda, who has stood with me throughout my entire graduate career and made even the hardest times easy to bear. Also for Jake, for staying in touch even when we have both been too busy to talk.

ACKNOWLEDGEMENTS

Over the course of the last several years I have received much support and encouragement from many people whom I am forever indebted to. First, I would like to thank my advisor, Dr. Hans-Conrad zur Loye for giving me the opportunity to work in his lab and the freedom to pursue many different avenues of research.

Although I have improved drastically in recent years, school has not always been my forte. Over the years, I have had several teachers and professors that I identify as being instrumental in helping me get to where I am now. For all of their support and caring, I would like to thank Dr. Preston Brown, for introducing me to chemistry and physics, and for being hard on me when I was slacking; Dr. Lisa Broadhacker, who was my academic advisor, for introducing me to Lander and for truly instilling a sense of passion for chemistry early on; Dr. Ralph Layland, for his extreme sarcasm and for introducing me to solid-state chemistry; and Dr. David Gardner, for forcing me to leave my reality in a bucket by the door and giving me my first taste of research.

Next, I want to thank the members of my committee: Drs. Dmitry Peryshkov, Donna Chen, and John Weidner. They have been both challenging and supportive during the course of my doctoral studies, not to mention incredibly flexible. I would particularly like to thank them (and Dr. zur Loye) for showing up during a flood to attend my research proposal. In particular I want to thank my chair, Dr. Dmitry Peryshkov for providing advice and help on fluorine chemistry over the past few years.

In the zur Loye lab we are fortunate to enjoy many state-of-the-art instruments, however for much of my time here we were without a single-crystal x-ray instrument. For that reason I want to thank Dr. Mark Smith for providing structural solutions to many of the materials that are discussed in this work, and also for his guidance in helping me learn the ways of crystallography after we acquired our new instrument.

Working in the zur Loye lab was an amazing experience, but the real pleasure was the people I was able to connect with over the course of my studies. Each person in the lab left his or her own impact on me, and helped me to grow as a scientist. Most of all I want to thank Dr. Jeongho Yeon for being my mentor for the first three years of my time here. He was single-handedly responsible for much of my learning and instilled a great sense for work ethic. I would also like to thank him for his help in crystallography and willingness to always stop what he was doing to help me if I was struggling with a problem.

I also want to thank Dr. Dileka Abeysinghe for her support and encouragement and scientific insight. I of course must also mention Timothy Ferreira for our many heated debates on the nature of the universe, gravity, quantum mechanics, Russel-Saunders coupling, and the dark side of the force.

Lastly, I want to thank my family for their support and encouragement not only through graduate school, but my undergraduate career as well. I would especially like to thank them for periodically feeding me, as I surely would have starved without them.

ABSTRACT

Research into crystalline matter has long been of interest to humanity, both in order to advance our society by creating new technologically useful materials and in order to better understand to nature of the properties we depend on for so much of our existing technology. In recent decades, solution-based crystal growth syntheses including hydrothermal and molten flux techniques have risen to the forefront of solid-state chemistry as superior methods of synthesizing new materials as single crystals ripe for structure determination and property measurements.

This work seeks to educate readers on recent advances in the hydrothermal realm of crystal growth: namely facile routes to the synthesis of transition-metal fluorides, uranium fluorides, and uranium oxides and compounds of related oxoanions (hydroxides, phosphates, phosphites). Work was done to characterize these new materials as completely as possible, and to work towards the goal of unraveling the structural contribution to magnetism in uranium compounds, namely how the coordination number of U(IV) affects the transition (or lack thereof) from the triplet to the nonmagnetic singlet ground state.

TABLE OF CONTENTS

LIST OF TABLES

LIST OF FIGURES

xiii

xvi

LIST OF SYMBOLS

Å   Angstrom. A unit of length equal to 0.1 nanometers.

°   Degrees. A unit of plane angle.

°C   Degrees Celsius. A unit of temperature.

K   Kelvin. An absolute unit of temperature where 0 K represents a total lack of thermal energy.

K_α X-ray emission caused by an electron transitioning from the $2p$ (L-shell) to the $1s$ (K-shell) orbital.

K_β X-ray emission caused by an electron transitioning from the $3p$ (M-shell) to the $1s$ (K-shell) orbital.

2θ The diffraction angle, two-theta.

F The structure factor.

F^2 The structure factor squared.

R   Residual factor.

R_1 Residual factor for refinement against F.

wR_2 Residual factor for refinement against F^2.

R_{int} Merging error; a measure of the precision/reproducibility.

R_{Bragg} Indicator of the quality of fit between observed and calculated integrated intensities in a Rietveld refinement of powder diffraction data.

M Magnetization, given in units of (Bohr magnetons/formular unit). The density of magnetic dipole moments in a magnetic material.

H Magnetic field, given in units of Tesla.

μ_B Bohr Magneton. A physical constant used to define the magnetic moment of an electron caused by its spin or orbital angular momentum. $1 \mu_B \approx$ the spin magnetic moment of one electron.

χ_m Molar magnetic susceptibility, given in units of (emu/mole • formula unit).

θ_w Weiss temperature. The point at which the inverse molar magnetic susceptibility intercepts the absolute temperature on a Curie-Weiss plot. The Weiss temperature can be either positive or negative.

λ Wavelength, usually expressed in nanometers.

υ Frequency, usually expressed in wavenumbers (cm^{-1})

T   Temperature. Expressed either in Kelvin (K) or degrees Celsius (°C).

e^- Electron.

d^x Notation to describe the number of d-orbital electrons available to an ionic species. x = 0-10.

f^y Notation to describe the number of f-orbital electrons available to an ionic species. y = 0-14.

LIST OF ABBREVIATIONS

BVS .... Bond Valence Sum

EDS .... Energy Dispersive Spectroscopy

FC(W) .... Field Cooled (Warming)

FT-IR .... Fourier Transform Infrared Spectroscopy

F. U. .... Formula Units

HAST-C .... Hastelloy-C

mmol .... millimoles

MPMS .... Magnetic Properties Measurement System

MvH .... Magnetization versus Field

NPD .... Neutron Powder Diffraction

PXRD .... Powder X-ray Diffraction

PTFE .... Polytetrafluoroethylene

RT .... Room Temperature

SCND .... Single-crystal Neutron Diffraction

SEM .... Scanning Electron Microscopy

SQUID .... Superconducting Quantum Interference Device

SXRD .... Single-crystal X-ray Diffraction

TGA. .... Thermogravimetric Analysis

UV-Vis .... Ultraviolet-Visible Spectroscopy

XRD .... X-ray Diffraction

ZFC .... Zero-Field Cooled

LIST OF COMPOUNDS BY CHAPTER

"The dark side of the force is a pathway to many abilities some consider to be…unnatural." - Emperor Palpatine

CHAPTER 1

CHEMISTRY IN THE SOLID-STATE: PROBING THE STRUCTURE AND PROPERTIES OF
CRYSTALLINE MATTER

Introduction

Solid-state materials have long been a source of fascination and wonder for humans; crystalline materials in particular have garnered a large amount of interest due to the gamut of properties they are capable of displaying. As we have advanced our understanding of the world we live in, we have also learned to harness the power of crystalline materials in order to transform our society. In today's world, humans utilize crystals for a staggering variety of purposes ranging from those as simple as using crystalline clays to create works of art and colored pigments to paint houses to those more suited to high technology: rare earth magnets [1], piezoelectrics [2], and experimental solid-state batteries [3] to power our homes, devices, and lives. While some of the most basic (and useful) solid-state materials such as silicate clays and borax can literally be dug up out of the ground, materials with more advanced and desirable properties have to be made synthetically. Synthetic solid-state chemistry has had great longevity over the past decades, and will continue to be an active area of research due to a technological cycle: Newly synthesized materials with desirable properties (such as Li^+ ion conductivity [4]) drive industrial research. These application-driven researches seek to perfect the desired property, however simultaneously different researchers seek to understand the origin and mechanism of said property, which inevitably yields new materials with new properties, and the cycle begins again.

Historically, solid-state chemists have relied on one tried and true synthetic technique: the solid-state ceramic synthesis. [5] In a traditional solid-state synthesis, researchers heat an intimate, stoichiometric mixture of reagent powders to high temperatures. During the reaction, the reagent powders diffuse through each other and

2

react in the process, creating a fine product powder. This method has many strengths, including its scalability, and tendency to result in phase-pure products. The solid-state method is not without drawbacks. Solid-state reactions are diffusion-limited, and even at elevated temperature solid-state diffusion is slow, occurring usually on the scale of several days. This often results in solid-state reactions requiring multiple intermediate grindings between heatings to encourage mixing of the reactant powders. The result is that many solid-state reactions are not complete even after a full week of heatings. Furthermore, since impurity phases cannot readily be separated from fine powders, a successful solid-state reaction requires a careful stoichiometric mixture of reactants. This means that any error in weighing reactants will result either in an incomplete reaction (one starting material remains in excess), or the formation of an undesired side product (impurity). In either case, it is often best to consider such reactions a wash and begin afresh rather than try to correct the imbalance of reagents. Secondly, careful stoichiometric mixing requires the preparer to know the target composition, which for obvious reasons is prohibitive toward exploratory chemistry.

Despite these drawbacks, the solid-state route remains one of the most reliable methods for synthesizing inorganic materials, especially refractory materials that require very high (>1000° C) temperatures in order to react. Researchers have developed several variations on the traditional solid-state route in order to improve (usually speed up) reactions. These usually include co-precipitating reagents so as to produce a powder mixed on the atomic scale. [6] These powders can then be further reacted (possibly by ignition). Researchers can also employ mechano-chemical means, such as ball milling, to mechanically activate the reactant powders before heating. [7, 8]

3

These types of solid-state reactions all have one commonality: the addition of a large amount of thermal energy. This thermal energy is necessary to improve the rate of diffusion and to overcome activation energy barriers; coupled with the fact that these reactions occur over several days means that there is sufficient time and energy to push reactions to produce only thermodynamically favorable products. This is not necessarily a bad thing, as many thermodynamic products have high thermal stability which is necessary in many applications, however it severely limits the types of phases that can be obtained from a given solid-state reaction.

To obtain products that are favored kinetically, rather than thermodynamically, it is necessary to move towards different synthetic techniques which use shorter reaction times and less thermal energy. While this is intuitive, one cannot simply mix reagent powders *a la* traditional solid-state and simply heat at a cooler temperature for a shorter time, as there would not be enough heat to overcome the activation energy or enough time to allow for diffusion. In order to circumvent this problem, researchers have turned to solution-based methods. In solution-based reactions, the activation energy is lowered as reactant species become solvated and mingle freely with other reactants in the solution. This also serves to greatly reduce the amount of time and effort necessary to complete a given reaction. Whereas typical solid-state reactions require hours of grinding to produce an intimately mixed powder coupled with days (at a time) worth of heating, solution based methods are capable of utilizing 'off the shelf' reagents without further grinding or modification, and can be completed in as little as a few hours (although reaction times of one to two days are most common).

4

In addition to speeding up reaction times, lowering reaction temperatures, and allowing for kinetically favorable products, solution based chemistry has another huge advantage over ceramic methods: the potential to grow high quality single crystals. [9] Single crystals provide enormous benefits to researchers primarily due to recent advancements in X-ray diffraction technology: with modern instrumentation a skilled crystallographer can collect data and elucidate the atomic crystal structure of a novel compound in just a few hours after synthesis. Furthermore, many crystals have properties that are anisotropic and, therefore, having single crystals allows researchers to measure properties in different orientations to uncover the anisotropic nature of these properties (such as conduction or magnetism). The following work will detail the application of crystal growth to the synthesis of new transition metals and uranium containing fluorides and oxides.

Crystal Growth Methods

In order to obtain a crystal from a solution, researchers rely on well-understood phenomenon: super-saturation. Super-saturation relies on the fact that the solubility of materials in a given solvent typically increases as the temperature of the solvent increases. This leads to the ability to dissolve more material (at elevated temperatures) in a solvent that should be possible at lower temperatures. As the material cools, this extra material stays in solution (at least temporarily) and the solution is termed super-saturated. As the super-saturated solution cools, crystallites can nucleate and grow using the 'extra' dissolved material as feedstock. [10–13]

Over roughly the past two decades, two solution-based methods of crystal growth have emerged as extremely powerful tools for synthetic chemists to perform exploratory

5

chemistry: hydrothermal crystal growth and flux crystal growth. [14, 15] Although there are many differences between a flux and a hydrothermal reaction, the basic principles are the same: heat a mixture of reactants in the presence of a solvent, hold at the reaction temperature until the reactants have dissolved and are able to interact, and cool the mixture slowly enough to allow the solution to become super-saturated, crystals to nucleate, and grow. After the reaction, the solvent is removed leaving the product crystals.

In a flux reaction, the solvent system is an inorganic salt (termed the flux) with a (relatively) low melting point. The reactants are mixed with an excess of flux inside a reaction vessel, and the charge is heated in a furnace to above the melting point of the flux. At this point, the flux is a liquid and the reactants will dissolve in it. The reaction temperature must be high enough that the charge can be effectively cooled through the liquid range of the flux allowing crystallization before the flux solidifies. There are a huge number of possible fluxes with different properties which allow crystallization of many types of materials, however all fluxes should share a few common properties. A good flux will be cheap, low melting (m.p. <1000° C), able to dissolve the chosen reactants while remaining inert to the reaction vessel, and be able to be easily removed from the product. The best fluxes will be water soluble, allowing it to be simply washed away, leaving pure product crystals behind [14].

While flux growth has been extremely successful at synthesizing new compounds, it is not the only method of exploring phase space by crystal growth. Hydrothermal synthesis involves the use of superheated water contained in a sealed pressure vessel as the solvent system. Hydrothermal reactions rely on the fact that the solubility of normally

6

insoluble metals increases as the temperature of the system increases. Traditional hydrothermal chemistry involves taking advantage of water as a supercritical fluid. Above 374° C in a sealed system, water becomes supercritical: a fluid with the viscosity and ability to fill its container like a gas, with the dissolving power of a liquid. Such reactions are typically run at >500° C, and can reach as high as 700° C. These reactions rival the temperature ranges of many fluxes, but are systems with extremely high pressures, which can result in many interesting materials. [16–18] Understandably, doing chemistry in high-pressure vessels is expensive and can be dangerous if the vessel becomes overpressurized. For that reason, chemists have developed softer hydrothermal methods, which are also more cost-effective.

The so-called mild hydrothermal method involves temperatures below the critical point of water, but still above the boiling temperature (100° C-374° C); but frequently remain below 250° C. Pressures generated in these systems are generally much less than those in traditional hydrothermal reactions, and so much smaller pressure vessels made of less exotic alloys can be employed, which ultimately cuts the cost of reactions significantly. Of course, the lower temperatures and subcritical nature of the water in a mild hydrothermal reaction means that the solvent has less dissolving power than a supercritical fluid. In order to get around this problem, researchers frequently utilize soluble salts and/or acid solvents to aid in the dissolution of precursors. The low cost and accessibility of mild hydrothermal chemistry means that it has enjoyed the attention of many researchers in recent years. [19–23]

Although the temperature range between 300° C and 450° C are well within the capabilities of researchers' equipment, it is not well explored. It has been hypothesized

7

that this is because researchers equipped only for mild hydrothermal reactions (PTFE lined vessels) cannot reach the regime beyond 250° C, and if researchers are equipped for supercritical temperatures, they typically 'go big' and ignore cooler temperature profiles. It has been hypothesized recently in the zur Loye group that it should be possible to obtain materials unique to this intermediate temperature range or at least obtain materials previously only synthesized at much higher temperatures. Thus, work has begun on exploring this intermediate range of hydrothermal chemistry.

There are many considerations to take into account when planning a hydrothermal reaction, and varying any of them can favor the formation of one product over another. The first two considerations to make are temperature and choice of reaction vessel. It has been observed in supercritical reactions that higher temperatures tend to result in more condensed framework materials, while lower temperatures tend to favor more open frameworks, however this does not necessarily hold true for mild conditions as there are reported cases of both open and closed framework materials resulting from mild reactions across a wide variety of temperatures. In such cases where there is no clear trend, researchers must rely on chemical intuition to decide which reaction temperature is best for a given reaction. It is more straightforward to choose an appropriate reaction vessel: a good vessel will be inert to reactants and solvent (this is more important than in a flux reaction, as even a small reaction with the vessel could weaken the structural integrity, causing a blowout), as well as able to withstand the pressure and temperature of the given reaction conditions. Mild hydrothermal reactions are often carried out in standard acid digestion bombs. These bombs consist of a PTFE crucible insert that fits into a stainless steel sleeve, or autoclave. Reactants are loaded into the PTFE liner, which provides

8

excellent chemical inertness. The liner is loaded into the autoclave, which serves as the pressure vessel by sealing the PTFE liner and providing structural support.

These bomb reactors have two main drawbacks. The first is that organic molecules (used either as a solvent or a reactant) tend to become trapped in the liner. Once this happens, the offending organic is often impossible to remove completely and the liner must then be designated only for reactions containing that organic species. This problem is easily avoided by sticking to purely inorganic methods. The second drawback is that PTFE begins to become soft around 230° C, and by the time it reaches 250° C will begin to break down and become unusable. There is no real way around this, and reactions that aspire to higher temperatures must use alternative reaction vessels.

For this reason, supercritical reactions often utilize reaction vessels constructed from noble metal (like gold or silver) tubing. These vessels do not quite provide the inertness of PTFE across all conditions (usually strongly acidic conditions can cause problems), however they are suitable for most applications. These tubes provide excellent thermal stability as silver will not begin to soften until above 900° C. These types of vessels have one major drawback: they cannot contain significant pressure alone. In order to be viable as hydrothermal vessels, these tubes must be placed inside a secondary container, which is a pressure vessel rated to the appropriate pressure and temperature. For supercritical reactions, these vessels are commonly made of HASTELLOY C (HAST C), a stainless steel alloy with high strength and good inertness to the corrosive nature of supercritical water. These vessels are loaded with the reaction tubes, and must be backfilled with water to provide counterpressure to the reaction tubes.

Once the temperature range and reaction vessel has been decided, all that remains is to decide upon appropriate starting materials. This of course greatly depends on the type of material being targeted, however not all precursors are suitable for all reactions. For example, nitrate and carbonate make excellent precursors for most hydrothermal reactions due to their solubility, however acetates and tartrates are only suitable for mild hydrothermal conditions as they will decompose and release gas under the heat required for supercritical reactions. Furthermore, tartrate is a fairly strongly chelating ligand, which can incorporate into products, while acetate is weakly chelating and likely will not. On the other side of the coin, oxides tend to make excellent precursors, as they do not introduce competing anions to the system, however the majority of transition metal oxides are quite insoluble under mild conditions and are only viable in the supercritical regime.

Ultimately, hydrothermal reactions are quite complex systems and researchers must rely a great deal on chemical intuition in order to decide upon the best set of conditions for a given reaction. Despite these challenges, hydrothermal synthesis is a rewarding area of research that often results in large single crystals perfectly suited for XRD and other property measurements.

Solid State Fluorides

Solid-state fluorides are a diverse class of materials that are both similar and different from oxides. Fluorine is of a similar size and electronegativity to oxygen, and therefore metal coordination environments tend to be the same with fluorine as oxygen, however, the lower charge of fluorine coupled with its propensity to favor terminal positions (this is not to say fluorine can not bridge metal centers, this is often the case)

mean that fluorides can often exhibit interesting and unique structural arrangements. [24–27] One such example of this is the so-called tailor effect [28], which occurs when an oxide is fluorinated. This typically results in a high dimensional (3D or 2D) oxide being cut into a lower (2D or 1D) dimensional structure. [29]

Beyond structural considerations, fluorine is an ion capable of effectively mediating superexchange between magnetic metal ions. [30] Hence fluorides have long been known as having rich magnetic properties. This being said, fluorine is slightly worse than oxygen at mediating a superexchange, which coupled with the unique structures found in fluorides means that researchers can expect to find quite different magnetic behavior in fluorides than are typically observed in oxide magnets.

Fluorine chemistry enjoyed a wealth of research in the early 1900's, however most of it was halted by the 1960's and 1970's. Put quite simply, this decline in research was primarily due to the dangers presented by traditional fluorine chemistry. Historically, fluorides have been made by a method called fluorine bomb calorimetry. This involves placing reagents inside a bomb calorimeter with a completely fluorine atmosphere. The reagents are then ignited inside the calorimeter, revealing the fluoride products. This method is quite fruitful; fluorine will react readily with nearly every element on the periodic table with only a few notable exceptions (He and Ne). Despite the success of fluorine combustion chemistry, the dangers outweighed the success. F_2 itself is highly corrosive, and would frequently corrode gas cylinders and tubing used to contain it unless it was treated properly. The combustion itself is highly exothermic and requires specialized equipment to safely contain, and HF gas (often a byproduct of the combustion, analogous to H_2O in an oxygen combustion) is itself highly corrosive and

11

toxic. [31] Finally, to complete the problem, the fluoride products created by combustion tended to contain metals in extremely oxidized (unstable) states. This means that even when handled with care, these materials often detonated, injuring those attempting to study them. It is then no surprise that fluorine chemistry all but died by the 1970's.

Today, there are still a few fluorine bomb calorimeters in use, however the technique is all but extinct. That is not to say that interest in solid-state fluorides has waned however. In recent years, chemists have adapted the modern crystal growth methods discussed previously to the synthesis of fluoride single crystals. These crystal growth methods focus on supplying fluoride species as available entities within the solution rather than on combustion, and therefore results in oxidation states which are far more reasonable and stable. In fact, when coupled with the mild hydrothermal approach, fluoride reactions can create reducing conditions which leads to the formation of metal fluorides with metals in reduced oxidation states. This is primarily achieved by including an organic reducing agent along with aqueous HF as an activator. [32, 33] Some could contend that the use of aqueous HF is still quite dangerous; while it is true that HF is acutely toxic [34, 35], typically very little is needed in a hydrothermal reaction and since the vessel is sealed to the point of being air tight, the researcher is never exposed to HF vapor. Furthermore, most of the corrosive F^- ion is sequestered in the fluoride products, and any remaining F^- can be neutralized by treating the product liquid with $CaCl_2$, thereby rendering it safe.

Uranium Chemistry

In the early 20th century it was discovered that atoms of uranium could be split in a chain reaction, releasing enormous amounts of energy; thus sparking the atomic age of

humanity. Immediately there was an explosion in research on uranium and its chemistry. Much of the scientific research on uranium in these early days focused on three things: processing uranium ore for enrichment, enriching the natural uranium for use in reactors and weapons, and reprocessing spent fuel for re-use. These processes involved multiple chemical transformations from uranium ore (primarily U_3O_8 and UO_2) into UF_6 for enrichment, then reconversion to UO_2 for use as fuel. Eventually concerns over the destructive ability of nuclear weapons led to the Nuclear Non Proliferation Treaty, and reprocessing of spent fuel was stopped, leading to an increase in the amount of generated nuclear waste (which was already reaching a staggering amount). Today, the chemistry of uranium processing is well understood, however we are left with an unfortunate legacy: hundreds of millions of tons of nuclear waste. [36, 37] Faced with the realization that 'sequestered' waste from the original weapons and reactor programs have begun leaking after only a few decades, a new wave of research has begun trying to find a better way to deal with radioactive waste storage. [38]

Beginning to tackle this problem begins with increasing our understanding of solid-state uranium chemistry, including structural and bonding motifs of uranium in the presence of various ions: primarily oxygen and fluorine. Uranium oxides are the primary naturally occurring uranium materials. Many uranium-bearing minerals exist, including pure oxides, hydroxides, and silicates. Understanding uranium oxides is also important because UO_2 is still the primary form of uranium used in nuclear fuel. Uranium fluorides are of great industrial interest because uranium ores are converted to UF_4, then UF_6 (a gas) to be enriched.

Explorations into the chemistry of uranium have revealed a rich redox chemistry that underlies a range of interesting properties. Uranium can exhibit oxidation states between +3 and +6, although only +4 and +6 are common in extended structures. [39] U(VI) is by far the most common, often showing a bright neon yellow color with accompanying fluorescence. U(IV) is often green or brown (although other colors have been observed), is not luminescent, and is paramagnetic ($5f^2$ system) until a transition to a nonmagnetic single state around 100 K. U(V) is rare, but not unheard of and can appear anywhere from yellow to red. U(V) is also (possibly) fluorescent and magnetic ($5f^1$), and cannot exhibit the transition to a singlet state. Despite this, U(V) often displays van Vleck paramagnetism which is characterized by a loss of thermally populated excited states. Only simple binary U(III) materials are known to exist as extended structures, however U(III) has been hypothesized to have interesting magnetic behavior as it should not exhibit a nonmagnetic singlet state. Ultimately it has been found that the properties of uranium materials are extremely sensitive to the coordination environment of uranium. [40] This is a theme that will be explored in detail later in this work.

U(VI), the most common oxidation state of uranium, exists nearly ubiquitously as the uranyl ($[O=U=O]^{2+}$; UO_2^{2+}) ion. [41–43] U(V) can also exist as a uranyl species (UO_2^+), however it will not be discussed further. The uranyl ion consists of a uranium center double bonded to two oxide ligands (referred to from here on as uranyl oxygens) at roughly 180° apart. Since these are essentially a bond order of 2, the uranyl oxygens are relatively inert and do not often participate in additional bonding. Structures where uranyl oxides do participate in additional bonding are said to contain cation-cation interactions (CCI's). [44–46] CCI's are fairly rare, and so the uranyl group can be thought of a structure-

directing agent. Since the uranyl oxides are inert, the uranium center has no choice but to heavily utilize its equatorial plane to fill its coordination sphere, and these equatorial ligands are the only ones capable of further bonding. Thus, the presence of uranyl groups heavily favors the formation of 1D chain and 2D sheet structural units. Fluoride ligands cannot participate in double bonding, and therefore cannot be present as uranyl anions. This means that U(VI) fluorides must either be non-uranyl species (rare), or contain mixed oxide/fluoride ions (with uranyl oxides and equatorial fluorides). [47, 48] Uranyl sheet structures are particularly common and form what are known as uranyl sheet-anions. Much work has been done on classifying uranyl materials by the topology of their uranyl sheet anions. [49–51]

Uranyl materials are often (though not always) fluorescent, and have historically found use in niche applications that may seem odd today. For example, uranyl materials have been used in paint (due to their strong yellow color), photography (called uranotypes), and even in depression-era glassware (uranium glass). These niche applications have of course ceased due to the radioactivity and toxicity of uranium. Today, the only application for uranium is nuclear fuel, and uranyl compounds are the major component of nuclear waste.

The synthesis of uranyl compounds can be accomplished by a variety of routes. Uranyl materials readily form at high temperatures, so standard ceramic routes are straightforward. Uranyl compounds can also easily be synthesized via the flux crystal growth method, as many fluxes solubilize oxygen, which provides an oxidizing environment. Finally, it also possible to synthesize uranyl materials via hydrothermal reaction although some additional considerations must be made, especially when

15

attempting to incorporate fluorine. HF solutions are naturally slightly reducing, and U(VI) will readily reduce to U(IV) under these conditions. [52–54] In order to select U(VI) species in hydrothermal reaction, it is often best to perform growths under basic conditions as the hydroxide ion stabilizes the uranyl group.

U(IV) is larger than U(VI) and does not form uranyl bonds, so the bipyramidal geometries associated with uranyl chemistry are not as prevalent with U(IV) materials. U(IV) compounds tend to form irregular polyhedra with high coordination numbers (>8, although lower CN's are known). Given this, U(IV) structures are not directed in an obvious way and can form utilizing a wide variety of structural motifs. It is not uncommon to see 3D U(IV) materials, although layered and chain materials are also prevalent.

While U(VI) materials range from bright fluorescent yellow to orange and red in color, U(IV) materials can be brown, or purple, but most often range from light pale green to an intense emerald green color. This intense coloration is due primarily to *f-f* electronic transitions arising from the $5f^2$ nature of U(IV). These unpaired *f* electrons provide U(IV) with a magnetic moment, that is strengthened (from calculated spin-only moment values) due to Russel-Saunders coupling. Despite the fairly strong moment (~3.55 μ_B) and greater *f* orbital extent than the lanthanides, magnetic ordering in uranium materials is extremely rare. This is due to the fact that excited *f* orbital states become thermally depopulated at low temperatures, leading to a pairing of *f* electrons and a nonmagnetic singlet state. It is suspected that the onset of the singlet state is extremely dependent on the coordination environment (and thus crystal electric field effects).

16

Characterization of New Materials

When in the business of making materials that have never before been made, it is prudent to characterize them as completely as possible (or risk a room-temperature super conductor sitting unknown on a benchtop)! The ability to adequately characterize a material begins with determining the actual chemical composition and structure of the material. Often, these can be determined simultaneously using single-crystal X-ray diffraction (SXRD) (although it is helpful to get some insight into the elemental makeup of crystals first). Using modern instrumentation and software, researchers can theoretically work up a reaction, select a suitable crystal, collect a full data set and solve the crystal structure all within 24 hours (of course it often takes longer). This is in stark contrast to the early days of diffraction when solving a structure could take several years (and constitute a thesis on its own). This dramatic improvement is primarily due to two things: improvement in instrumentation, and small but powerful computers able to refine structural data quickly. Computerization has certainly been a boon for instrument design, but the most advantageous improvements to instrumentation has been the development of high-intensity (and yet relatively low power) X-ray sources which can enable the detection of low intensity reflections quickly, and large, sensitive area-detectors with superior signal-to-noise ratios.

Despite this, SXRD is still not a routine measurement and it takes time to select suitable crystals and properly align them in the X-ray beam. Furthermore, structure solution still relies a great deal on chemical intuition. For these reasons, it is often inconvenient to jump to SXRD as the first step in characterizing new materials. Instead, powder X-ray diffraction (PXRD) can be a powerful tool for quickly identifying solid-

17

state materials (if they have been previously made) and obtaining preliminary information regarding crystal symmetry and establishing if it is indeed a new material. Like SXRD, PXRD instruments benefit from low-power high-intensity X-ray sources, however they typically do not employ the same area-detectors as SXRD instruments. Instead, cutting-edge PXRD instruments utilize 1D strip detectors which can collect a publication quality diffraction pattern in under an hour, or a scan suitable for phase identification in as little as fifteen minutes. Furthermore, PXRD is an excellent method for confirming that bulk samples match the structures determined by SXRD.

Once the structure of a new material has been elucidated, it is up to the researcher to decide what property measurements should be performed, but in general as many characterizations as are appropriate should be done. Often the easiest measurements are optical spectroscopy measurements as they are performed using simple, relatively inexpensive instruments such as UV(Ultraviolet)/visible and FTIR (Fourier Transform Infrared) spectrometers. In cases where fluorescence is expected, a special UV/vis spectrometer (this instrument is set up as a standard UV/vis spectrometer, but with an additional detector to pick up emitted light) known as a fluorimeter can be used to quantify the fluorescent property. In general, these measurements rarely reveal earth-shattering properties, however they can be used to confirm structural features that are ambiguous based on the XRD patterns. For example, IR spectroscopy can be used to differentiate between water and hydroxyl groups by looking for H-O-H bending modes, and UV/visible spectroscopy can be used to tell the presence of many transition metal ions based on characteristic *d-d* absorption bands. Furthermore, UV/vis data can be used

18

to estimate the band gap of materials, which could reveal semiconducting or metallic behavior.

In addition to optical spectroscopy, thermogravimetric analysis (TGA) often reveals unexpected thermal behavior, and will give a good indication of the thermal stability of the new material. TGA can help determine if it is possible to dehydrate a crystal, and can reveal otherwise hidden polymorphic structural transitions. Such crystal-to-crystal transitions are fairly rare and often lead to a change in the observed properties.

In cases where a material contains ions with unpaired valence electrons (most transition metals, lanthanides, actinides where applicable), the magnetic properties can be probed using SQUID magnetometry. A SQUID (superconducting quantum interference device) magnetometer indirectly measures the magnetic moment of a material, and can perform moment versus temperature or moment versus field measurements. Typically, a suite of three measurements are performed for new materials: two moment versus temperature measurements, and one moment versus field measurement. The two moment versus temperatures measurements are called zero field-cooled (ZFC) and field-cooled (FC) measurements. These data are analyzed to give magnetic susceptibility versus temperature plots and provide insight into the presence and, if present, type of magnetic ordering in a material. The moment versus field (MvH) measurement is typically performed as a five-quadrant field sweep (start at zero field, increase to maximum field, decrease through zero to minimum field, increase through zero to maximum field) and is useful for determining subtle differences in ferro- and ferri- magnetic orderings.

Although SQUID magnetometry is a powerful technique, ultimately it is a bulk measurement and at best will give the sum of magnetic interactions in a substance. In

19

order to glean more precise information regarding the nature of magnetic ordering, neutron diffraction is necessary. Powder neutron diffraction (NPD) operates using the same principles as PXRD, however neutrons, unlike X-ray diffraction, possess a magnetic moment and therefore will diffract differently off electrons with spins of different orientations. This means that one can 'solve' a magnetic structure in much the same way as one can solve a crystal structure [55, 56], as electronic spins must follow the same symmetry laws as the atoms in a crystal lattice (although the magnetic spins are allowed to possess less symmetry than the atomic nuclei).

Beyond magnetic diffraction, using neutrons can be useful to glean structural information that may be difficult to obtain with X-rays. For example, X-ray scattering power has a direct relationship with the atomic number Z of an atom or ion. In principle this means that light atoms such as oxygen or hydrogen will be difficult to detect and their positions located, especially in the presence of heavy lanthanides or actinides. Neutron scattering lengths however do not follow the same rules and oxygen is quite easy to observe, no matter what other elements are present.

Ultimately, the goal of elucidating the structure and properties of new materials is to glean some information regarding structure-property relationships. Some of these relationships are well known: such as the fact that materials must crystallize in a non-centrosymmetric space group in order to be piezoelectric. Other properties like magnetic ordering have 'semi-quantitative' rules such as the Goodenough-Kanamori-Anderson (GKA) rules, but do not always apply or attempt to explain the origin of the property. It is for this reason that basic research into crystalline materials and their properties must continue.

Outline

This work will cover the synthesis of several new materials and their measured properties as well as attempt to use structure to justify the properties that have been observed. This work is divided into three parts based upon the type of anion(s) that are present in each material. Part 1 will primarily discuss novel transition metal fluorides (Chapters 2 and 3), although some uranium fluorides are also discussed (Chapter 4). Part 2 deals with mixed anionic oxyfluoride systems with Chapters 5 and 6 discussing transition metal materials and Chapter 7 focuses on new 1D uranyl oxyfluorides. Finally Part 3 delves into uranium oxides with Chapter 8 discussing $K_5U_5O_{17}(OH)$ and Chapters 9 and 10 discussuranium polyoxophosphorous materials. Appendices A, B, and C will detail the synthesis and structure of three materials which are already known.

References

(1) Muller, K.-H.; Krabbes, G.; Fink, J.; Grub, S.; Kirchner, A.; Fuchs, G.; Schultz, L. *J. Magn. Magn. Mater.* **2001**, *226*, 1370-1376.

(2) Kim, S.-G.; Priya, S.; Kanno, I. *MRS Bulletin* **2012**, *37*, 1039-1031.

(3) Huen, P.; Ravnsbæk, D. B. *Electrochemistry Communications* **2018**, *87*, 81-85.

(4) Gai, J.; Zhao, E.; Ma, F.; Sun, D.; Ma, X.; Jin, Y.; Wu, Q.; Cui, Y. *J. Eur. Ceram. Soc.* **2018**, *38*, 1673-1678.

(5) Parkin, I. P. *Chemistry & Industry* **1997**, *18*, 725-728.

(6) Levashov, E. A.; Mukasyan, A. S.; Rogachev, A. S.; Shtansky, D. V. *International Materials Reviews* **2016**, *62*, 203-239.

(7) Heise, M.; Scholz, G.; Düvel, A.; Heitjans, P.; Kemnitz, E. *Solid State Sciences* **2018**, *77*, 45-53.

(8) Pal, P.; Saha, S.; Banik, A.; Sarkar, A.; Biswas, K. *Chemistry* **2018**, *24*, 1811-1815.

(9) Morrison, G.; Abeysinghe, D.; Felder, J. B.; Egodawatte, S.; Ferreira, T.; zur Loye, H.-C. *Journal of the South Carolina Academy of Science* **2016**, *15*, 1.

(10) Chen, A. N.; Scanlan, M. M.; Skrabalak, S. E. *ACS Nano* **2017**, *11*, 12624-12631.

(11) Chernov, A. A. *J. Cryst. Growth* **2004**, *264*, 499-518.

(12) Lewis, B. *J. Cryst. Growth* **1974**, *21*, 29-39.

(13) Lewis, B. *J. Cryst. Growth* **1974**, *21*, 40-50.

(14) Bugaris, D. E.; zur Loye, H.-C. *Angew Chem Int Ed Engl* **2012**, *51*, 3780-3811.

(15) McMillen, C. D.; Kolis, J. W. *Dalton Transactions* **2016**, *45*, 2772-2784.

(16) Sanjeewa, L. D.; McGuire, M. A.; McMillen, C. D.; Garlea, V. O.; Kolis, J. W. *Chem. Mater.* **2017**, *29*, 1404-1412.

(17) Smith Pellizzeri, T. M.; McMillen, C. D.; Wen, Y.; Chumanov, G.; Kolis, J. W. *Inorg. Chem.* **2017**, *56*, 4206-4216.

(18) Terry, R.; Vinton, D.; McMillen, C. D.; Kolis, J. W. *Angew Chem Int Ed Engl* **2018**, *57*, 2077-2080.

(19) Chang, K. B.; Edwards, B. W.; Frazer, L.; Lenferink, E. J.; Stanev, T. K.; Stern, N.

P.; Nino, J. C.; Poeppelmeier, K. R. *J. Solid State Chem.* **2016**, *236*, 78-82.

(20) Cortese, A. J.; Wilkins, B.; Smith, M. D.; Yeon, J.; Morrison, G.; Tran, T. T.; Halasyamani, P. S.; zur Loye, H. C. *Inorg. Chem.* **2015**, *54*, 4011-4020.

(21) Holland, M.; Donakowski, M. D.; Pozzi, E. A.; Rasmussen, A. M.; Tran, T. T.; Pease-Dodson, S. E.; Halasyamani, P. S.; Seideman, T.; Van Duyne, R. P.; Poeppelmeier, K. R. *Inorg. Chem.* **2014**, *53*, 221-228.

(22) Yeon, J.; Kim, S.-H.; Halasyamani, P. S. *J Chem Crystallogr* **2011**, *41*, 328-331.

(23) Wang, S.; Wu, X.; Yuan, L.; Zhang, C.; Lu, D. *Cryst Eng Comm* **2017**, *19*, 6436-6442.

(24) Kim, S. W.; Zhang, R.; Halasyamani, P. S.; Hayward, M. A. *Inorg. Chem.* **2015**, *54*, 6647-6652.

(25) Kirik, S. D.; Zaitseva, Y. N.; Leshok, D. Y.; Samoilo, A. S.; Dubinin, P. S.; Yakimov, I. S.; Simakov, D. A.; Gusev, A. O. *Inorg. Chem.* **2015**, *54*, 5960-5969.

(26) Sayed, F. N.; Mandal, B. P.; Jayakumar, O. D.; Arya, A.; Kadam, R. M.; Dixit, A.; Naik, R.; Tyagi, A. K. *Inorg. Chem.* **2011**, *50*, 11765-11772.

(27) Underwood, C. C.; McMillen, C. D.; Chen, H.; Anker, J. N.; Kolis, J. W. *Inorg. Chem.* **2013**, *52*, 237-244.

(28) Huang, C. Z.; Liu, B.; Wen, L.; Zhuang, R. C.; Zhao, J. T.; Pan, Y.; Mi, J. X.; Huang, Y. X. *Inorg. Chem.* **2015**, *54*, 6978-6985.

(29) Tulsky, E. G.; Long, J. R. *Chem. Mater.* **2001**, *13*, 1149-1166.

(30) Tressaud, A.; Dance, J. M. *Advances in Inorganic Chemistry and radiochemistry* **1977**, *20*, 133.

(31) Peters, D.; Mithchen, R. *J. Fluorine Chem.* **1996**, *79*, 161.

(32) Yeon, J.; Smith, M. D.; Sefat, A. S.; Tran, T. T.; Halasyamani, P. S.; zur Loye, H. C. *Inorg. Chem.* **2013**, *52*, 8303-8305.

(33) Yeon, J.; zur Loye, H.-C. *J Chem Crystallogr* **2017**, *47*, 129-132.

(34) Bertolini, J. C. *J. Emerg. Med.* **1992**, *10*, 163.

(35) Segal, E. B. *Chem. Health Saf.* **2000**, *7*, 18.

(36) Meena, A. H.; Arai, Y. *Environ Chem Lett* **2017**, *15*, 241-263.

(37) Vasconcelos, R. G. W.; Beaudoin, N.; Hamilton, A.; Hyatt, N. C.; Provis, J. L.; Corkhill, C. L. *Applied Geochemistry* **2018**, *89*, 180-189.

(38) Li, Z.; Li, H.; Guan, X.; Tang, J.; Yusran, Y.; Li, Z.; Xue, M.; Fang, Q.; Yan, Y.; Valtchev, V.; Qiu, S. *J. Am. Chem. Soc.* **2017**, *139*, 17771-17774.

(39) Zachariasen, W. H. *Actinide Elements* **1954**, 769-796.

(40) Yeon, J.; Smith, M. D.; Tapp, J.; Möller, A.; zur Loye, H. C. *Inorg. Chem.* **2014**, *53*, 6289-6298.

(41) Alekseev, E. V.; Suleĭmanov, E. V.; Chuprunov, E. V.; Marychev, M. O.; Ivanov, V. A.; Fukin, G. K. *Crystallogr. Rep.* **2006**, *51*, 29-33.

(42) Read, C. M.; Morrison, G.; Yeon, J.; Smith, M. D.; zur Loye, H. C. *Inorg. Chem.* **2015**, *54*, 6993-6999.

(43) Wylie, E. M.; Burns, P. C. *Canadian Mineralogist* **2012**, *50*, 147-157.

(44) Alekseev, E. V.; Krivovichev, S. V.; Depmeier, W.; Siidra, O. I.; Knorr, K.; Suleimanov, E. V.; Chuprunov, E. V. *Angew Chem Int Ed Engl* **2006**, *45*, 7233-7235.

(45) Read, C. M.; Yeon, J.; Smith, M. D.; zur Loye, H.-C. *CrystEngComm* **2014**, *16*, 7259-7267.

(46) Volkringer, C.; Henry, N.; Grandjean, S.; Loiseau, T. *J. Am. Chem. Soc.* **2012**, *134*, 1275-1283.

(47) Brusset, H.; Nguyen, Q. D.; Sadok, C. *Acta Cryst.* **1974**, *B30*, 768.

(48) Chen, F.; Wang, C.; Shi, W.; Zhang, M.; Liu, C.; Zhao, Y.; Chai, Z. *CrystEngComm* **2013**, *15*, 8041.

(49) Liu, H. K.; Ramachandran, E.; Chen, Y. H.; Chang, W. J.; Lii, K. H. *Inorg. Chem.* **2014**, *53*, 9065-9072.

(50) Obbade, S.; Yagoubi, S.; Dion, C.; Saadi, M.; Abraham, F. *J. Solid State Chem.* **2004**, *177*, 1681-1694.

(51) Unruh, D. K.; Baranay, M.; Pressprich, L.; Stoffer, M.; Burns, P. C. *J. Solid State Chem.* **2012**, *186*, 158-164.

(52) Yeon, J.; Smith, M. D.; Sefat, A. S.; zur Loye, H. C. *Inorg. Chem.* **2013**, *52*, 2199-2207.

(53) Yeon, J.; Smith, M. D.; Tapp, J.; Möller, A.; zur Loye, H. C. *J. Am. Chem. Soc.* **2014**, *136*, 3955-3963.

(54) Yeon, J.; Smith, M. D.; Morrison, G.; zur Loye, H. C. *Inorg. Chem.* **2015**, *54*, 2058-2066.

(55) Kohlmann, H.; Hansen, T. C.; Nassif, V. *Inorg. Chem.* **2018**, *57*, 1702-1704.

(56) Petrillo, C.; Postorino, P.; Orecchini, A.; Sacchetti, F. *J. Magn. Magn. Mater.* **2018**, *449*, 552-557.

CHAPTER 2

COMPOSITIONAL AND STRUCTURAL VERSATILITY IN AN UNUSUAL FAMILY OF *ANTI*-PEROVSKITE FLUORIDES: [Cu(H$_2$O)$_4$]$_3$[(MF$_6$)(M'F$_6$)]*

Introduction

The chemistry of inorganic fluorides has been intensively pursued in order to create new mixed metal fluoride phases for a range of potential applications.[1-3] This widespread research activity peaked during the middle of the twentieth century before declining rapidly by the early 1970's. In those days the synthetic approaches often relied on the use of highly oxidizing elemental fluorine gas or anhydrous hydrogen fluoride to create materials containing elements in very high oxidation states.[4] This synthetic approach, while extremely successful, was ultimately tainted by the hazards of working with elemental fluorine and hydrogen fluoride gas, as well as by the inherent instability and frequently explosion prone products that resulted from this methodology. This earned fluorine chemistry a reputation for being quite dangerous and the rapid decline of inorganic fluorine research by the 1970's can be directly attributed to this reputation.

Despite the reputation of fluorine chemistry, there has been a slow resurgence in the number of groups conducting research focused on the synthesis of new inorganic fluorides in recent years, where the shift to safer synthesis methods that do not require the use of elemental fluorine, such as hydrothermal[5-8] and flux[9-12] crystal growth techniques, is largely responsible for this resurgence. Synthetic techniques such as these tend to result in compounds with less highly oxidized, and even reduced elements. In particular, many research groups have discovered that the simultaneous use of a mild hydrothermal method utilizing hydrofluoric acid as a fluorinating and complexing agent, together with an aqueous reducing agent, is highly successful for the synthesis of extended inorganic fluorides.[13-21]

27

The coordination of transition metals by fluorine can lead to the formation of complex anions, which may be used as structural building blocks in the formation of complex three-dimensional networks. The use of complex ions, furthermore, can result in interesting variations on known structure types, such as the perovskite structure, as described in this work. The simple cubic perovskite structure is best described by the ABX_3 stoichiometry, where A and B typically are monoatomic cations, while X is an anion, most commonly O^{2-}, although halide (including fluoride) perovskites are also quite numerous.[22-26] In the latter case, however, the small -3 charge resulting from the three halide ions per formula unit greatly limits the choice of cations that can be used in pure halide perovskites, such as $CsNiF_3$, as the sum of their oxidation states cannot exceed +3. The introduction of complex ions formed from metal fluoride coordination polyhedra greatly increases the variety of species that can be introduced into the family of fluoride perovskites, which opens up compositional opportunities along with increased potential for realizing specific physical properties in these materials.

Perovskites have been and continue to be studied extensively for optical properties,[27] piezoelectricity,[28] superconductivity,[29] ferromagnetism,[30] as well as other complex magnetic behaviors,[31] and the multitude of structural variations that they can exhibit. For example, the simple cubic single perovskite (ABX_3) can be modified in a number of different ways, including by changing the sizes of the A and B cations to induce monoclinic[32-35] tetragonal[36] or hexagonal[37] distortions, by doubling the formula to $A_2B_2X_6$ and placing additional cations into the structure to form $A_{2-x}A'_xB_{2-y}B'_yX_6$ double[31] perovskites or similar triple and quadruple perovskites,[38-40] by using mixed X and X' anions, and by introducing complex ions onto the traditional A, B, or X sites. The

structural *anti* designation is of particular importance to this work. The *anti* designation of the perovskite,[41, 42] or any other structure for that matter, is given when the positions of the cations and anions are reversed in the structure. Thus, in an *anti*-perovskite ABX$_3$ structure, the A and B sites that normally hold the cations are occupied by anions, while the X site that normally holds the anion is occupied by cations. *Anti*-perovskites have been shown to exhibit interesting magnetism[43] and superconductivity[44] and the perovskites reported in this work represent unusual examples of a complex *anti*-perovskite structure type.

Herein we report on a family of *anti*-perovskites of the form $[Cu(H_2O)_4]_3(M_{1-x}M'_xF_6)_2$ and report a new synthetic approach for the *anti*-perovskite phases $[Cu(H_2O)_4]_3(VF_6)_2$ **2.1**, $[Cu(H_2O)_4]_3(CrF_6)_2$ **2.2**, $[Cu(H_2O)_4]_3(MnF_6)_2$ **2.3**, and $[Cu(H_2O)_4]_3(FeF_6)_2$ **2.4**,[45, 46] as well as two novel bi-metal compositions, $[Cu(H_2O)_4]_3(FeF_6)(VF_6)$, **2.5** and $[Cu(H_2O)_4]_3(Fe_{1.09}F_6)(Cr_{0.91}F_6)$ **2.6**. The synthesis, structures and magnetic properties are discussed.

Experimental

Materials and Method

V$_2$O$_5$ (Alfa Aesar, 99.6%), CrF$_3$•xH$_2$O (Alfa Aesar), MnF$_3$ (Alfa Aesar, 98%), FeF$_3$ (Alfa Aesar, 99%), Cu(CH$_3$CO$_2$)$_2$•H$_2$O (Sigma Aldrich, 98+%), CuF$_2$ (Alfa Aesar, 99.5%), NaF (Alfa Aesar, 99%), and HF (EMD, 48%) were used as received.

Caution: Hydrofluoric acid is acutely toxic and corrosive, and must be handled with extreme caution and while using appropriate protective gear. If contact with the liquid or vapor occurs, proper treatment procedures should immediately be followed and medical attention should be immediately sought.[47-49]

Compound **1** was synthesized using a 1:8 molar ratio of vanadium (V) oxide to copper (II) acetate. 2 molar equivalents of sodium fluoride were added as a mineralizer.

29

Compounds **2.2,** and **2.4** were synthesized using a 2:3 metal precursor to copper (II) acetate ratio. The exact metal precursors are listed in Table 2.1. The synthesis for **2.3** was identical except copper (II) fluoride was used instead of copper (II) acetate. The two bi-metal phases **2.5** and **2.6** were synthesized using a 1:1:3 iron (III) fluoride to metal precursor to copper ratio. Table 2.1 lists the exact species and quantities used for all syntheses.

For all reactions the solid reagents were combined with 1 mL of deionized water in a 23 mL PTFE vessel. 1 mL of hydrofluoric acid was added slowly to the vessel after all other reagents had been combined. The vessel was then sealed in a stainless steel autoclave and placed inside a programmable oven. The oven was ramped from room temperature to 200° C at a rate of 8.0° C/minute, dwelled for 24 hours, followed by slow cooling at a rate of 0.1° C/minute to 40° C, at which point the oven was shut off and cooled naturally to room temperature. Once cool, the autoclave was removed and the vessel was carefully opened. The product crystals were isolated by decanting the mother liquor followed by vacuum filtration. The solid product was washed thoroughly with deionized water and acetone, respectively. The resulting liquid waste was treated with calcium chloride to precipitate the fluoride ions as calcium fluoride.

Single-Crystal X-Ray Diffraction

X-ray diffraction intensity data from block shape crystals of **2.1, 2.2,** and **2.4** were measured at room temperature on a Bruker SMART APEX diffractometer (Mo Kα radiation, λ = 0.71073 Å). The raw area detector data frames were processed with

30

Table 2.1: Synthetic Precursors for Compounds 2.1-2.6

Compound	Reagent 1	Amount	Reagent 2	Amount	Copper Source	Amount
1	V_2O_5	1 mmol	NaF	2 mmol	$Cu(CH_3CO_2)_2$	8 mmol
2	$CrF_3 \bullet x H_2O$	2 mmol	N/A	N/A	$Cu(CH_3CO_2)_2$	3 mmol
3	MnF_3	2 mmol	N/A	N/A	CuF_2	3 mmol
4	FeF_3	2 mmol	N/A	N/A	$Cu(CH_3CO_2)_2$	3 mmol
5	V_2O_5	½ mmol	FeF_3	1 mmol	$Cu(CH_3CO_2)_2$	3 mmol
6	$CrF_3 \bullet x H_2O$	1 mmol	FeF_3	1 mmol	$Cu(CH_3CO_2)_2$	3 mmol

SAINT+. An absorption correction based on the redundancy of equivalent reflections was applied to the data with SADABS.[50] The reported unit cell parameters were determined by least-squares refinement of a large array of reflections taken from each data set. Difference Fourier calculations and full-matrix least-squares refinement against F^2 were performed with SHELXTL.[51]

X-ray intensity datasets for **2.3, 2.5,** and **2.6** were collected at 100(2) K using a Bruker D8 QUEST diffractometer equipped with a PHOTON 100 CMOS area detector and an Incoatec microfocus source (Mo Ka radiation, $\lambda = 0.71073$ Å).[41] The detector was operated in the shutterless mode with an additional low-angle 'fast-scan' to account for overtopped pixels. Data collections covered the full sphere of reciprocal space to $2\theta_{max} = 72.8º$ (d = 0.60 Å), with an average reflection redundancy of at least 8.0. The raw area detector data frames were reduced and corrected for absorption effects using the SAINT+ and SADABS programs. [50] Final unit cell parameters were determined by least-squares refinement of large sets (> 9800) of reflections taken from the data sets. An initial structural model was obtained with SHELXS using direct methods.[51] Subsequent difference Fourier calculations and full-matrix least-squares refinement against F^2 were performed with SHELXL-2014[51] using the ShelXle interface.[51]

The compounds are isostructural and crystallize in the space group *P*-1 (No. 2) of the triclinic system. No indication of an alternative (larger) unit cell was observed from careful inspection of indexed data frames and precession images. The asymmetric unit of the structures consist of three independent copper atoms and two independent metal atom sites, or mixed metal (M/M') atom sites (for **2.5** and **2.6**), all located on crystallographic

32

inversion centers, six fluorine and six oxygen and twelve independent hydrogen atoms, all located on general positions. Alternatively, the asymmetric unit consists of half each of three $Cu(H_2O)_4^{2+}$ cations and half each of two $(M,M')F_6^{3-}$ anions, with the cations and anions located on crystallographic inversion centers. After identification of the basic structure, each dataset was evaluated for metal atom site mixing as follows. The metal atoms in both independent $(M,M')F_6^{3-}$ anions (site M1 = Wyckoff position 1c, site M2 = position 1f) were initially set as either (a) 100% iron or (b) 100% V or Cr. The site occupation factors (*sofs*) for the (a) "Fe" or (b) "V or Cr" sites were then refined. Model (a) resulted in a significant decrease from 100% occupancy by iron (average over both independent sites ca. 0.92(1) for the **2.5** dataset and 0.95(1) for the **2.6** dataset). For model (b) the M' *sof* refined to greater than 100% (ca. 1.10(1) for M' = V and 1.06(1) for M' = Cr). These observations were interpreted as statistical Fe/M' site mixing occurring on both independent anion sites. For the final refinements, the total site occupancy was constrained to one and the ratio of Fe to V or Cr was refined for each site. This yielded physically sensible values and is therefore preferred to manually fixing both sites at 50% Fe / 50% M'. No deviation from full occupancy was observed for the three independent copper atoms sites in either dataset. All non-hydrogen atoms were refined with anisotropic displacement parameters. Hydrogen atoms were located in difference maps and refined isotropically with O-H distances restrained to be approximately equal (SHELX SADI instructions). The largest residual electron density peaks and holes in the final difference maps are: **2.3** dataset, +0.52 and -0.57 e-/Å3, located 0.58 Å from F3 and 0.69 Å from Cu2, respectively, **2.5** dataset, +0.43 and -0.59 e-/Å3, located 0.63 Å from V1/Fe1 and 0.59 Å from Cu2, respectively, **2.6** dataset, +0.59 and -0.57 e-/Å3, located

0.65 Å from Cu1 and 0.72 Å from Cu3, respectively. Table 2.2 gives structure refinement details for all reported compounds

Powder X-Ray Diffraction

Powder X-ray diffraction (PXRD) data were collected on polycrystalline samples ground from the product single crystals. Data were collected on a Rigaku Ultima IV diffractometer utilizing Cu K_α radiation. The data were collected over the range 10° to 65° 2θ, with a step size of 0.02°.

Optical Properties

UV/visible spectra were recorded using a Perkin-Elmer lambda 35 UV/visible scanning spectrophotometer used in diffuse reflectance mode equipped with an integrating sphere. Diffuse reflectance spectra were recorded in the 200 nm – 900 nm range. Reflectance data was converted to absorbance by the instrument via the Kubelka-Munk function.[52] All optical measurements were performed on polycrystalline powders obtained by grinding the product single crystals.

Energy Dispersive Spectroscopy (EDS)

EDS was performed on product single crystals using a Tescan Vega-3 SEM equipped with a Thermo EDS attachment. The SEM was operated in low-vacuum mode. Crystals were mounted on an SEM stud with carbon tape, and analyzed using a 30 kV accelerating voltage and a 20 second accumulating time.

34

Table 2.2: Crystallographic Data for Compounds 2.1-2.6

Compound	1	2	3	4	5	6
Empirical Formula	$[Cu(H_2O)_4]_3(VF_6)_2$	$[Cu(H_2O)_4]_3(CrF_6)_2$	$[Cu(H_2O)_4]_3(MnF_6)_2$	$[Cu(H_2O)_4]_3(FeF_6)_2$	$[Cu(H_2O)_4]_3(FeF_6)(VF_6)$	$[Cu(H_2O)_4]_3(Fe_{1.09}F6)(V_{0.91}F_6)$
Color	Green	Green	Dark Red	Blue	Green	Green
Crystal Size (mm)	0.24 x 0.16 x 0.08	0.20 x 0.16 x 0.08	0.14 x 0.10 x 0.08	0.32 x 0.16 x 0.12	0.22 x 0.20 x 0.18	0.22 x 0.18 x 0.16
Formula Weight (g/mol F.U.)	736.69	738.81	744.69	746.51	741.65	743.01
Temperature	294(2) K	294(2) K	100(2) K	294(2) K	100(2) K	100(2) K
Wavelength	0.71073 Å	0.71073 Å	0.71073 Å	0.71073 Å	0.71073 Å	0.71073 Å
Crystal System	Triclinic	Triclinic	Triclinic	Triclinic	Triclinic	Triclinic
Space Group	P-1	P-1	P-1	P-1	P-1	P-1
Unit Cell Parameters:						
a (Å)	7.5088(2)	7.4725(2)	7.5023(3)	7.5077(4)	7.4684(4)	7.4527(3)
b (Å)	7.6077(2)	7.5977(2)	7.5151(3)	7.6132(4)	7.5767(3)	7.5692(4)
c (Å)	8.1254(2)	8.1009(2)	8.1081(3)	8.1249(4)	8.0918(4)	8.0839(4)
α (°)	88.9660(10)	89.3160(10)	88.4530(11)	89.1900(10)	88.8324(14)	88.9921(14)
β (°)	89.8530(10)	89.9300(10)	89.8350(12)	89.8460(10)	89.9075(15)	88.9745(14)
γ (°)	87.1710(10)	87.13	87.3294(12)	87.0530(10)	86.8817(14)	86.8181(15)
Volume (Å^3)	463.52(2)	459.31(2)	456.48(3)	463.74(4)	457.11(4)	455.25(4)
Z	1	1	1	1	1	1
Density (calculated)	2.639 Mg/m^3	2.671 Mg/m^3	2.709 Mg/m^3	2.673 Mg/m^3	2.694 Mg/m^3	2.710 Mg/m^3
Absorption Coefficient	4.523 mm^{-1}	4.729 mm^{-1}	4.952 mm^{-1}	5.077 mm^{-1}	4.870 mm^{-1}	4.989 mm^{-1}
Reflections Collected	6379	6304	31127	6300	36030	35705
Independent Reflection	2284	2270	4900	2283	4469	4456
Data/Restraints/Parameters	2284/0/188	2270/0/188	4900/66/188	2283/0/188	4469/66/190	4456/66/190
Goodness-of-Fit on F^2	1.088	1.076	1.014	1.087	1.089	1.072
Final R Indices	$R_1 = 0.0283$ $wR_2 = 0.0805$	$R_1 = 0.0279$ $wR_2 = 0.0801$	$R_1 = 0.0266$ $wR_2 = 0.0485$	$R_1 = 0.0259$ $wR_2 = 0.0700$	$R_1 = 0.0202$ $wR_2 = 0.0457$	$R_1 = 0.0207$ $wR_2 = 0.0463$
Largest diff. Peak and Hole	0.799 and -0.789 e$^-$/Å^3	0.728 and -1.015 e$^-$/Å^3	0.516 and -0.573 e$^-$/Å^3	0.681 and -1.031 e$^-$/Å^3	0.431 and -0.589 e$^-$/Å^3	0.591 and -0.573 e$^-$/Å^3

Magnetism

Magnetic property measurements were performed on a Quantum Design MPMS 3 SQUID magnetometer. Field cooled (FC) and zero-field cooled (ZFC) magnetic susceptibility measurements were taken from 2K – 300K in an applied field of 0.1 T. Magnetization measurements were taken at 2K with the applied field sweeping from -5 T – 5 T. The raw data was corrected for radial offset and sample shape effects according to the method described by Morrison.[53] All magnetic data was collected on polycrystalline powders obtained by grinding the product single crystals.

Results and Discussion

Synthetic Considerations

The synthesis of single crystals of the six compositions was achieved using a variation of the method used by Kummer and Babel to synthesize phases **2.1**, **2.2**, and **2.4**,[45] and quite different from the one used to synthesize phase **2.3**,[46] which involved dissolving the reactants in hot HF and evaporating the liquid until crystallization occurred. Our method provides a way to synthesize all of the reported compounds (**2.1-2.6**) without the necessity of varying the temperature profile. In addition, the method of synthesizing compound **2.3** is greatly improved, as there is no risk of exposure to HF vapor during the synthesis. While the previous method for synthesizing **2.3** was indeed successful, it is our experience that the mild hydrothermal method described in this paper produces higher quality crystals in greater yield than did the evaporative technique reported previously.

All product crystals were formed in excellent yield, greater than 90%. The reducing conditions of the synthesis created by the interplay between HF and the acetate ion was sufficient to produce metallic copper as a small impurity. The product crystals are easily large enough to be physically separated; alternatively, the copper metal impurity can readily be dissolved in concentrated nitric acid without substantially affecting the product crystals.

Energy Dispersive Spectroscopy (EDS) and Powder X-Ray Diffraction (PXRD)

EDS was performed for the purpose of qualitative non-destructive elemental analysis. Elemental analysis confirmed the presence of all metals in the reported phases. This was especially important for compounds **2.5** and **2.6**, which are visually indistinguishable from **2.1** and **2.2**. EDS confirmed the presence of V, Fe, and Cu in **2.5** as well as Cr, Fe, and Cu in **2.6**, demonstrating that these crystals contained mixed vanadium and iron and mixed chromium and iron, respectively.

Powder diffraction patterns of the six compositions were collected and compared to the calculated powder pattern generated from the respective crystallographic information (CIF) files. The data matched the generated pattern, as shown in Figure 2.1, which illustrates the powder patterns in comparison with the calculated data.

Crystal Structure

All six reported compounds are isostructural with only minor differences in unit cell parameters, bond lengths and angles. Compound **2.3** is slightly different in that it contains a second Jahn-Teller ion (Mn^{3+}), in addition to the Jahn-Teller distorted copper

37
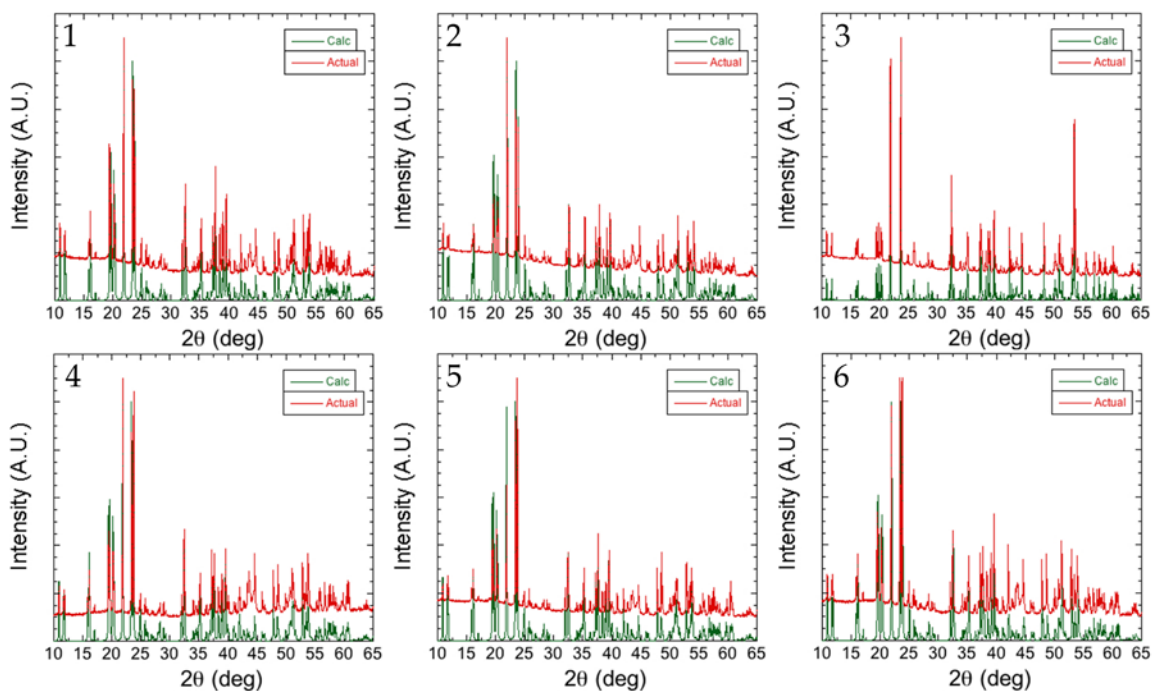
Figure 2.1: PXRD Patterns for Compounds 2.1-2.6. The PXRD patterns of materials 2.1-2.6 (red) compared to their respective CIF's (green). The experimental and calculated patterns are in excellent agreement with no extra peaks, indicating phase purity and a high degree of crystallinity.

ion that is present in all six materials. The presence of a second Jahn-Teller ion does not significantly impact the structure however. Compounds **2.5** and **2.6** are structurally distinct due to the presence of two types of complex metal anions. The crystal structure will be described in a general fashion, as it is the same for all six compounds, and the description will emphasize its connection to the perovskite structure type. Compounds **2.5** and **2.6** be discussed in detail to describe the positions of the different metal centers within the crystal structure. Table 2.3 lists selected bond distances for the reported compounds.

The structure is built up of complex ions that are formed from metal coordination polyhedra. The complex ions form units that are denoted 'A', 'B', and 'X', to correspond with the crystallographic sites typically associated with the perovskite structure. In this example, the A and B units are composed of the same ion, which is uncommon among perovskites; typically A is larger than B.

The X site is composed of $[Cu(H_2O)_4]^{2+}$ square planar ions, of which an example is shown in Figure 2.2. These square planes are arranged in a fashion similar to how oxide ions are arranged in a cubic perovskite structure, the difference being the X site complexes are much further apart (nearest neighbor coppers ~5.2 – 5.5 Å) than are close packed oxide ions. Nevertheless, the arrangement of X complexes forms large octahedral holes in which the B site $(MF_6)^{3-}$ ions sit. Figure 2.3 is a representation of the local inner-sphere coordination of the B site metal. The B site ions are coordinated to each of the six surrounding X site complexes through a bridging fluoride, which forms a large octahedron around the B site anion. Figure 2.4 shows an example of the large octahedron created by the outer coordination sphere of the B site metal. This is consistent with the

39

six-coordinate environment of the B site in a typical perovskite structure.

The large $(MF_6)[Cu(H_2O)_4)]_6$ octahedra are corner shared to each other through the X site copper complexes forming infinite M-F-Cu-F-M chains that run in all three dimensions, forming a network of corner sharing octahedra. Each X site is shared by two B site ions, so the octahedra can be written $(MF_6)[Cu(H_2O)_4)]_{6/2}^{3+}$, forming a cationic framework. This framework of octahedra has large voids in the center of a cube formed by eight cone.cted octahedra. Figure 2.5 shows the three-dimensional framework of the perovskite structure. The A site $(MF_6)^{3-}$ ions sit within these voids, and balance the positive charge of the BX_3 framework. As previously discussed, the A and B sites are occupied by the same type of complex ion $(MF_6)^{3-}$, which is rare in perovskites. A structural depiction of this ion can be reviewed in Figure 2.2. In a typical cubic perovskite, the A site is coordinated to 12 oxide ions, which are part of the B site octahedra. In this case, the copper X site complexes are too far from the A site ions to form true bonds, however there are hydrogen bonding interactions between the hydrogen atoms of the $[Cu(H_2O)_4)]^{2+}$ complex and the fluoride ions of the A site $(MF_6)^{3-}$ ions. In fact, each A site ion is hydrogen bonded to 12 unique X site complexes: the same X site ions that they would be bonded to in a typical perovskite. Figure 2.6 illustrates the twelve X complexes that the A site is hydrogen bonded to. Figure 2.7 shows an overall structural representation of the reported materials in comparison to a typical cubic perovskite.

Compounds **2.5** and **2.6** are isostructural with **2.1-2.4**, however they possess two different trivalent complex anions, MF_6^{3-} and $M'F_6^{3-}$. Due to the minute difference in ionic radii between V^{3+} and Fe^{3+}, and Cr^{3+} and Fe^{3+}, there is no segregation of the different cations to different crystallographic sites. Instead, the A and B sites contain

40

Table 2.3: Interatomic Distances (Å) in Compounds 2.1-2.6

Compound	1	2	3	4	5	6
Cu – X*						
Cu(1) – O(1)	1.9772(15)	1.9789(15)	1.9626(9)	1.9802(12)	1.9726(8)	1.9768(8)
Cu(1) – O(2)	1.9841(16)	1.9778(16)	1.9771(10)	1.9811(13)	1.9861(7)	1.9837(8)
Cu(1) – F(1)	2.2034(12)	2.2034(12)	2.2199(7)	2.2006(10)	2.1903(6)	2.1887(6)
Cu(2) – O(3)	1.9405(16)	1.9353(16)	1.9586(10)	1.9369(13)	1.9398(8)	1.9383(8)
Cu(2) – O(4)	1.9680(16)	1.9634(17)	1.9678(10)	1.9665(13)	1.9685(7)	1.9660(8)
Cu(2) – F(3)	2.4026(12)	2.426(1)	2.3294(8)	2.4139(10)	2.3928(6)	2.4059(6)
Cu(3) – O(5)	1.9469(15)	1.9514(16)	1.9426(9)	1.9505(12)	1.9477(7)	1.9506(8)
Cu(3) – O(6)	1.9760(16)	1.9667(16)	1.9848(10)	1.9712(13)	1.9771(8)	1.9730(8)
Cu(3) – F(2)	2.3275(12)	2.3268(12)	2.3358(8)	2.3294(10)	2.3185(6)	2.3193(6)
M – F	**Monometallic Phases**				**Bimetallic Phases**	
M(1) – F(1)	1.8932(12)	1.8900(12)	1.8178(7)	1.8980(10)	**V:** 1.8931(6) **Fe:** 1.8931(6)	**Cr:** 1.9382(6) **Fe:** 1.8907(6)
M(1) – F(2)	1.9484(11)	1.9208(11)	1.9064(7)	1.9471(10)	**V:** 1.9464(6) **Fe:** 1.9464(6)	**Cr:** 1.9382(6) **Fe:** 1.9382(6)
M(1) – F(3)	1.9979(12)	1.9373(11)	2.1122(8)	1.9748(10)	**V:** 1.9923(6) **Fe:** 1.0023(6)	**Cr:** 1.9616(6) **Fe:** 1.9616(6)
M(2) – F(4)	1.9167(13)	1.9036(13)	1.8468(8)	1.9204(11)	**V:** 1.9173(6) **Fe:** 1.9173(6)	**Cr:** 1.9119(6) **Fe:** 1.9119(6)
M(2) – F(5)	1.9315(12)	1.9054(12)	1.8701(7)	1.9269(10)	**V:** 1.9268(6) **Fe:** 1.9268(6)	**Cr:** 1.9165(6) **Fe:** 1.9165(6)
M(2) – F(6)	1.9786(13)	1.9227(12)	2.0930(8)	1.9584(10)	**V:** 1.9730(6) **Fe:** 1.9730(6)	**Cr:** 1.9432 (6) **Fe:** 1.9432(6)

*X = O,F
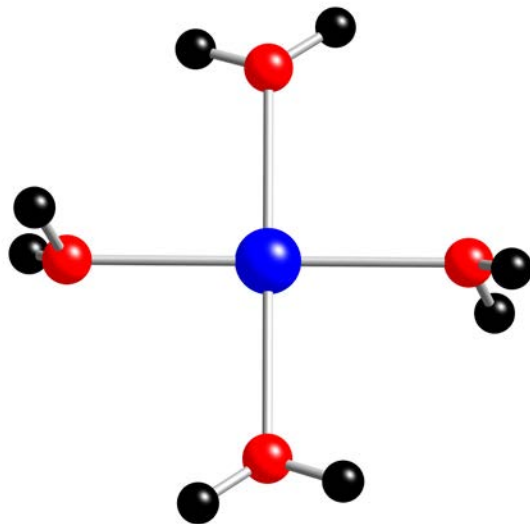
Figure 2.2: Local Coordination of Cu^{2+} in Compounds 2.1-2.6. The local coordination environment of Cu^{2+} in the title compounds. The copper ion is coordinated by four neutral aqua ligands, giving the complex an overall 2+ charge. The $[Cu(H_2O)_4]^{2+}$ complex comprises the X site in the title perovskite. Copper is shown in blue, oxygen in red, and hydrogen in black.

42
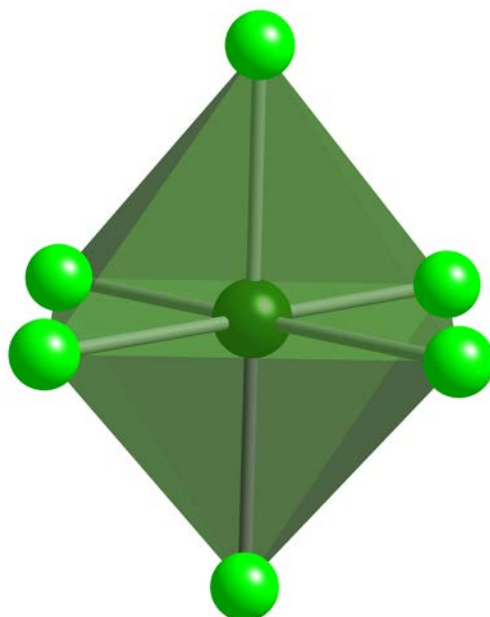
Figure 2.3: Local Coordination of the M^{3+} Ion in Compounds 2.1-2.6. The local coordination environment of the A and B site metals. In all cases (except for **2.3**, which shows an elongation of the axial bonds due to the Jahn-Teller effect) the metals are present in regular octahedra. This coordination polyhedron represents the inner coordination sphere, and has an overall 3- charge. M^{3+} is shown in dark green and fluorine is shown in bright green.
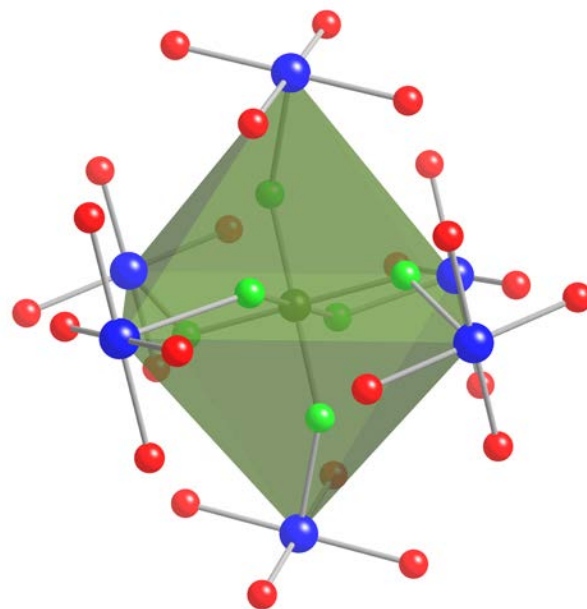
Figure 2.4: B Site Coordination in Compounds 2.1-2.6. The B site metal ion within its outer coordination polyhedron (shown as the green octahedron). Each $(M\mathrm{F}_6)^{3-}$ octahedron is coordinated to six X site copper complexes via a fluorine bridge. The long Cu-F bonds are explained by the Jahn-Teller distorted d^9 Cu^{2+} ion. The B site metal is shown in dark green, copper in blue, oxygen in red, and fluorine in bright green. Hydrogen atoms are omitted for clarity.

44
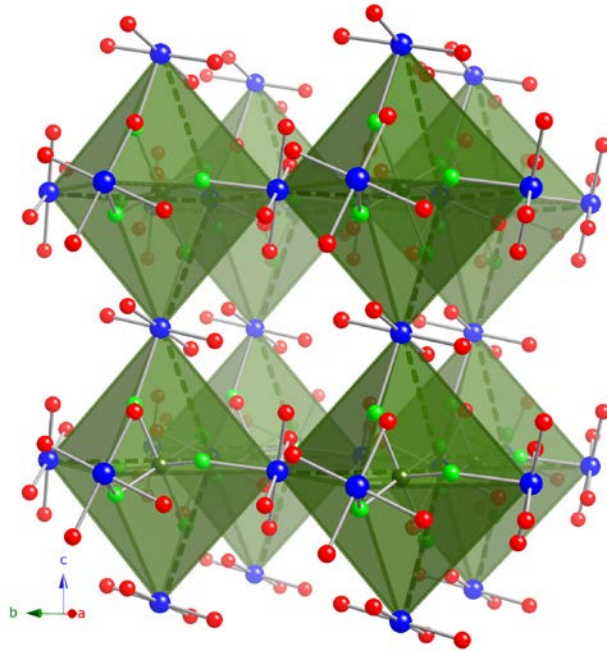
Figure 2.5: The BX₃ Cationic Framework of Compounds 2.1-2.6. The cationic framework in the reported materials. The B site octahedra are corner shared via the copper X site complexes. The framework forms large voids in the center of four octahedra. Each copper complex is shared by two octahedra, and the framework has an overall 3+ charge. The B site metal is shown in dark green, copper in blue, oxygen in red, and   fluorine   in   bright   green.   Hydrogens   are   omitted   for   clarity.
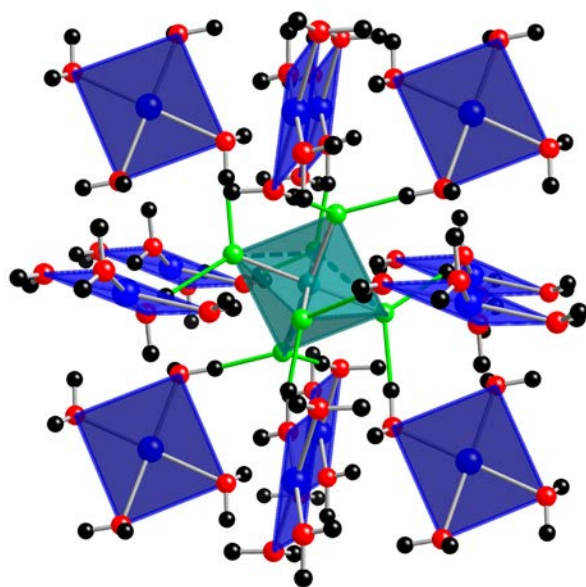
Figure 2.6: 12-Coordinate Second-Sphere Coordination of the A Site of Compounds 2.1-2.6. The A site metal anion surrounded by twelve square planar copper X site complexes. Each fluorine in the A site ion is hydrogen bonded to two separate X site ions, bringing the outer sphere coordination number of the A site to 12, consistent with a cubic perovskite. Hydrogen bonds are shown in bright green for clarity. The A site metal is shown in teal, copper square planar complexes are shown as blue squares, oxygen is shown in red, fluorine in bright green, and hydrogen in black.
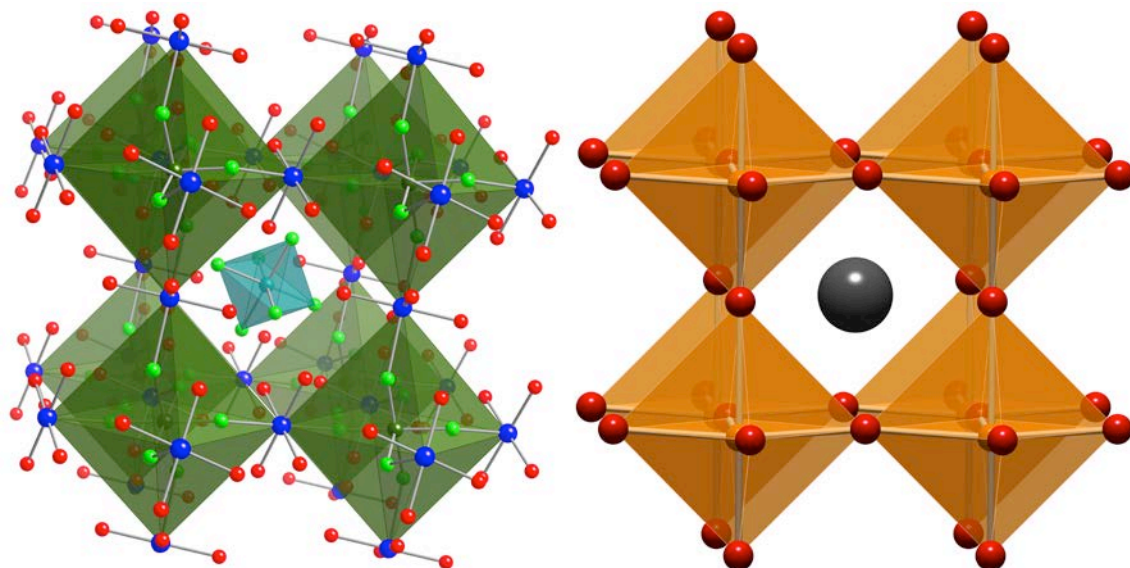
Figure 2.7: Comparison of Compounds 2.1-2.6 with a Cubic Perovskite. An overall representation of the reported *anti*-perovskites (*left*) in comparison to a typical cubic perovskite (*right*). *Left:* B site ions are shown as large green octahedra, A site ions are small teal octahedra, and X site ions are blue spheres. Oxygen is shown in red, fluorine in bright green. Hydrogen has been omitted for clarity. *Right:* A cation shown in grey, B polyhedra in blue, and oxygen in red.

roughly equal quantities of the two metals (V and Fe for **2.5**, and Cr and Fe for **2.6**). Compounds **2.5** and **2.6** can be written as $[Cu(H_2O)_4]_3(M_{2-x}M'_xF_6)_2$ to take into account the site mixing. In compound **2.5**, M = Fe and M' = V where x = 0.995. In this case there is a nearly equal amount of V and Fe in the structure. There is a slight excess of vanadium on the $M(1)$ (B) site, and conversely a slight excess of iron on the $M(2)$ (A) site. For compound **2.6**, M = Fe and M' = Cr, where x = 0.91, indicating a slight excess of iron across both crystallographic metal sites.

Optical Properties

The UV/visible spectra were interpreted using the Tanabe-Sugano diagrams[54] for d^2 (V^{3+}), d^3 (Cr^{3+}), d^4 (Mn^{3+}), and d^5 (Fe^{3+}) metal complexes. Cu^{2+} is d^9 with only one allowed electronic transition. Figure 2.8 shows the UV/visible spectra for all of the reported compounds. All of the reported materials show an intense absorption band at ~800 nm. This band is due to the $^2E_g \square ^2T_{2g}$ transition of Cu^{2+}. All the reported materials show an absorption edge below ~350 nm. The optical band gaps are shown in Table 4. In addition, there are absorptions between the absorption edge and copper absorption that is due to the M^{3+} *d-d* electronic transitions. Table 2.4 also lists the assignments of these peaks based on the Tanabe-Sugano diagrams.

Magnetic Properties

The reported *anti*-perovskite phases all exhibit complex magnetism. Magnetic susceptibility measurements were collected on all samples in an applied field of 0.1 T, over the temperature range of 2 K – 300 K. Full range susceptibility plots showing FC and ZFC measurements for compounds **2.1-2.6** can be found in Figure 2.9. A Curie-

48

Weiss fit was performed on the inverse susceptibility data using the 150 K – 300 K temperature range. Table 2.5 contains the results of the linear regression for all reported materials. Figure 2.10 shows magnetization plots for all materials.

Compounds **2.1-2.4** have two magnetic ions, a M^{3+} species and Cu^{2+}. Compounds **2.5** and **2.6** have three magnetic ions: 2 different M^{3+} species and one Cu^{2+}. The B site ions are connected with each other via the copper X site ions in a three dimensional structure. This forms M^{3+}-F-Cu^{2+}-F-M^{3+} chains, which run in all three dimensions. Superexchange interactions have been well documented to occur in fluorides[55] and it is reasonable to expect that magnetic coupling via the superexchange mechanism can occur in this system. The Goodenough-Kanamori-Anderson (GKA) Rules[55] provide a set of semi-quantitative guidelines for determining the type of magnetic interactions present in a system with magnetic coupling via superexchange. According to the GKA rules, strong antiferromagnetic coupling is to be expected when magnetic ions are bonded at 180° apart. This antiferromagnetic interaction is weakened as the bond angles deviate from 180°, opening up the potential for other interactions to prevail. Compound **2.1** contains V^{3+} and Cu^{2+}, possessing 2 and 1 unpaired electrons, respectively. No magnetic ordering is observed in this compound, although there is very slight deviation from Curie-Weiss behavior below 10 K, which accounts for the slightly negative Weiss temperature. Compound **2.2** also does not display magnetic ordering; in fact it is a model paramagnet. The Weiss temperature of **2.2** is nearly exactly 0 K, exemplifying its Curie-Weiss behavior through 2 K. The calculated spin-only magnetic moments agree well with the observed magnetic moment, attained from the Curie-Weiss fit of the inverse magnetic susceptibility data.

49
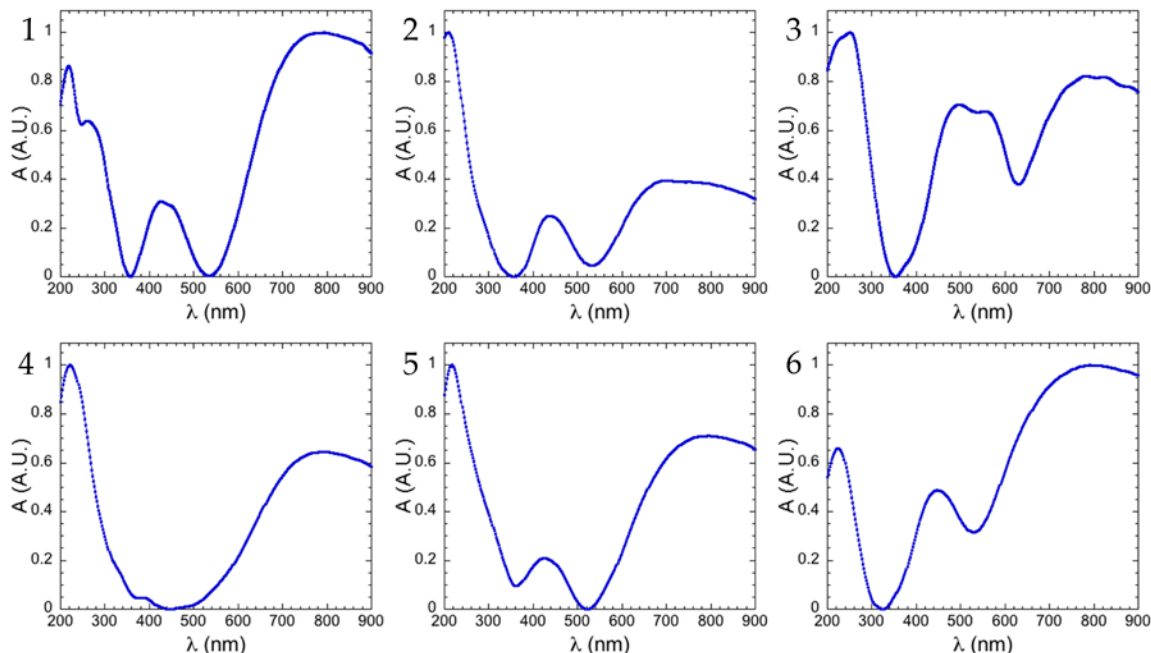
Figure 2.8: UV-Visible Spectra for Compounds 2.1-2.6. The normalized UV/Visible spectra for compounds **2.1-2.6**. All compounds show an absorption edge at low wavelength, a M^{3+} specific *d-d* absorption, and an absorption corresponding to Cu^{2+}. Table 1.4 details these absorbances.

Table 2.4: UV-Vis Band Assignments for Compounds 2.1-2.6

Compound	Band Gap	UV/vis Peak and Assignment	
1	3.48 eV	λ_{max} = 426, 264 nm	$^3T_{1g} \rightarrow {}^3T_{2g}$, $^3T_{1g} \rightarrow {}^3T_{1g}$ (^3P)
2	3.51 eV	λ_{max} = 439 nm	$^4A_{2g} \rightarrow {}^4T_{2g}$
3	3.49 eV	λ_{max} = 496 nm	$^5E_g \rightarrow {}^5T_{2g}$
4	3.41 eV	None	No Spin-Allowed Transitions
5	3.43 eV	λ_{max} = 426 nm	$^3T_{1g} \rightarrow {}^3T_{2g}$
6	3.96 eV	λ_{max} = 447 nm	$^5E_g \rightarrow {}^5T_{2g}$
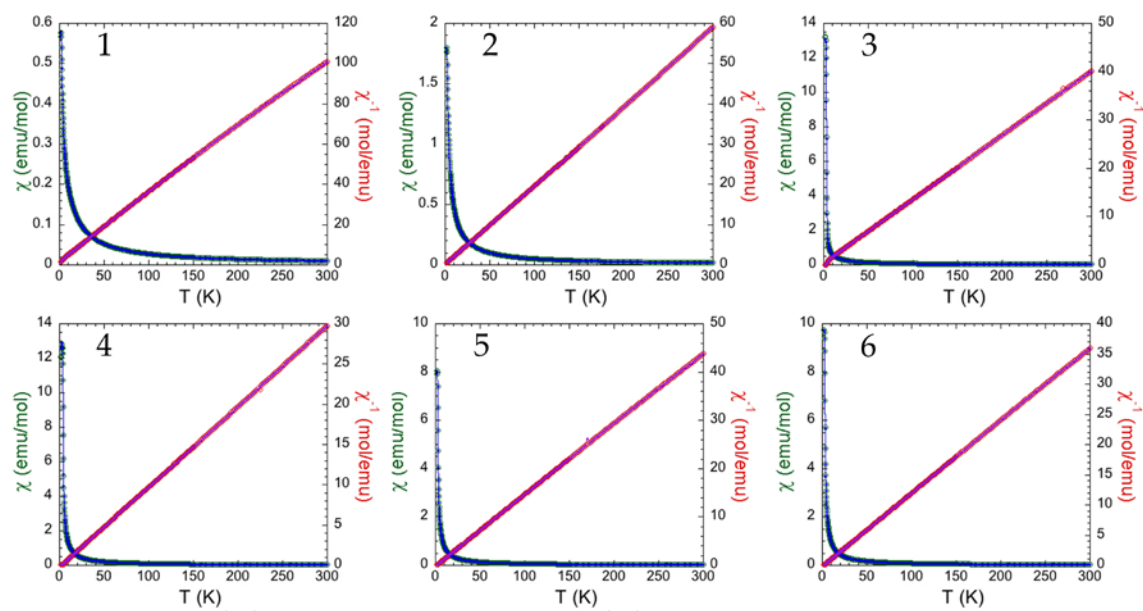
50

Figure 2.9: Magnetic Susceptibility Data for Compounds 2.1-2.6. The magnetic susceptibility and inverse magnetic susceptibility of materials **2.1-2.6**. Both the field cooled and zero-field cooled data is shown, and overlay perfectly for all materials except **2.3**, which shows slight field dependence at 2 K.

Table 2.5: Curie-Weiss Constants for Compounds 2.1-2.6

Compound	1	2	3	4	5	6
μ_{eff} (μ_B/F.U.)	4.88	6.39	7.78	8.95	7.43	8.17
μ_{calc}* (μ_B/F.U.)	5.00	6.24	7.55	8.89	7.21	7.80
θ		-6.7 K	-0.6 K	-2.2 K	2.3 K	-2.7	-0.9 K

*Moment calculated from spin-only values
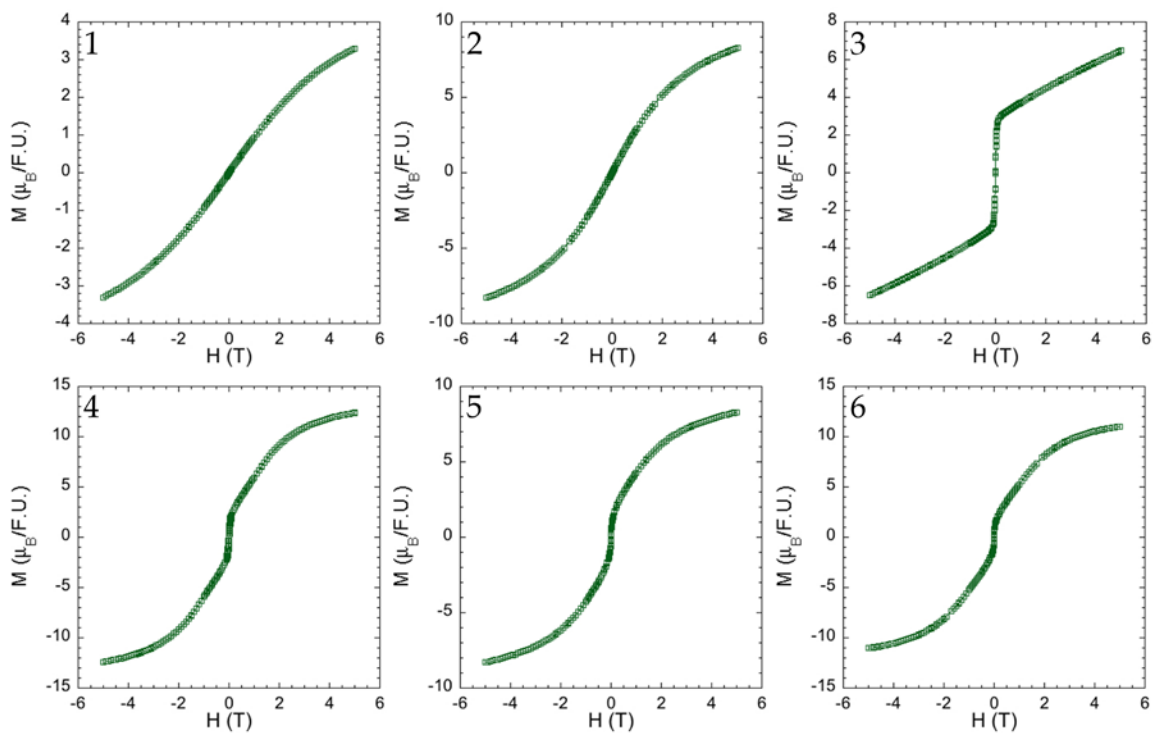
Figure 2.10: Magnetization Data for Compounds 2.1-2.6. The magnetization plots for materials **2.1-2.6**. Five quadrant measurements were performed at 2 K for all reported compounds.

Compound **2.3**, which contains Mn^{3+}, exhibits more complicated magnetic behavior. It has been observed that magnetically coupled ions can undergo a cooperative Jahn-Teller effect[56]. This cooperative effect may be ferrodistortive, which results in antiferromagnetic coupling, or antiferrodistortive, which in turn leads to ferromagnetic coupling. Ferrodistortive ordering occurs between two Jahn-Teller ions where the elongated (axial) axis of one ion is bonded to the non-elongated (equatorial) axis of the other ion. Since the Mn^{3+} ions are bonded to Cu^{2+} ions through a fluoride bridge (both of which exhibit a strong Jahn-Teller effect), this cooperative distortive effect is expected. In fact, **2.3** exhibits ferrodistortive ordering, consisting of the elongated Cu-F bonds being connected to the short Mn-F bonds, shown in Figure 2.11. Compound **3** displays Curie-Weiss behavior above ~10 K, and deviates significantly from Curie-Weiss behavior at temperatures below 10 K. At ~5.8 K there is a ferromagnetic deviation, followed by a sharper antiferromagnetic deviation at 3.8 K. The magnetic susceptibility and inverse susceptibility are shown in Figure 2.12. The paper by Nunez *et al*[46] provides an in depth analysis of the magnetism of this sample, however in our sample, consisting of ground crystals, we do not observe the spontaneous magnetization they report below 4 K. Instead, the FC and ZFC data agree perfectly down to 2 K, and no hysteresis is observed, even at 2 K. Figure 2.13 shows the magnetization plot. It is likely that the magnetic ordering is due to antiferromagnetic interactions. This notion is strengthened by the fact that the Mn^{3+} and Cu^{2+} Jahn-Teller ions are arranged in a ferrodistortive manner, which is expected to lead to antiferromagnetic ordering, suggesting that the observed magnetization is due to a canted antiferromagnetic spin alignment. Despite the ferrodistortive ordering of the crystal structure, there is a clear ferromagnetic-like

53
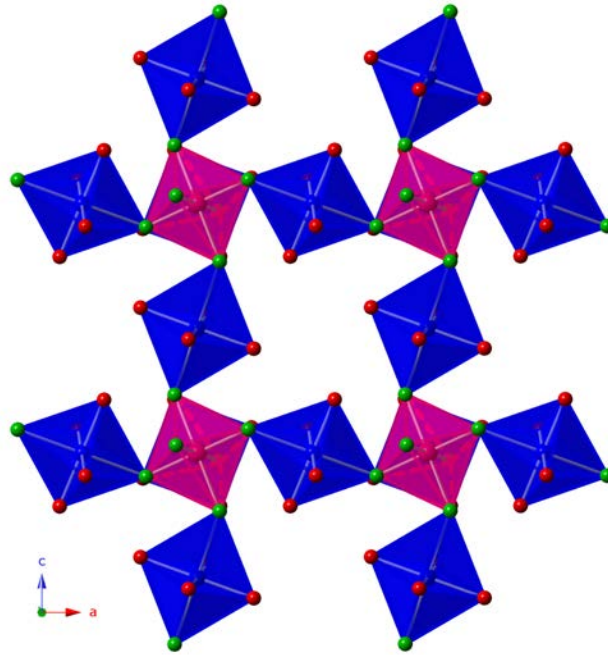
Figure 2.11: Ferrodistortive Ordering in 2.3. A view down the *b* crystallographic axis showing ferrodistortive ordering. Ferrodistortive ordering occurs between two Jahn-Teller ions where elongated (axial) axis of one is bonded to the non-elongated (equatorial) axis of the other. Manganese is shown as purple octahedra, copper is shown as blue octahedra, oxygen is shown in red, fluorine in bright green, and hydrogens have been omitted for clarity.
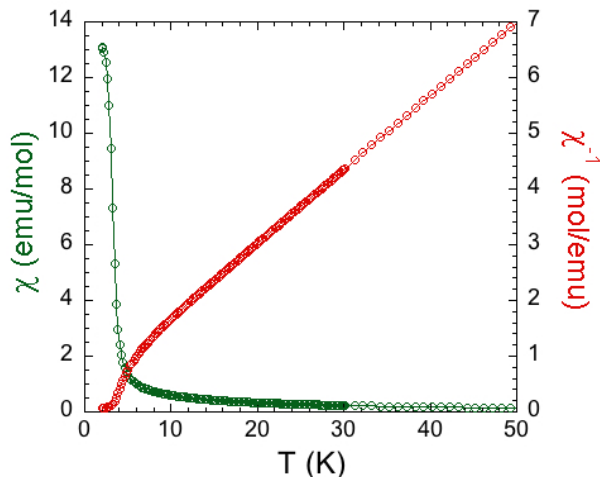
Figure 2.12: Low Temperature Susceptibility of 2.3. The magnetic susceptibility and inverse susceptibility data for **2.3**. Data was collected in a ZFC measurement with a 0.1 T applied field. The temperature range is 2 K to 50 K to highlight the low temperature magnetic transitions at ~8 K and 3.8 K. Magnetic transitions can be clearly seen in the inverse susceptibility (red).

55
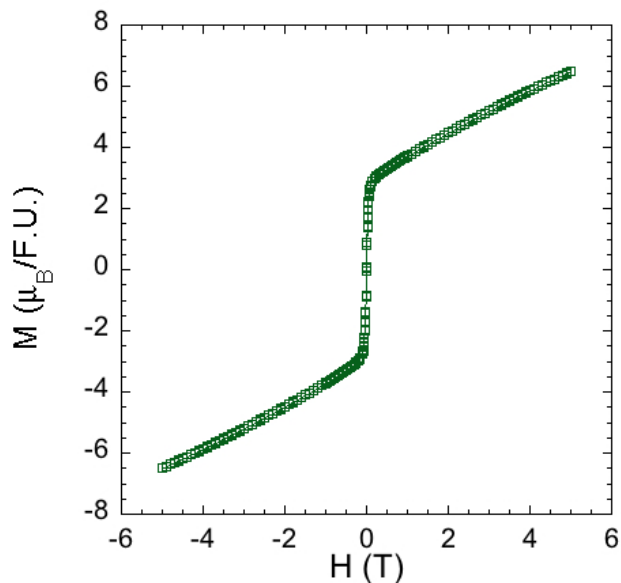
Figure 2.13: Magnetization of 2.3. The magnetization plot for compound **3**. The applied field swept from -5 T – 5 T, and the measurements were taken at 2 K. The magnetization plot shows ordering corresponding to a sharp jump in magnetization at low fields. There is no hysteresis, indicating an antiferromagnetic ordering. Above the ordering, there is a linear dependence with field that does not saturate, even at 5 T.

56
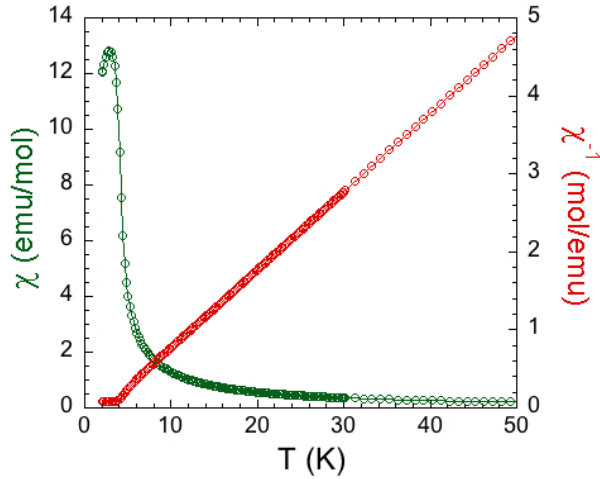
Figure 2.14: Low Temperature Susceptibility of 2.4 The magnetic susceptibility and inverse susceptibility plot of **2.4**. Data was collected in a ZFC measurement with a 0.1 T applied magnetic field. Data is shown in the range of 2 K – 50 K to highlight the antiferromagnetic transition at ~3.8 K.

transition ~9 K, which can be seen in Figure 2.12. As canted spins are likely for Mn^{3+} and Cu^{2+} based on the Mn-F-Cu bond angles of ~124°, we suppose that this is due to a canted antiferromagnetic ordering of the spins. The magnetic susceptibility plot for compound **2.4** is shown in Figure 2.14. Fe^{3+} is not a Jahn-Teller ion and so the cooperative effect is not to be expected. There is, however, a distinct antiferromagnetic magnetic transition ~ 4 K, which is accompanied by a weak field dependence at 2 K. This field dependence is replicated in the magnetization plot, although the coercive field is quite weak. The observed field dependence is likely due to a small degree of spin-canting of the antiferromagnetic interactions. The magnetization plot is shown in Figure 2.15.

Compounds **2.5** and **2.6** each possess two trivalent metals in addition to divalent copper. The magnetic ions are disordered, which could interfere with any magnetic ordering. **2.5** contains vanadium and iron, and is paramagnetic, following Curie-Weiss behavior all the way to 2 K. Likewise, **2.6** appears to follow the paramagnetic regime across most temperatures. Unlike **2.5** however, there is slight deviation from Curie-Weiss behavior at low temperature, similar to the deviation found in **2.4**. Figure 2.16 shows the magnetic susceptibility and inverse magnetic susceptibility data. This is potentially due to the presence of excess iron in **2.6**, which could contribute to some localized magnetic ordering at low temperatures. It was expected that materials **2.5** and **2.6** would display similar magnetic properties to compound **2.4**, due the similarity in structure and the presence of Fe(III) in the B site; however any magnetic interactions that occur arise below 2 K, thus we cannot see them. It is possible that compounds **2.5** and **2.6** possess a similar magnetic structure, but that the interactions are weakened by the severe disorder across the metal(III) sites.

58
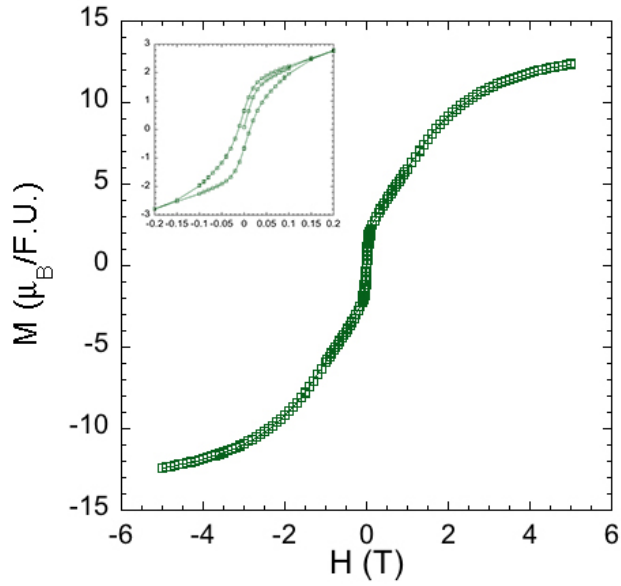
Figure 2.15: Magnetization of 2.4. The magnetization plot of **2.4**. Data was collected at 2 K in fields ranging from -5 T – 5 T. Material **2.4** shows magnetic ordering accompanied by weak hysteresis, which is shown in the inset. The material saturates at high field with a moment of 12.3 μ_B/F.U.
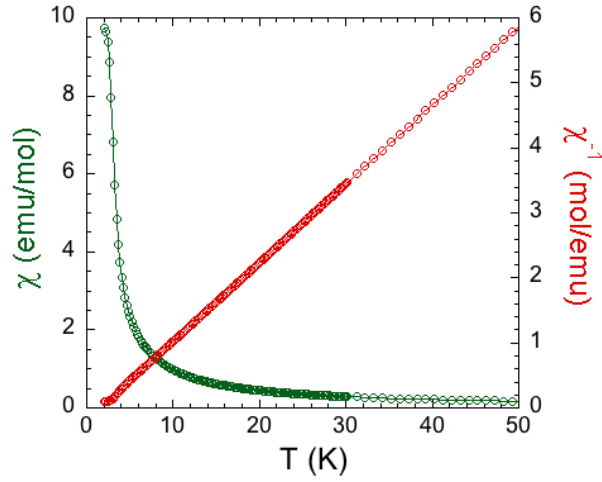
Figure 2.16: Low Temperature Susceptibility of 2.6. The magnetic susceptibility and inverse magnetic susceptibility of **2.6**. Data was taken from a ZFC measurement in an applied field of 0.1 T. Data is shown from 2 K – 50 K. There is a slight transition just above 2 K that appears to be antiferromagnetic in nature.

Altogether it is extremely difficult to derive the spin-structure of magnetic materials from bulk measurements, such as SQUID magnetometry, except in the clearest of cases and typically neutron scattering data are collected to determine the magnetic structures. To enable such measurements, we are in the process of preparing deuterated samples of **2.3** and **2.4** to use neutron diffraction studies to determine the magnetic structure of these materials and to understand the underlying nature of the observed magnetic phenomena.

Acknowledgements

References

(1) Iorgulescu, M.; Roussel, P.; Tancret, N.; Renaut, N.; Tiercelin, N.; Mentre, O. *J. Solid State Chem.* **2013**, *198*, 210-217.

(2) Blank, H. R.; Frank, M.; Geiger, M.; Greneche, J. M.; Ismaier, M.; Kaltenhaeuser, M.; Kapp, R.; Kreische, W.; LeBlanc, M. *Z. Naturforsch., A: Phys. Sci.* **1994**, *49*, 361-366.

(3) Lieser, G.; Biasi, L. D.; Gesswein, H.; Indris, S.; Draeger, C.; Schroeder, M.; Glatthaar, S.; Ehrenberg, H.; Bindera, J. R. *J. Electrochem. Soc.* **2014**, *161*, A1869-A1876.

(4) Leblanc, M.; Maisonneuve, V.; Tressaud, A. *Chem. Rev.* **2015**, *115*, 1191-1254.

(5) Underwood, C. C.; McMillen, C. D.; Chen, H.; Anker, J. N.; Kolis, J. W. *Inorg. Chem.* **2013**, *52*, 237-244.

(6) Sayed, F. N.; Mandal, B. P.; Jayakumar, O. D.; Arya, A.; Kadam, R. M.; Dixit, A.; Naik, R.; Tyagi, A. K. *Inorg. Chem.* **2011**, *50*, 11765-11772.

(7) Kirik, S. D.; Zaitseva, Y. N.; Leshok, D. Y.; Samoilo, A. S.; Dubinin, P. S.; Yakimov, I. S.; Simakov, D. A.; Gusev, A. O. *Inorg. Chem.* **2015**, *54*, 5960-5969.

(8) Kim, S. W.; Zhang, R.; Halasyamani, P. S.; Hayward, M. A. *Inorg. Chem.* **2015**, *54*, 6647-6652.

(9) Latshaw, A. M.; Hughey, K. D.; Smith, M. D.; Yeon, J.; zur Loye, H.-C. *Inorg. Chem.* **2015**, *54*, 876-884.

(10) Xia, M.; Li, R. K. *J. Solid State Chem.* **2016**, *233*, 58-61.

(11) Suzuki, S.; Teshima, K.; Wakabayashi, T.; Nishikiori, H.; Yubuta, K.; Shishido, T.; Oishi, S. *Cryst. Growth Des.* **2011**, *11*, 4825-4830.

(12) Wang, X.; Liu, L.; Wang, X.; Bai, L.; Chen, C. *Cryst. Eng. Comm.* **2015**, *17*, 925-929.

(13) Yeon, J.; Smith, M. D.; Sefat, A. S.; Tran, T. T.; Halasyamani, P. S.;zur Loye, H.-C. *Inorg. Chem.* **2013**, *52*, 8303-8305.

(14) Yeon, J.; Smith, M. D.; Tapp, J.; Moller, A.;zur Loye, H.-C. *J. Am. Chem. Soc.* **2014**, *136*, 3955-3963.

(15) Yeon, J.; Smith, M. D.; Tapp, J.; Moller, A.;zur Loye, H.-C. *Inorg. Chem.* **2014**, *53*, 6289-6298.

(16) Yeon, J.; Felder, J. B.; Smith, M. D.; Morrison, G.;zur Loye, H.-C. *Cryst. Eng. Comm.* **2015**, *17*, 8428-8440.

(17) Yeon, J.; Smith, M. D.; Morrison, G.;zur Loye, H.-C. *Inorg. Chem.* **2015**, *54*, 2058-2066.

(18) Leblanc, M.; Ferey, G.; Pape, R. D. *Mater. Res. Bull.* **1984**, *19*, 1581-1590.

(19) Ding, M.; Chen, D.; Wan, Z.; Zhou, Y.; Zhong, J.; Xi, J.; Ji, Z. *J. Mater. Sci.* **2015**, *50*, 6779-6785.

(20) Ge, L.; Yuan, L.; Huang, K.; Feng, W.; Feng, H.; Feng, S. *New J. Chem.* **2015**, *39*, 5080-5083.

(21) Li, H.; Hia, Z.; Shi, C. *Chem. Lett.* **2000**, *9*, 1106-1107.

(22) Oleaga, A.; Salazar, A.; Skrzypek, D. *J. Alloys Compd.* **2015**, *629*, 178-183.

(23) Slavney, A. H.; Hu, T.; Lindenberg, A. M.; Karunadasa, H. I. *J. Am. Chem. Soc.* **2016**, *138*, 2138-2141.

(24) Mitzi, D. B.; Feild, C. A.; Schlesinger, Z.; Laibowitz, R. B. *J. Solid State Chem.* **1995**, *114*, 159-163.

(25) Smith, E. H.; Benedek, N. A.; Fennie, C. J. *Inorg. Chem.* **2015**, *54*, 8536-8543.

(26) Mortier, M.; Piriou, B.; Buzare, J. Y.; Rousseau, M.; Gesland, J. Y. *Phys. Rev. B* **2003**, *67*, 115126.

(27) Wang, Y.; Chen, Z.; Ye, Z.; Huang, J. Y. *J. Cryst. Growth* **2012**, *341*, 42-45.

(28) Delorme, F.; Bah, M.; Schoenstein, F.; Jean, F.; Jabli, M. Z.; Monot-Laffez, I.; Giovannelli, F. *Mater. Lett.* **2016**, *162*, 24-27.

(29) Rubel, M. H. K.; Takei, T.; Kumada, N.; Ali, M. M.; Miura, A.; Tadanaga, K.; Oka, K.; Azuma, M.; Yashima, M.; Fujii, K.; Magome, E.; Moriyoshi, C.; Kuroiwa, Y.; Hester, J. R.; Avdeev, M. *Chem. Mater.* **2016**, *28*, 459-465.

(30) Nagata, Y.; Yashiro, S.; Mitsuhashi, T.; Koriyama, A.; Kawashima, Y.; Samata, H. *J. Magn. Magn. Mater.* **2001**, *237*, 250-260.

(31) Ferreira, T.; Morrison, G.; Yeon, J.; zur Loye, H.-C. *Cryst. Growth Des.* **2016**, *16*, 2795-2803.

(32) Davis, M. J.; III, S. J. M.; Glab, K. I.; Smith, M. D.; zur Loye, H.-C. *Solid State Sci.*

63

2004, *6*, 413-417.

(33) Currie, R. C.; Vente, J. F.; Frikkee, E.; Ijdo, D. J. *J. Solid State Chem.* **1995**, *116*, 199-204.

(34) Samuel J. M III.; Smith, M. D.;zur Loye, H.-C. *J. Solid State Chem.* **2005**, *178*, 200-206.

(35) Samuel J. M. III; Fox, A. H.; Smith, M. D.;zur Loye, H.-C. *J. Solid State Chem.* **2010**, *183*, 465-470.

(36) Yu, R.; Hojo, H.; Okaa, K.; Watanuki, T.; Machida, A.; Shimizu, K.; Nakano, K.; Azuma, M. *Chem. Mater.* **2015**, *27*, 2012-2017.

(37) Takeda, Y.; Kanamaru, F.; Shimada, M.; Koizumi, M. *Acta Cryst.* **1976**, *B32*, 2464-2466.

(38) Casallas, F. M.; Vera-Lopeza, E.; Tellez, D. A. L.; Mesa, D. E. S.; Roa-Rojas, J. *J. Phys. Conf. Ser.* **2014**, *480*, 012034.

(39) Yamada, I.; Murakami, M.; Hayashi, N.; Mori, S. *Inorg. Chem.* **2016**, *55*, 1715-1719.

(40) Kim, M. K.; Moon, J. Y.; Choi, H. Y.; Oh, S. H.; Lee, N.; Choi, Y. J. *J. Phys.: Condens. Matter* **2015**, *27*, 426002.

(41) Sullivan, E.; Avdeev, M.; Blom, D. A.; Gahrs, C. J.; Green, R. L.; Hamaker, C. G.; Vogt, T. *J. Solid State Chem.* **2015**, *230*, 279-286.

(42) Chen, Z.; Huang, R.; Chu, X.; Wu, Z.; Liu, Z.; Zhou, Y.; Li, L. *Cryogenics* **2012**, *52*, 629-631.

(43) Houben, A.; Sepelak, V.; Becker, K.-D.; Dronskowski, R. *Chem. Mater.* **2009**, *21*, 784-788.

(44) Bendjemil, B. *Int. J. Self-Propag. High-Temp Synth.* **2010**, *19*, 52-56.

(45) Kummer, S.; Babel, D. *Z. Naturforsch.* **1987**, *42b*, 1403-1410.

(46) Nunez, P.; Tressaud, A.; Darriet, J.; Hagenmuller, P.; Massa, W.; Kummer, S.; Babel, D. *J. Solid State Chem.* **1988**, *77*, 240-249.

(47) Bertolini, J. C. *J. Emerg. Med.* **1992**, *10*, 163.

(48) Peters, D.; Miethchen, R. *J. Fluorine Chem.* **1996**, *79*, 161.

(49) Segal, E. B. *J. Chem. Health Saf.* **2000**, *7*, 18.

(50) B., H. C.; M., S. G.; B., B. *J. Appl. Cryst.* **2011**, *44*, 1281-1284.

(51) M., S. G. *Acta Cryst.* **2008**, *A64*, 112-122.

(52) Kubelka, P.; Munk, F. Z. *Tech. Phys.* **1931**, *12*, 593.

(53) Morrison, G.;zur Loye, H.-C. *J. Solid State Chem.* **2015**, *221*, 334-337.

(54) Tanabe, Y.; Sugano, S. *J. Phys. Soc. Jpn.* **1956**, *11*, 864-877.

(55) Tressaud, A.; Dance, J. M. *Adv. Inorg. Chem. Radiochem.* **1977**, *20*, 133-188.

(56) Reinen, D.; Friebel, C. *Struct. Bond.* **1979**, *37*, 26-40.

CHAPTER 3

MAGNETIC AND THERMAL BEHAVIOR OF A FAMILY OF COMPOSITIONALLY
RELATED ZERO-DIMENSIONAL FLUORIDES*

Introduction

The hydrothermal synthesis method has been used to great effect in order to synthesize a host of new materials exhibiting a wide variety of properties. [1–6] Hydrothermal synthesis is a term that encompasses a large array of synthetic conditions with one commonality: they all employ superheated water as a solvent. Traditional hydrothermal syntheses make use of high-temperature high-pressure autoclaves to create supercritical water. [7–9] These supercritical water reactions have been extremely effective for exploring the phase space of many materials since the supercritical fluid has is able to dissolve and crystallize a number of materials, including highly refractory ones. [8]

As effective as this method has been, it has a high cost to entry into the field due to the necessity of acquiring specialized equipment. Furthermore, without the proper expertise these supercritical reactions can easily result in violent depressurizations of the reaction vessel. For these reasons, many researchers have turned to the so-called mild hydrothermal approach. The mild hydrothermal method involves utilizing (relatively) inexpensive PTFE (polytetrafluoroethylene) lined autoclaves as reaction vessels and lower temperatures (and thus lower pressures). The superheated water in a mild reaction (100° - 250° C) does not have the dissolving power of a supercritical fluid (>374° C), however by carefully choosing the starting reagents researchers have shown that these milder reactions can result in a wealth of new materials, including oxides and fluorides[10-12].

It has been well documented that introducing fluoride ions into a system can result in dimensional reduction, or 'cutting' a high-dimensional structure into lower-dimensional units[13, 14]. Fluorine's ability to effect this dimensional reduction is a

function of its size and its charge: it is large enough to fit into the same coordination environments as oxygen, but with half the anionic charge it is easily charge balanced by metal centers (especially highly oxidized metal centers). These effects cause fluorine to be more likely to occupy terminal positions than oxygen, which drive the 'cutting' effect. Within the field of fluorine chemistry, these phenomena are colloquially known as the 'Tailor effect'. [13] These cutting and Tailor effects have been used to direct the formation of low-dimensional materials, although less so for systematic investigations directed at synthesizing dimensionally reduced materials under mild hydrothermal conditions. [15]

In this work we report the formation of materials with completely isolated metal coordination polyhedra: so-called 'zero-dimensional' structures. In essence, these are pseudo-molecular inorganic structures where metal centers are bound to inorganic ligands to form coordination polyhedra; however these polyhedra are connected only *via* intermolecular forces, H-bonds in this case. Although we believe the presence of fluorine in this structure certainly contributed to the zero-dimensionality of these crystals, the large number of aqua ligands is likely similarly responsible. Aqua ligands are electrically neutral, and greatly prefer terminal positions. This should, in theory, give rise to an even more pronounced 'Tailor effect' than from fluorine alone, as they take up coordination sites without contributing any anionic charge.

Zero-dimensional crystals are an interesting class of materials because researchers usually associate many properties, for example long-range magnetism, with certain multiple dimensionality features. In zero-dimensional crystals these features are often missing, and the structural units are completely isolated. This would lead one to think that zero-dimensional crystals would have few interesting properties, however the literature

68

shows that this is not the case as these types of materials have been shown to exhibit fascinating electrical and magnetic properties. [16]

Herein we report the syntheses, crystal structures, optical, thermal, and magnetic properties of four new zero-dimensional fluoride-based structures with antiferromagnetic ordering. Table 3.1 lists each stoichiometry along with a number assignment, which will be used to refer to these materials from this point forward.

Experimental

Synthesis

The following materials were used as received without further modification: $Ni(CH_3COO)_2 \bullet 4H_2O$ (98%, Aldrich), MnF_3 (98%, Alfa Aesar), $CrF_3 \bullet xH_2O$ (Alfa Aesar), FeF_3 (99%, Alfa Aesar), V_2O_5 (99.6%, Alfa Aesar), and HF (48%, EMD).

Caution!! HF is corrosive and acutely toxic. HF exposure causes severe burns that may not be immediately painful, and may cause permanent injury or death. Appropriate personal protective equipment should be worn at all times when handling HF, and proper technique for using HF safely should always be followed. [17–19]

3.1-3.4 were synthesized using a mild hydrothermal crystal growth technique. The syntheses were carried out in 23 mL PTFE crucibles that were loaded with appropriate amounts of the starting materials. Typically, the metal precursors were mixed in a 1:1 molar ratio with 1 mL of distilled water. Secondly, 1 mL of HF was added slowly to the aqueous mixture. After loading, the crucibles were closed and placed inside stainless steel

69

Table 3.1: Reported Materials for Chapter III and their Number Assignments

Material Number Assignment	Material Composition
3.1	$[Ni(H_2O)_6]_2[MnF_6][MnF_4(H_2O)_2]$
3.2	$[Ni(H_2O)_6][CrF_5(H_2O)]$
3.3	$[Ni(H_2O)_6][FeF_5(H_2O)]$
3.4	$[Ni(H_2O)_6][VOF_4(H_2O)]$

autoclaves. The autoclaves were sealed and placed in a programmable oven which was then heated to 200° C in one hour and allowed to dwell for 24 hours. After dwelling, the oven was cooled to 40° C at a rate of 0.1°/minute, after which the oven was shut off and allowed to return to room temperature.

Once cool, the autoclaves were removed and unsealed. The crucibles were opened revealing large crystals (>1 mm on edge) within the mother liquor. The liquor was decanted off and the crystals were collected *via* vacuum filtration. As some of the product crystals are soluble in water, the product crystals were washed thoroughly with acetone before being allowed to dry under vacuum. Once dry, the crystals were collected for property measurements. Any remnant fluoride ions were immobilized by titrating the liquid waste with excess $CaCl_2$.

Single-Crystal X-ray Diffraction (SXRD)

Single crystal X-ray diffraction data for all of the reported materials were collected on a Bruker D8 QUEST diffractometer equipped with an Incoatec microfocus source (Mo K_α radiation, $\lambda = 0.71073$ Å). The diffractometers utilized either a PHOTON 100- or PHOTON II- CMOS area detector. For all compounds, the raw area detector data frames were reduced and corrected for absorption effects using the SAINT+ and SADABS[20] programs. Final unit cell parameters were determined by least-squares refinement of a large number of reflections taken from the data sets. Initial structural models were obtained with SHELXS[21] using direct methods, and subsequent difference Fourier calculations and full-matrix least-squares refinements against F^2 were performed with SHELXL-2016[21] using either the ShelXle[22] or OLEX^2 [23]graphical interfaces. Data were collected at both 300 K and at 100 K, and in most cases yielded identical solutions.

In the case of **3.3** there were differences in the 300 K and 100 K data, due to a structure transition, discussed in detail in later sections. Table 3.2 details the refinement data for all 5 materials.

Material **3.1** was found to crystallize in the triclinic space group *P*-1. The asymmetric unit consists of half each of four independent metal complexes: two $Ni(H_2O)_6^{2+}$ cations, one $MnF_4(H_2O)_2^-$ anion, and one MnF_6^{3-} anion, all of which are located on crystallographic inversion centers (Ni1 on site 1*e*, Ni2 on site 1*f*, Mn1 on site 1*a* and Mn2 on site 1*g*). There are also five fluorine atoms, seven water oxygen atoms and 14 independent hydrogen atoms, all located on positions of general crystallographic symmetry (site 2*i*). All non-hydrogen atoms were refined with anisotropic displacement parameters. Reasonable positions for all water hydrogen atoms were located in difference maps. They were refined isotropically with their O-H distances restrained to be approximately equal. One exception is the hydrogen atoms bonded to O7. The positions of these hydrogen atoms were refined subject to restraint, but their displacement parameters were treated as riding on the parent oxygen atom with $U_{iso,H} = 1.5U_{eq,O}$. The refined H atoms generate good water molecule and hydrogen bonding geometries and displacement parameter values, giving excellent support for the correct position assignments. O/F assignments were made on the basis of displacement parameter behavior, M-O/F distances, trial refinements of O or F site occupation factors and the appearance or absence of electron density corresponding to reasonable hydrogen atom positions near the site. The largest residual electron density peak and hole in the final difference map are +0.95 and -0.47 e$^-$/Å^3, located 0.87 Å from F4 and 0.70 Å from O5, respectively.

Table 3.2: Crystallographic and Refinement Data for Materials 3.1-3.4

Material	1	2	α-3	β-3	4
Empirical Formula	$F_{10} H_{28} Mn_2 Ni_2 O_{14}$	$Cr F_5 H_{14} O_7$	$F_5 H_{14} Fe Ni O_7$	$F_5 Fe H_{12} Ni O_7$	$F_4 H_{14} Ni O_8 V$
F.W. (g/mol F. U.)	669.52	331.82	335.67	333.66	327.76
Temperature (K)	301(2)	100(2)	100(2)	301(2)	100(2)
Wavelength (Å)	0.71073	0.71073	0.71073	0.71073	0.71073
Space Group	P-1	P-1	P-1	$C2/c$	P-1
a (Å)	6.4149(2)	6.4661(4)	6.4783(3)	10.9229(3)	6.4480(3)
b (Å)	8.9609(2)	8.6504(5)	8.699(3)	13.9060(3)	10.9120(6)
c (Å)	8.9609(2)	8.8679(5)	8.9131(4)	13.0252(4)	13.9456(7)
α (°)	104.1985(10)	104.6606(19)	104.5130(10)	90	88.22829(17)
β (°)	95.9379(10)	96.584(2)	96.9280(10)	100.2400(10)	88.1665(17)
γ (°)	96.6946(10)	94.423(2)	94.5090(10)	90	80.1749(17)
Volume (Å^3)	491.22(2)	473.67(5)	479.31(4)	1946.93(9)	966.01(8)
Z	1	2	2	8	4
Density (Mg/m^3)	2.263	2.327	2.326	2.277	2.254
Absorption Coefficient (mm^{-1})	3.291	3.227	3.569	3.514	3.000
F(000)	336	334	338	1336.0	660
Crystal Size (mm)	0.10 x 0.08 x 0.05	0.18 x 0.12 x 0.04	0.14 x 0.10 x 0.08	0.16 x 0.09 x 0.03	0.18 x 0.12 x 0.08
Theta range for data collection	2.367 – 32.629	2.398 – 35.197	2.386 – 35.080	2.395 – 32.603	2.363 – 35.114
Reflections	39493	34067	13402	67362	62409
Unique reflections	3599	4231	4225	3466	8581
Completeness	100.0%	99.9%	99.3%	97.0%	99.9%
Data/Restraints/ Parameters	3599/91/88	4231/6/178	4225/0/177	3466/66/195	8581/378/372
Goodness of Fit on F^2	1.139	1.148	1.041	1.134	1.059
Final R Indices	$R_1 = 0.0329$; $wR_2 = 0.0678$	$R_1=0.0403$; $wR_2=0.1072$	$R_1=0.0208$; $wR_2=0.0474$	$R_1=0.0296$; $wR_2=0.0766$	$R_1=0.0237$; $wR_2=0.0553$
R Indices (all data)	$R_1=0.0514$; $wR_2=0.0734$	$R_1=0.0572$; $wR_2=0.1143$	$R_1=0.0284$; $wR_2=0.0525$	$R_1=0.0325$; $wR_2=0.0782$	$R_1=0.0314$; $wR_2=0.0593$
Extinction Coefficient	0.0083(7)	0.0106(15)	0.0256(8)	0.0034(8)	0.0036(2)

Material **3.2** crystallizes in the triclinic system. The space group *P*-1 (No. 2) was determined by successful structure solution. The asymmetric unit consists of half each of four crystallographically independent moieties: two centrosymmetric $[Ni(H_2O)_6]^{2+}$ cations (Ni1 on site 1*e*, Ni2 on site 1*f*) and two centrosymmetric $[CrF_5(H_2O)]^{2-}$ anions (Cr1 on site 1*a*, Cr2 on site 1*g*). Both $[Ni(H_2O)_6]^{2+}$ cations refine without issue, except for one water (O4 bonded to Ni2) in which the water hydrogen atoms are disordered and coupled to the chromium anion disorder, discussed see below. The acentric $CrF_5(H_2O)^{2-}$ anion is inconsistent with inversion symmetry and is therefore disordered. F/H_2O scrambling was observed affecting one (unique) ligand site around each chromium. There are two well-behaved fluorine sites (F1/F2 on Cr1, F3/F4 on Cr2), whose site occupation factors and U_{eq} values suggest no deviation from full occupancy. The third unique site (F7/O7 bonded to Cr1 and F8/O8 bonded to Cr2) is a 50/50 mixture of fluorine and oxygen, giving an anion composition of $[CrF_5(H_2O)]^{2-}$. This was identified by trial refinements of these sites as either 100% F or 100% O, giving either CrF_6^{3-} anions or $CrF_4(H_2O)_2^{-}$ anions, respectively. Neither was satisfactory. The CrF_6 model resulted in abnormally large displacement parameters for the unique F sites of each anion, along with two electron density peaks consistent with water hydrogen atoms. Refinement of this "F" site occupation factor (*sof*) for this site gave *ca*. 0.95, indicating less electron density. Conversely the $CrF_4(H_2O)_2$ model gave an abnormally small U_{eq} value for the unique "O" sites of each anion, again with hydrogen atom electron density apparent. The *sof* for these "O" sites refined to *ca*. 1.15, consistent with greater electron density on the site. The *sof* results suggest both sites have a scattering power between O and F, *i.e.* a disordered O/F site. Appearance of hydrogen atom electron density near both sites is

74

consistent with partial occupancy by water and discounts a disordered CrF_6^{3-} / $CrF_4(H_2O)_2^-$ model, which was also observed in the similar manganese crystal. For these reasons, these two sites are understood to be a statistically disordered mixture of fluoride and water, giving one $CrF_5(H_2O)^{2-}$ anion per formula unit. O7/F7 and O8/F8 atoms were refined with a fixed occupancy of 0.5 each, with identical atomic coordinates and U_{ij} parameters for each unique site. H atom positions associated with the water component (O7 and O8) were clearly located in difference maps and refined with half-occupancy. O4, bonded to Ni2, was refined with three H atoms position, one with full occupancy (H4A) and two with half-occupancy (H4B, H4C). Water O4 is thus disordered over two orientations such that when F7 is present in a given asymmetric unit, the H4B position is present and H4C absent, and when water O7 is present, H4B is absent and H4C is present. A similar relationship exists between water O4 and O8/F8 site. The two mixed O/F sites, coupled with water O4 are correlated and form a physically sensible disorder assembly (see figure). Solution in the acentric space group $P1$ showed similar F/H_2O disorder along with an unstable refinement. This material is thus a genuinely disordered structure best described in the centrosymmetric space group P-1. The difference in R-values between an ordered CrF_6^{3-} / $CrF_4(H_2O)_2^-$ model and the reported disordered $CrF_5(H_2O)^{2-}$ model is modest but significant: $R1/wR2 = 0.043$ / 0.120 compared with 0.040 / 0.107, respectively. All atoms were refined with anisotropic displacement parameters. Hydrogen atoms were located in difference maps; most were refined freely. Hydrogen atoms with half-occupancy were refined with a common isotropic displacement parameter, and same-distance restraints were used for the O-H bonds of waters O2 and O5. No deviation from full occupancy was observed for any of the metal

atoms. The largest residual electron density peak and hole in the final difference map are +2.15 and -0.84 $e^-/Å^3$, located 0.78 Å from Ni2 and 0.63 Å from Cr1, respectively.

Data for material **3.3** were different at 300 K and at 100 K. Initially, the structure was assumed to be similar to the other reported materials, however at 300 K no triclinic cell gave suitable refinements, so the crystal was cooled to 100 K. At low temperature, it was confirmed that **3.3** crystallizes in the triclinic space group *P*-1. After structure solution, **3.3**$_{100 K}$ was confirmed to be isostructural with **3.1** and **3.2**. Given this result, the room temperature data was puzzling, and therefore data were collected on several crystals. After data collection on a suitable crystal, the 300 K structure was confirmed to be a polymorph of **3.3**$_{100}$, indicating that a polymorphic transition took place between 300 K and 100 K. **3.3**$_{300 K}$ (hereafter named β-[Ni(H$_2$O)$_6$][FeF$_5$(H$_2$O)], or β-**3.3**, with the 100 K form designated as the α-phase). β-**3.3** was found to crystallize in the monoclinic space group *C*2/*c* and consists of the same Ni(H$_2$O)$_6$ and FeF$_5$(H$_2$O) units as α-**3.3**. The FeF$_5$(H$_2$O) unit consists of two fully occupied fluorine sites, two split fluorine sites, and two split disordered O/F sites. The water hydrogens belonging to the Fe unit could not be located in the difference map.

Finally, material **3.4** crystallizes in the triclinic *P*-1 space group. The asymmetric unit consists of half each of four centrosymmetric Ni(H$_2$O)$_6^{2+}$ cations and two complete VOF$_4$(H$_2$O)$^{2-}$ anions. The four nickel centers are located on the following inversion centers: Ni1, site 1*a;* Ni2, site 1*b*; Ni3, site 1*c*; Ni4, site 1*g*. All other atoms are located on positions of general crystallographic symmetry (site 2*i*). O/F scattering factor assignments were clearly made on the basis of metal-O/F bond distances (esp. O1 – O4), displacement parameter behavior, and the presence or absence of hydrogen atom electron

density near the site. All non-hydrogen atoms were refined with anisotropic displacement parameters. Hydrogen atoms were located in difference maps and refined isotropically, with all O-H distances restrained to be similar (SHELX SADI). No deviation from full occupancy was observed for any of the metal atoms. The largest residual electron density peak and hole in the final difference map are +0.67 and -1.11 e⁻/Å^3, both located < 0.6 Å from V(2).

Powder X-ray Diffraction (PXRD)

PXRD data were collected using a Rigaku Ultima IV diffractometer. Data were collected in the angular range of 5° - 65° 2θ with a step size of 0.02°. All data were collected using Cu K$_\alpha$ radiation (λ = 1.5418 Å).

Energy Dispersive Spectroscopy (EDS)

EDS was performed directly on crystals mounted on an SEM stub with carbon tape. EDS was performed using a Tescan Vega-3 SEM equipped with a Thermo EDS attachment. The SEM was operated in low-vacuum mode with a 30 kV accelerating voltage and a 20 second accumulating time.

Optical Spectroscopy

UV-Vis spectra were recorded using a Perkin-Elmer lambda 35 scanning spectrophotometer. The spectrophotometer was operated in diffuse reflectance mode and was equipped with an integrating sphere. Reflectance data were converted internally to absorbance *via* the Kubelka-Munk function. [24] Spectra were recorded in the 200 – 900 nm range. Vibrational spectra were recorded in the spectral range of 4000 cm^{-1} to 650 cm^{-1} using a Perkin-Elmer spectrum 100 FT-IR spectrometer equipped with a diamond ATR attachment.

77

Thermogravimetric Analysis (TGA)

The thermal properties were probed using an SDT Q600 DTA/TGA from room temperature to 600° C under a flow of 100 mL/min of nitrogen gas. Samples were heated in an alumina crucible lined with silver foil from room temperature to 600° C at a rate of 10° /minute, then allowed to cool to room temperature.

Magnetic Properties

Magnetic property measurements were carried out using a Quantum Design MPMS3 SQUID magnetometer. Magnetic susceptibility measurements (both ZFC and FC) were carried out from 2 – 300 K under an applied magnetic field of 0.1 T. The data were corrected for radial offset and shape effects using the method developed by Morrison. [25]

Heat Capacity

Specific heat data were obtained using a Quantum Design PPMS via the relaxation method for material β-**3.3**. Specific heat data were collected over the temperature range 2 K – 300 K.

Results and Discussion

Crystal Structures

The crystal structures of **3.1. [Ni(H$_2$O)$_6$]$_2$[MnF$_6$][MnF$_4$(H$_2$O)$_2$], 3.2. [Ni(H$_2$O)$_6$][CrF$_5$(H$_2$O)]** and **3.3. α-[Ni(H$_2$O)$_6$]$_2$[FeF$_5$(H$_2$O)] (α-3)** are all triclinic zero-dimensional structures with the same pseudo-layered arrangement of the ionic complexes. These layers are arranged in an *ABAB* sequence, with the octahedral ionic complexes arranged in a rock-salt type arrangement within each layer. The layers are

78

staggered causing the metal centers to lie within voids created by the layers above and below it. The structure can be viewed in Figure 3.1.

Although the arrangement of complex ions is identical in all three structures, the octahedral units are slightly different. All three structures contain the same $[Ni(H_2O)_6]^{2+}$ complex. In structure **3.1**, there are two unique Mn coordination polyhedra: one $[MnF_6]^{3-}$ unit and one $[MnF_4(H_2O)_2]^-$ unit that are ordered and reside in different layers; the two units are balanced by two Ni hexa-aqua complexes.

Materials **3.2** and α-**3.3** present the same overall structure, however the two unique metal octahedra from structure **3.1** ($[MnF_6]^{3-}$ and $[MnF_4(H_2O)_2]^-$) are averaged into a single $[MF_5(H_2O)]^{2-}$ (M = Cr, Fe) ionic unit which is distributed into both A and B layers. It is possible that this averaging is simply caused by disorder of the two complexes present in material **3.1**, which would be impossible to distinguish by diffraction. The coordination octahedra present in these three materials are also shown in Figure 3.1.

3.3. $[Ni(H_2O)_6][FeF_5(H_2O)]$

Material **3.3** was found to exhibit two thermal polymorphs, referred to as α-**3.3** and β-**3.3** respectively, and undergoes a structural transition between 100 K and 300 K. The structure proved difficult to solve at 300 K due to the high thermal motion of the H-atoms within the crystal, prompting a 100 K data collection. The 100 K data were of high quality, rapidly yielding a very good structure solution. Using this solution, it became obvious that the 300 K structure had undergone a structural transition to a different polymorph, β-**3.3**, the structure of which was finally determined after collecting on several crystals. β-**3.3** is monoclinic and crystallizes in the space group *C*2/*c*. Consistent
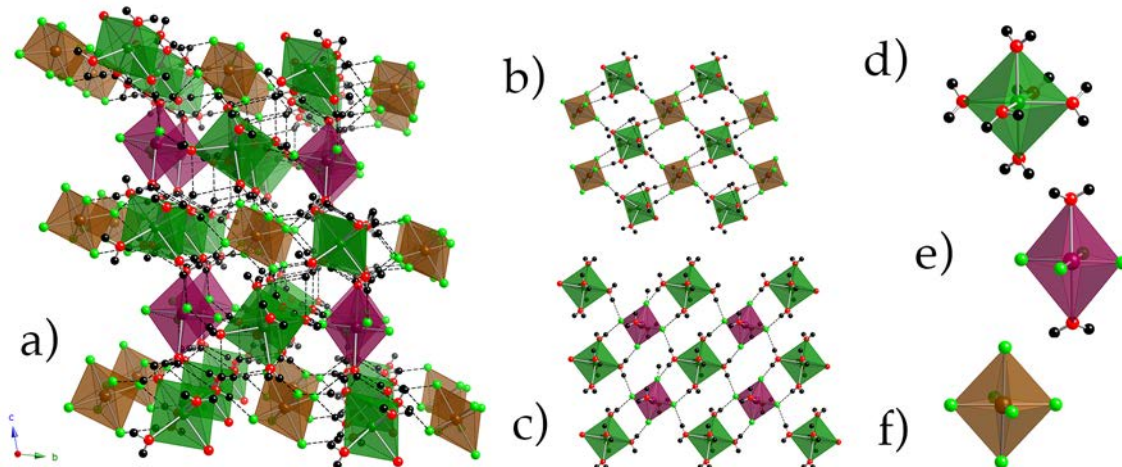
Figure 3.1: The crystal structure of materials 3.1-3.3. The overall zero-dimensional structure is shown (a) next to pseudolayer A (b) and B (c). The local coordination environments of Ni (d), M(1) (e) and M(2) (f) are shown to the right where M = Cr, Mn, Fe. For M = Cr, and Fe, the polyhedra shown in (e) and (f) are averaged to form a $MF_5(H_2O)$ polyhedron. This polyhedron appears identical to (e), with the axial positions occupied by a split O/F disordered site. Ni is shown as dark green polyhedra, M(1) as maroon polyhedra, M(2) as brown polyhedra; O is shown as red spheres, F as green spheres, and H as black spheres. H-bonds are depicted as dashed lines.

with the polymorphic character, β-**3.3** contains the same $[Ni(H_2O)_6]^{2+}$ and $[FeF_5(H_2O)]^{2-}$ units as the α-phase, however the arrangement of the $[Ni(H_2O)_6]^{2+}$ and $[FeF_5(H_2O)]^{2-}$ units is quite different. This is illustrated in Figure 3.2, which depicts the crystal structure of β-**3.3**. When viewing the structure down the *c* crystallographic axis, pseudolayers again make an appearance. Much like in the α polymorph, the layers are segregated by complex ions, however in the β case, in the *A* layer, every other $[Ni(H_2O)_6]^{2+}$ octahedron is rotated by 90° relative to the neighboring one. The $[FeF_5(H_2O)]^{2-}$ ions, again, lie in the voids created by the *A* layer above and below, and the octahedra are slightly rotated to form a corrugated pseudolayer. The axial F ligands (pointing roughly down the *c* axis) are well-behaved and fully occupied, however the equatorial ligands are all disordered. As in the α polymorph, two equatorial ligands are F, and two are half occupied F/O, however in this case all four are split into 8 sites, yielding four sites that are 100% fluorine, and four sites that are disordered 50% F and 50% O. We hypothesize that the site splitting is caused by a resonant rotation of the octahedra, which also influences the H-atom positions on the $[Ni(H_2O)_6]^{2+}$ octahedra in the layers above and below. The water protons on the $[FeF_5(H_2O)]^{2-}$ octahedron could not be located due to the extreme disorder.

3.4. $[Ni(H_2O)_6][VOF_4(H_2O)]$

Material **3.4** crystallizes in the triclinic space group *P*-1 like materials **1-3**, however the structure more closely resembles the monoclinic structure of β-**3** in that the pseudolayers that make up the structure are segregated by metal complex: layer A contains all $[Ni(H_2O)_6]^{2+}$ ions while layer B contains all $[VOF_4(H_2O)]^{2-}$ ions. This results in a pseudolayered structure with each layer consisting of only one type of ion. For example, layer A contains all $[Ni(H_2O)_6]^{2+}$ ions while layer B contains only

www.manaraa.com
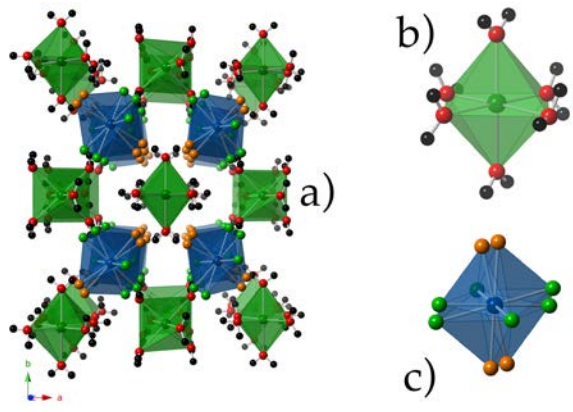
Figure 3.2: The crystal structure of β-3.3. (a) is a monoclinic zero-dimensional structure with pseudolayers that are segregated by metal complex. The regular $Ni(H_2O)_6$ octahedron (b) forms layer A and heavily disordered $FeF_5(H_2O)$ octahedra (c) make up the B layer and sit within voids formed by the A layers. Ni is shown by green polyhedra, Fe is shown by blue polyhedra, F is shown as green spheres, oxygen as red spheres, disordered O/F atoms are shown by orange spheres, and H is shown by black spheres.

$[VOF_4(H_2O)]^{2-}$ ions. An additional distinguishing feature of material **3.4** is that the V cation forms a coordination polyhedron consisting of three different ligands: O, F, and H_2O. By charge balance considerations, this requires that V is in the +4 oxidation state. The crystal structure of material **3.4** is depicted in Figure 3.3.

PXRD and EDS

EDS was used as an initial elemental analysis tool to aid in the crystal structure determination. EDS indicated the presence of all of the ions that were present in the final crystal compositions. PXRD was used to confirm the purity of the bulk product. Powder patterns generated using the single crystal CIF's were compared to the observed PXRD patterns and found to be in agreement for all compounds. Figure 3.4 shows the PXRD patterns for all of the reported materials.

UV-Vis Spectroscopy

All reported compositions contain transition metals in an octahedral coordination environment, making the Tanabe-Sugano diagrams useful tools for assigning *d-d* absorption bands[26]. The reported crystals contain ions ranging from V^{4+} to Fe^{3+} as well as Ni^{2+}, meaning that the T-S diagrams for d^1-d^5 and d^7 and d^8 ions will be used for peak assignments. Figure 3.5 shows all of the UV-Vis spectra, and Table 3.3 details absorption maxima (band locations), and band assignments.

All of the materials contain Ni^{2+} where the Tanabe-Sugano diagram for d^8 octahedral complexes supports that Ni(II) resides in a $^3A_2$ ground state, with three spin-allowed electronic transitions: $^3A_2 \rightarrow {}^3T_2$, $^3A_2 \rightarrow {}^3T_1(F)$, and $^3A_2 \rightarrow {}^3T_1(P)$. It is difficult to attempt to assign absorption bands in the presence of multiple absorbing ions, however material **3.3** contains high-spin Fe(III), for which there are no spin-allowed *d-d*

83
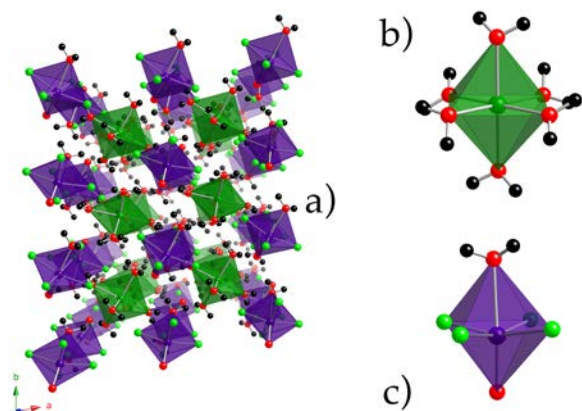
Figure 3.3: The crystal structure of 3.4. (a) is triclinic, however closely resembles the monoclinic structure of **3.3**. The pseudolayers A and B are segregated by complex ion with layer A occupied by $Ni(H_2O)_6$ octahedra (b) and layer B occupied by $VOF_4(H_2O)$ octahedra (c). Nickel ions are displayed as green polyhedra, V as purple polyhedra, F as green spheres, oxygen as red spheres, and H as black spheres.
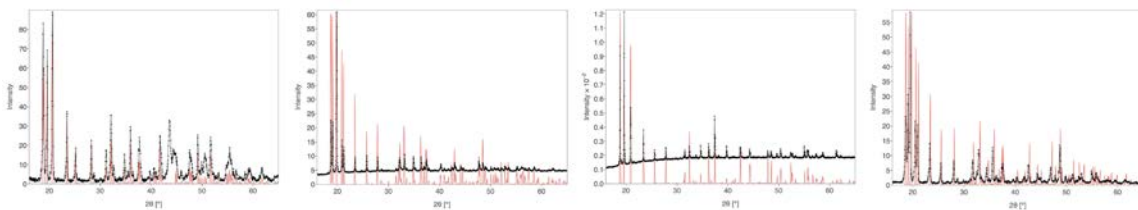
Figure 3.4: PXRD patterns of materials 3.1-3.4. (in order from left to right). The observed patterns (black) agree well with the patterns calculated from their respective .CIFs (red). For material **3.3**, the α polymorph was used to calculate the red pattern.
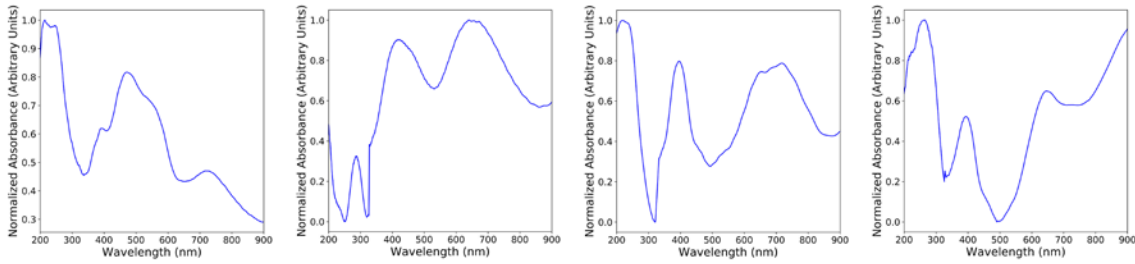
Figure 3.5: The solid-state UV/visible spectra for materials 3.1-3.4. (in order from left to right). Each of the materials show absorption from Ni(II) ions as well as the absorptions from their respective second transition metal. Material **3.3** contains Fe(III), a high spin d^5 element which has no additional d-d electronic transitions. The vertical break in data at 326 nm is apparent to varying degrees across the spectra and is an artifact of the UV/visible lamp change.

Table 3.3: UV/Visible d-d Absorptions and Assignments for Materials 3.1-3.4

Material	Absorption Maxima (nm)	Band Assignments
1	472	$^5E_g \rightarrow {}^5T_{2g}$
2	410	$^4A_{2g} \rightarrow {}^4T_{2g}$
3	N/A	No Fe^{3+} spin-allowed transitions
4	900^	$^2E_g \rightarrow {}^2T_{2g}$

85

transitions; therefore only the Ni(II) absorptions should be observed. The strong band at ~400 nm was therefore assigned to the highest energy transition: $^3A_2 \rightarrow {}^3T_1(P)$., the band at λ_{max} = ~700 nm to the $^3A_2 \rightarrow {}^3T_1(F)$ transition. The lowest energy transition, $^3A_2 \rightarrow {}^3T_2$, was determined to lie in the Near-IR region, and therefore could not be observed with the available instrumentation. The strongest absorption below 300 nm is believed to be an absorption band edge, and is present in all of the materials.

Band assignments for all of the other materials were made based on assigning the Ni(II) bands using **3.3** as a reference and the appropriate Tanabe-Sugano diagrams. The break in the observed spectra at 326 nm is a result of the UV-visible lamp change.

Infrared Spectroscopy

The infrared spectra are straightforward for all reported compositions, revealing the expected O-H stretching bands and H-O-H bending bands associated with the high water content of the reported crystals. The full range IR spectra can be seen in Figure 3.6.

Magnetic Properties

All of the reported materials are considered zero-dimensional crystals, meaning that there is no direct bridging between structural elements in the crystal structure. In lieu of real bonds, the structural units are held together purely by intermolecular forces, in these cases H-bonding. This means that the structural units could be considered to be magnetically isolated and, therefore, we might not expect to observe any long-range magnetic order due to the seeming absence of strong exchange pathways between magnetic ions.

In accordance with this, most of the materials reported herein are indeed simple paramagnets at room temperature (full temperature range magnetic susceptibility plots
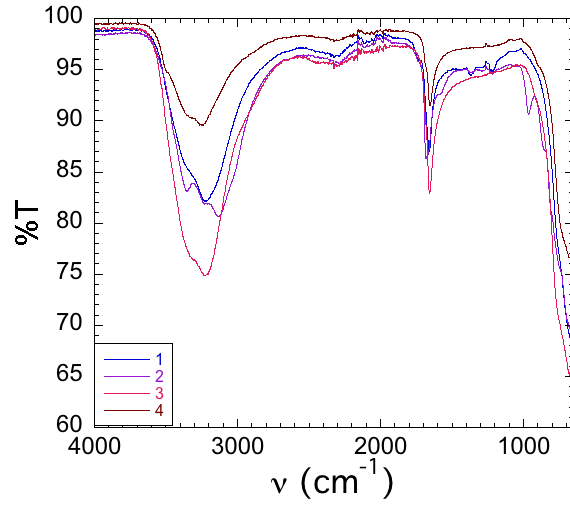
Figure 3.6: The FTIR spectra for materials 3.1-3.4. The IR spectra are simple, containing O-H stretching and H-O-H bending modes.

are shown in Figure 3.7), however they exhibit long range antiferromagnetic ground states. In the case of **3.1**, there is weak antiferromagnetism present at low temperatures, with a T_N = 3 K. The antiferromagnetic transition appears to be extremely weak, which is in line with our expectations that the magnetic exchange between isolated ions should also be weak. Figure 3.8 shows the low temperature portion of the magnetic susceptibility of **3.1**. In the case of material **3.3** however, there is a clear, strong antiferromagnetic transition at T_N = 5 K. This antiferromagnetic transition is shown in Figure 3.9. The nature of this ordering is unknown at the present, however there are two different magnetic ions present within each unit cell, Ni^{2+} (½ of four total centers, 2 equivalent ions) and Fe^{3+} (⅛ of eight centers, ½ of two centers, 2 equivalent ions). The paramagnetic moment is consistent with high-spin iron, suggesting that antiparallel ordering of Ni^{2+} and Fe^{3+} spins (the simplest conceivable ordering) would result in a ferrimagnet which, however, is not consistent with our data. Since our data point to a strong, pure antiferromagnet with no remnant magnetization, we can propose that either a) one of the magnetic ions does not participate in the ordering, or b) there is complex ordering which involves independent antiferromagnetic sublattices (the 2 equivalent iron atoms order independently from the 2 equivalent Ni atoms, but both are antiferromagnetic). The Curie-Weiss fit of the inverse magnetic susceptibility reveals a Weiss temperature of -5 K, which agrees perfectly with the observed T_N = 5 K. This is indicative of the absence of magnetic frustration and supports that the observed magnetic behavior is simple antiferromagnetism. In principle, neutron diffraction data could shed light on the magnetic structure. Unfortunately, the high H-content of these crystals greatly increases the difficulty of collecting high quality neutron

88
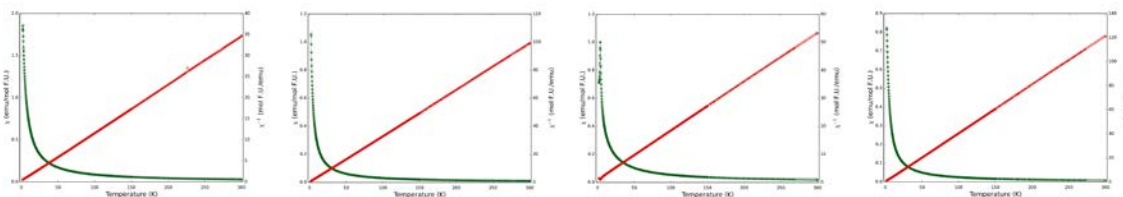
Figure 3.7: Magnetic Susceptibility of Materials 3.1-3.4. The full range magnetic susceptibility and inverse magnetic susceptibility plots for materials **3.1-3.4** (in order from left to right). Magnetic susceptibility is shown in green while inverse magnetic susceptibility is shown in red. ZFC data is shown by open circles and FC data is shown by closed points. In all cases the ZFC and FC data agree well down to 2 K.
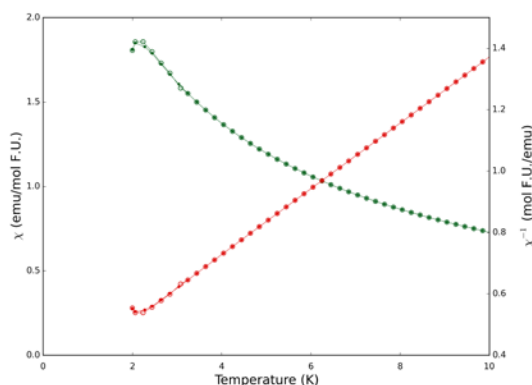
Figure 3.8: The Low Temperature Magnetism of 3.1. The low-temperature magnetic susceptibility (green) and inverse magnetic susceptibility (red) of **3.1**. The magnetic susceptibility obeys the Curie-Weiss law down to low temperatures, but deviates antiferromagnetically at $T_N = 3$ K. There is good agreement between ZFC (open circles) and FC (closed points) data.

89
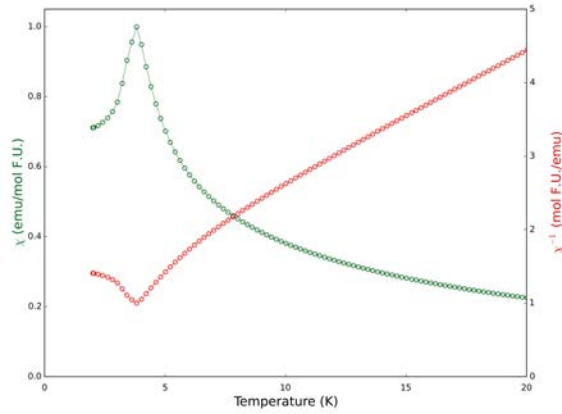
Figure 3.9: The Antiferromagnetism of 3.3. The magnetic susceptibility (green) and inverse magnetic susceptibility (red) of material **3.3**. There is a sharp and seemingly strong antiferromagnetic ordering at $T_N = 5$ K, which agrees with the Weiss temperature θ = -5.00 K.

diffraction data. The inverse magnetic susceptibility data of all four reported materials was fit to the Curie-Weiss law in the paramagnetic regime, and the extracted constants and agreement with calculated values are listed in Table 3.4. The calculated spin-only moments agree well with the observed moments in all cases, and the magnetic moment of **3.4** confirms the presence of V^{4+}.

Heat Capacity

Even though material **3.3** clearly undergoes a structural change from the monoclinic system to the triclinic system on cooling, no transitions were observed in the magnetic susceptibility data between 100 K and 300 K. In order to better identify the transition temperature, we performed heat capacity measurements on single-crystals of **3.3**. The heat capacity revealed a sharp lambda transition at the T_N of 5 K, confirming the long-range magnetic transition observed from the SQUID data. Unfortunately, the heat capacity data revealed no transitions in the 100 K – 300 K range, frustrating our attempts to pin down the exact transition temperature for the β-**3.3** to α-**3.3** transformation. The heat capacity data is plotted along with the inverse magnetic susceptibility in Figure 3.10. As a result of this result, we collected unit cell data in 10 K intervals from 300 K to 100 K. An analysis of this data indicates that the transition is quite broad and occurs over a 20K range (~130 – ~150 K). This broadness, coupled with the fact that the structural change is very small and most probably second order, prevents us from observing the transition in the heat capacity data. [27]

Thermal Properties

Each of the materials was expected to have interesting thermal behavior due to the presence of atomic-scale mixing of the constituent metal ions. Based on the TGA curves,

91

Table 3.4: Extracted Curie-Weiss Constants for Materials 3.1-3.4

Material	μ_{calc} (μ_B/F.U.)*	μ_{eff} (μ_B/F.U.)	θ (K)
3.1	8.00	8.73	-1.49
3.2	4.80	4.93	-0.12
3.3	6.56	6.75	-5.04
3.4	3.32	3.77	-8.71
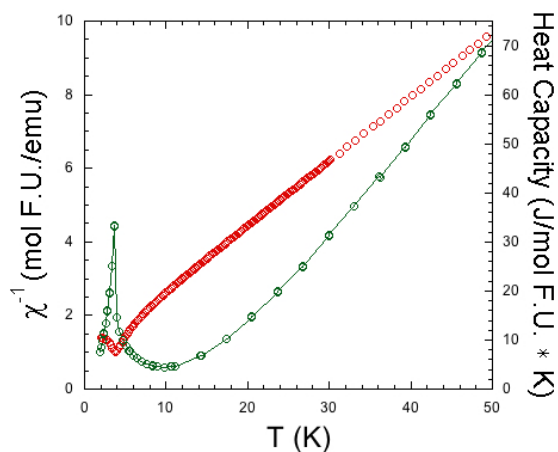
Figure 3.10: The Heat Capacity of Material 3.3. The heat capacity (green) and inverse magnetic susceptibility (red) for material **3.3**. There is a clear lambda anomaly in heat capacity that corresponds to long-range antiferromagnetic order at $T_N = 5$ K.

all four materials start to lose water in a single step beginning at ~100° C. This thermal weight loss is followed by a second gradual weight loss that is complete by 600° C, at which point the thermal products were analyzed by PXRD. Figure 3.11 shows the TGA curves, and Figure 3.12 shows the post-TGA PXRD patterns for the four reported compositions.

Material **3.1** was transformed to an unknown crystalline phase by thermal treatment. The PXRD pattern suggests that **3.1** retains a high degree of crystallinity, however no match in the ICSD database for the thermal product. Furthermore, attempts to thermally treat a single crystal and investigate the structure after the weight loss resulted in sufficient loss of crystal quality to make it unsuitable for single crystal diffraction, and the phase remains unidentified. The thermal products of material **3.2** were impossible to identify due to a severe loss of crystallinity. As the PXRD shows, there are no identifiable peaks in the post-TGA XRD pattern. Material **3.3** thermally decomposes into a mixture of FeOF and the binary NiO phase. Most interestingly, material **3.4** thermally decomposes into the multiferroic material $Ni_3V_2O_8$ upon heating at 600° C. This phase contains a 3:2 Ni:V ratio, which is different than the starting Ni:V ratio of 1:1. It is likely that the "missing" vanadium is present as an amorphous vanadium oxide species that is impossible to detect via PXRD.

Conclusions

The power and versatility of the hydrothermal synthetic method was utilized to synthesize four new zero-dimensional fluoride crystals. These crystals exhibit atomic-scale mixing of the constituent elements, which allows for both interesting metal-metal interactions and a large degree of structural flexibility. This is exemplified by material

93
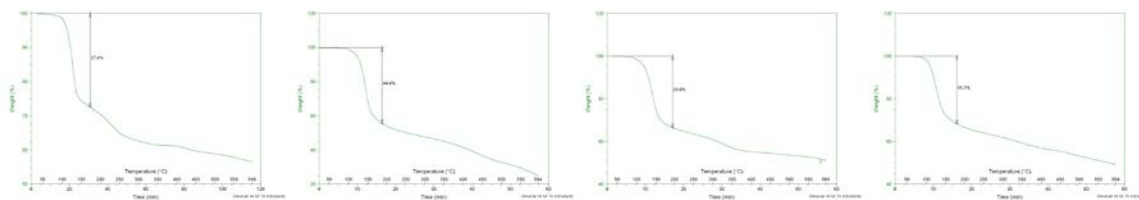
Figure 3.11: TGA curves of materials 3.1-3.4. (in order from left to right). All of the reported materials exhibit what is presumed to be a water loss at 100° C immediately followed by gradual decomposition. The percentage weight loss of the initial weight loss step is shown.
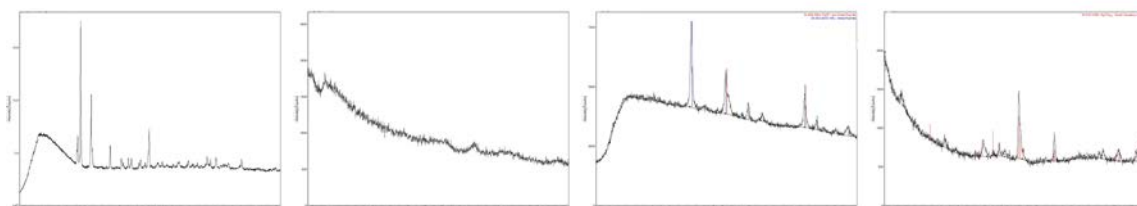
Figure 3.12: Post-TGA PXRD Patterns of Materials 3.1-3.4. The post-TGA XRD patterns of the four reported materials, in order from left to right. Material **3.1** retains a high degree of crystallinity, however was not identifiable. **3.2** was rendered amorphous after TGA. **3.3** transformed into simple Fe and Ni compounds. Finally, **3.4** was converted into $Ni_3V_2O_8$, a multiferroic, after heating.

3.3, which undergoes reasonably a fairly significant polymorphic structural transition and which also exhibits antiferromagnetic magnetic order. The atomic-scale mixing of elements coupled with the flexibility of a zero-dimensional structure led us to investigate the potential use of these crystals as precursors for more condensed functional materials. While most of the compounds decomposed to simple binary or ternary oxides/oxyfluorides, material **3.4** thermally transformed at 600 K into the multiferroic material $Ni_3V_2O_8$. Despite the fact that there is an excess of vanadium in this product structure, we believe that zero-dimensional crystals could potentially be used to target the synthesis of industrially important functional materials.

Acknowledgements

References

(1)   Abeysinghe, D.; Smith, M. D.; zur Loye, H.-C. *Solid State Sci.* **2017**, *69*, 1-6.

(2)   Felder, J. B.; Yeon, J.; Smith, M. D.; Zur Loye, H.-C. *Inorg. Chem.* **2016**, *55*, 7167-7175.

(3)   Felder, J. B.; Yeon, J.; zur Loye, H.-C. *Solid State Sci* **2015**, *48*, 212-217.

(4)   Fulle, K.; Sanjeewa, L. D.; McMillen, C. D.; Wen, Y.; Rajamanthrilage, A. C.; Anker, J. N.; Chumanov, G.; Kolis, J. W. *Inorg. Chem.* **2017**, *56*, 6044-6047.

(5)   Sanjeewa, L. D.; Garlea, V. O.; McGuire, M. A.; Frontzek, M.; McMillen, C. D.; Fulle, K.; Kolis, J. W. *Inorg. Chem.* **2017**, *56*, 14842-14849.

(6)   Yeon, J.; Felder, J. B.; Smith, M. D.; Morrison, G.; zur Loye, H.-C. *Crystal Engineering Communications* **2015**, *17*, 8428.

(7)   Grzechnik, A.; Comer, S.; Kolis, J. W.; Friese, K. *Solid State Sci.* **2015**, *39*, 40-44.

(8)   Mann, J. M.; McMillen, C. D.; Kolis, J. W. *Cryst. Growth Des.* **2015**, *15*, 2643-2651.

(9)   Sanjeewa, L. D.; McGuire, M. A.; McMillen, C. D.; Willett, D.; Chumanov, G.; Kolis, J. W. *Inorg. Chem.* **2016**, *55*, 9240-9249.

(10)   Ali, S. I.; Zhang, W.; Halasyamani, P. S.; Johnsson, M. *J. Solid State Chem.* **2017**, *256*, 158-161.

(11)   Yeon, J.; Smith, M. D.; Sefat, A. S.; Tran, T. T.; Halasyamani, P. S.; zur Loye, H.-C. *Inorg. Chem.* **2013**, *52*, 8303-8305.

(12)   Zhang, R.; Gibbs, A. S.; Zhang, W.; Halasyamani, P. S.; Hayward, M. A. *Inorg. Chem.* **2017**, *56*, 9988-9995.

(13)   Huang, C. Z.; Liu, B.; Wen, L.; Zhuang, R. C.; Zhao, J. T.; Pan, Y.; Mi, J. X.; Huang, Y. X. *Inorg. Chem.* **2015**, *54*, 6978-6985.

(14)   Tulsky, E. G.; Long, J. R. *Chem. Mater.* **2001**, *13*, 1149-1166.

(15)   Felder, J. B.; Smith, M.; zur Loye, H.-C. *Cryst. Growth Des.* **2018**, *18*, 1236-1244.

(16)   Shi, P.-P.; Ye, Q.; Li, Q.; Wang, H.-T.; Fu, D.-W.; Zhang, Y.; Xiong, R.-G. *Chem. Mater.* **2014**, *26*, 6042-6049.

(17)   Bertolini, J. C. *J. Emerg. Med.* **1992**, *10*, 163.

(18) Peters, D.; Miethchen, R. *J. Fluorine Chem.* **1996**, *79*, 161.

(19) Segal, E. B. *Chem. Health Saf.* **2000**, *7*, 18.

(20) APEX2 Version 2014.9-0, SAINT+ Version 8.34A and SADABS Version 2014/4. Bruker Analytical X-ray Systems Inc., Madison Wisconsin, USA, 2014.

(21) Sheldrick, G. M. *Acta Cryst.* **2008**, *A64*, 112-122.

(22) Hubschle, C. B.; Sheldrick, G. M.; Bittrich, B. *J. Appl. Cryst.* **2011**, *44*, 1281-1284.

(23) Dolomanov, O. V.; Bourhis, L. J.; Gildea, R. J.; Howard, J. A. K.; Puschmann, H. *J. Appl. Cryst. 42*, 339-341.

(24) Kubelka, P.; Munk, F. Z. *Tech. Phys.* **1931**, *12*, 593.

(25) Morrison, G.; zur Loye, H.-C. *J. Solid State Chem.* **2015**, *221*, 334-337.

(26) Tanabe, Y.; Sugano, S. *J. Phys. Soc. Jpn.* **1956**, *11*, 864-877.

(27) Saparov, B.; Cantoni, C.; Pan, M.; Hogan, T. C.; Ratcliff, W.; Wilson, S. D.; Fritsch, K.; Gaulin, B. D.; Sefat, A. S.; Tachibana, M. *Sci Rep* **2014**, *4*, 4120.

CHAPTER 4:

APPLICATION OF A MILD HYDROTHERMAL METHOD TO THE SYNTHESIS OF MIXED TRANSITION-METAL(II)/URANIUM(IV) FLUORIDES*

Introduction

Research in the field of uranium crystal chemistry has become more widespread due to the continued interest by the scientific community in the reaction and crystal chemistry of uranium, especially reduced uranium. Uranium bearing materials have become prevalent due to the large-scale use of uranium in nuclear fuel rods and the resulting unused or unwanted materials remaining within the spent fuel rods. Consequently, research continues to explore new uranium containing materials to better understand the chemistry of such phases and to develop advanced materials for use in the construction of new efficient fuel rod assemblies. Finally, the realization that we have to sequester these materials for long time periods in a safe form inside repositories has driven the study of safe and stable wasteform materials to store existing as well as the continually newly generated radioactive waste that is currently stored at various locations across the United States, as well as in other nuclear power utilizing countries.[1-5]

Over the past decade an ever increasing number of oxides and fluorides containing uranium in reduced oxidation states have been reported [6-10], in part due to the development of convenient synthetic techniques that provide ready access to oxidation states other than U(VI). Overall, however, the majority of existing and reported new materials still contain uranium in its most oxidized state of U(VI). [11-18] We have been interested in exploring the U(IV) chemistry of fluorides and in developing facile synthetic methods to help us reach our goal. We have previously reported a mild hydrothermal method for synthesizing U(IV) fluorides that employs the acetate ion as an organic reducing agent along with a dilute hydrofluoric acid solution that acts as solvent and fluorinating agent. Although other organic reducing agents are available and effective,

the use of acetate allows the convenient use of $UO_2(CH_3COO)_2$ as a starting material, combining the uranium source and the reducing agent. [19]

Our previous reports have included the discovery of various binary, ternary, and quaternary U(IV) fluorides, including alkali- and transition-metal containing materials. These reports represent an extensive increase in the number of known U(IV) materials and have enabled the exploration of the intriguing optical and magnetic properties of the U(IV) ion. [20-24] Herein we continue to expand the library of U(IV) materials and report on the synthesis, thermal, and magnetic properties of five new compositions belonging to two distinct families of uranium fluorides: $MUF_6 \bullet 3H_2O$, and $M(H_2O)_6U_2F_{10} \bullet 2H_2O$.

Experimental

Materials and Methods

$UO_2(CH_3COO)_2 \bullet H_2O$ (International Bio-Analytical Industries, ACS grade), $Mn(CH_3COO)_2 \bullet 4H_2O$ (Alfa Aesar), $Co(CH_3COO)_2 \bullet 4H_2O$ (Alfa Aesar, 98%), $Ni(CH_3COO)_2 \bullet 4H_2O$ (Aldrich, 98%), $Zn(CH_3COO)_2 \bullet 2H_2O$ (Fisher Scientific) and HF (EMD, 48%) were used as received.

Caution: Although the uranyl acetate used in this experiment contains depleted uranium, standard precautions for handling radioactive materials should be observed. All uranium-containing materials were handled in labs specially designated for the study of radioactive materials.

Caution: Hydrofluoric acid is acutely toxic and corrosive, and must be handled with extreme caution while using appropriate protective gear. If contact with the liquid or

vapor occurs, proper treatment procedures should immediately be followed and medical attention promptly sought.

All reported materials were synthesized using a mild hydrothermal technique. MUF$_6$•3H$_2$O, where M = Mn (**4.1**) and Zn (**4.2**), were prepared by mixing 2 mmol of uranyl acetate and 2 mmol of manganese acetate or zinc acetate with 1 mL of distilled water in a 23 mL PTFE crucible. Likewise, M(H$_2$O)$_6$U$_2$F$_{10}$•2H$_2$O, where M = Co (**4.3**), Ni (**4.4**) and Zn (**4.5**), were prepared by mixing 2 mmol of uranyl acetate and 2 mmol of cobalt acetate, nickel acetate, or zinc acetate with 1 mL of distilled water in a 23 mL PTFE crucible. Additionally, 1 mL of aqueous HF was added slowly to each of the five reaction mixtures. Each crucible was then sealed in a stainless-steel autoclave and placed in a programmable oven. The oven was ramped to 200° C and held at that temperature isothermally for 24 hours. After dwelling, the oven was cooled at a rate of 0.1° C/minute to 40° C, at which point it was allowed to cool naturally to room temperature.

Once cool, the autoclaves were opened to reveal the product present in the form of single crystals sitting within the reaction liquid. The mother liquor was decanted and the product single crystals were collected by vacuum filtration. The product was washed thoroughly with distilled water, and acetone respectively, and allowed to dry under vacuum. Although each reaction yield was relatively low (~35% based on uranium), the product was present as a single pure phase except in the case of the zinc materials, which crystallize as approximately 50% ZnUF$_6$•3H$_2$O and 50% Zn(H$_2$O)$_6$U$_2$F$_{10}$•2H$_2$O, making isolating individual products difficult.

X-ray diffraction intensity data were collected using a Bruker SMART APEX diffractometer (Mo Kα radiation, λ = 0.71073 Å) or a Bruker D8 QUEST diffractometer equipped with a PHOTON 100 CMOS area detector and an Incoatec microfocus source (Mo K_α radiation, λ = 0.71073 Å).[25] The raw area detector data frames were processed with SAINT+.[26] An absorption correction based on the redundancy of equivalent reflections was applied to the data with SADABS.[26] The reported unit cell parameters were determined by least-squares refinement of a large array of reflections taken from each data set. Initial structural models were obtained with SHELXS using direct methods.[27] Subsequent difference Fourier calculations and full-matrix least-squares refinement against F^2 were performed with SHELXTL[28] or SHELXL-2014[27] using the ShelXle interface. [29]

The compounds $MnUF_6 \bullet 3H_2O$ and $ZnUF_6 \bullet 3H_2O$ crystallize in the monoclinic system. The space group $C2/c$ was consistent with the pattern of systematic absences in the intensity data, and was confirmed by structure solution. The compounds are isostructural with the $NiUF_6 \bullet 3H_2O$ phase.[30] The asymmetric unit consists of a manganese or zinc atom located on a crystallographic inversion center (Wyckoff site 4c), one uranium atom and one water oxygen atom located on a two-fold axis of rotation (site 4e), and three fluorine atoms and one oxygen atom located on general positions (site 8f). All atoms were refined with anisotropic displacement parameters. All hydrogen atoms were located in difference maps and refined free with isotropic displacement parameters.

The compounds $Co(H_2O)_6U_2F_{10} \bullet 2H_2O$, $Ni(H_2O)_6U_2F_{10} \bullet 2H_2O$, and $Zn(H_2O)_6U_2F_{10} \bullet 2H_2O$ crystallize in the monoclinic system. The space group $P2_1/c$ was

102

consistent with the pattern of systematic absences in the intensity data, and was confirmed by structure solution. The compounds are isostructural with the cobalt/neptunium analog $CoNp_2F_{10}(H_2O)_8$.[31] The asymmetric unit consists of a M(II) atom located on a crystallographic inversion center (Wyckoff site 2d), one uranium, five fluorine, four oxygen and eight hydrogen atoms, all of which are located on positions of general crystallographic symmetry (site 4e). All atoms were refined with anisotropic displacement parameters. All hydrogen atoms were located in difference maps and refined isotropically with their O-H distances restrained to be similar (SHELX SADI instruction). The H-H distance in water O4 of $Zn(H_2O)_6U_2F_{10}\cdot2H_2O$ was further restrained to 1.25(4) Angstroms using a SHELX DANG instruction. No deviation from full occupancy was observed for either of the metal atoms. Crystallographic data and selected interatomic distances for all reported materials can be found in Tables 4.1 and 4.2 respectively.

Powder X-Ray Diffraction

Powder X-ray diffraction (PXRD) data were collected on polycrystalline samples that were ground from the product single crystals. Powder data were collected on a Rigaku Ultima IV diffractometer using Cu K$_\alpha$ radiation. Data were collected over the two-theta range 10° to 65°, with a 0.02° step size.

Energy Dispersive Spectroscopy (EDS)

Energy dispersive spectroscopy was performed directly on product single crystals mounted on an SEM stud with carbon tape. EDS was performed with a Tescan Vega-3 SEM equipped with a Thermo EDS attachment. The SEM was operated in low vacuum mode and utilized a 30 kV accelerating voltage and 20 second accumulating time.

103

Table 4.1: Crystal Data and Refinement Information for Compounds 4.1-4.5

	1	2	3	4	5
Empirical Formula	$MnUF_6(H_2O)_3$	$ZnUF_6(H_2O)_3$	$CoU_2F_{10}(H_2O)_8$	$NiU_2F_{10}(H_2O)_8$	$ZnU_2F_{10}(H_2O)_8$
Color	Green	Green	Green	Green	Green
Crystal Size (mm)	0.06 x 0.08 x 0.12	0.04 x 0.07 x 0.10	0.02 x 0.16 x 0.20	0.04 x 0.06 x 0.08	0.04 x 0.06 x 0.08
F.W. (g/mol F.U.)	461.02	471.45	869.12	868.9	875.56
Temperature (K)	294(2)	100(2)	294(2)	100(2)	100(2)
Wavelength (Å)	0.71073	0.71073	0.71073	0.71073	0.71073
Crystal System	Monoclinic	Monoclinic	Monoclinic	Monoclinic	Monoclinic
Space Group	$C2/c$	$C2/c$	$P2_1/c$	$P2_1/c$	$P2_1/c$
Unit Cell Parameters					
a (Å)	12.366(4)	12.1137(7)	11.0745(4)	10.9605(7)	11.0116(5)
b (Å)	6.975(2)	6.9186(4)	7.0989(3)	7.0441(4)	7.0571(3)
c (Å)	8.081(3)	7.9813(4)	8.8499(3)	8.8514(6)	8.8476(4)
β (°)	93.201(6)	92.9113(15)	94.1040(10)	94.532(2)	94.2424(13)
Volume (Å^3)	695.90(4)	668.05(6)	693.87(5)	681.25(7)	685.66(5)
Z	4	4	2	2	2
Density (Mg/m^3)	4.4	4.687	4.16	4.236	4.241
Absorption Coefficient (mm^{-1})	25.134	27.884	24.614	25.234	25.448
Number of Reflections Collected	4427	14520	8989	40599	28820
Number of Independent Reflections	872	1221	1728	3655	2015
Data/Constraints/Parameters	872/0/65	1221/0/66	1728/6/129	3655/28/130	2015/29/130
Goodness-Of-Fit on F^2	1.077	1.13	1.102	1.125	1.104
Final R Indices	$R_1 = 0.0152$ $wR_2 = 0.0372$	$R_1 = 0.01$ $wR_2 = 0.0235$	$R_1 = 0.0210$ $wR_2 = 0.0524$	$R_1 = 0.0150$ $wR_2 = 0.0272$	$R_1 = 0.0118$ $wR_2 = 0.0272$
Largest Diff. Peak and Hole (e$^-$/Å^3)	0.817 and -1.245	1.281 and -0.84	1.314 and -1.410	1.382 and -1.005	1.099 and -1.106

104

Table 4.2: Selected Interatomic Distances for Compounds 4.1-4.5

M = Mn, Zn	1	2	M = Co, Ni, Zn	3	4	5
U(1) - F(1)	2.238(2)	2.2947(11)	U(1) - F(1)	2.215(3)	2.2075(11)	2.2092(15)
U(1) - F(2)	2.284(2)	2.2461(11)	U(1) - F(2)	2.301(2)	2.3052(11)	2.3055(14)
U(1) - F(3)	2.318(2)	2.3143(11)	U(1) - F(2)	2.423(2)	2.4136(10)	2.4168(13)
U(1) - F(3)	2.431(2)	2.4040(12)	U(1) - F(3)	2.340(2)	2.3341(10)	2.3371(13)
U(1) - O(2)	2.585(5)	2.536(2)	U(1) - F(3)	2.363(2)	2.3497(10)	2.3437(13)
			U(1) - F(4)	2.343(2)	2.3424(11)	2.3412(13)
M(1) - F(1)	2.093(2)	2.0278(11)	U(1) - F(4)	2.347(2)	2.3549(11)	2.3553(13)
M(1) - F(2)	2.103(2)	2.0079(11)	U(1) - F(5)	2.351(2)	2.3489(10)	2.3498(13)
M(1) - O(1)	2.199(3)	2.1090(15)	U(1) - F(5)	2.353(2)	2.3511(10)	2.3506(13)
			M(1) - O(1)	2.075(3)	2.0498(13)	2.0796(18)
			M(1) - O(2)	2.088(3)	2.0442(14)	2.0767(18)
			M(1) - O(3)	2.120(3)	2.0722(14)	2.1085(18)

Magnetic Properties

Magnetic measurements were carried out using a Quantum Design MPMS 3 SQUID magnetometer. Field cooled (FC) and zero-field cooled (ZFC) measurements were performed under an applied magnetic field of 0.1 T in the temperature range of 2 K – 300 K. Magnetization measurements were collected at 2K by sweeping the applied magnetic fields between -5 T and 5 T. All magnetic data were collected on polycrystalline powders obtained by grinding the single crystal products. The raw data were corrected for radial offset and shape effects according to the method described by Morrison. [32]

Thermal Properties

Thermal property measurements were performed on both single crystals and polycrystalline powder samples on a TA SDT Q600 TGA. Samples were heated in a nitrogen flow from room temperature to 600° C. Low temperature, isothermal measurements were performed in an attempt to dehydrate the samples by heating single crystals at 60° C for 6 hours.

Results and Discussion

Synthetic Considerations

Mild hydrothermal synthesis provides many advantages over existing solid state reactions, including the ability to access reduced oxidation states of many species. This is especially important for uranium chemistry where the reduced U(IV) ion is much larger and thus significantly less soluble than the more oxidized U(VI) ion. This makes the synthesis of U(IV) containing materials difficult; however, by utilizing an *in situ* reduction step that uses the aqueous acetate ions activated by HF, soluble U(IV)

106

precursors are created that are incorporated into reduced U(IV) containing products, especially fluorides. Although other organic reducing agents are effective, including tartrates and oxalates[33,34], the commercial availability of uranyl acetate makes the co-availability of the uranium source and reducing agent convenient. In addition to uranyl acetate, transition metal (M^{2+}) acetates may be used to provide soluble metal species while simultaneously increasing the concentration of the reducing acetate ion.

In addition to providing the stated advantages over conventional solid-state synthetic techniques, the mild hydrothermal synthesis is often preferred to high temperature (~350 – 700 °C) and high pressure hydrothermal methods because of its much lower operating temperature (~150-250 °C) and low autogenous pressures enabling these reactions to be run in inexpensive off the shelf PTFE-lined steel autoclaves. Our definition of mild hydrothermal reactions are those run below the critical point of water, while regular hydrothermal reactions are run above the critical point of water. Overall, the lower cost, temperature, and pressure requirements of mild hydrothermal syntheses make it an attractive option for materials discovery.

This synthetic technique works well for the reported compositions, providing phase-pure single crystal samples for facile property measurements, purity analysis (by PXRD), and structure determination. The one exception is the two zinc containing compositions that crystallize as an approximate 50% mixture. The similarity in size and crystal morphology between the two phases made separating them exceedingly difficult and, while crystals suitable for structure determination are present for both families, the difficulty in separating the two phases prevents certain bulk property measurements, such

107

as magnetic susceptibility, from being conducted. Attempts to optimize the synthesis to favor one phase over the other were unsuccessful.

Crystal Structure

<u>*M*UF$_6$•3H$_2$O</u>

MnUF$_6$•3H$_2$O and ZnUF$_6$•3H$_2$O crystallize in the monoclinic space group *C*2/*c*, and are isostructural. The structure is built of two unique structural units: 9-coordinate U(IV) polyhedra and 6-coordinate *M*(II) octahedra, which are both shown in Figure 4.1. The metal octahedra are distorted, consisting of four short equatorial fluoride ions, and two long axial aqua ligands. The uranium polyhedron consists of 8 fluoride ions capped by an aqua ligand. The uranium polyhedra each share four fluoride ions with each other to form infinite UF$_4$F$_{4/2}$(H$_2$O) chains running along the *c* crystallographic direction. The polyhedra within the chains alternate orientation by 180° so that the capping aqua ligand is alternately up (+*b* direction) or down (-*b* direction). This is shown in Figure 4.2, which depicts the one-dimensional uranium fluoride chains. The metal octahedra are isolated from one another, but are connected to the uranium fluoride chains. Each of the four equatorial fluoride ions of the metal octahedron is shared by a different uranium ion, so that each octahedron can be said to be corner sharing with four different uranium polyhedra. In addition, two of the uranium polyhedra belong to one uranium fluoride chain, and the other two to another, such that the metal octahedra function to bridge the one-dimensional uranium chains. Figure 4.3 shows a representation of the metal octahedra bridging two uranium fluoride chains. Figure 4.4 shows the overall structure that emphasizes the three-dimensional nature of the crystal structure

.
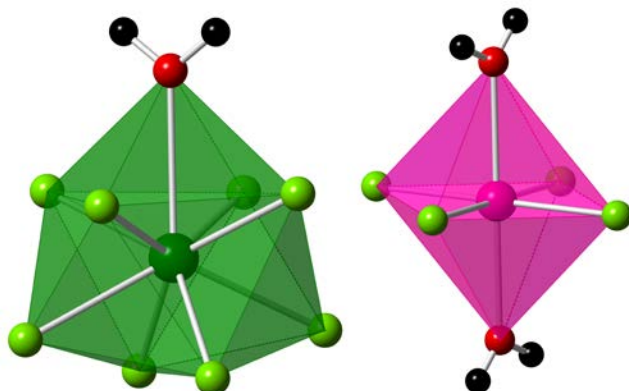
Figure 4.1: Local Coordination Environments in Compounds 4.1 and 4.2. The local coordination environments of both the U^{4+} and M^{2+} ions in structures 4.1 and 4.2 ($MUF_6 \cdot 3H_2O$). The uranium (left) is coordinated by eight fluoride ligands, and one aqua ligand. The metal (right) is coordinated by four fluoride ligands and two aqua ligands. Uranium is shown in dark green, the M^{2+} in purple, fluorine in light green, oxygen in red, and hydrogen in black.
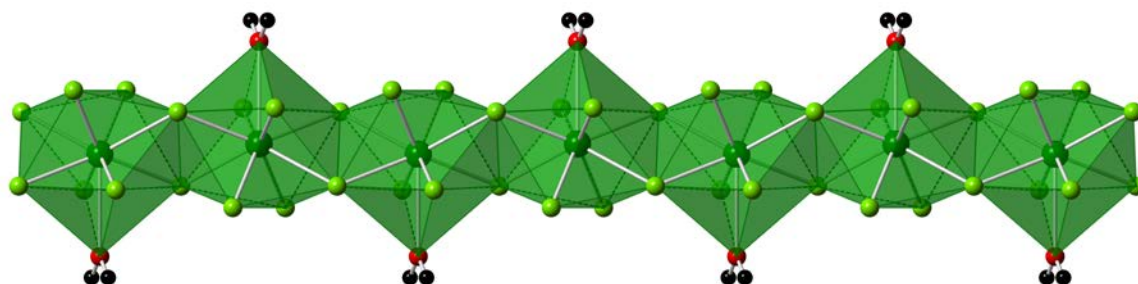
Figure 4.2: Infinite Uranium Chains in Compounds 4.1 and 4.2. The connectivity of uranium polyhedra in compounds 4.1 and 4.2. The $UF_4F_{4/2}(H_2O)$ polyhedra share an edge via two bridging fluoride ligands and form infinite chains along the [c] direction. The polyhedra alternate orientation by 180 degrees so that the aqua ligands remain as far apart as possible. Uranium is shown in dark green, fluorine in light green, oxygen in red, and hydrogen in black.
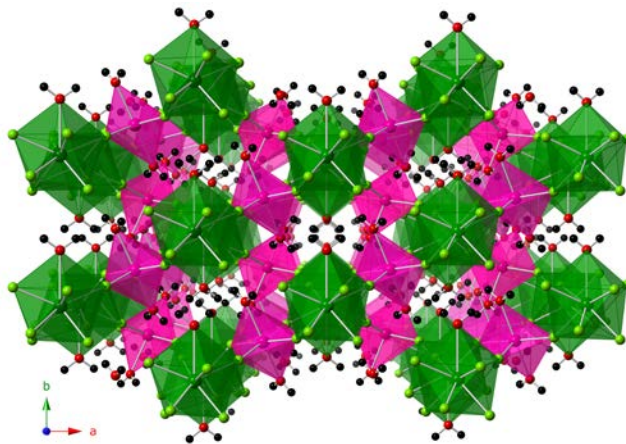
Figure 4.3: Bridging of Uranium Chains in Compounds 4.1 and 4.2. The infinite $UF_4F_{4/2}(H_2O)$ chains are bridged by the metal octahedra. Each metal octahedron is connected to four uranium polyhedra, two per chain. Each chain connects to four other chains in this manner, although only one of these connections is shown here. Metal polyhedra are shown in purple, uranium in dark green, fluorine in light green, oxygen in red, and hydrogen in black.
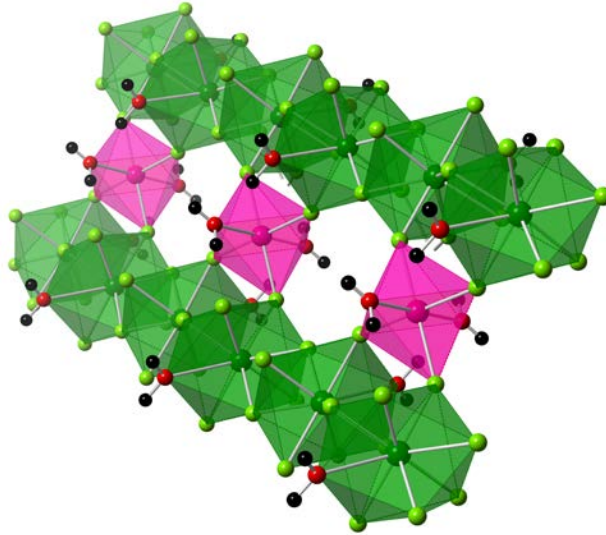
Figure 4.4: The Overall Crystal Structure of Compounds 4.1 and 4.2. An overall depiction of materials 4.1 and 4.2 as seen down the [*c*] direction. The structure is built up of one dimensional chains of $UF_8(H_2O)$ polyhedra which connect to four other chains via bridging metal octahedra. Alternatively, this three-dimensional structure can be thought of as being constructed from layers (in the [*b,c*] plane) of uranium chains separated and connected by layers of metal polyhedra. The metal octahedra are shown in purple, uranium in dark green, fluorine in light green, oxygen in red, and hydrogen in black.

<u>M(H$_2$O)$_6$U$_2$F$_{10}$•2H$_2$O</u>

Co(H$_2$O)$_6$U$_2$F$_{10}$•2H$_2$O , Ni(H$_2$O)$_6$U$_2$F$_{10}$•2H$_2$O , and Zn(H$_2$O)$_6$U$_2$F$_{10}$•2H$_2$O crystallize in a two-dimensional structure that is more typical of a mild hydrothermal synthesis. Again, the structure is built of two different units, a UF$_9$ polyhedron and a M(H$_2$O)$_6$ octahedron. Figure 4.5 shows both local coordination environments. The uranium centers share fluoride ions via either corner or edge sharing with other uranium centers thus creating a two-dimensional layer. These layers are separated by layers of isolated metal hexa-aqua octahedra and interstitial waters, which are held in place between the aqua and fluoride ligands solely by hydrogen bonding. Figure 4.6 shows these layers as they relate to the overall structure. The uranium-containing layer is present as a two-dimensional U$_2$F$_8$F$_{2/2}$$^{2-}$ sheet formed by corner and edge sharing UF$_9$ polyhedra. These polyhedra corner share along the c axis, and edge share along the b-axis, which can be seen in Figure 4.7.

The U(IV) ion commonly exists in high coordination environments with 8 or more ligands surrounding the U(IV) center. As the library of U(IV) materials expands, it becomes possible to observed recurring structural motifs across series of U(IV) containing materials. One such structural motif is the capped trigonal prismatic coordination environment that U(IV) often adopts. This trigonal prismatic environment can be found in numerous previously reported U(IV) containing materials[8,22,24,35,37], and also all five compositions reported herein. The trigonal prism may be capped by two or three ligands on the rectangular faces of the prism depending on the particular compound. The high coordination of uranium dictates that any given U center will be surrounded by at least 8 ligands. In the case of fluoride ligands, each polyhedron would have an overall
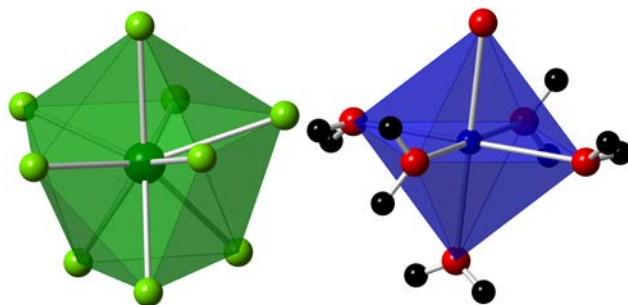
Figure 4.5: Local Coordination Environments in Compounds 4.3-4.5. The local coordination polyhedra of both uranium and the metal(II) ion in structures 4.3-4.5. Uranium (left) is present as UF_9 polyhedra. The high coordination number is characteristic of U(IV). The *M*(II) ion is present as hexa-aqua octahedral complexes. The *M*(II) polyhedra are shown in blue to differentiate them from structures 4.1 and 4.2. As before, uranium is dark green, fluorine is light green, oxygen is red and hydrogen is black.
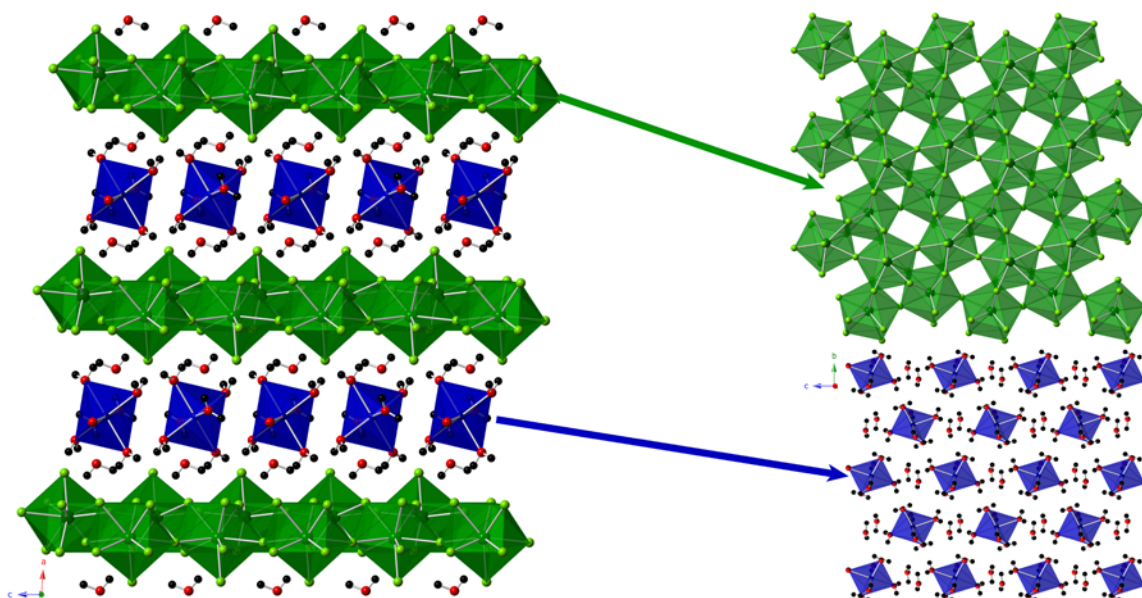
Figure 4.6: The Overall Crystal Structure of Compounds 4.3-4.5. An overall depiction of structures 4.3-4.5 along with a break down of the layered structure. The uranium fluoride layer forms a two-dimensional $U_2F_{10}^{2-}$ sheet with polyhedra that both corner- and edge share. These uranium fluoride layers are interspersed by metal layers. The metal polyhedra are isolated and separated by interstitial waters. This represents a true layered structure where the layers are connected only by intermolecular forces, in this case hydrogen bonding interactions. Uranium is shown in green, the metal ions in blue, fluorine in light green, oxygen in red, and hydrogen in black.
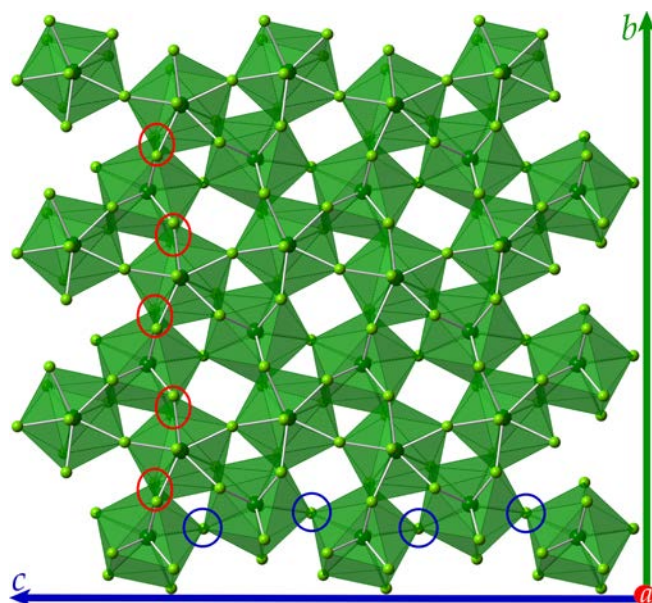
Figure 4.7: The 2-D Uranium Fluoride Layer in Compounds 4.3-4.5. A close look at the uranium fluoride layer. Uranium centers are bridged by two fluoride ligands in the [*b*] direction (edge sharing), and in the [*c*] direction by one fluoride ligand (corner sharing). Red circles highlight shared edges, and shared corners are highlighted by blue circles for clarity. Uranium is shown in dark green, and fluorine in light green.

negative charge, favoring the polyhedra to condense into chains, layers, or 3D frameworks, rather than remaining isolated molecular species. In the case of $MnUF_6 \cdot 3H_2O$ and $ZnUF_6 \cdot 3H_2O$ the uranium centers are present in the aforementioned tricapped trigonal prismatic environment. In this particular case, the trigonal prism is highly distorted due to the presence of a capping aqua ligand.

In the case of $Co(H_2O)_6U_2F_{10} \cdot 2H_2O$, $Ni(H_2O)_6U_2F_{10} \cdot 2H_2O$, and $Zn(H_2O)_6U_2F_{10} \cdot 2H_2O$, the uranium centers form two-dimensional layers that are separated by the charge balancing M(II) octahedra. These two-dimensional sheets are identical to layers found in AU_2F_9 (A = K, Rb).[22] Unlike AU_2F_9, where the layers are connected vertically, the layers in $Co(H_2O)_6U_2F_{10} \cdot 2H_2O$, $Ni(H_2O)_6U_2F_{10} \cdot 2H_2O$, and $Zn(H_2O)_6U_2F_{10} \cdot 2H_2O$ are separated, a consequence of the large hexa-aqua complexes that reside between the layers.

Powder X-Ray Diffraction and EDS

Powder diffraction data, which were collected over the range $10°$ - $65°$ 2θ, are displayed in Fig 4.8-4.11 for all materials. $ZnUF_6 \cdot 3H_2O$ and $Zn(H_2O)_6U_2F_{10} \cdot 2H_2O$ could not physically be separated into phase-pure samples and, consequently, the powder diffraction data for the mixed-phase sample are shown. A Whole Pattern Fit was performed on the powder diffraction data for all other samples to demonstrate phase purity.

Energy dispersive spectroscopy confirmed the presence of U and the respective transition metal in all of the reported materials. EDS is a semi-quantitative measurement that cannot be used to deduce any reliable quantitative information about lighter elements such as oxygen or fluorine. Nonetheless, EDS was able to confirm the presence of both

116
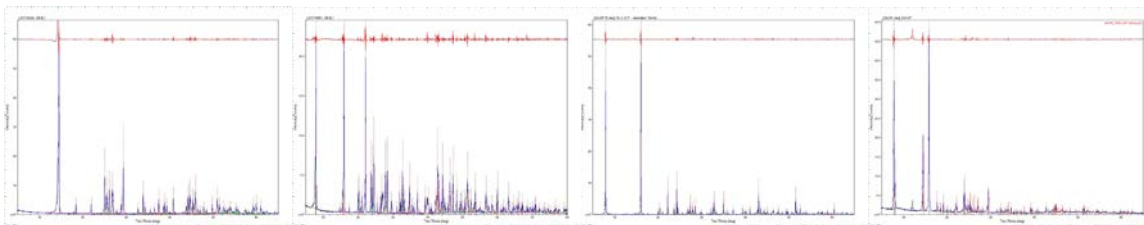
Figures 4.8, 4.9, 4.10, 4.11 (from left to right): PXRD Patterns of Compounds 4.1, 4.3, 4.4, and a 4.2/4.5 mix. Observed (black) and calculated (blue) powder X-ray diffraction data for the reported materials. A Le Bail fit was performed to confirm phase purity, and the difference map is shown in red. Figure 4.11 (far right) represents a mixture of materials 4.2 and 4.5, which are unable to be separated.

oxygen and fluorine in the crystals as a qualitative measure. EDS measurements were performed on several crystals in a batch to confirm that results were representative of the entire set.

Magnetic Properties

Each material contains two magnetic ions: U^{4+} and a M^{2+} species (M = Mn, Co, and Ni). Accurate magnetic measurements on the Zn phases were unable to be obtained due to difficulties in separating the pure phases from the reaction mixture, and are thus not reported here.

<u>MUF$_6$•3H$_2$O</u>

The structure of MnUF$_6$•3H$_2$O consists of infinite chains of UF$_4$F$_{4/2}$(H$_2$O) polyhedra that are edge shared through two fluoride ligands. Additionally, the infinite chains are connected by MnF$_4$(H$_2$O)$_2$ octahedra via fluoride ligands, which also serve to bridge two uranium polyhedra on each chain. Magnetic coupling via the superexchange mechanism has been well documented to occur in fluorides [36], and the greater orbital extent of the of the 5f uranium orbitals compared to 4f lanthanide orbitals open up the potential for interesting *f-d* magnetic coupling that is not typically observed. The full magnetic susceptibility data are shown in Fig 4.12.

The magnetic susceptibility versus temperature data of MnUF$_6$•3H$_2$O are shown in Fig 4.13. The inverse susceptibility data were fit to the Curie-Weiss law over the region of 200 K – 300 K where the sample exhibits paramagnetic behavior. The material deviates slightly from Curie-Weiss behavior below 50 K. The observed magnetic moment of 6.92 μ_B agrees with the calculated value of 6.92 μ_B. For the calculation the moment for
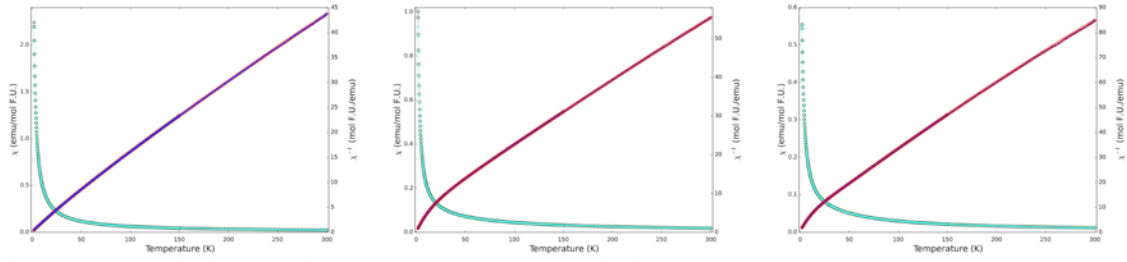
Figure 4.12: Magnetic Susceptibilities of Compounds 4.1, 4.3, and 4.4. The magnetic and inverse magnetic susceptibility for the reported materials overlay perfectly, suggesting an absence of field dependence. *Left:* $MnUF_6 \cdot 3H_2O$, *Middle:* $Co(H_2O)_6U_2F_{10} \cdot 2H_2O$, *Right:* $Ni(H_2O)_6U_2F_{10} \cdot 2H_2O$.
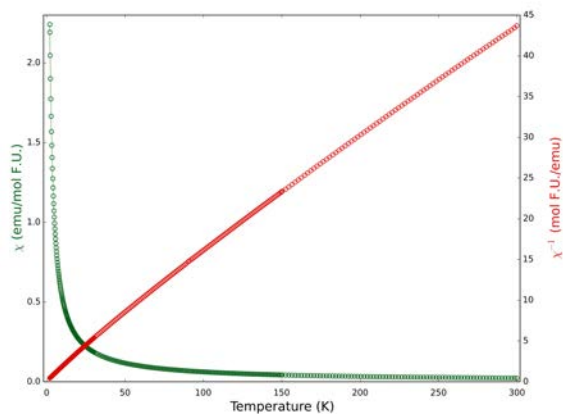
Figure 4.13: Magnetic Susceptibility of Compound 4.1. The magnetic susceptibility and inverse magnetic susceptibility of material 4.1. The measurement was taken from 2 K to 300 K in an applied field of 0.1 T. The zero-field cooled data is shown. The material is paramagnetic down to 2 K, with only slight deviation from Curie-Weiss behavior at low temperature. The expected transition to a non-magnetic singlet ground state is not observed.

manganese was assumed to be the spin-only value, while a uranium moment of 3.58 μ_B, based on full Russel-Saunders, coupling was used.

The slight ferromagnetic deviation seen in the susceptibility data is difficult to attribute to any one cause. It is unlikely that the manganese ions order magnetically since such a large moment would contribute greatly to the magnetic susceptibility. The uranium chains present the possibility of magnetic order; however, no long-range spin ordering is observed in the magnetic susceptibility data. Interestingly, we do not observe the transition from a magnetic triplet state to a low temperature nonmagnetic singlet state that we have previously observed in U(IV) fluoride systems. [37-39] It is possible that the strong moment of manganese overshadows the nonmagnetic transition, however the moment of uranium is strong enough that its loss should be observed, indicating that it remains paramagnetic through 2 K.

$M(H_2O)_6U_2F_{10} \cdot 2H_2O$

Compounds $Co(H_2O)_6U_2F_{10} \cdot 2H_2O$ and $Ni(H_2O)_6U_2F_{10} \cdot 2H_2O$ also have two different magnetic ions, however the transition metal is present in isolated octahedra, connected only by hydrogen bonding interactions and is thus not expected to order. The uranium ions are present as UF_9 polyhedra which both corner and edge share to form a two-dimensional sheet. The complex interconnectedness of uranium polyhedra allows for several possible exchange pathways. Figure 4.14 shows the magnetic susceptibility for $Co(H_2O)_6U_2F_{10} \cdot 2H_2O$ and $Ni(H_2O)_6U_2F_{10} \cdot 2H_2O$. Both compounds show a broad deflection from Curie-Weiss behavior at approximately 25 K. The Curie-Weiss fit for these materials was performed over the temperature range of 150 K – 300 K.
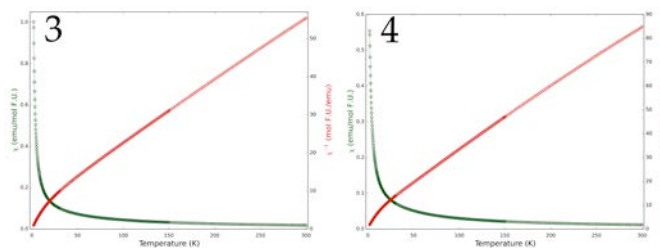
Figure 4.14: The Magnetic Properties of Compounds 4.3 and 4.4. The magnetic susceptibility and inverse magnetic susceptibility of materials 4.3 and 4.4. The measurement was taken from 2 K to 300 K in an applied field of 0.1 T. The zero-field cooled data is shown. The materials are paramagnetic except for a slight positive deviation from Curie-Weiss behavior below 50 K. The expected transition to a non-magnetic singlet state is not observed.

122

The use of spin-only magnetic contributions for the transition metal and full Russel-Saunders coupling for uranium generated effective magnetic moments of 7.26 μ_B calculated for $Co(H_2O)_6U_2F_{10} \bullet 2H_2O$ (7.02 μ_B observed) and 5.65 μ_B calculated (5.64 μ_B observed) for $Ni(H_2O)_6U_2F_{10} \bullet 2H_2O$, both of which are in good agreement with the observed values. Unlike material **4.1** which has a complex three-dimensional structure, the layered structure and isolated M^{2+} cations suggest that any magnetic ordering is likely to come only from U-F-U interactions. As with $MnUF_6 \bullet 3H_2O$, the slight deviation from Curie-Weiss behavior is too ambiguous to suggest the presence of magnetic ordering.

Unexpectedly, both materials in this family also do not exhibit the expected transition to a low temperature nonmagnetic ground state, remaining paramagnetic down to 2 K. In fact, where a decreased moment is expected for a nonmagnetic transition, we observe a slightly increased moment (compared to Curie-Weiss behavior) at low temperatures.

Thermal Properties

Both reported material families contain crystalline water, both interstitial and bound water (in the case of $M(H_2O)_6U_2F_{10} \bullet 2H_2O$) or only bound water in the case of $MUF_6 \bullet 3H_2O$. We were motivated to perform thermal experiments to probe the structural transformations observed by the movement of water in and out of the structure. The powder diffraction data for the thermal decomposition products are found in Figs 4.15-4.17.

<u>$MUF_6 \bullet 3H_2O$</u>

Fig 4.18 shows the TGA plot for $MnUF_6 \bullet 3H_2O$. Two distinct dehydration events can be observed, the first beginning at 80° C, and the second at 128° C. The material
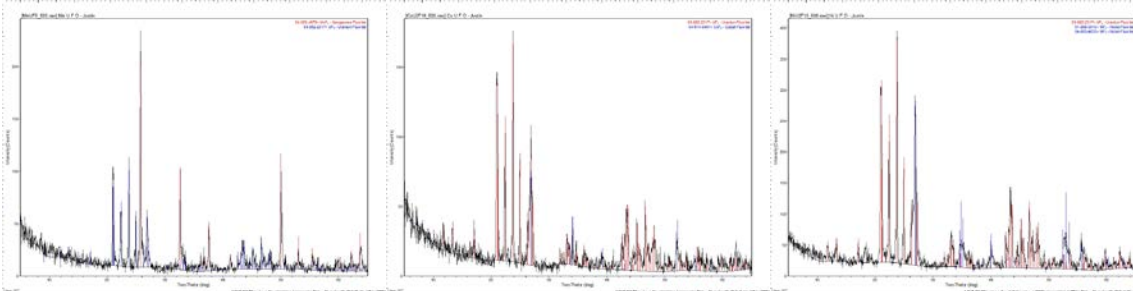
Figure 4.15 (left), 4.16 (middle), and 4.17 (right): Post-TGA PXRD Patterns of Compounds 4.1, 4.3, and 4.4. PXRD patterns showing the thermal decomposition products of the reported materials. The materials thermally decompose into binary oxides and fluorides upon heating under N_2 gas.
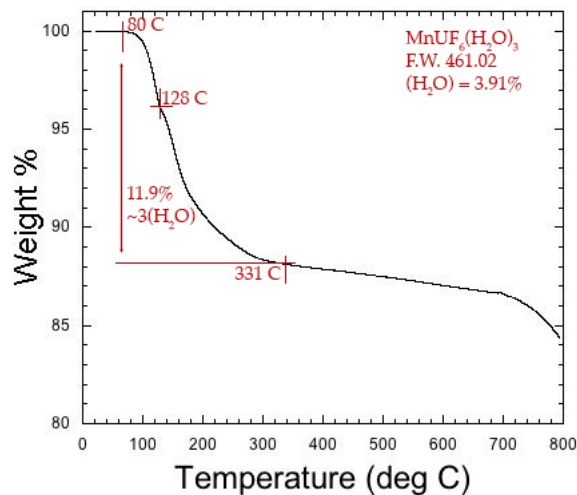
Figure 4.18: TGA Curve of Compound 4.1. Thermogravimetric analysis results for 4.1. Shown is the plot of weight loss as a function of temperature. Results show that one water is lost by 130° C, with the final two waters lost by 331° C, accompanied by the decomposition of the material.

124

decomposes into the binary fluorides UF_4 and MnF_2 as a direct result of the second dehydration. Attempts to dehydrate single crystals of the compound at 90° C to force a single crystal to single crystal transition almost succeeded. Preliminary structural studies revealed that the $UF_8(H_2O)$ polyhedron is dehydrated, leaving infinite chains of UF_8 polyhedra with only minor changes to the lattice parameters. Fig 4.19 shows the transformation of the infinite uranium fluoride chains. Attempts to obtain full structure solutions on the dehydrated crystals, however, were unsuccessful due to the deteriorated crystal quality during heating and the accompanying water loss. Table 4.3 gives atomic positions, and Table 4.4 gives lattice parameters and R factors from the preliminary single crystal study.

$M(H_2O)_6U_2F_{10} \bullet 2H_2O$

$Co(H_2O)_6U_2F_{10} \bullet 2H_2O$ and $Ni(H_2O)_6U_2F_{10} \bullet 2H_2O$ undergo four distinct dehydration events. Fig 4.20 shows the TGA plot for $Co(H_2O)_6U_2F_{10} \bullet 2H_2O$, which is representative of both $Co(H_2O)_6U_2F_{10} \bullet 2H_2O$ and $Ni(H_2O)_6U_2F_{10} \bullet 2H_2O$. The initial dehydration at 53° C yields a polycrystalline powder, which was determ6ined via PXRD to be $CoU_2F_{10} \bullet 4H_2O$. This represents a total loss of four waters, two of which are interstitial. The other waters are lost from the cobalt hexa-aqua octahedron, leaving square planar $Co(H_2O)_4$. Fig 4.21 shows the change in the powder diffraction data due to the dehydration. Further heating destroys the crystal structure and leaves UF_4 and CoF_2 as the major decomposition products.

Conclusions

The mild hydrothermal technique coupled with a convenient *in situ* reduction by the acetate ions was shown again to be a versatile tool for synthesizing new U(IV)
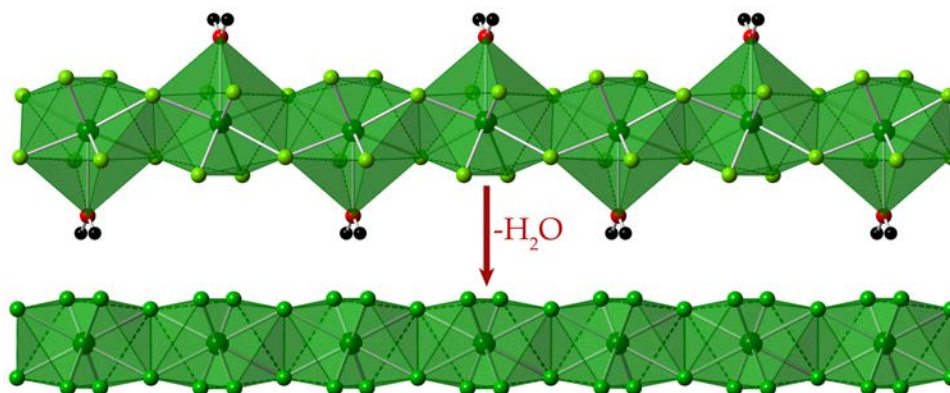
Figure 4.19: Structural Transformation of the Uranium Chains in Compounds 4.1 and 4.2. The transformation of the uranium fluoride chain induced by the loss of a crystalline water. Results obtained from preliminary single crystal diffraction data. Uranium is shown in dark green, fluorine in light green, oxygen in red, and hydrogen in black.

Table 4.3: Atomic Positions of MnUF$_6$ 2(H$_2$O)

Atom	x	y	z
U(1)	0.5	-0.0003	0.75
Mn(1)	0.25	0.25	0
O(1)	0.3	0.546	-0.003
F(1)	0.3645	0.194	0.1869
F(2)	0.3652	0.192	-0.1897
F(3)	0.445	0.149	0.4993

Table 4.4: Lattice Parameters and R Factors of MnUF$_6$ 2(H$_2$O)

a	12.366
b	6.975
c	8.081
α	90
β	93.201
γ	90
R$_1$	0.0918
wR$_2$	0.2078
Goodness-of-Fit on F^2	1.296

126
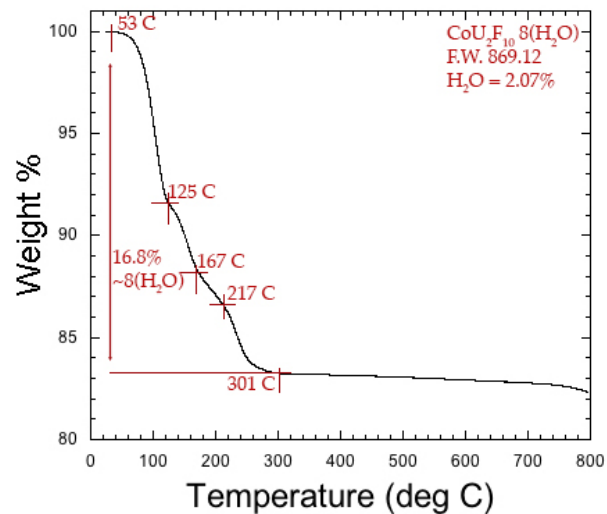
Figure 4.20: TGA Curve of Compound 4.3. Thermogravimetric analysis for material 4.3. Shown is the plot of weight loss versus temperature. Results show that the first dehydration is accompanied by four waters lost, rapidly followed by the remaining four waters and decomposition by 301° C.

127
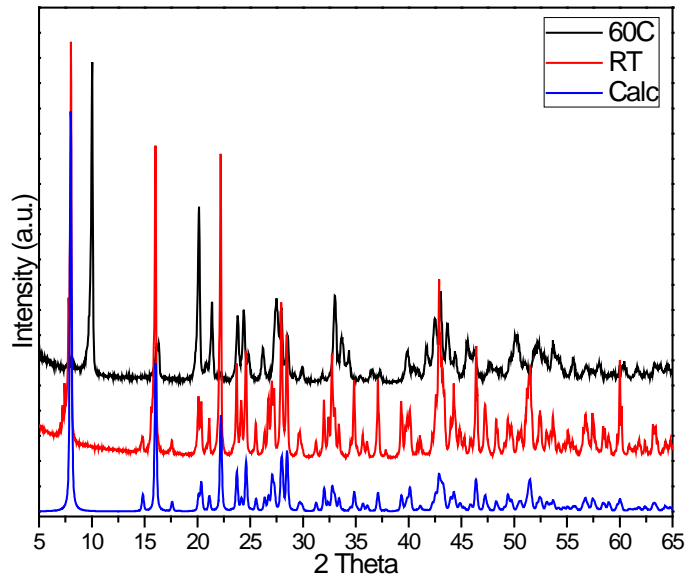
Figure 4.21: PXRD Pattern Showing the Structural Transformation of Compound 4.3. Powder x-ray diffraction data before and after TGA of material 4.3. Blue is the calculated powder pattern of material 4.3 obtained from the single crystal structure solution. Red is the observed pattern before TGA. Black shows the change in the pattern caused by the thermal dehydration at 60° C.

containing materials. The materials presented herein showcase the structural versatility of the U(IV) ion by adopting both three dimensional and layered two dimensional structures under nearly identical synthetic conditions. In addition, the magnetic properties demonstrate that, although there is a lack of apparent magnetic order, the 5f unpaired electrons can remain viable for potential long-range order despite the fact that they commonly undergo a transition to a low temperature nonmagnetic singlet ground state due to thermal depopulation of excited f orbital states.

Acknowledgements

References

(1)   Burns, P. C.; Olson, R. A.; Finch, R. J.; Hanchar, J. M.; Thibault, Y. *J. Nucl. Mater.* **2000**, *278*, 290-300.

(2)   Jackson, J. M.; Burns, P. C. *The Can. Mineral.* **2001**, *39*, 187-195.

(3)   Kim, K.-T. *J. Nucl. Mater.* **2010**, *404*, 128-137.

(4)   Ling, J.; Morrison, J. M.; Ward, M.; Poinsatte-Jones, K.; Burns, P. C. *Inorg. Chem.* **2010**, *49*, 7123-7128.

(5)   Akifumi, Y.; Yoshihiro, N.; Sadao, U.; Tsutomu, O. *Nucl. Technol.* **2012**, *179*, 309-322.

(6)   Jin, G. B.; Soderholm, L. *J. Solid State Chem.* **2015**, *221*, 405-410.

(7)   Keskar, M.; Sali, S. K.; Krishnan, K.; Kannan, S. *J. Nucl. Mater.* **2016**, *478*, 245-255.

(8)   Ward, M. D.; Oh, G. N.; Mesbah, A.; Lee, M.; Sang Choi, E.; Ibers, J. A. *J. Solid State Chem.* **2015**, *228*, 14-19.

(9)   Ward, M. D.; Pozzi, E. A.; Lee, M.; Van Duyne, R. P.; Choi, E. S.; Ibers, J. A. *Inorg. Chem.* **2015**, *54*, 3055-3060.

(10)   Yu, N.; Klepov, V. V.; Neumeier, S.; Depmeier, W.; Bosbach, D.; Suleimanov, E. V.; Alekseev, E. V. *Eur. J. Inorg. Chem.* **2015**, *2015*, 1562-1568.

(11)   Betke, U.; Wickleder, M. S. *Eur. J. Inorg. Chem.* **2012**, *2012*, 306-317.

(12)   Mer, A.; Obbade, S.; Rivenet, M.; Renard, C.; Abraham, F. *J. Solid State Chem.* **2012**, *185*, 180-186.

(13)   Plášil, J.; Kampf, A. R.; Kasatkin, A. V.; Marty, J.; Škoda, R.; Silva, S.; Čeka, J. *Mineral. Mag.* **2013**, *77*, 2975-2988.

(14)   Read, C. M.; Morrison, G.; Yeon, J.; Smith, M. D.; zur Loye, H.-C. *Inorg. Chem.* **2015**, *54*, 6993-6999.

(15)   Reynolds, E.; Kennedy, B. J.; Thorogood, G. J.; Gregg, D. J.; Kimpton, J. A. *J. Nucl. Mater.* **2013**, *433*, 37-40.

(16)   Serezhkina, L. B.; Grigor'ev, M. S.; Makarov, A. S.; Serezhkin, V. N. *Radiochemistry* **2015**, *57*, 20-25.

130

(17) Wu, S.; Kowalski, P. M.; Yu, N.; Malcherek, T.; Depmeier, W.; Bosbach, D.; Wang, S.; Suleimanov, E. V.; Albrecht-Schmitt, T. E.; Alekseev, E. V. *Inorg. Chem.* **2014**, *53*, 7650-7660.

(18) Collomb, A.; Gondrand, M.; Lehmann M., S.; Capponi J., J.; Joubert J., C. *J. Solid State Chem.* **1976**, *16*, 41-48.

(19) Yeon, J.; Smith, M. D.; Sefat, A. S.; Tran, T. T.; Halasyamani, P. S.; zur Loye, H.-C. *Inorg. Chem.* **2013**, *52*, 8303-8305.

(20) Yeon, J.; Smith, M. D.; Sefat, A. S.; zur Loye, H.-C. *Inorg. Chem.* **2013**, *52*, 2199-2207.

(21) Yeon, J.; Smith, M. D.; Tapp, J.; Möller, A.; zur Loye, H.-C. *J. Am. Chem. Soc.* **2014**, *136*, 3955-3963.

(22) Yeon, J.; Smith, M. D.; Tapp, J.; Möller, A.; zur Loye, H.-C. *Inorg. Chem.* **2014**, *53*, 6289-6298.

(23) Yeon, J.; Smith, M. D.; Morrison, G.; zur Loye, H.-C. *Inorg. Chem.* **2015**, *54*, 2058-2066.

(24) Yeon, J.; Smith, M. D.; Tapp, J.; Möller, A.; zur Loye, H.-C. *J. Solid State Chem.* **2016**, *236*, 83-88.

(25) APEX2 Version 2014.9-0, SAINT+ Version 8.34A and SADABS Version 2014/4. Bruker Analytical X-ray Systems, Inc., Madison Wisconsin, USA, **2014**

(26) SMART Version 5.625, SAINT+ Version 6.45 and SADABS Version 2.05, Bruker Analytical X-ray Systems, Inc., Madison, Wisconsin, USA, **2001**

(27) Sheldrick, G. M. *Acta Cryst.* **2008**, A64, 112-122

(28) APEX2 Version 2014.9-0, SAINT+ Version 8.34A and SADABS Version 2014/4. Bruker Analytical X-ray Systems, Inc., Madison Wisconsin, USA, **2014**

(29) *ShelXle:* a Qt graphical user interface for *SHELXL.* Hubschle, C. B.; Sheldrick G. M.; Bittrich B. J. *J. Appl. Cryst.* **2011**, *44*, 1281-1284

(30) Bean, A. C.; Sullens, T. A.; Runde, W.; Albrecht-Schmitt, T. E. *Inorg. Chem.* **2003**, *42*, 2628-2633.

(31) Cousson, A.; Abazli, H.; Jove, J. *J. Less-Common Met.* **1985**, *109*, 155-168.

(32) Morrison, G.; zur Loye, H.-C. *J. Solid State Chem.* **2015**, *221*, 334-337.

(33) Cortese, A. J.; Wilkins, B.; Smith, M. D.; Yeon, J.; Morrison, G.; Tran, T. T.; Halasyamani, P. S.; zur Loye, H. -C. *Inorg. Chem.* **2015,** *54,* 4011

(34) Abeysinghe, D.; Smith M. D.; Yeon, J.; Morrison, G.; zur Loye, H. -C. *Cryst. Growth Des.* **2014,** *14,* 4749-4758.

(35) Abazli, H.; Cousson, A.; Tabuteau, A.; Pages, M.; Gasperin, M. *Acta Cryst.* **1980**, *B36*, 2765-2766.

(36) Tressaud, A.; Dance, J. M. *Adv. Inorg. Chem. Radiochem.* **1977**, *20*, 133-188.

(37) Almond, P. M.; Deakin, L.; Mar, A.; Albrecht-Schmitt, T. E. *J. Solid State Chem.* **2001**, *158*, 87-93.

(38) Lai, Y.-L.; Chiang, R.-K.; Lii, K.-H.; Wang, S.-L. *Chem. Mater.* **2008**, *20*, 523-530.

(39) Wang, C.-M.; Liao, C.-H.; Chen, P.-L.; Lii, K.-H. *Inorg. Chem.* **2006**, *45*, 1436-1438.

CHAPTER 5:

SYNTHESIS OF ANHYDROUS K$_2$TiOF$_4$ VIA A MILD HYDROTHERMAL METHOD*

*Adapted with permission from Felder, J. B.; Yeon, J.; zur Loye, H.-C. *Solid State Sci.*

2015, *48*, 212-217. © 2015 Elsevier.

Introduction

Compounds containing Ti^{4+} have been studied extensively for their photocatalytic activity, [1] as well as for their ability to support the reduction of CO_2 into fuels such as methane. [2] Given the success of TiO_2, it is not surprising that more recent work has focused on developing even more efficient catalysts – either by doping TiO_2 with other transition metals or by synthesizing entirely new Ti^{4+} containing materials. One approach to improving TiO_2 via doping includes the introduction of fluoride ions into the structure as well as the preparation and investigation of new titanium-containing fluorides and oxyfluorides. [3] [4] [5]

A good starting point for the preparation of new titanium containing fluorides and oxyfluorides is the substitution of titanium for vanadium in existing vanadium fluorides and oxyfluoride phases. The K/V/O/F phase space has been well explored, and within it there exists several potassium vanadium fluoride and oxyfluoride structures in which the vanadium can be substituted for by titanium. These substitutions have been quite successful, and these as well as other titanium fluorides and oxyfluorides are of interest for their photocatalytic activity. Among this group, K_2TiF_6, K_3TiOF_5, $K_2Ti(O_2)F_4$, $K_2TiOF_4\cdot(H_2O)$, and $K_7Ti_4O_4F_7$ have been structurally characterized. However, the synthesis and structural characterization of K_2TiOF_4, first reported by Ginsberg and Holder and attempted by numerous groups since, has apparently not yet been achieved. [3] [6] [5] [7]

There are extensive reports in the literature describing work aimed at preparing K_2TiOF_4. The reported structure characterizations indicate that two polymorphs, I and II, exist. Synthetically, for example, Schmitz-Dumont and Deddmore [8] [9] showed that the

134

thermal decomposition of K_2TiF_6 requires moisture to result in the target phase of K_2TiOF_4 plus HF, while according to Drossbach, [10] the electrolytic reaction of K_2TiF_6 yields K_2TiOF_4 as an intermediate via the reaction of $K_2TiF_6 + TiO_2 + 2KF$. The group of Pausewang [11] [12] has pursued the preparation of K_2TiOF_4 via a number of synthetic approaches, including a solid state reaction between K_2TiF_6, TiO_2 and KF, the thermal decomposition of $K_2Ti(O_2)F_4 \cdot H_2O$, and the pyrohydrolysis of K_2TiF_6.

The dehydration of the peroxide containing $K_2Ti(O_2)F_4 \cdot H_2O$ was reported to proceed via a $K_2Ti(O_2)F_4$ intermediate to K_2TiOF_4 (I) where the decomposition of the peroxo group required temperatures of at least 230 °C. [8] Unfortunately, due to the reported instability of K_2TiOF_4 (I), this has so far led to only mixed phase products containing K_2TiOF_4 (I), the cryolite composition $K_{2.67}TiO_{0.67}F_{5.33}$, and TiO_2. K_2TiOF_4 (I) is reported to be tetragonal with $a = 7.697(1)$, and $c = 11.539(2)$ Å. High pressure thermal decompositions of $K_2Ti(O_2)F_4 \cdot H_2O$ were reported to proceed via the formation of $K_2TiOF_4 \cdot H_2O$ (130-230 °C) followed by a dehydration step (T > 300°C), resulting in K_2TiOF_4 (II). The crystal structure of K_2TiOF_4 (II) was reported to adopt the K_2FeF_5 type orthorhombic structure with space group $Pn2_1a$, and lattice parameters: a = 20.253(2), b = 7.366(1) and c = 12.951(1) Å. [11] Interestingly, while K_2TiOF_4 was originally reported as being a possible member of the potassium oxyfluorotitanate family, to date it has proven impossible to synthesize this composition via preparation from precursors, such as the hydrate and peroxide forms. [11] [12]

Often a different synthetic route can enable the synthesis of an elusive material, [13] [14] and in the case of K_2TiOF_4 the use of a hydrothermal route has now resulted in the facile synthesis of K_2TiOF_4 in single crystal form. In this paper we report the

135

hydrothermal synthesis of high quality single crystals of K_2TiOF_4 and the determination of its structure in space group *Pnma*. In addition, we discuss why the dehydration of the hydrated form is unlikely to result in the anhydrous K_2TiOF_4 due to the major structural rearrangement that would be required.

2. Experimental

2.1 Materials and Method

The following reagents were used as received: TiF_3 (Alfa Aesar), KF (Alfa Aesar, 99%), and HF (EMD, 48%). 1 mmol of TiF_3 and 5.00 g of KF were placed in a 23 mL PTFE lined stainless steel autoclave along with 2.5 mL of HF and 2.5 mL of H_2O. The autoclave was sealed and placed in a programmable oven and ramped to 200° C at a rate of 10.00°/min. It was held at 200°C for 24 hours. The oven was then cooled at a rate of 0.1°/minute until it reached a temperature of 40° C. The oven was then allowed to cool naturally to room temperature. After cooling, the autoclave was removed and the product obtained by vacuum filtration. Excess KF was removed by dissolution with water, and the product was washed thoroughly with water and acetone and then allowed to dry under vacuum at room temperature. The synthesis resulted in approximately 75% yield after washing, with an unknown side product being present as clear colorless crystals.

2.2 Structure Determination

X-ray intensity data was measured from a yellow polyhedral crystal of approximate dimensions 0.20 mm × 0.16 mm × 0.16 mm at 294(2) K on a Bruker SMART APEX CCD diffractometer utilizing Mo Kα radiation ($\lambda = 0.71073$ Å). The raw area detector data frames were reduced using SAINT+. [15] The multi-scan technique in SADABS was used to correct for absorption effects. [15][15] The unit cell parameters were

determined by least-squares refinement of sets of strong reflections. Full matrix least-squares refinement against F^2 of the structural models and difference Fourier calculations were performed with SHELXTL. [16]

Crystallographic data from the structure refinements for K_2TiOF_4 can be found in Table 5.1. Atomic coordinates as well as selected interatomic distances are listed in Tables 5.2 and 5.3, respectively.

2.3 Scanning Electron Microscopy

Single crystals of K_2TiOF_4 were analyzed by SEM using an FEI Quanta SEM instrument in high vacuum mode. Energy dispersive spectroscopy (EDS) was used to verify the presence of K and Ti.

3. Results and Discussion

3.1 Structure Description of K_2TiOF_4 and Comparison to $K_2TiOF_4 \cdot H_2O$[11, 12]

K_2TiOF_4, as well as its hydrate, $K_2TiOF_4 \cdot H_2O$, are composed of one-dimensional chains of corner shared titanium octahedra. In the title compound, the infinite chains are composed of TiO_2F_4 octahedra that corner share exclusively through the F(1) position to yield staggered chains. Figure 5.1 shows the connectivity of the polyhedra that gives rise to the infinite chains. The oxide positions are *cis* equatorial with the F(1) position occupying the other equatorial sites. The F(3) and F(4) sites occupy the axial positions of the octahedra. The titanium octahedra are heavily distorted with the Ti^{4+} ion being offset significantly from the center. This is caused by the fact that *M*-O bonds are generally shorter than *M*-F bonds and explains why the Ti^{4+} ion appears to be pulled closer to the *cis* oxide ions. Figure 5.2 shows a close up of the local coordination environment of the Ti^{4+} ions. The hydrate is similar in that it is also composed of TiO_2F_4 octahedra that

137

Table 5.1: Crystal Data and Structure Refinement for K_2TiOF_4

Empirical Formula	K_2TiOF_4
Color	Yellow
Crystal Size	0.20 mm × 0.16 mm × 0.16 mm
Formula Weight	218.10 g/mol F.U.
Temperature	294(2) K
Wavelength	0.71073 Å
Crystal System	Orthorhombic
Space Group	*Pnma*
Unit Cell Parameters	a = 7.3891(2) Å
	b = 5.6458(2) Å
	c = 11.4220(4) Å
	$\alpha = 90°$
Volume	476.50(3) $Å^3$
Z	4
Density (calculated)	3.040 Mg/m^3
Absorption Coefficient	3.524 mm^{-1}
Reflections Collected	6633
Independent Reflections	791
Absorption Correction	Semi-empirical from equivalents
Data / Restraints / Parameters	791 / 0 / 46
Goodness-of-Fit on F^2	1.196
Final R Indices	$R_1 = 0.0303$ $wR_2 = 0.0787$
Largest Diff. Peak and Hole	0.460 and -1.333 $e.Å^3$

Table 5.2: Atomic Coordinates and Equivalent Isotropic Displacement Parameters

$(Å^2)$ for K_2TiOF_4

	x	y	z	U(eq)*
Ti(1)	0.1989(1)	0.2500	0.5693(1)	0.014(1)
K(1)	0.6904(1)	0.2500	0.5927(1)	0.024(1)
K(2)	-0.0220(1)	0.2500	0.2827(1)	0.021(1)
O(1)	0.3221(2)	0.0223(2)	0.6115(1)	0.028(1)
F(1)	0.3221(2)	0.0223(2)	0.6115(1)	0.028(1)
F(2)	0	0	0.5000	0.022(1)
F(3)	0.0358(2)	0.2500	0.6952(1)	0.025(1)
F(4)	0.2741(2)	0.2500	0.4081(1)	0.022(1)

*U(eq) is defined as one third of the trace orthogonalized U^{ij} tensor.

138

Table 5.3: Selected Interatomic Distances (Å) for K₂TiOF₄

Ti(1)-O(1)	1.6472(13)
Ti(1)-F(1)	1.6472(13)
Ti(1)-F(2)	2.1860(3)
Ti(1)-F(3)	1.8768(16)
Ti(1)-F(4)	1.9231(15)
K(1)-O(1)	2.7947(14)
K(1)-O(1)	3.0174(15)
K(1)-F(1)	2.7947(14)
K(1)-F(2)	2.8892(5)
K(1)-F(3)	2.6783(17)
K(1)-F(3)	2.8078(18)
K(1)-F(4)	2.83509(18)
K(2)-O(1)	2.8935(13)
K(2)-O(1)	2.9565(14)
K(2)-F(1)	2.8935(13)
K(2)-F(1)	2.9565(14)
K(2)-F(2)	2.8596(5)
K(2)-F(3)	2.83597(19)
K(2)-F(4)	2.6146(16)
K(2)-F(4)	2.6494(15)

139
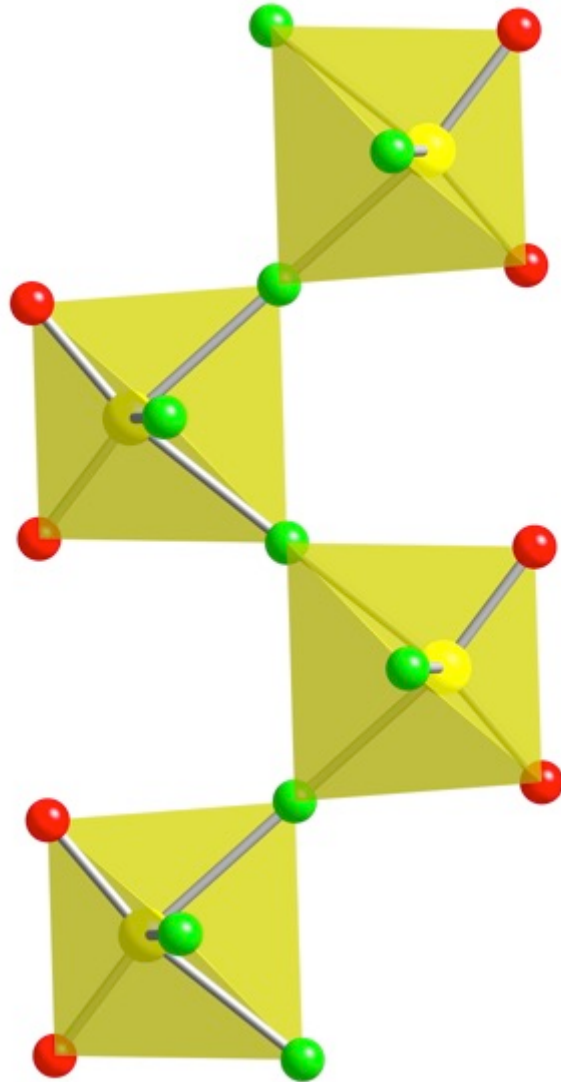
Figure 5.1: 1-D Chains in K₂TiOF₄. Staggered one-dimensional chain consisting of TiO_2F_4 octahedra. The octahedra corner-share exclusively through the F(1) crystallographic site.
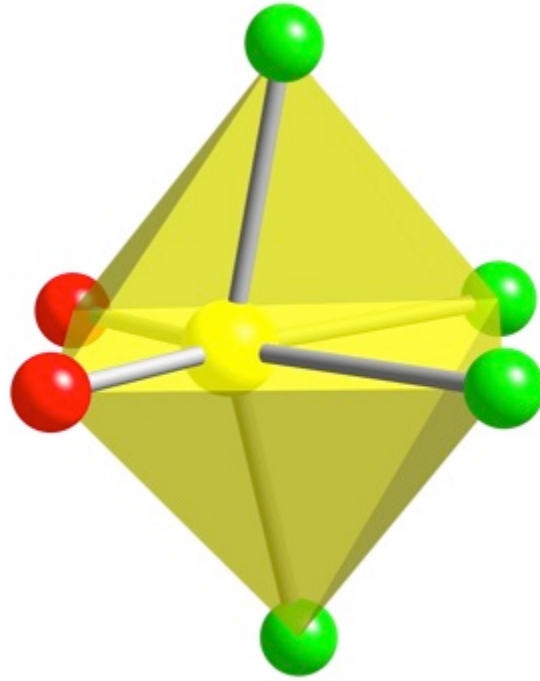
Figure 5.2: Local Environment of Ti in K$_2$TiOF$_4$. The local environment of the Ti^{4+} ion. The octahedron is distorted with the Ti^{4+} ion being shifted toward the oxide containing edge.

corner share to form infinite one-dimensional chains. Unlike the title compound, however, the hydrate octahedra are connected only through the O(1) site and form linear chains. Figure 5.3 illustrates the linear chains of the hydrated compound. The O(1) oxide positions occupy the axial sites of the octahedra with the equatorial sites being occupied only by F(1) and F(2). In this case, the M-O bond is actually longer than the M-F bond due to the fact that the oxide ions linearly bridge two Ti^{4+} ions. The bond length is therefore increased to prevent the cations from being too close together. Figure 5.4 shows a single, fairly regular, TiO_2F_4 octahedron.

In the hydrated compound, the linear chains of octahedra create channels in which the waters of hydration reside. This is illustrated in Figure 5.5, which shows four chains surrounding the channel. The waters of hydration within these channels can form hydrogen bonds with the fluoride ions of the titanium octahedra and act to connect the infinite chains to each other, which strengthens the lattice. In the title compound, K_2TiOF_4, the staggered nature of the chains accompanied by a canting of the chains relative to the hydrated compound fills the space occupied by the channels in the hydrated compound. This leaves no room for waters of hydration. Figure 5.6 illustrates the absence of channels in the title compound.

In both compounds, the structure is held together by the potassium ion. In the hydrated compound, the ten-coordinate potassium polyhedra fill all space. The three-dimensional potassium lattice is formed by face- and edge-sharing KO_4F_6 polyhedra that connect along all three axes, as illustrated in Figure 5.7, which shows a slab of potassium polyhedra. In K_2TiOF_4, there are two unique potassium sites that are located between the one-dimensional chains that hold the structure together. The K(1) site forms infinite

142
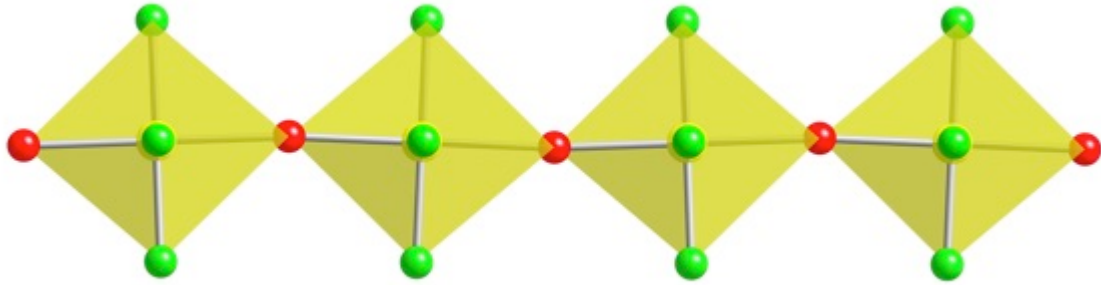
Figure 5.3: Linear Chains the K₂TiOF₄ Hydrate. The nearly perfectly linear chains of the hydrated compound. The chains are formed by corner-sharing octahedra. The sharing occurs only through the oxide ions.
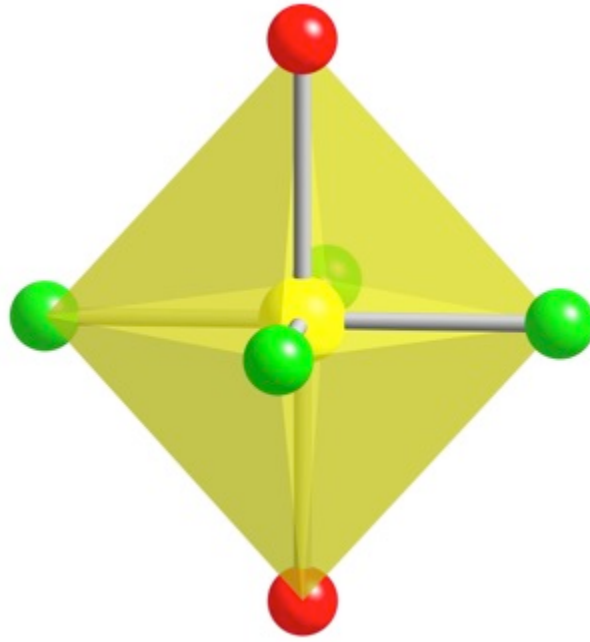
Figure 5.4: Ti Local Environment of the Hydrate. The local environment of the titanium ion in the hydrate. The octahedron is not distorted, and the oxide ions are located *trans* to one another.
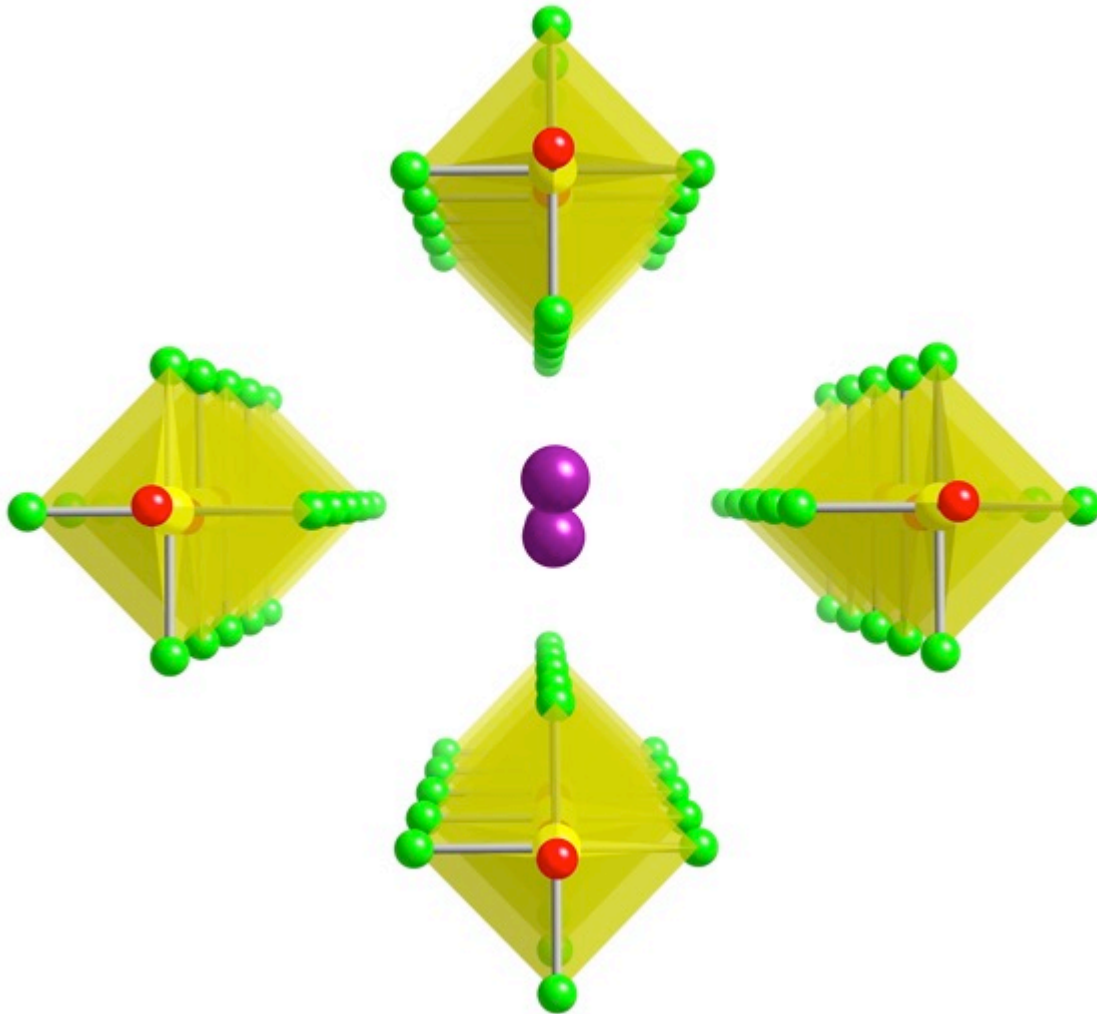
Figure 5.5: Channels in the K$_2$TiOF$_4$ Hydrate. A channel created by four infinite chains in the hydrated compound. The channel is occupied by waters of hydration (shown in purple). The waters can hydrogen bond to the fluoride ions in the chains allowing for reinforcement of the structure.
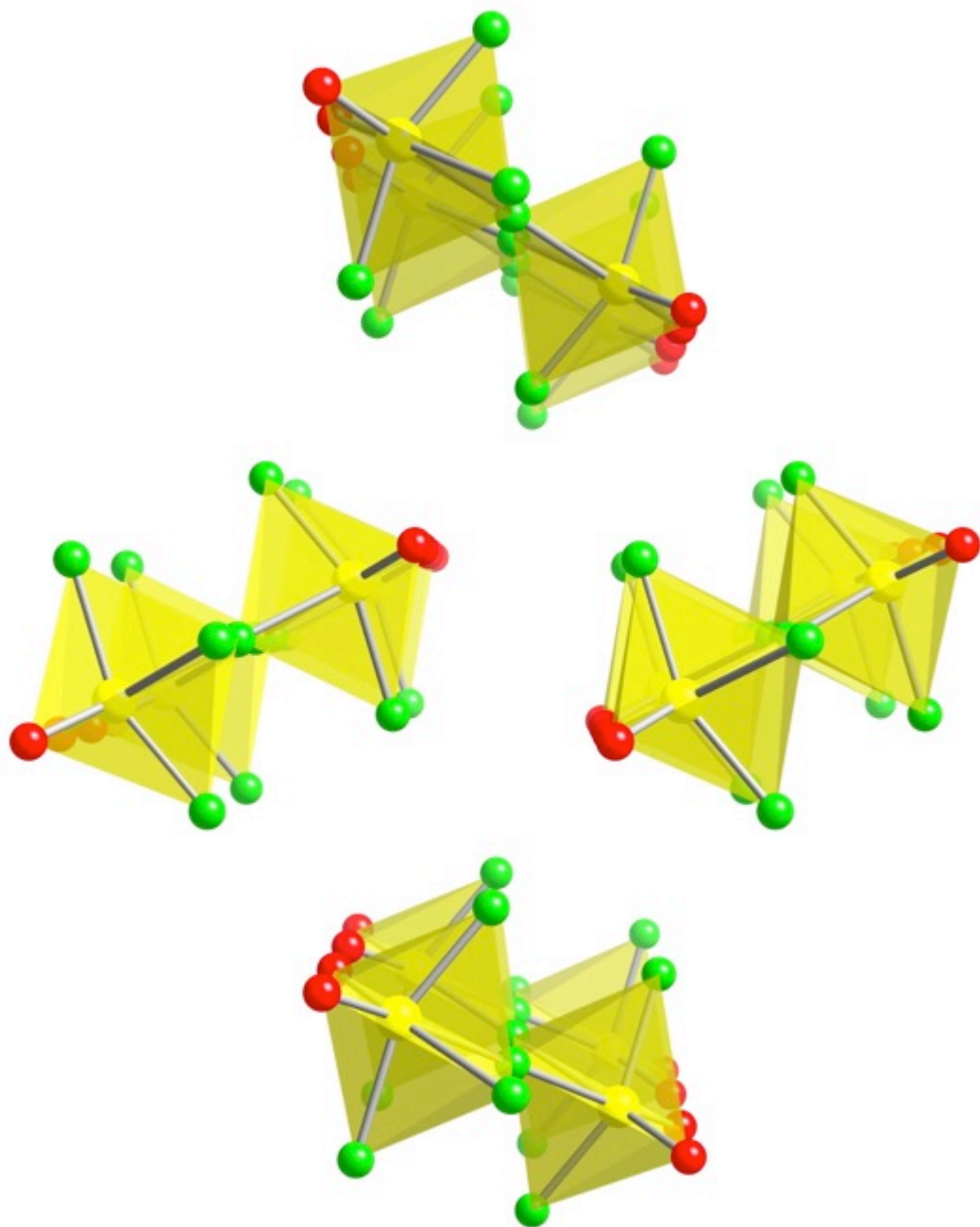
Figure 5.6: Absence of Channels in K_2TiOF_4. The arrangement of the one-dimensional chains of K_2TiOF_4 in space. The staggered nature and rotation of the chains relative to each other fill the space occupied by the waters in the hydrate.
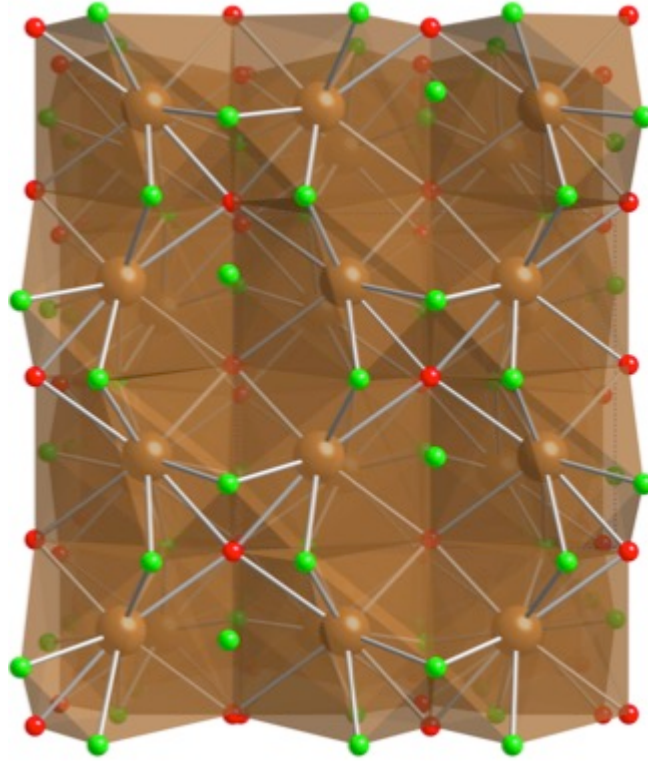
Figure 5.7: Potassium Slab in the K₂TiOF₄ Hydrate. The arrangement of the potassium polyhedra in the hydrate fills all space. The polyhedra consist of potassium coordinating four oxide and 6 fluoride ions.

staggered one-dimensional chains of ten-coordinate potassium polyhedra. The polyhedra consist of four oxide ions arranged in a *cis* fashion to form a square face. The remaining vertices of the polyhedron are fluoride ions. The polyhedra are connected via edge sharing exclusively through the oxide positions to form the staggered chains. Each polyhedron corner shares through each of the fluoride positions, connecting to six additional polyhedra; this connects the staggered chains to each other. Figure 5.8 shows the one-dimensional potassium chains as well as their connectivity to one another. The K(2) position forms staggered one-dimensional chains of face shared polyhedra. These chains are corner-shared to form layers. The ten coordinate polyhedra have four oxide ions arranged in pairs *trans* to one another. Fluoride ions make up the remaining vertices. Face sharing occurs exclusively through the triangular face formed by the two O(1) sites and the F(4) site. Corner sharing within layers occurs exclusively through the F(3) position. The layers are interconnected via corner-sharing through the F(2) position. Figure 5.9 shows two views highlighting the chains of face-shared polyhedra and the layers. Figure 5.10 highlights the differences between the title compound and the hydrate by giving an overall structural representation.

Bond Valence Sum (BVS) calculations were performed for the title compound. BVS calculations were performed for the Ti^{4+}, $K(1)^+$, and $K(2)^+$ sites. The results are 4.408, 1.037, and 1.246. These values all fall within expected values for their respective oxidation states.[17][18][19][20]

3.2 Synthetic Considerations

K_2TiOF_4 has been a sought after compound for many years, and several methods for its synthesis have been tested. Specifically, past groups have tried to synthesize the
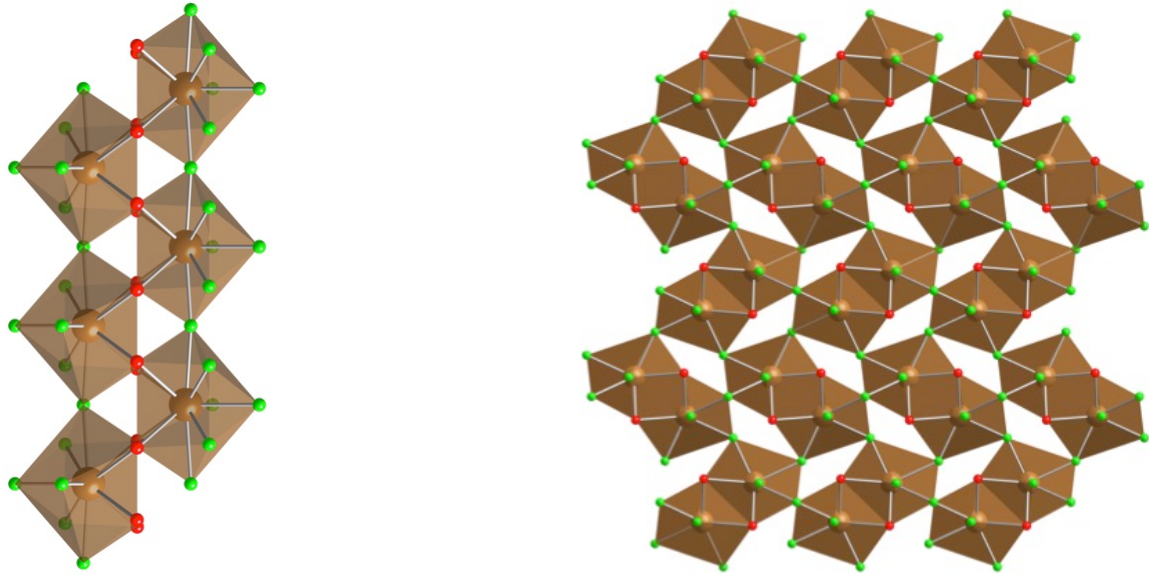
Figure 5.8: K(1) Coordination in K₂TiOF₄. The staggered one-dimensional chains formed by ten coordinate potassium polyhedra in K_2TiOF_4. The four oxide ions are arranged *cis* to one another (Left). The connectivity of the chains in space. Each chain corner shares with another to form a three-dimensional network (Right).

149
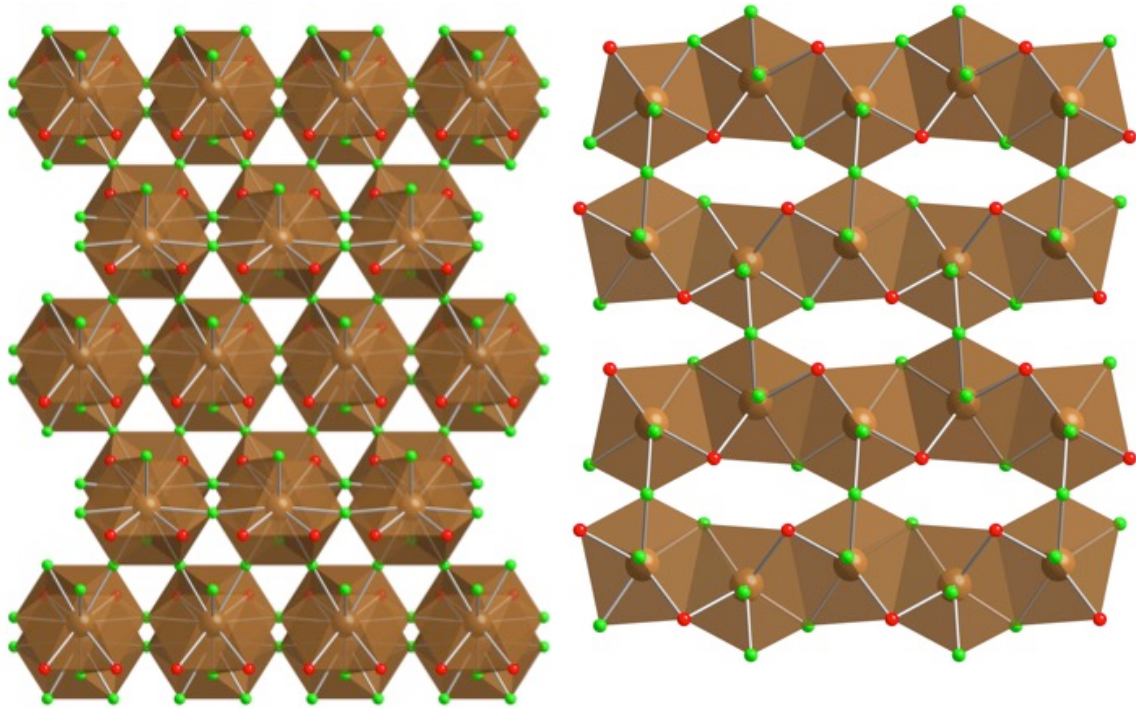
Figure 5.9: K(2) Coordination in K₂TiOF₄. The layered structure of the K(2) site of K_2TiOF_4. The layers are connected via corner-sharing, and are offset from one another. Unlike in the K(1_ position, the oxide ions are arranged in pairs which are *trans* to one another (Left). A 90° rotation of the left image. This view shows how the layers are made up of face sharing polyhedra (Right).
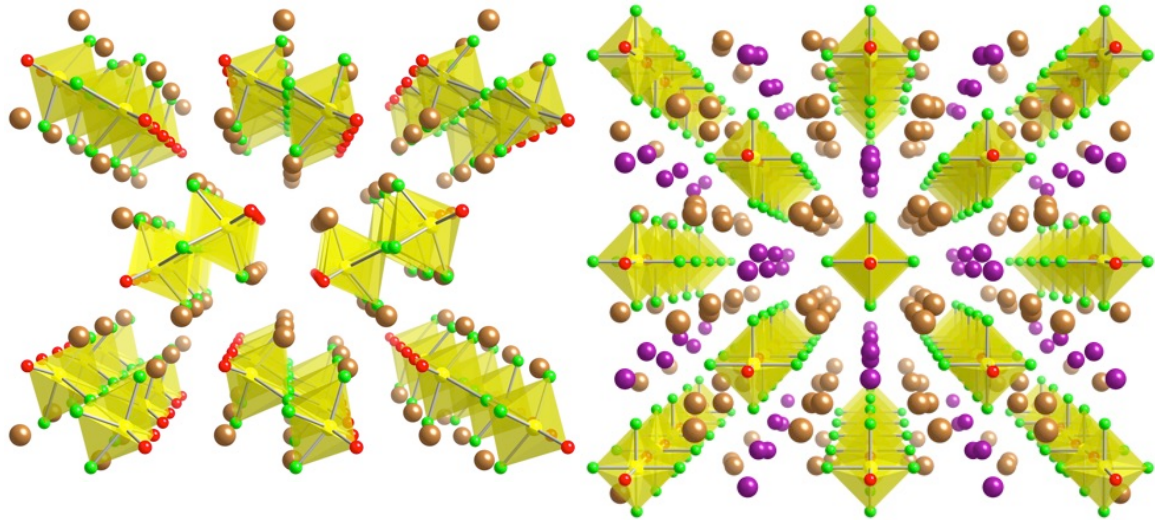
Figure 5.10: Overall Structure Depictions of K$_2$TiOF$_4$ and its Hydrate. An overall representation of K$_2$TiOF$_4$ (Left) and the hydrate (Right) for comparison.

title compound by thermal decomposition of the peroxide precursor $K_2Ti(O_2)F_4$ and by dehydration of the hydrated precursor $K_2TiOF_4 \cdot H_2O$. The previous section compared the crystal structures of the title compound and the hydrate. By comparing the two different structures, some conclusions can be drawn as to why previous synthetic attempts have been unsuccessful.

In order to successfully transform the structure from that of the hydrate to that of the title compound, several large changes have to occur. First, the dehydration would have to occur. This would involve removing the waters of hydration from inside the channels formed by the linear one-dimensional chains of the hydrate. This is problematic because the waters play a role in the integrity of the structure due to the hydrogen bonding between the waters and the fluoride ions in the octahedra. Without hydrogen bonding to stabilize the structure, it would collapse.

Secondly, the connectivity of the titanium octahedra and the one-dimensional chains would have to change during the structural transformation. Both compounds are composed of TiO_2F_4 octahedra, but in the hydrate the oxide ions are located axially and *trans* to one another while in the title compound they are located equatorially and *cis* to one another. In the hydrate the octahedra are connected exclusively through the oxide site, while the octahedra are only connected via fluoride in the title compound. Additionally, the chains would have to go from linear to a staggered configuration as well as rotate to fill the space left by the hydration waters.

Finally, the potassium polyhedra must transform from a cubic configuration filling all space to a much more complicated structure of interconnected one-dimensional chains and layers of face-, edge-, and corner-sharing polyhedra. Such drastic changes

would be surprising under the mild dehydration conditions and render such a crystal-to-crystal transition unlikely. It is for this reason that a direct synthesis of the title compound, such as the one discussed herein, is a more favorable approach for this system than a synthesis utilizing precursors such as the peroxide or hydrated compounds.

3.3. Energy Dispersive Spectroscopy (EDS)

EDS was used to confirm the presence of potassium, titanium, oxygen, and fluorine. EDS suggested that potassium and titanium are present in roughly a 2:1 potassium to titanium ratio. EDS does not give reliable quantitative data for oxygen and fluorine.

4. Conclusion

K_2TiOF_4 is a compound that has been long sought after due to its potential photocatalytic activity, but previous attempts at its synthesis have proven to be problematic. Attempts to synthesize K_2TiOF_4 from the peroxide and hydrate precursors have been unsuccessful, and led to the reporting of incorrect structural data. This work has determined that K_2TiOF_4 crystallizes in the orthorhombic space group *Pnma*. In fact, K_2TiOF_4 crystallizes in the same space group and with similar lattice parameters as its vanadium analog, K_2VOF_4. This work has determined that synthesis of the title compound from precursors is unlikely due to the structural differences, and thus a direct synthetic method such as the one reported here should be utilized.

Acknowledgements

References

(1) Shiraishi, Y.; Hirai, T. *J. Jpn. Petrol. Inst*. **2012** *55,* 287-298.

(2) Yamagata, S.; Nishijo, M.; Murao, N.; Ohta, S.; Mizoguchi, I. *Zeolites* **1995** *15*, 490-493.

(3) Hattori, A. *J. Sol-Gel Sci. Technol.* **2001** *22*, 47.

(4) Kou, J.; Gao, J.; Li, Z.; Yu, H.; Zhou, Y.; Zou, Z. *Catal. Lett.* **2015**, 640.

(5) Sheng, J.; Tang, K.; Cheng, W.; Wang, J.; Nie, Y.; Yang, Q. *J. Hazard. Mater*. **2009** *171*, 279-287.

(6) Aldous, D. W.; Lightfoot, P. *Solid State Sci.* **2009** *11*, 315-319.

(7) Ginsberg, V. H.; Holder, G., *Z. anorg. allg. Chem.* **1931**, 188.

(8) Schmitz-Dumont, O.; Poggenhoff, P. *Z. Anorg. Allg. Chem*. **1952** 268, 57.

(9) Deddmore, D. Z.; Machin, J. G.; Allen, Q. W. *J. Amer. Ceram. Soc.* **1962** *45*, 120.

(10) Drossbach, P.; Rossberger, E. *Z. Elektrochem. Ber. Bunsenges. Phys. Chem*. **1956** *60*, 470.

(11) Schabert, M.; Pausewang, G. *Z. Anorg. Allg. Chem*. **1988**, 143.

(12) Schmidt, R.; Pausewang, G. *Z. Anorg. Allg. Chem*. **1985**, 213.

(13) Yeon, J.; Sefat, A. S.; Tran, T. T.; Halasyamani, P. S.; zur Loye, H. -C. *Inorg. Chem*. **2013** *52*, 6179-6186.

(14) Bugaris, D. E.; zur Loye, H. -C. *Angew. Chem. Int. Ed. Engl*. **2012** *51*, 3780-3811.

(15) SMART Version 5.625, SAINT+ Version 6.45 and SADABS Version 2.05, Bruker Analytical X-ray Systems, Inc., Madison, Wisconsin, USA, (2001)

(16) SHELXTL Version 6.14, Bruker analytical X-ray Systems, Inc., Madison, WI, (2000)

(17) Adams, S. *Acta. Cryst*. **2001** *B57*, 287-287.

(18) Allmann, R. *Monatshefte Chem*. **1975** *106*, 779.

(19) Brese, N. E.; O'Keefe, M. *Acta. Cryst*. **1991** *B47*, 192-197.

(20) Brown, I. D.; Altermatt, D. *Acta. Cryst.* **1985** *B41*, 244-247.

CHAPTER 6:

UTILIZING AN *IN SITU* REDUCTION IN THE SYNTHESIS OF BAMoOF₅*

*Adapted from Felder; J. B., Smith, M. D.; zur Loye, H. –C. *J. Chem. Cryst.* **2018** *submitted.*

156

Introduction

Hydrothermal synthesis is an extremely versatile tool for synthetic chemists that can utilize a wide range of conditions to synthesize an impressive variety of solid-state products, ranging from oxides[1–5], to halides[6–10], to inorganic-organic hybrid materials[11–16]. Hydrothermal synthesis can be used in so many ways primarily because it can utilize a wide temperature range, with a wide variety of compatible precursors. Temperatures ranging from 50° C to 150° C have been used to great effect synthesizing many soft materials like hybrid organic-inorganic crystals[17–19]. Increasing the temperature range slightly to 170° C to 250° C can yield a wide variety of products including zero-dimensional crystals[20] to dense 3D frameworks[21–23]. Hydrothermal techniques can even be taken to extremes: 500° C and beyond, which can yield complicated structures grown from highly refractory materials[24–26].

The versatility of hydrothermal synthesis couples perfectly with the fact that many real-world problems faced by society today involve complicated aqueous systems. One such problem is the storage of nuclear waste resulting from spent nuclear fuel [27]. In the United States, much of this waste has accumulated from the production of nuclear weapons, and continues to accumulate from the use of commercial nuclear reactors to produce electricity. Currently, this waste is vitrified and stored in special containers, which has many advantages, including immobilization and a reduction in waste volume[28–30]; however the vitrification process is complicated by low solubility of certain species in borosilicate glasses used to vitrify the waste.

One such species is the tetrahedral molybdate $[MoO_4]^{2-}$ ion[31]. The molybdate ion has low solubility in borosilicate glass, and so tends to form species such as $CsLiMoO_4$[32]

157

which forms regions of high crystallinity within the vitreous product. This serves to limit the amount of waste that can be vitrified, and inhibits the integrity of the waste glass itself. This problem has motivated us to begin to use mild hydrothermal synthetic routes as a laboratory to explore the interactions of molybdenum and uranium (the primary component of spent nuclear fuel) in aqueous conditions. Reported herein is the synthesis and structure of $BaMoOF_5$, which resulted from our early explorations of this chemistry.

Experimental

Materials and Methods

The following reagents were used as received, with no further modification: $Ba(CH_3CO_2)_2$ (99%, Alfa Aesar), MoO_3 (99.5%, Alfa Aesar), $UO_2(CH_3CO_2)_2$ (ACS grade, IBI Labs), and HF (48%, EMD).

Caution: Hydrofluoric acid is toxic and corrosive, and must be handled with extreme caution and the appropriate protective gear! If contact with the liquid or vapor occurs, proper treatment procedures should immediately be followed.

Caution: Although the uranium precursor used in this synthesis contains depleted uranium, proper procedures for handling radioactive materials should be observed. All handling of radioactive materials were performed in labs specially designated for the study of radioactive actinide materials.

A one-step hydrothermal synthesis was performed. First, 1 mmol amounts of each starting reagent was added to 1mL of distilled water in a PTFE liner. 1 mL of HF was added slowly to the reagent mixture, immediately followed by capping the liner. The PTFE liner was loaded into a stainless steel autoclave and then placed into a

158

programmable convection oven. The oven was programmed to ramp to 200° C at a rate of 10°/minute, hold at 200° C for 24 hours, the cool slowly to 40° C at a rate of 0.1°/minute. Once at 40° C the oven was shut off and allowed to cool naturally to room temperature.

Once cool, the autoclaves were opened and the liners removed. The liners contained blue crystals of the product phase $BaMoOF_5$ in a green solution. The mother liquor was decanted off and the crystals were collected by vacuum filtration. The product crystals were washed thoroughly with water, then acetone, and allowed to dry under vacuum for 10 minutes before collection.

Single-Crystal X-ray Diffraction (SXRD)

X-ray intensity data from a light blue fragment cleaved from a polyhedral crystal were collected at 300(2) K using a Bruker D8 QUEST diffractometer equipped with a PHOTON 100 CMOS area detector and an Incoatec microfocus source (Mo Kα radiation, $\lambda = 0.71073$ Å) [33]. The data collection covered 99.9% of reciprocal space to $2\theta_{max} =$ 75.6º, with an average reflection redundancy of 24.5 and $R_{int} = 0.026$ after absorption correction. The raw area detector data frames were reduced and corrected for absorption effects using the SAINT+ and SADABS programs [33]. Final unit cell parameters were determined by least-squares refinement of 9952 reflections taken from the data set. An initial structural model was obtained with SHELXS using direct methods [34]. Subsequent difference Fourier calculations and full-matrix least-squares refinement against F^2 were performed with SHELXL-2014 [34] using the ShelXle interface [35]. Details about the single-crystal refinement are given in Table 6.1.

Table 6.1: Crystallographic and Refinement Data for BaMoOF$_5$

Empirical Formula	Ba F$_5$ Mo O
Formula Weight (g/mol F.U.)	344.28
Temperature (K)	300(2)
Wavelength (Å)	0.71073
Crystal System	Orthorhombic
Space Group	*Cmcm*
a (Å)	7.1445(3)
b (Å)	6.7894(3)
c (Å	10.1969(4)
Volume (Å^3)	494.62(4)
Z	4
Density (Mg/m^3)	4.623
Absorption Coefficient (mm^{-1})	10.465
F(000)	604
Crystal Size (mm)	0.08 x 0.06 x 0.05
Theta range for data collection	3.997° - 37.802°
Reflections	18632
Unique reflections	739
Completeness to θ = 32.575°	99.9%
Data/Restraints/Parameters	739/0/29
Goodness of Fit on F^2	1.199
Final R Indices	R$_1$ = 0.0126, wR$_2$ = 0.0315
R indices (all data)	R$_1$ = 0.0137, wR$_2$ = 0.0317
Extinction coefficient	0.00193(17)
Largest diff. peak and hole (e$^-$/Å^3)	0.895 and -0.486

160

The compound crystallizes in the orthorhombic system. Systematic absences were consistent with space groups *Ama*2, *Cmc*2$_1$ and *Cmcm*, the latter of which was confirmed by structure solution. The asymmetric unit in *Cmcm* consists of five atoms: one barium atom (Ba1, site 4*a*, site symmetry 2/*m*), one molybdenum atom (Mo(1), site 4*c*, symmetry *m*2*m*), one oxygen atom (O(1), site 8*f* with symmetry m.. and disordered over site 4*c*), and two fluorine atoms (F(1) on a general position, site 16*h*; F(2) on site 4*c*). All atoms were refined with anisotropic displacement parameters. If refined with a single position, the U_{ij} parameters for the unique oxygen atom O(1) describe a somewhat prolate ellipsoid, with $U_3/U_1 = 5.2$, suggesting a deviation from a single average oxygen atomic position. Several structural models were refined to investigate this: (a) simple two-site disorder across the mirror plane perpendicular to [001], (b) various lower symmetry space groups (*Cmc*2$_1$, *Ama*2, *C*2/*m*, C2). The disorder model (a) with O(1) on site 8*f* (site symmetry *m*) is stable and yields a more spherical oxygen ellipsoid ($U_3/U_1 = 2.5$). This generates two equivalent Mo-O bond distances of 1.667(3) Å, slightly longer than the Mo-O distance in the 'ordered' single-site model, 1.659(3) Å. The apparent shortening of the Mo-O distance in the latter case is then due to libration. *R*-factors and difference map features were essentially identical between the two models. Lowering the symmetry (models (b)) did not produce satisfactory refinements. In the orthorhombic space groups *Cmc*2$_1$ and *Ama*2, and the monoclinic space group *C*2/*m*, the anisotropic displacement parameters of O(1) are still elongated across a mirror plane, with U_3/U_1 values > 5.0. Decreasing the space group symmetry to *C*2, where oxygen is on a general position, resulted in an unstable refinement and O(1) U_3/U_1 remaining high (7.9). Considering the above observations, the best structure description, reported herein, is in space group

Cmcm with a disordered, two-site oxygen model. The oxygen displacement is modest, with O(1)-O(1)* = 0.37 Å. There is no indication of O/F site mixing from the data. Refined site occupation factors (*sof*s) for O(1), F(1), and F(2) were 0.508(5), 1.02(1) and 1.02(1), within experimental error of full occupancy. The oxygen atom was therefore refined with a fixed *sof* of 0.5 and the F atoms as fully occupied. The Ba and Mo *sof*s refined to 1.004(2) and 0.993(2), respectively. The largest residual electron density peak and hole in the final difference map are +0.89 and -0.49 e⁻/Å³, located 0.80 Å from F(2) and 0.62 Å from Mo(1), respectively. Final atomic coordinates were standardized with the Structure Tidy program, and are shown in Table 6.2 [36–38]. Selected bond distances are given in Table 6.3.

Results and Discussion

Synthetic Considerations

The title molybdenum compound was obtained serendipitously while targeting the Ba-U-Mo-F phase space, due to the high molybdenum content of nuclear waste streams. The reaction products include blue product crystals and a green solution, suggesting that the uranium precursor was dissolved and reduced to U(IV), however did not precipitate. While this is unusual in our experience, this suggests a potential way to remove molybdenum selectively from nuclear waste streams. While the uranium did not precipitate, the end product of $BaMoOF_5$ is a testament to the versatility of the *in situ* reduction typically employed to synthesize reduced oxides and fluorides hydrothermally.

Attempts were made to synthesize the title compound without using uranium, however these trials resulted in no precipitation of any crystalline products. This suggests that the uranium plays some role in the formation of $BaMoOF_5$ crystals. It is possible that

162

Table 6.2: Atomic Coordinates (x10^4) and Equivalent Isotropic Displacement

Parameters (Å^2 x10^3) for BaMoOF$_5$

	Occupancy	x	y	z	U$_{eq}$
Ba(1)	1	0	0	0	17(1)
Mo(1)	1	0	4080(1)	2500	14(1)
O(1)	0.5	0	6521(4)	2319(8)	29(2)
F(1)	1	1329(1)	3580(2)	1114(1)	27(1)
F(2)	1	0	1002(3)	2500	21(1)

*U$_{eq}$ is defined as one third of the trace of the orthogonalized U$_{ij}$ tensor

Table 6.3: Selected Interatomic Distances for BaMoOF$_5$

Ba(1) – F(2)	2.6384(5)
Ba(1) – F(1)	2.7116(5)
Ba(1) – F(1)	2.9843(11)
Mo(1) – O(1)	1.667(3)
Mo(1) – F(1)	1.9545(9)
Mo(1) – F(2)	2.0902(17)

163

the uranium species was reduced, and the poorly soluble U(IV) species helps saturate the mother liquor, encouraging the crystallization of the title phase.

Crystal Structure

The structure of BaMoOF$_5$ is a dense three-dimensional oxide-fluoride framework consisting of corner-shared barium polyhedra decorated by Mo(V) octahedra. The molybdenum units are isolated from each other. Figure 6.1 shows a view of the overall structure. Each barium atom is coordinated by 10 fluorine atoms in a slightly distorted pentagonal antiprismatic environment, which can be seen in Figure 6.2. These barium antiprisms connect by sharing a fluorine vertex to form chains running in the *c* direction. These chains are cross-linked by edge sharing forming a three-dimensional barium network, shown in Figure 6.3.

Molybdenum ions reside in a MoOF$_5$ octahedron, where the oxygen atom resides on a split site. The octahedron is only slightly distorted (edges 2.8 Å x 2.6 Å x 2.6 Å), however the barium atom is offset from the center by 0.19 Å (closer to oxygen), which is caused by it's proximity to barium polyhedra which share two faces below the equatorial plane. The equatorial fluorine atoms also share edges with barium polyhedra, leaving the axial oxygen as the only non-shared vertex. Figure 6.4 depicts the local coordination of molybdenum as well as its coordination to barium.

Conclusions

The Mo(V) oxyfluorides compound BaMoOF$_5$ was synthesized *via* a mild hydrothermal route. The molybdenum was reduced *in situ* from a starting oxidation state of 6+ to 5+ utilizing a method previously employed to synthesize U(IV) fluorides. Although the target of this synthesis was to synthesize uranium/molybdenum containing

164
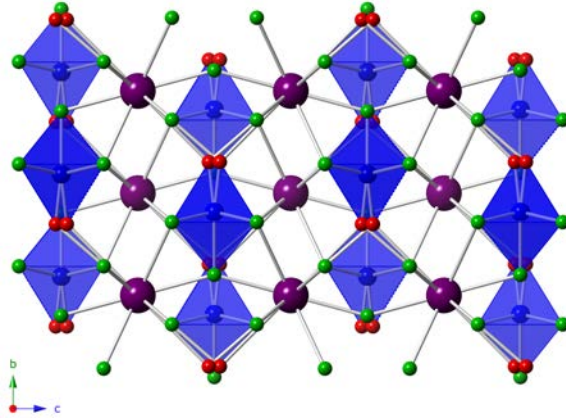
Figure 6.1: The Overall Structure of BaMoOF₅. An overall structural representation of BaMoOF₅. The Mo(V) octahedra are isolated from each other, but connected *via* barium atoms. Each barium is coordinated to 10 F atoms. Molybdenum ions are shown as blue polyhedra, barium as purple spheres, oxygen as red spheres, and fluorine as green spheres.
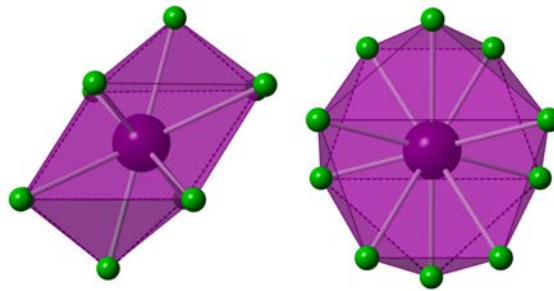
Figure 6.2: The Local Coordination Environment of Ba in BaMoOF₅. *Left:* The barium pentagonal antiprism shown from the side. *Right:* The same antiprism shown from the top-down. Each barium is coordinated by 10 fluorine atoms in this squashed pentagonal antiprism. Barium is shown as purple polyhedra and fluorine as green spheres.

165
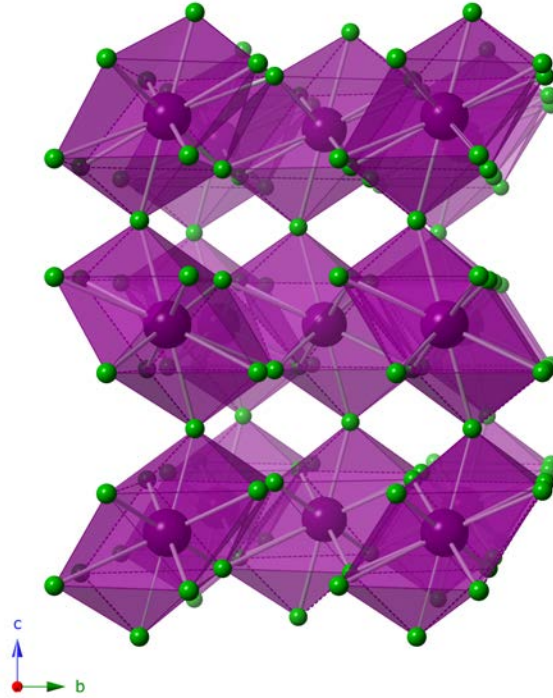
Figure 6.3: Ba Network in BaMoOF$_5$. The three-dimensional network formed by barium atoms in BaMoOF$_5$. The network is formed by corner-shared chains of barium polyhedra. The chains are cross-linked by edge-sharing in the [*ab*] plane. Barium polyhedra are shown in purple, and fluorine atoms are shown in green.

166
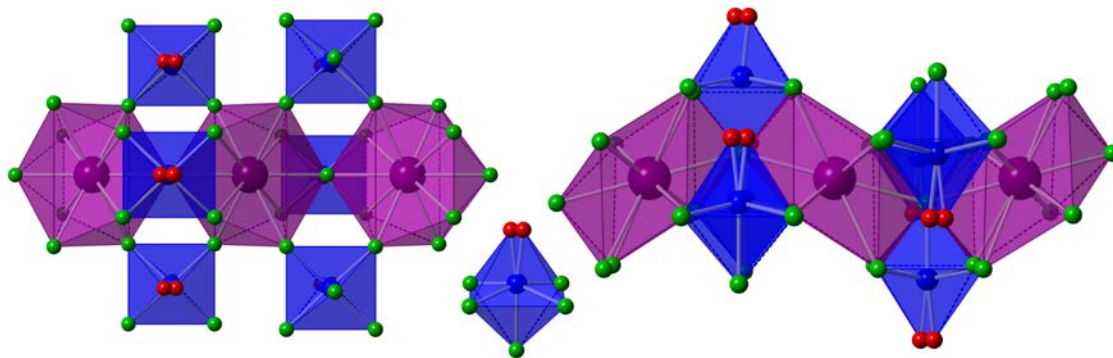
Figure 6.4: Ba and Mo Coordination in BaMoOF5. *Left:* The coordination of Mo with Ba shown from the top-down. Mo polyhedra offset from the barium polyhedra are corner shared, but face share with un-shown barium polyhedra. *Right:* The same unit, rotated to show the Mo polyhedra face sharing with Ba polyhedra. *Center:* The MoOF5 polyhedron with the Mo center offset. In all frames, molybdenum is shown in blue, barium in purple, fluorine in gree, and oxygen in red.

crystals, the precipitation of the Mo(V) crystals is a positive result due to the high amount of molybdenum present in nuclear waste streams. This shows that selectively precipitating Mo-containing crystals could be used as a way to remove molybdenum from these streams.

Acknowledgments

References

(1) Boivin, E.; Masquelier, C.; Croguennec, L.; Chotard, J. N. *Inorg. Chem.* **2017**, *56*, 6776-6779.

(2) Fulle, K.; Sanjeewa, L. D.; McMillen, C. D.; Wen, Y.; Rajamanthrilage, A. C.; Anker, J. N.; Chumanov, G.; Kolis, J. W. *Inorg. Chem.* **2017**, *56*, 6044-6047.

(3) Hamchaoui, F.; Alonzo, V.; Marlart, I.; Auguste, S.; Galven, C.; Rebbah, H.; Le Fur, E. *J. Solid State Chem.* **2017**, *255*, 8-12.

(4) Shen, C.; Mei, D.; Sun, C.; Liu, Y.; Wu, Y. *Z. Anorg. Allg. Chem.* **2017**, *643*, 1082-1087.

(5) Zaitseva, N. A.; Krasnenko, T. I.; Onufrieva, T. A.; Samigullina, R. F. *Russ. J. Inorg. Chem.* **2017**, *62*, 168-171.

(6) Cui, M.; He, Z.; Tang, Y.; Qiu, C. *J. Cryst. Growth* **2017**, *475*, 256-260.

(7) He, L.; Yuan, H.; Huang, K.; Yan, C.; Li, G.; He, Q.; Yu, Y.; Feng, S. *J. Solid State Chem.* **2009**, *182*, 2208-2212.

(8) Jo, V.; Woo Lee, D.; Koo, H.-J.; Ok, K. M. *J. Solid State Chem.* **2011**, *184*, 741-746.

(9) Liu, L.; Yang, Y.; Dong, X.; Zhang, B.; Wang, Y.; Yang, Z.; Pan, S. *Chem.--Eur. J.* **2016**, *22*, 2944-2954.

(10) Yeon, J.; zur Loye, H.-C. *J Chem Crystallogr* **2017**, *47*, 129-132.

(11) Ay, B.; Yildiz, E.; Felts, A. C.; Abboud, K. A. *J. Solid State Chem.* **2016**, *244*, 61-68.

(12) Hmida, F.; Ayed, B.; Haddad, A. *J. Mol. Struct.* **2017**, *1150*, 566-573.

(13) Marinho, M. V.; Reis, D. O.; Oliveira, W. X.; Marques, L. F.; Stumpf, H. O.; Déniz, M.; Pasán, J.; Ruiz-Pérez, C.; Cano, J.; Lloret, F.; Julve, M. *Inorg. Chem.* **2017**, *56*, 2108-2123.

(14) Xie, Y. C.; Cheng, Q. R.; Pan, Z. Q. *J. Mol. Struct.* **2018**, *1154*, 232-238.

(15) Zhao, E.-X.; Li, F.-F.; Shi, Z.-Z.; Zhang, R.-H.; Zhao, D. *Inorganic and Nano-Metal Chemistry* **2017**, *47*, 1175-1178.

(16) Łyszczek, R.; Głuchowska, H.; Cristóvão, B.; Tarasiuk, B. *Thermochim. Acta* **2016**, *645*, 16-23.

169

(17) Lin, Z. J.; Zheng, H. Q.; Zheng, H. Y.; Lin, L. P.; Xin, Q.; Cao, R. *Inorg. Chem.* **2017**, *56*, 14178-14188.

(18) Lu, B. B.; Yang, J.; Liu, Y. Y.; Ma, J. F. *Inorg. Chem.* **2017**, *56*, 11710-11720.

(19) Park, H. J.; Jang, J. K.; Kim, S. Y.; Ha, J. W.; Moon, D.; Kang, I. N.; Bae, Y. S.; Kim, S.; Hwang, D. H. *Inorg. Chem.* **2017**, *56*, 12098-12101.

(20) Thao Tran, T.; Shiv Halasyamani, P. *J. Solid State Chem.* **2014**, *210*, 213-218.

(21) Abeysinghe, D.; Smith, M. D.; Yeon, J.; Morrison, G.; zur Loye, H.-C. *Cryst. Growth Des.* **2014**, *14*, 4749-4758.

(22) Felder, J. B.; Yeon, J.; Smith, M. D.; zur Loye, H.-C. *Inorg. Chem.* **2016**, *55*, 7167-7175.

(23) Yeon, J.; Smith, M. D.; Tapp, J.; Möller, A.; zur Loye, H.-C. *J. Am. Chem. Soc.* **2014**, *136*, 3955-3963.

(24) Mann, J. M.; McMillen, C. D.; Kolis, J. W. *Cryst. Growth Des.* **2015**, *15*, 2643-2651.

(25) McMillen, C. D.; Kolis, J. W. *J. Cryst. Growth* **2008**, *310*, 1939-1942.

(26) Underwood, C. C.; McMillen, C. D.; Kolis, J. W. *J Chem Crystallogr* **2014**, *44*, 493-500.

(27) Page, B. *Mater. World.* **2011**, *19*, 28

(28) Prado, M. O.; Messi, N. B.; Plivelic, T. S.; Torriani, I. L.; Bevilacqua, A. M.; Arribere, M. A. *J. Non-Cryst. Solids* **2001**, *289*, 175

(29) Schweiger, M. J.; Hrma, P.; Humrickhouse, C. J.; Marcial, J.; Riley, B. J.; TeGrotenhuis, N. E. *J. Non-Cryst. Solids* **2010**, *356*, 1359-1367.

(30) Xu, K.; Hrma, P.; Rice, J. A.; Schweiger, M. J.; Riley, B. J.; Overman, N. R.; Kruger, A. A. *J. Am. Ceram. Soc.* **2016**, *99*, 2964-2970.

(31) Short, R. J.; Hand, R. J.; Hyatt, N. C.; Möbus, G. *J. Nucl. Mater.* **2005**, *340*, 179-186.

(32) Hand, R. J.; Short, R. J.; Morgan, S.; Hyatt, N. C.; Mobus, G.; Lee, W. E. *Glass Technol.* **2005**, *46*, 121

(33) APEX2 Version 2014.9-0, SAINT+ Version 8.34A and SADABS Version 2014/4. Bruker Analytical X-ray Systems, Inc., Madison Wisconsin, USA, **2014**

170

(34) Sheldrick, G. M. *Acta Cryst.* **2008**, *A64*, 112

(35) Hubschle, C. B.; Sheldrick, G. M.; Bittrich, B. *J. Appl. Cryst.* **1987**, *20*, 139

(36) Gelato, L. M.; Parthe, E. *J. Appl. Cryst.* **1987**, *20*, 139

(37) S.-Z., H.; Parthe, E. *Chinese J. Struct. Chem.* **2004**, *23*, 1150

(38) Parthe, E.; Gelato, L. M. *Acta Cryst.* **1984**, *A40*, 169

CHAPTER 7:

$[Co(H_2O)_6]_3[U_2O_4F_7]_2$: A MODEL SYSTEM FOR UNDERSTANDING THE FORMATION OF DIMENSIONALLY REDUCED MATERIALS*

Introduction

The continuing efforts of the inorganic research community[1–5] have ensured that uranium crystal chemistry remains a vibrant field of research; partly because of the rich crystal chemistry offered by uranium[6, 7] and partly due to the continuing need for a viable long-term nuclear waste storage solution. The redox chemistry of uranium is of particular interest to the zur Loye group, which probes the conditions under which hexavalent uranium can (or can not) be reduced to tetravalent uranium[8–13]. Furthermore, the exploration of the bonding motifs of uranium in the presence of various anions, particular fluorine[14–17] is of general interest due to the use of uranium fluorides in the processing of nuclear fuel, followed by their subsequent conversion to oxides as the final fuel species.

Hexavalent uranium exists nearly ubiquitously as the linear uranyl (UO_2^{2+} ; $[O=U=O]^{2+}$) ion, which results in the uranyl oxide crystal chemistry being dominated by two-dimensional uranyl oxide sheet-anion structures[18–24]. The formation of these layered structural motifs is favored by the relative inertness of the axial uranyl oxygens that typically do not participate in bonding[25–30], leaving only the equatorial anions to bond, resulting in the aforementioned sheet topology. Fluoride ligands do not possess the ability to form double bonds and, therefore, are unable to form uranyl bonds with uranium. As a result, hexavalent uranium fluorides form either non-uranyl structures, or mixed anion structures where fluoride ions are located in the equatorial positions and uranyl oxygens occupy the axial positions[13, 31, 32]. These latter mixed anion species often lead to interesting structural characteristics that arise from fluorine's unique properties.

It has been shown that the addition of fluorine to a structure can result in a dimensional reduction (i.e. from a 2D layered material to a 1D chain structure) [33].

173

Traditionally, dimensional reduction refers to the addition of anions (such as fluoride) into a metal-anion framework (such as a metal-oxide framework) in order to cut the framework into smaller pieces of lower dimensionality. Fluorine, although perfectly capable of bridging metal centers, would prefer to reside in a terminal position. This property of fluorine is referred to as the 'tailor effect' and is responsible for the 'scissoring' of high-dimensional structures into lower-dimensional ones. The addition of fluorine into an oxide framework lowers the overall anionic charge, alleviating the metal center from having to share anions to limit the overall negative charge. This charge compensation allows the metal to retain the same coordination number with, however, a reduced overall negative charge and, thus, the previously bridging sites can become terminal, breaking 3D structures into 2D sheets, 2D sheets into 1D chains, or 1D chains into molecular species[34].

The dimensionality of a structure is a complex interplay between the oxidation state of metal ions, and a combination of the coordination number and identity of the anionic species. Typical uranyl species tend to form condensed 3D or 2D framework materials. This is due to the fact that uranium exists in the hexavalent state and prefers coordination numbers between 6-8. With a coordination number of 6, a hypothetical uranyl ion with the formula UO_6 would have an overall charge of -6, which would favor condensation of uranyl polyhedra by sharing oxygen anions, thereby reducing the overall charge by -1 for each oxygen that is shared by two uranium polyhedra (by -1.33 if three polyhedra share the bridging oxygen). With coordination numbers of 7 and 8 hypothetical uranyl ions would have anionic charges of -8 and -10, respectively, creating an even greater driving force for condensation into 2- or 3D structures to allow sharing of oxygen

174

anions, and indeed this observation has been extensively noted in the literature[18, 20–22, 35–39].

By providing anions with a lower negative charge (such as fluorine), the hypothetical uranyl polyhedral ions have reduced anionic charges of -2 for UO_2F_4 to -4 for UO_2F_8 (as discussed previously, fluoride ligands cannot form the double bonds necessary to occupy the uranyl positions). This reduced overall negative charge tends to reduce the amount of condensation required to compensate for more negatively charged anions, resulting in dimensionally reduced materials. Again, this observation has been noted in the literature[12, 31, 32].

If one choses the case of a uranyl fluoride sheet consisting only of edge-sharing pentagonal bipyramids $[UO_2F_5]$ as a model, then each polyhedron can be written as $UO_2F_{5/3}$ since each equatorial fluoride is shared by three uranium centers. This results in each uranium ion experiencing a net -5.667 charge (-4 from the oxygen anions and -1.67 from the 5 fluoride anions contributing -1/3 charge each) resulting in an overall positive charge for the sheet, with a +0.333 charge per uranium. Such an arrangement of cationic units has not been reported and would require anions to be present between uranyl sheets. These anions would be sandwiched between two close packed fluoride layers, which is energetically unfavorable; therefore, we consider cationic polyhedra to be unstable and unlikely to result in stable structures. To achieve an overall negative sheet charge would require either additional anions or less sharing of anions with neighboring polyhedra.

If the same pentagonal bipyramids are reduced dimensionally to give edge-sharing chains, with two fluoride anions shared between each adjacent uranyl center, then we can revise the polyhedra to be written as $UO_2F_1F_{4/2}$. This results in a net negative

175

charge for each uranyl polyhedra and each uranium experiences a net -7 charge for an overall -1 charge. Further dimensional reduction to vertex-shared chains results in $UO_2F_3F_{2/2}$ polyhedra (-8 net, -2/unit) and, ultimately isolating each uranyl polyhedron gives rise to the molecular UO_2F_5 unit, experiencing a -9 net charge from the ligands and an overall -3 charge per isolated polyhedron.

Given this progression, it is easy to see how the addition of fluoride ligands into a system favors low-dimensional structures, ultimately resulting in isolated polyhedra. Conversely, the replacement of fluoride ligands with oxide ligands will favor condensation of molecular species into chains and ultimately sheets to prevent the condition in which sheets or chains have a net negative charge, which is unfavorable. This argument leads to a rather intuitive result, however, one that has been difficult to confirm given the dearth of low-dimensional uranyl structures in the literature. Herein, we report the synthesis and properties of a 1-D uranyl chain structure, $[Co(H_2O)_6]_3[U_2O_4F_7]_2$, which we use as a model system to improve our understanding of the formation of dimensionally reduced uranyl systems.

Experimental

Materials and Synthetic Methods

The following materials were used as received without further modification: $UO_2(CH_3COO)_2$ (International Bio-Analytical Labs, ACS grade), $Co(CH_3COO)_2$ (Matheson, reagent grade), and HF (EMD, 48%).

Caution! Hydrofluoric acid is corrosive and acutely toxic. HF should be handled with extreme caution while wearing the appropriate protective gear. Emergency medical treatment should be sought immediately following exposure to HF liquid or vapor [40–42].

176

Caution! Even though the uranium precursor used in this experiment contains depleted uranium, the appropriate safety precaution for handling radioactive material should be observed. All work with uranium-containing materials was done in labs specially designated for the study of radioactive materials[43].

2 mmols of uranyl acetate and 2 mmols of cobalt (II) acetate were mixed with 1 mL of distilled water in a 23 mL PTFE crucible. After mixing the metal precursors, 1 mL HF was added slowly to the reaction mixture. After the reagents were added, the crucible was sealed into a stainless steel autoclave and placed in a programmable oven. The oven was ramped to 200° C and held for 24 hours. After holding, the oven was cooled at a rate of 0.1°/minute to 40° C, at which point the oven was shut off and allowed to cool to room temperature.

Once cool, the autoclaves were opened, and the resulting orange-red solution was set aside. The solution was allowed to crystallize for three days, revealing orange plate crystals. The crystals were collected by decanting off the remaining solution. The product crystals were washed thoroughly with acetone and allowed to dry under vacuum. The yield of the isolated crystals, based on U, was greater than 90%.

Single-Crystal X-ray Diffraction

X-ray intensity data from an irregular orange chunk were collected at 300(2) K using a Bruker D8 QUEST diffractometer equipped with a PHOTON 100 CMOS area detector and an Incoatec microfocus source (Mo K_α radiation, $\lambda = 0.71073$ Å). The data collection covered 100% of reciprocal space to $2\theta_{max} = 65.2°$, with an average reflection redundancy of 8.6 and $R_{int} = 0.047$ after absorption correction. The raw area detector data

frames were reduced and corrected for absorption effects using the SAINT+ and SADABS programs[44]. Final unit cell parameters were determined by least-squares refinement of 9910 reflections taken from the data set. An initial structural model was obtained with SHELXS using direct methods[45]. Subsequent difference Fourier calculations and full-matrix least-squares refinement against F^2 were performed with SHELXL-2014[45] using the ShelXle interface[46]. Table 7.1 lists crystallographic data and selected refinement statistics.

The compound crystallizes in the monoclinic system. Systematic absences in the intensity data were uniquely consistent with space group, $P2_1/n$, which was confirmed by structure solution. The asymmetric unit consists of two independent uranium atoms, two cobalt atoms, seven fluorine atoms, four uranyl group oxygen atoms and nine water oxygen atoms with their associated hydrogen atoms. All atoms are located on general positions (Wyckoff site 4e) except for Co2, which is located on a crystallographic inversion center (site 2b). Alternatively, the asymmetric unit contains one $[U_2O_4F_7]^{6-}$ repeating unit and one and a half $Co(H_2O)_6^{2+}$ cations, one of which is on an inversion center. All atoms were refined with anisotropic displacement parameters. Reasonable positions for the water hydrogens could be located from Fourier difference maps. They were refined isotropically with d(O-H) = 0.85(2) Å distance restraints, and with all H-H distances in each water molecule restrained to be similar within an effective standard deviation of 0.02 (SHELX SADI). Table 7.2 lists selected interatomic distances.

Powder X-ray Diffraction (PXRD)

Powder X-ray diffraction data were collected on a Rigaku Ultima IV X-ray diffractometer utilizing Cu Kα radiation (λ = 1.5418 Å). Data were collected over the

178

Table 7.1: Crystallographic and Refinement Data for [Co(H₂O)₆]₃[U₂O₄F₇]₂

Empirical Formula	$Co_3 F_{14} H_{36} O_{26} U_4$
Formula Weight (g/mol F.U.)	1847.2
Temperature (K)	300(2)
Wavelength (Å)	0.71073
Crystal System	Monoclinic
Space Group	$P2_1/n$
a (Å)	9.1592(4)
b (Å)	12.6138(5)
c (Å)	15.5892(6)
β(°)	97.7671(10)
Volume (Å³)	1784.53(13)
Z	2
Density (kg/m³)	3437.5
Absorption Coefficient (mm⁻¹)	19.593
F(000)	1638
Crystal Size (mm)	0.12 x 0.08 x 0.05
Theta range for data collection	2.084° - 32.625°
Reflections	57103
Unique reflections	6502
Completeness to θ = 32.575°	100%
Data/Restraints/Parameters	6502/54/285
Goodness of Fit on F^2	1.045
Final R Indices	$R_1 = 0.0225$, $wR_2 = 0.0384$
R indices (all data)	$R_1 = 0.0301$, $wR_2 = 0.0400$
Extinction coefficient	0.00106(2)
Largest diff. peak and hole (e⁻/Å³)	1.368 and -1.079

179

Table 7.2: Selected Interatomic Distances (Å) for [Co(H₂O)₆]₃[U₂O₄F₇]₂

U(1) - O(2)	1.777(2)	Co(1) - O(14)	2.048(3)
U(1) - O(1)	1.777(2)	Co(1) - O(11)	2.051(3)
		Co(1) - O(12)	2.069(3)
U(1) - F(2)	2.241(2)	Co(1) - O(15)	2.082(3)
U(1) - F(1)	2.2812(18)	Co(1) - O(16)	2.115(3)
U(1) - F(5)	2.2886(19)	Co(1) - O(13)	2.116(3)
U(1) - F(4)	2.3075(18)		
U(1) - F(3)	2.3889(18)	Co(2) - O(23)	2.058(2)
		Co(2) - O(23)	2.058(2)
U(2) - O(3)	1.775(2)	Co(2) - O(22)	2.063(3)
U(2) - O(4)	1.779(2)	Co(2) - O(22)	2.063(3)
		Co(2) - O(21)	2.090(3)
U(2) - F(6)	2.222(2)	Co(2) - O(21)	2.090(3)
U(2) - F(7)	2.2830(18)		
U(2) - F(1)	2.2864(18)		
U(2) - F(4)	2.3256(18)		
U(2) - F(3)	2.3928(18)		

angular range of 5° - 65° 2θ, with a step size of 0.02°. PXRD data were collected on ground single crystals of the as-synthesized product, as well as on it's thermal decomposition products.

Optical Spectroscopy

UV-visible Spectroscopy

UV-visible spectra were recorded using a Perkin-Elmer lambda 35 UV-visible scanning spectrophotometer used in diffuse reflectance mode. The instrument is equipped with an integrating sphere and the reflectance data was converted to absorbance internally via the Kubelka-Munk function[47]. Spectra were recorded over the 200 nm – 900 nm wavelength range.

IR Spectroscopy

Infrared spectra were recorded with a Perkin-Elmer Spectrum 100 FT-IR spectrometer. The spectrometer is equipped with a diamond ATR cell to allow measurements on solid-state materials. The final spectrum is composed of 16 averaged scans. Spectra were recorded over the 4000 cm^{-1} – 600 cm^{-1} range.

Magnetic Property Measurements

The magnetic property measurements were performed using a Quantum Design MPMS3 SQUID magnetometer. ZFC and FC data were collected between 2 K – 300 K under an applied magnetic field of 0.1 T. Magnetization measurements were performed at 2 K by sweeping the applied field between -5 T and 5 T. The data were corrected for radial offset and shape effects using the method put forth by Morrison[48].

181

Thermal Properties

The thermal properties were probed using thermogravimetric analysis. TGA data were collected using an SDT Q600 DTA/TGA from room temperature to 900 °C under a 100 mL/min nitrogen flow. The sample was heated in a silver lined alumina crucible at a rate of 10 °C/minute, held isothermal for one hour, then allowed to cool to room temperature.

Energy Dispersive Spectroscopy (EDS)

Energy dispersive spectroscopy (EDS) was performed on product single crystals affixed directly to an SEM stub by carbon tape. EDS was performed using a Tescan Vega-3 SEM equipped with a Thermo EDS attachment. The SEM was operated in low-vacuum mode with a 30 kV accelerating voltage and a 20 second accumulating time. Several crystals in the batch were analyzed to ensure results were representative of the bulk sample.

Results and Discussion

Crystal Structure

The most prominent structural characteristics of $[Co(H_2O)_6]_3[U_2O_4F_7]_2$ are the one-dimensional chains running along the [101] direction, shown in Figure 7.1. The chains are built up of $[U_2O_4F_7]$ uranyl dimers that share a fluoride vertex. Each dimer is formed by two pentagonal bipyramids that are joined along one edge. Figure 7.2 shows the $[U_2O_4F_7]$ dimer as well as the local coordination of uranium in the $[UO_2F_5]$ pentagonal bipyramid. Bipyramidal geometries are common in uranyl compounds and in this instance the uranyl oxide ligands in the axial positions point perpendicular to the [101] direction (perpendicular to the chains), leaving the equatorial fluoride ligands to

182
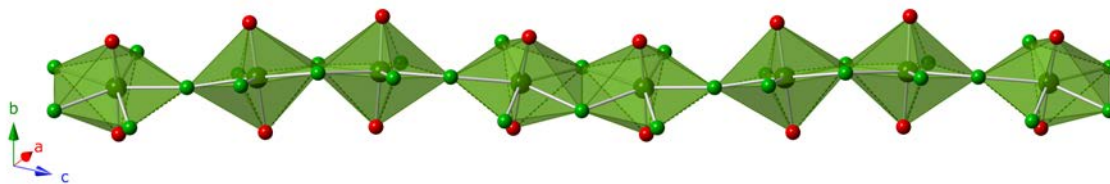
Figure 7.1: Infinite Uranyl Fluoride Chains. The 1-D chains of uranyl fluoride dimers running parallel to the [101] direction. The chains are composed of $[U_2O_4F_7]^{3-}$ dimers that are connected *via* a bridging fluoride. Uranium polyhedra are shown in dark green, oxygen is shown in red, and fluorine is shown in light green.
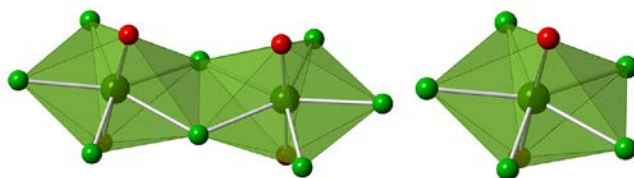
Figure 7.2: Local Coordination and Dimers of Uranyl Centers. *Left:* The $[U_2O_4F_7]$ dimer that forms the 1-D chains in the title compound. The two uranium centers are bridged through F(3) and F(4) with U-F-U angles of 112.04° and 117.68° respectively. *Right:* The local coordination of the U(VI) ions, with typical uranyl (U=O) distances of ~1.78 Å. The U-F distances range from 2.22 to 2.39 Å. Uranium polyhedra are shown in dark green, oxygen in red, and fluorine in light green.

183

participate in the building of the dimer units and connecting them into chains. Each dimer unit is slightly rotated about the U-F(1)-U bond in alternating fashion; presumably to reduce repulsion between pairs of uranyl oxides.

The uranyl chains are isolated from one another; however they are organized into pseudo-layers forming slabs. While one-dimensional chains are a common uranyl structural motif, two-dimensional uranyl sheets are much more common. It is thought that the presence of fluoride in the equatorial positions of the uranyl polyhedra gives rise to a 'tailor effect'[33], which in this case favors the one-dimensional chain over the two-dimensional sheet motif.

Each uranyl chain contributes a -3 overall charge to the structure, combining to contribute a -6 overall charge per unit cell. These anionic slabs are charge balanced by slabs of isolated $Co(H_2O)_6^{2+}$ octahedra, shown along with the cobalt local coordination in Figure 7.3. The neutral aqua ligands allow the full +2 charge of each cobalt center to contribute to balancing the anionic uranyl chains. Figure 7.4 gives an overall representation of the structure. This motif where slabs of condensed anionic uranium centers are balanced by hydrated, isolated transition metal centers is a fairly common occurrence among hydrothermally grown uranium materials[49].

When considering the formation of structures with reduced dimensionality, such as chains or slabs, the concept of solution speciation needs to be brought up as it is a potential influence on the structures that crystallize from solutions. In the area of uranyl bearing hybrid materials the concept of speciation has been explored[50] and a correlation between solution pH and primary building unit (PBU) was invoked based on solution phase studies that indicate that oligomeric species become more prevalent above pH 4.5,

184
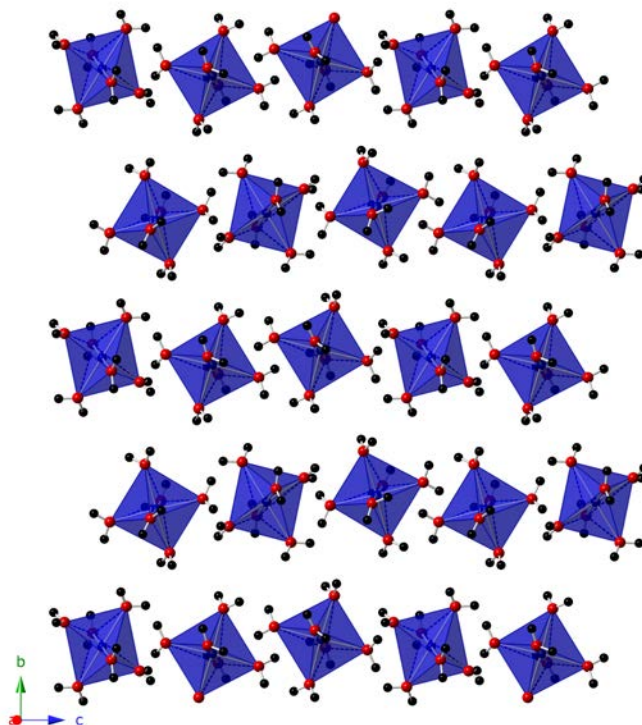
Figure 7.3: Hexa-aqua Cobalt Layer in [Co(H₂O)₆]₃[U₂O₄F₇]₂. The layer of hexaaqua cobalt ions, which are isolated from each other. These ions serve to charge balance the anionic uranyl chains. Each cobalt ion is coordinated solely by six aqua ligands which form the basis for an extensive hydrogen bonding network. Cobalt polyhedra are shown in blue, oxygen in red, and hydrogen in black.
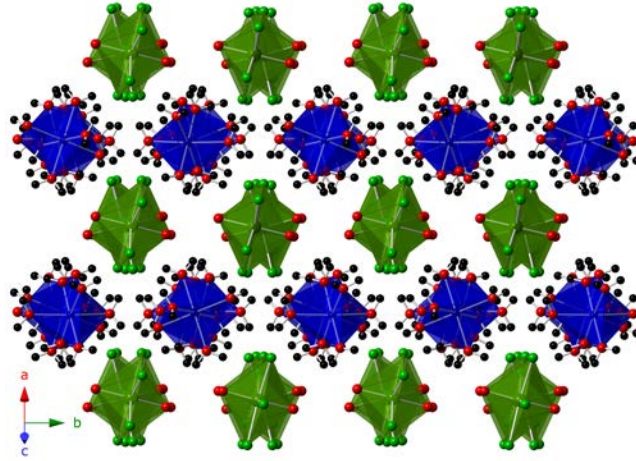
Figure 7.4: Overall Structure of [Co(H₂O)₆]₃[U₂O₄F₇]₂. An overall structural depiction of $[Co(H_2O)_6]_3[U_2O_4F_7]_2$. The uranyl fluoride chains form layers which are interspersed by the cobalt ions. The cobalt hexaaqua ions form an extensive H-bonding network both between terminal hydrogens and water oxygens as well between terminal hydrogens and fluorines from the uranyl polyhedra. Uranium polydra are shown in dark green, cobalt polyhedra are shown in blue, oxygen is shown in red, fluorine is shown in light green, and hydrogen in shown in black.

consistent with the crystallization of monomeric species at low pH. In order to rationalize the existence of high yield, single product hydrothermal reactions, it was proposed that the organic linkers selectively remove a specific solution species, from among the many that are in equilibrium, and incorporate them into the final structure. It is worth noting that even at high pH, however, monomeric species can be isolated and under acidic conditions, dimeric species[51, 52]. Nonetheless, the concept of speciation is important and should be considered in all solution based crystallizations, even those not containing organic complexing agents or those from molten salts[53].

It would be consistent to hypothesize that the pH dependence of hydrolysis of the uranyl species, which favors oligomeric species at high pH, could be used to selectively crystallize monomeric species under low pH conditions. The hydrothermal crystallization of uranyl fluorides, in the absence of organic complexing agents, could be one way to test this hypothesis by structurally characterizing the crystals that form. The description herein of the hydrothermal crystallization of $[Co(H_2O)_6]_3[U_2O_4F_7]_2$ in HF, consisting of infinite uranyl chains, seems to contradict this hypothesis. One reason for this might be the fact that fluoride ligands readily bridge between uranyl centers, both with U(IV) and U(VI) species[11, 14, 54]. Consequently, it would seem reasonable to look for an additional explanation governing the formation of monomeric, dimeric, chain and sheet structures in uranyl fluoride systems.

Understanding the Drive to Reduce Dimensionality

In order to understand which coordination environment favors reduced dimensionality, we conceptualized common uranyl oxide polyhedra and modeled the systematic substitution of the equatorial oxide ligands with fluoride ligands. For

187

consistency, we decided to focus on fluorides only and to ignore other halides and peroxides. In regards to the former, the heavier halides tend to be less prone to bridging even than F, and so we can expect this reduction in dimensionality to be exaggerated, however there are few reports of these in the literature. The latter could be considered a charge analog to fluoride, however, with the caveat that it exists as a bidentate unit, $(O_2)^{2-}$, that could possibly influence the structure of the uranyl polyhedra. An extension of peroxides would be the inclusion of oxalates[55, 56] or tartrates, but that quickly moves beyond the scope of this paper and the argument we are trying to present; namely the relationships between identical polyhedra with various charges and how they influence the bulk crystal structure. An example of this concept is the peroxide mineral studtite, whose crystal structure was reported by Burns and Hughes[57]. Studtite can be considered a 1-D uranyl chain material; with uranyl polyhedra edge-sharing through bidentate peroxo ligands. As we discussed previously, it is true that the $(O_2)^{2-}$ peroxo ligand has a reduced anionic charge due to O-O interactions, however the bidentate nature of the peroxo group and the short O-O distance within the ligand distort the polyhedron, which serves to direct the structure into chains. In this case, the reduced dimensionality results from multiple causes, whose analysis is beyond the scope of this work.

The conceptualized uranyl oxide polyhedra were modeled via the systematic substitution of the equatorial oxide ligands with fluoride ligands and we compiled these results for uranyl fluorides in Table 7.3. Once we derived all possible polyhedra with bipyramidal geometries having coordination numbers between 6-8, we began constructing common structural motifs by condensing identical polyhedra. Care was taken to consider all possible connectivities for chain and sheet motifs. These results are

Table 7.3: Hypothetical Uranyl Structural Units and their Charges

Structural Motif → Uranyl Polyhedron	Isolated Polyhedra			Chain: Corner Sharing			Chain: Hybrid Sharing			Chain: Edge Sharing		
	Composition	Anionic Charge	Net Charge	Composition	Anionic Charge	Net Charge	Composition	Anionic Charge	Net Charge	Composition	Anionic Charge	Net Charge
Square Bipyramid	$(UO_2)O_4$	-12	-6	$(UO_2)O_2O_{2/2}$	-10	-4	$(UO_2)O_1O_{3/2}$	-9	-3	$(UO_2)O_{4/2}$	-8	-2
	$(UO_2)O_3F_1$	-11	-5	$(UO_2)O_1F_1O_{2/2}$	-9	-3	$(UO_2)F_1O_{3/2}$	-8	-2	$(UO_2)O_{3/2}F_{1/2}$	-7.5	-1.5
				$(UO_2)O_2O_{1/2}F_{1/2}$	-9.5	-3.5	$(UO_2)O_1O_{2/2}F_{1/2}$	-8.5	-2.5			
	$(UO_2)O_2F_2$	-10	-4	$(UO_2)F_2O_{2/2}$	-8	-2	$(UO_2)F_1O_{2/2}F_{1/2}$	-7.5	-1.5	$(UO_2)O_{2/2}F_{2/2}$	-7	-1
				$(UO_2)O_1F_1O_{1/2}F_{1/2}$	-8.5	-2.5	$(UO_2)O_1O_{1/2}F_{2/2}$	-8	-2			
				$(UO_2)O_2F_{2/2}$	-9	-3						
	$(UO_2)O_1F_3$	-9	-3	$(UO_2)F_2O_{1/2}F_{1/2}$	-7.5	-1.5	$(UO_2)F_1O_{1/2}F_{2/2}$	-7	-1	$(UO_2)O_{1/2}F_{3/2}$	-6.5	-0.5
				$(UO_2)O_1F_1F_{2/2}$	-8	-2	$(UO_2)O_1F_{3/2}$	-7.5	-1.5			
	$(UO_2)F_4$	-8	-2	$(UO_2)F_2F_{2/2}$	-7	-1	$(UO_2)F_1F_{3/2}$	-6.5	-0.5	$(UO_2)F_{4/2}$	-6	0
Pentagonal Bipyramid	$(UO_2)O_5$	-14	-8	$(UO_2)O_3O_{2/2}$	-12	-6	$(UO_2)O_2O_{3/2}$	-11	-5	$(UO_2)O_1O_{4/2}$	-10	-4
	$(UO_2)O_4F_1$	-13	-7	$(UO_2)O_2F_1O_{2/2}$	-11	-5	$(UO_2)F_1O_1O_{3/2}$	-10	-4	$(UO_2)F_1O_{4/2}$	-9	-3
				$(UO_2)O_3O_{1/2}F_{1/2}$	-11.5	-5.5	$(UO_2)O_2O_{2/2}F_{1/2}$	-10.5	-4.5	$(UO_2)O_1O_{3/2}F_{1/2}$	-9.5	-3.5
	$(UO_2)O_3F_2$	-12	-6	$(UO_2)O_1F_2O_{2/2}$	-10	-4	$(UO_2)F_2O_{3/2}$	-9	-3	$(UO_2)F_1O_{3/2}F_{1/2}$	-8.5	-2.5
				$(UO_2)O_2F_1O_{1/2}F_{1/2}$	-10.5	-4.5	$(UO_2)O_1F_1O_{2/2}F_{1/2}$	-9.5	-3.5	$(UO_2)O_1O_{2/2}F_{2/2}$	-9	-3
				$(UO_2)O_3F_{2/2}$	-11	-5	$(UO_2)O_2O_{1/2}F_{2/2}$	-10	-4			
	$(UO_2)O_2F_3$	-11	-5	$(UO_2)F_3O_{2/2}$	-9	-3	$(UO_2)F_2O_{2/2}F_{1/2}$	-8.5	-2.5	$(UO_2)F_1O_{2/2}F_{2/2}$	-8	-2
				$(UO_2)O_1F_2O_{1/2}F_{1/2}$	-9.5	-3.5	$(UO_2)O_1F_1O_{1/2}F_{2/2}$	-9	-3	$(UO_2)O_1O_{1/2}F_{3/2}$	-8.5	-2.5
				$(UO_2)O_2F_1F_{2/2}$	-10	-4	$(UO_2)O_2F_{3/2}$	-9.5	-3.5			
	$(UO_2)O_1F_4$	-10	-4	$(UO_2)F_3O_{1/2}F_{1/2}$	-8.5	-2.5	$(UO_2)F_2O_{1/2}F_{2/2}$	-8	-2	$(UO_2)O_1F_{4/2}$	-8	-2
				$(UO_2)O_1F_2F_{2/2}$	-9	-3	$(UO_2)O_1F_1F_{3/2}$	-8.5	-2.5			
	c $(UO_2)F_5$	-9	-3	$(UO_2)F_3F_{2/2}$	-8	-2	$(UO_2)F_2F_{3/2}$	-7.5	-1.5	$(UO_2)F_1F_{4/2}$	-7	-1
Hexagonal Bipyramid	$(UO_2)O_6$	-16	-10	$(UO_2)O_4O_{2/2}$	-14	-8	$(UO_2)O_3O_{3/2}$	-13	-7	$(UO_2)O_2O_{4/2}$	-12	-6
	$(UO_2)O_5F_1$	-15	-9	$(UO_2)O_3F_1O_{2/2}$	-13	-7	$(UO_2)O_2F_1O_{3/2}$	-12	-6	$(UO_2)O_1F_1O_{4/2}$	-11	-5
				$(UO_2)O_4O_{1/2}F_{1/2}$	-13.5	-7.5	$(UO_2)O_3O_{2/2}F_{1/2}$	-12.5	-6.5	$(UO_2)O_2O_{3/2}F_{1/2}$	-11.5	-5.5
	$(UO_2)O_4F_2$	-14	-8	$(UO_2)O_2F_2O_{2/2}$	-12	-6	$(UO_2)O_1F_2O_{3/2}$	-11	-5	$(UO_2)F_2O_{4/2}$	-10	-4
				$(UO_2)O_3F_1O_{1/2}F_{1/2}$	-12.5	-6.5	$(UO_2)O_2F_1O_{2/2}F_{1/2}$	-11.5	-5.5	$(UO_2)O_1F_1O_{3/2}F_{1/2}$	-10.5	-4.5
				$(UO_2)O_4F_{2/2}$	-13	-7	$(UO_2)O_3O_{1/2}F_{2/2}$	-12	-6	$(UO_2)O_2O_{2/2}F_{2/2}$	-11	-5
	$(UO_2)O_3F_3$	-13	-7	$(UO_2)O_1F_3O_{2/2}$	-11	-5	$(UO_2)F_3O_{3/2}$	-10	-4	$(UO_2)F_2O_{3/2}F_{1/2}$	-9.5	-3.5
				$(UO_2)O_2F_2O_{1/2}F_{1/2}$	-11.5	-5.5	$(UO_2)O_1F_2O_{2/2}F_{1/2}$	-10.5	-4.5	$(UO_2)O_1F_1O_{2/2}F_{2/2}$	-10	-4
				$(UO_2)O_3F_1F_{2/2}$	-12	-6	$(UO_2)O_2F_1O_{1/2}F_{2/2}$	-11	-5	$(UO_2)O_2O_{1/2}F_{3/2}$	-10.5	-4.5
							$(UO_2)O_3F_{3/2}$	-11.5	-5.5			
	$(UO_2)O_2F_4$	-12	-6	$(UO_2)F_4O_{2/2}$	-10	-4	$(UO_2)F_3O_{2/2}F_{1/2}$	-9.5	-3.5	$(UO_2)F_2O_{2/2}F_{2/2}$	-9	-3
				$(UO_2)O_1F_3O_{1/2}F_{1/2}$	-10.5	-4.5	$(UO_2)O_1F_2O_{1/2}F_{2/2}$	-10	-4	$(UO_2)O_1F_1O_{1/2}F_{3/2}$	-9.5	-3.5
				$(UO_2)O_2F_2F_{2/2}$	-11	-5	$(UO_2)O_2F_1F_{3/2}$	-10.5	-4.5	$(UO_2)O_2F_{4/2}$	-10	-4
	$(UO_2)O_1F_5$	-11	-5	$(UO_2)F_4O_{1/2}F_{1/2}$	-9.5	-3.5	$(UO_2)F_3O_{1/2}F_{2/2}$	-9	-3	$(UO_2)F_2O_{1/2}F_{3/2}$	-8.5	-2.5
				$(UO_2)O_1F_3F_{2/2}$	-10	-4	$(UO_2)O_1F_2F_{3/2}$	-9.5	-3.5	$(UO_2)O_1F_1F_{4/2}$	-9	-3
	$(UO_2)F_6$	-10	-4	$(UO_2)F_4F_{2/2}$	-9	-3	$(UO_2)F_3F_{3/2}$	-8.5	-2.5	$(UO_2)F_2F_{4/2}$	-8	-2

190

Structural Motif: →	Sheet: α-U3O8			Sheet: β-U3O8			Sheet: A5U5O17(OH)						Sheet: K4Sr4[(UO2)13(B2O5)2(BO3)2O12]					
Uranyl Polyhedron	Composition	Anionic Charge	Net Charge	Composition	Anionic Charge	Net Charge	Composition 1	Anionic Charge 1	Net Charge 1	Composition 2	Anionic Charge 2	Net Charge 2	Composition 1	Anionic Charge 1	Net Charge 1	Composition 2	Anionic Charge 2	Net Charge 2
Square Bipyramid				*a(UO2)O4/3	-6.667	-0.667	(UO2)O4/3	-6.667	-0.667									
				(UO2)O3/3F1/3	-6.333	-0.333	(UO2)O3/3F1/3	-6.333	-0.333									
				(UO2)O2/3F2/3	-6	0	(UO2)O2/3F2/3	-6	0									
				(UO2)O1/3F2/3	-5.667	0.333	(UO2)O1/3F2/3	-5.667	0.333									
				(UO2)F4/3	-5.333	0.667	(UO2)F4/3	-5.333	0.667									
Pentagonal Bipyramid	(UO2)O5/3	-7.33	-1.33	(UO2)O5/3O4/3	-7.667	-1.667	(UO2)O5/3	-7.33	-1.33	(UO2)O1/2O4/5	-7.667	-1.667	(UO2)O14/5	-7.167	-1.167	a(UO2)O5/5	-7.333	-1.333
	(UO2)O4/3F1/3	-7	-1	(UO2)O1/2O4/5	-7.167	-1.167	(UO2)O4/5F1/5	-7	-1	(UO2)O1/5O4/5	-7.167	-1.167	(UO2)O1/6O4/5	-6.917	-0.917	(UO2)O4/5F1/5	-7	-1
				(UO2)O1/2O3/3F1/3	-7.333	-1.333				(UO2)O1/2O3/5F1/3	-7.333	-1.333	(UO2)O1/5O3/5F1/3	-6.833	-0.833			
	(UO2)O3/3F2/3	-6.667	-0.667	(UO2)O1/2O3/3F2/3	-6.833	-0.833	(UO2)O3/5F2/5	-6.667	-0.667	(UO2)O1/3O3/5F2/3	-6.833	-0.833	(UO2)O1/4O3/5F1/5	-6.583	-0.583	(UO2)O3/5F2/5	-6.667	-0.667
				(UO2)O1/2O1/2F2/3	-7	-1				(UO2)O1/3O1/5F2/3	-7	-1	(UO2)O1/4O1/5F2/3	-6.5	-0.5			
	{i}(UO2)O2/3F3/3	-6.333	-0.333	(UO2)O3/12O2/3F2/3	-6.5	-0.5	(UO2)O2/3F3/5	-6.333	-0.333	(UO2)O1/2O3/5F2/3	-6.5	-0.5	(UO2)O2/5F2/5	-6.25	-0.25	(UO2)O2/5F3/5	-6.333	-0.333
				(UO2)O1/12O1/3F3/3	-6.667	-0.667				(UO2)O1/10O1/5F3/3	-6.667	-0.667	(UO2)O1/4O1/5F3/3	-6.167	-0.167			
	(UO2)O1/3F4/3	-6	0	(UO2)F2/2F3/3	-6.167	-0.167	(UO2)O4/5F4/5	-6	0	(UO2)F2/5O1/5F4/5	-6.167	-0.167	(UO2)O1/6O1/2F3/3	-5.917	0.083	(UO2)O1/5F4/5	-6	0
				(UO2)O3/3F4/3	-6.333	-0.333				(UO2)O1/3F3/3	-6.333	-0.333	(UO2)F2/5F3/5	-5.833	0.167			
	(UO2)F5/3	-5.667	0.333	(UO2)O1/12F4/3	-5.833	0.167	(UO2)F5/3	-5.667	0.333	(UO2)F5/3	-5.833	0.167	(UO2)F4/5F4/5	-5.583	0.417	(UO2)F5/5	-5.667	0.333
Hexagonal Bipyramid													(UO2)O5/4O1/4	-7.833	-1.833	a(UO2)O4/3O3/4	-7.667	-1.667
													(UO2)O4/6F1/6	-7.5	-1.5	(UO2)O1/2F1/4	-7.333	-1.333
													(UO2)O2/5F1/4	-7.583	-1.583	(UO2)O4/6F1/4	-7.417	-1.417
													(UO2)O3/3F2/4	-7.167	-1.167	(UO2)O5/6F1/4	-7	-1
													(UO2)O4/3F1/4	-7.25	-1.25	(UO2)O1/2O1/4F1/4	-7.083	-1.083
																(UO2)O1/3F1/4	-7.667	-1.667
													(UO2)O3/5O1/6O3/4	-6.833	-0.833	(UO2)O1/6F1/4O3/4	-6.667	-0.667
													(UO2)O3/3F2/6F2/4	-6.917	-0.917	(UO2)O2/9F2/3O1/6F2/4	-6.75	-0.75
																(UO2)O1/3F1/6F2/4	-6.833	-0.833
													(UO2)O3/5F4/6O1/4	-6.5	-0.5	(UO2)O1/6F4/5O3/4	-6.333	-0.333
													(UO2)O2/5F3/6F1/4	-6.583	-0.583	(UO2)O1/6F4/6O1/4F1/4	-6.417	-0.417
																(UO2)O2/9F2/6F2/4	-6.5	-0.5
													(UO2)F3/3O3/6O1/4	-6.167	-0.167	(UO2)F4/9O1/6F2/4	-6.083	-0.083
													(UO2)O2/5F4/6F1/4	-6.25	-0.25	(UO2)O1/3F4/6F1/4	-6.167	-0.167
													(UO2)F5/6O1/4	-5.917	0.083	(UO2)F4/6F1/4	-5.833	0.167

also shown in Table 7.3. Finally, we analyzed existing structures and determined which model coordination unit they matched. These structures are denoted by letters in Table 7.3, and identified in Table 7.4.

In order to determine if any trends existed in these data, we plotted the results, shown in Table S1. The plot shows net anionic charge per polyhedron as a function of structural unit, from 0-D structures to 2-D sheet structures, and is shown in Figure 7.5. The shape of each point denotes the coordination environment, and the color of each point denotes the amount each polyhedron was fluorinated. In order to see how known structures fit into this scheme, we determined where the polyhedra of several reported uranyl systems fell on the plot, and outlined the appropriate point in blue. In order to broaden the availability of real structures, we considered hydroxyl groups as a suitable analog for fluorine and treated them as such.

By examining Figure 7.5, it is immediately obvious that an increase of dimensionality will reduce the net anionic charge per polyhedron. This is due to the fact that ligands become shared between uranyl centers, spreading the same charge between two or more ions. Also readily apparent is the fact that fluorinating a polyhedron has the same effect as reducing the anionic charge. By combining fluorination with increased dimensionality we find that some hypothetical combinations result in non-physical structures with a net positive polyhedral charge. As was discussed previously, we consider this to be energetically unfavorable, and highly unlikely to exist; an extensive search of the literature failed to turn up a single example. We highlight this fact by including points on Figure 7.5 that represent a selection of 10 reported structures.

191

Table 7.4: Reference Materials Pertaining to Table 7.3.

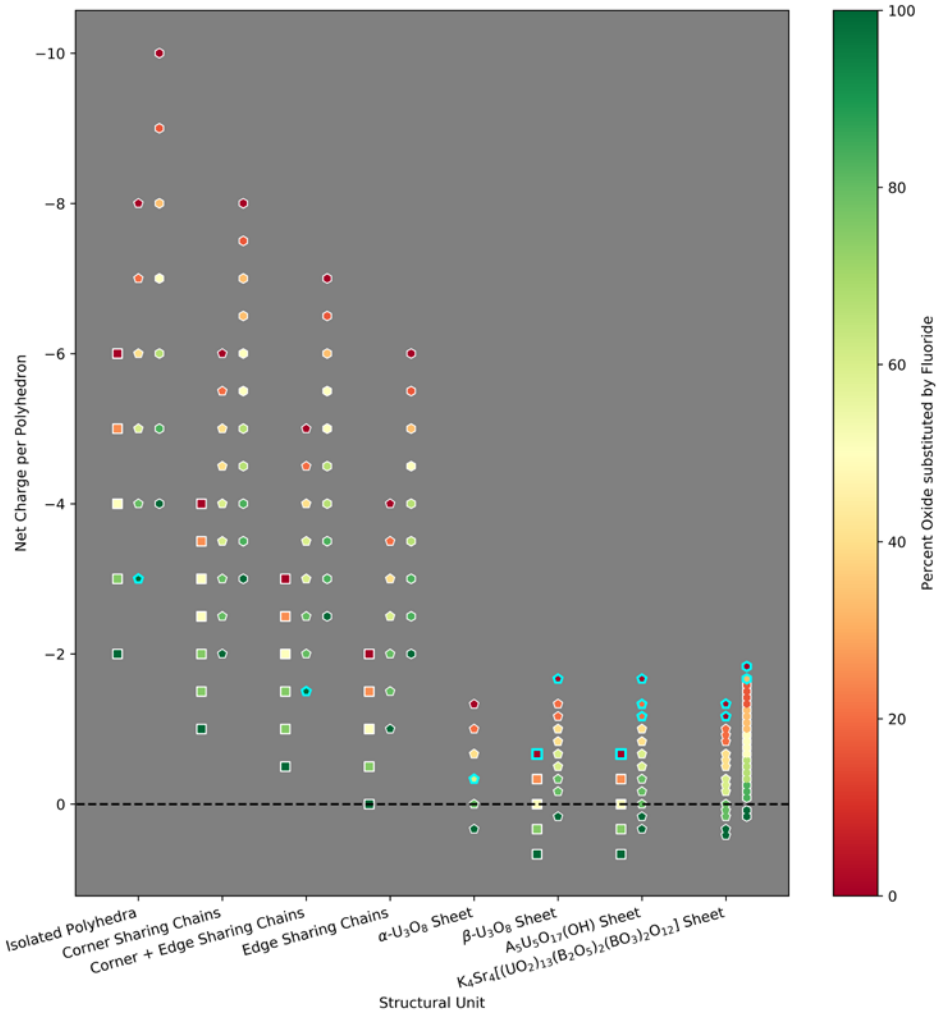| Letter	Structure	Reference
a	$[Co(H_2O)_6]_3[U_2O_4F_7]_2$	This Work
b	$K_5U_5O_{17}(OH)$	18
c	$A_3(UO_2)F_5$	29
d	$Na_3(UO_2)_2F_3(OH)_4(H_2O)_2$	28
e	$A_2MnU_3O_{11}$	19
f	$K_4Sr_4[(UO_2)_{13}(B_2O_5)_2(BO_3)_2O_{12}]$	64
g	$K_4[(UO_2)_5(BO_3)_2O_4] \cdot H_2O$	51
h	$K_{15}[(UO_2)_{18}(BO_3)_7O_{15}]$	51
i	$K_4M(OH)_3(H_2O)_9[(UO_2)_{12}O_7(OH)_{13}]$	37
j	$K_4U_5O_{16}Cl_2$	25

192

Figure 7.5: Plot of Hypothetical Uranyl Structural Units Versus their Anionic Charge. A plot of anionic charge versus structural unit for a set of hypothetical uranyl structural units. The structural units range from isolated polyhedra (0-D) to model uranyl sheets (2-D). The shape of each point represents the uranyl coordination (square = square bipyramid, pentagon = pentagonal bipyramid, hexagon = hexagonal bipyramid). The color of each point represents the amount of fluoride substitution, and follows the color scale on the right side of the figure. Hypothetical units that correspond to real structures are highlighted in blue.

At the top end of the graph, the high anionic charge end, we find very few reported materials. We hypothesize that the reason for this is two-fold: firstly low-dimensional uranyl structures are difficult to prepare synthetically and, therefore, are not plentiful in the literature and not extensively studied, and secondly because we hypothesize that polyhedra with high anionic charges should be less stable due to the fact that it is difficult to fit enough cations in these structures to adequately balance the anionic charge. Although this intuitively makes sense, it is difficult to quantify and we suspect there is not a hard limit, but rather a general trend. An expansion of the library of low-dimensional uranyl materials is warranted in order to test our hypothesis.

Powder X-Ray Diffraction (PXRD) and EDS

PXRD was used to confirm the phase purity of the as-synthesized material. Product crystals were ground in an agate mortar and loaded into a sample well for analysis. The resulting powder diffraction pattern was compared with the calculated powder pattern derived from the single-crystal structure refinement. The diffraction pattern was found to be in excellent agreement with the calculated pattern with no extra peaks, indicating that the bulk sample represents a phase pure sample of $[Co(H_2O)_6]_3[U_2O_4F_7]_2$. The powder diffraction pattern can be seen compared to the calculated pattern in Figure 7.6.

EDS was used to qualitatively identify the constituent elements in the reported single-crystals. EDS identified all constituent elements (Co, U, O, F) except for hydrogen, which is not detectable using the available instrumentation, and confirmed the absence of extraneous elements in the crystals.
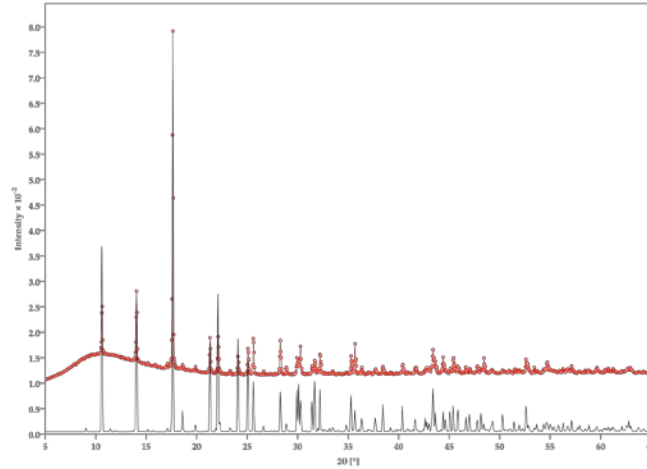
Figure 7.6: Calculated and Observed PXRD Patterns of $[Co(H_2O)_6]_3[U_2O_4F_7]_2$. The powder diffractogram of $[Co(H_2O)_6]_3[U_2O_4F_7]_2$ is shown from $5°$ - $65°$ 2θ in red. The black diffractogram was calculated from the CIF obtained from the single crystal structure refinement. The two patterns agree well with no extra peaks, indicating a crystalline phase pure sample. The hump which appears at low angles in the observed pattern has been determined to be iron x-ray fluorescence which arises from our steel sample holders, not an amorphous component to the sample.

195

Optical Properties

The UV-Vis spectrum is expected to have contributions from both *d-d* electronic transitions within the cobalt ion as well as from weak uranyl absorptions. $Co^{II}(H_2O)_6^{2+}$ is a high-spin d^7 ion, for which the Tanabe-Sugano diagram for octahedral d^7 ions is a useful tool for assigning the absorption bands[58]. The observed spectrum contains two main features: the absorption edge onset, which occurs below 350 nm, as well as a broad absorbance band from 350 – 575 nm. The observed UV-vis spectrum can be seen in Figure 7.7.

The Tanabe-Sugano diagram reveals three possible transitions for the high-spin d^7 ion from the quartet ground state of $^4T_1(P)$. The lowest energy transition, $^4T_1(F) \Box ^4T_2$ is known to occur in the infrared range and is therefore not observable in this spectrum[59]. The other two transitions, $^4T_1(F) \Box ^4T_1(P)$ and $^4T_1(F) \Box ^4A_2$, both occur at roughly 500 nm and below. These transitions usually overlap, explaining the broad absorbance band[59]. In the observed spectrum, there is a fine structure appearing on top of the Co *d-d* absorbance band that is attributed to the uranyl absorptions, which also occur below 500 nm[60].

The major features of the IR spectrum can be attributed to the aqua ligands coordinated to the cobalt ions. The broad band at 3400 cm^{-1} is characteristic of O-H stretching modes, while the O-H bending modes can be seen above 1500 cm^{-1}. In addition to the O-H vibrational modes, the intense peak at 900 cm^{-1} is attributed to the uranyl U-O stretch[60]. The vibrational spectrum is shown in Figure 7.8, with the band assignments displayed in Table 7.5
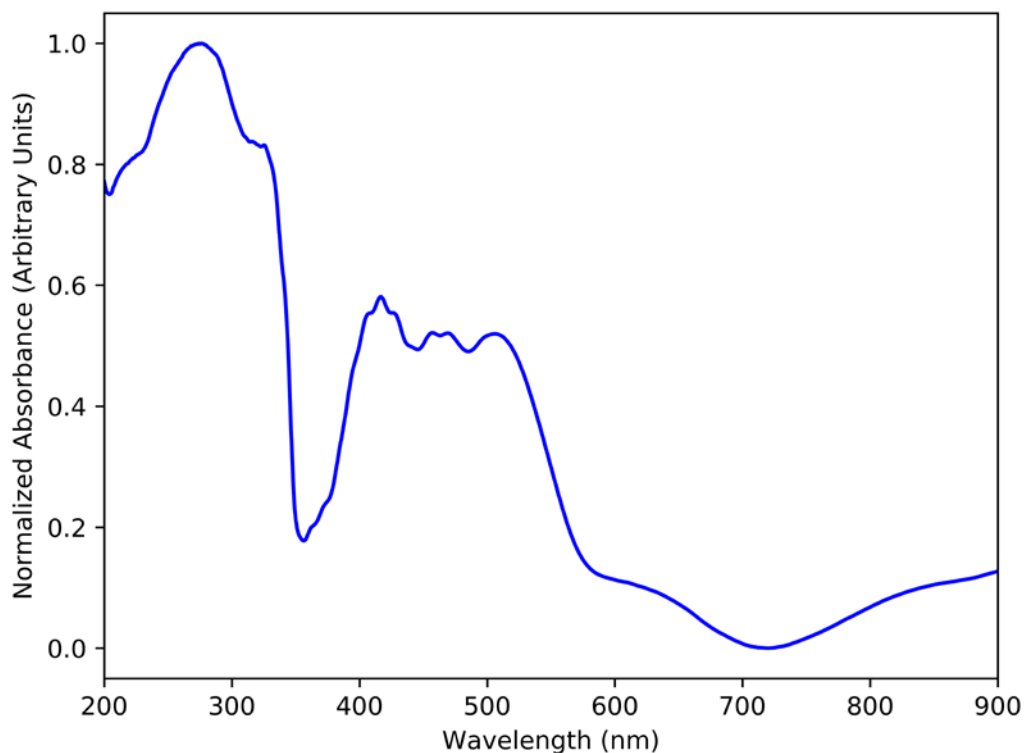
Figure 7.7: The UV/Visible Spectrum of $[Co(H_2O)_6]_3[U_2O_4F_7]_2$. The UV-visible spectrum of $[Co(H_2O)_6]_3[U_2O_4F_7]_2$. The spectrum is dominated by the absorption band below 350 nm, however also contains bands corresponding to Co *d-d* transitions and U *f-f* transitions. The intense band from 350 nm to 580 nm represents the $^4T_1(F) \rightarrow {}^4T_1(P)$ transition, and the fine structure on top of the band represents the uranium *f-f* transitions. The shoulder from 580 nm – 720 nm represents the $^4T_1(F) \rightarrow {}^4A_2$ of cobalt.

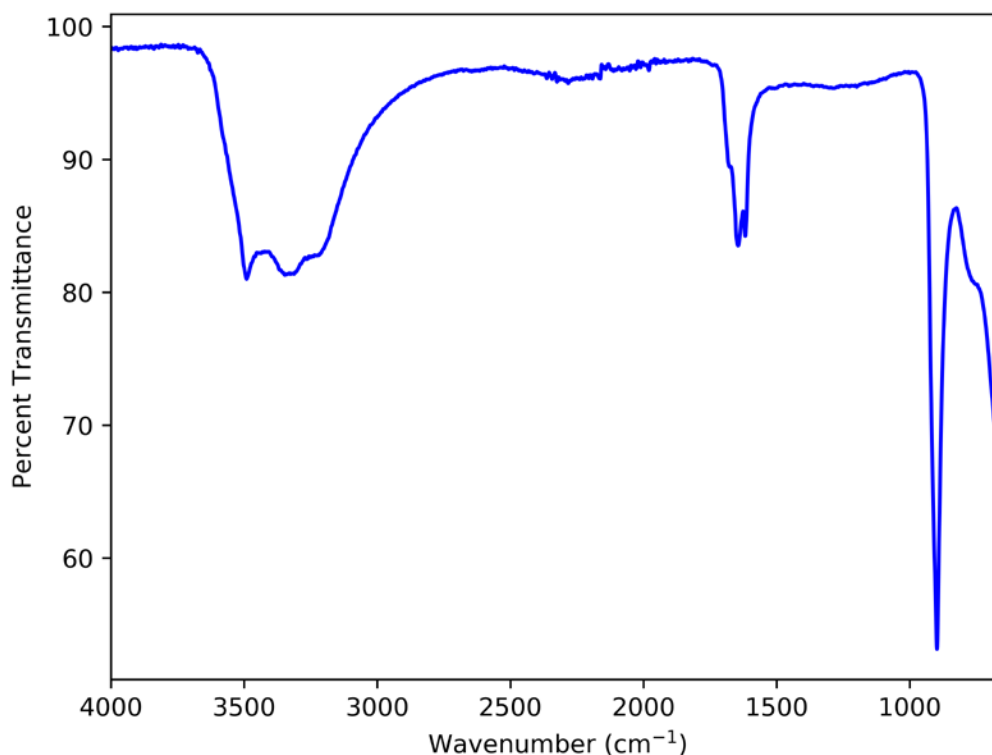**Figure 7.8: The IR Spectrum of [Co(H₂O)₆]₃[U₂O₄F₇]₂.** The infrared vibrational spectrum of $[Co(H_2O)_6]_3[U_2O_4F_7]_2$. The spectrum is dominated by bands at ~3500 cm^{-1}, ~1600 cm^{-1}, and ~900 cm^{-1}. These bands are assigned to various stretching modes in Table 7.5.

Table 7.5: IR Band Assignments for [Co(H₂O)₆]₃[U₂O₄F₇]₂.

Band	Vibrational Mode	Structural Feature
3500 cm^{-1}	O-H Stretching	$Co(H_2O)_6$ Octahedra
1600 cm^{-1}	H-O-H Bending	$Co(H_2O)_6$ Octahedra
900 cm^{-1}	O=U=O Stretching	$(U_2O_4F_7)_\infty$ Chains

198

Magnetic Properties

The magnetism of $[Co(H_2O)_6]_3[U_2O_4F_7]_2$ consists only of contributions from the high-spin Co^{II} ions. Since the cobalt ions are isolated and separated by a relatively large distance (approximately 5.8 angstroms at a minimum), we do not expect to observe evidence of magnetic coupling between the cobalt centers. In line with our expectations, $[Co(H_2O)_6]_3[U_2O_4F_7]_2$ is paramagnetic down to the lowest temperatures measured, with only very slight deviation from Curie-Weiss behavior below 5 K. The inverse of the molar magnetic susceptibility was fit to the Curie-Weiss law from 20 K to 300 K. The effective magnetic moment and the Weiss temperature were extracted from the fit. Figure 7.9 shows the Curie-Weiss fit. The effective moment per formula unit was found to be 8.71 μ_B, which agrees well with a calculated spin-only moment of 8.48 μ_B. The Weiss temperature of -9.59 K suggests weak antiferromagnetic interactions; however we do not observe any evidence for magnetic ordering. The magnetic susceptibility and magnetization data can be seen in Figure 7.10.

Thermal Properties

The TGA curve shows three distinct weight loss events, ending with the thermal decomposition of $[Co(H_2O)_6]_3[U_2O_4F_7]_2$ to the antiferromagnet $CoUO_4$[61]. The complete TGA curve is shown in Figure 7.11. The residue after each weight loss step was isolated and analyzed via powder X-ray diffraction. The resulting powder patterns can be seen in Figure 7.12. The first thermal event occurs at 100° C and corresponds to a 15.5% weight loss. The decomposition product was isolated and identified by powder X-ray diffraction as $CoUO_2F_4 \cdot 4H_2O$, representing a partial dehydration[62]. The second thermal event corresponds to a small weight loss of 3.73% and begins at 600° C. This corresponds to
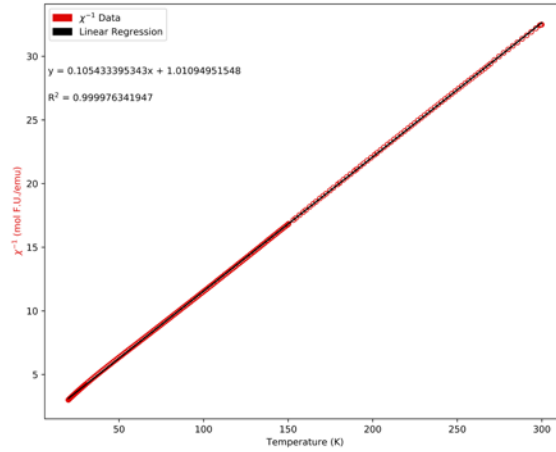
Figure 7.9: Curie-Weiss Plot for [Co(H₂O)₆]₃[U₂O₄F₇]₂. The Curie-Weiss plot for [Co(H$_2$O)$_6$]$_3$[U$_2$O$_4$F$_7$]$_2$. The data shown in red is the inverse magnetic susceptibility taken from the zero-field cooled measurement. The data was fit using a linear regression and the extracted constants are shown. The extracted effective moment agrees well with calculated spin-only moments for Co(II).

200

www.manaraa.com
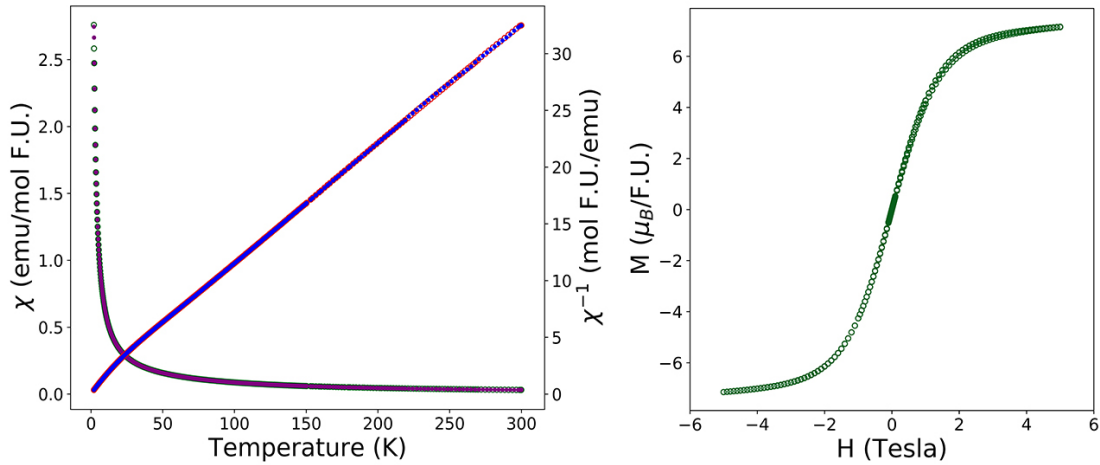
Figure 7.10: Susceptibility and Magnetization Plots for [Co(H₂O)₆]₃[U₂O₄F₇]₂. *Left:* The magnetic susceptibility and inverse magnetic susceptibility of [Co(H₂O)₆]₃[U₂O₄F₇]₂. The ZFC and FC data overlay perfectly, suggesting the absence of field dependence. *Right:* The magnetization versus field plot of [Co(H₂O)₆]₃[U₂O₄F₇]₂. The lack of hysteresis confirms that no field dependence is observed.

201
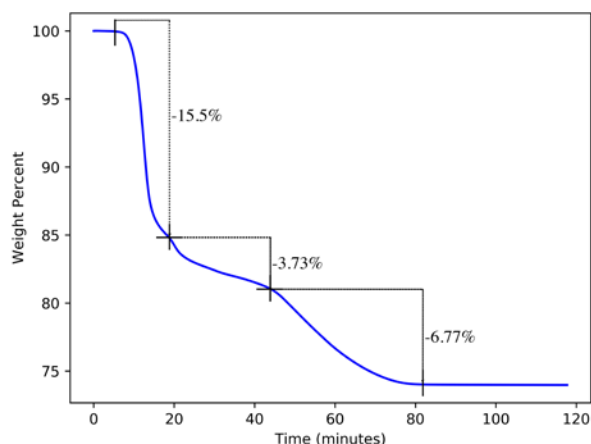
Figure 7.11: TGA Curve of [Co(H₂O)₆]₃[U₂O₄F₇]₂. TGA curve of [Co(H₂O)₆]₃[U₂O₄F₇]₂ heating from room temperature to 900° C under nitrogen gas over the course of two hours. The TGA curve shows three distinct weight loss events, culminating in the formation CoUO₄ as the final thermal product. This results in an overall Co:U ratio of 1:1, which is a change from the original ratio of 3:4. The thermal decomposition is a complicated process involving the loss of water, which likely occurs as a combination of dehydration and dehydrogenation *via* the loss of HF during heating. The loss of HF explains the oxide final product when the TGA curve was measured under inert N₂.

202
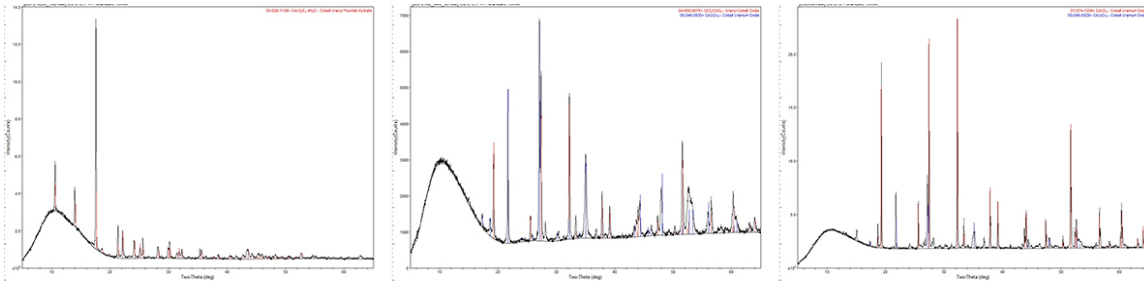
Figure 7.12: Post-TGA PXRD Patterns of [Co(H$_2$O)$_6$]$_3$[U$_2$O$_4$F$_7$]$_2$. Powder diffractograms of bulk samples of [Co(H$_2$O)$_6$]$_3$[U$_2$O$_4$F$_7$]$_2$ after heating for 12 hours at various temperatures. *Left:* Heating at 100° C. The pattern was identified as Co(UO$_2$)F$_4$ • 4H$_2$O. *Middle:* Heating at 600° C. The pattern corresponds to CoU$_3$O$_{10}$ and unidentified phases. *Right:* Heating at 900° C. The pattern is primarily CoUO$_4$ with additional CoU$_3$O$_{10}$ and small amounts of unidentified products. Further heating did not drive the decomposition further towards CoUO$_4$.

,

the final dehydration step and results in CoU_3O_{10} plus several unidentified phases, which are likely fluoride products[63]. The final decomposition which occurs gradually above $600°$ C is a result of the loss of fluorine and gives the decomposition product $CoUO_4$ by $900°$ C. Scheme 7.1 shows the progression of the formation of the major phases during thermal decomposition:

$$[Co(H_2O)_6]_3[U_2O_4F_7]_2 \xrightarrow{100°\ C} Co(UO_2)F_4 \bullet 4H_2O \xrightarrow{600°\ C} CoU_3O_{10} \xrightarrow{900°\ C} CoUO_4$$
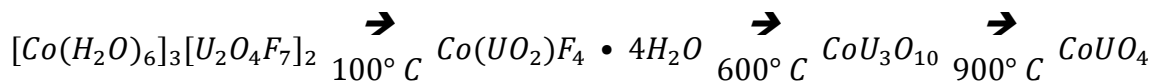
Scheme 7.1

All of the identified phases can be seen on the PXRD patterns shown in Figure 7.12.

Conclusions

The synthesis of new uranium containing fluorides continues to expand and advance our understanding of uranium chemistry. In particular, the structures obtained from the use of hydrothermal syntheses improves our understanding of the conditions under which uranium is or is not reduced, which is important for the nuclear waste industry. This structure of $[Co(H_2O)_6]_3[U_2O_4F_7]_2$ exhibits one-dimensional uranyl chains consisting of corner-shared $[U_2O_4F_7]^{3-}$ dimers. Although uranyl materials do possess one-dimensional structures, two-dimensional sheets are much more common. We believe this reduction in dimensionality was caused by the presence of fluorine, which allows the uranyl cations to better compensate the anionic charge.

We developed a system for analyzing the dimensionality of structures, and believe that this can be generalized to apply to other anions, such as hydroxide and chloride, and perhaps be extended to include aqua ligands, to help predict which compositions are likely to result in a dimensionally reduced structure. Furthermore, we provide a method for researchers to target which existing materials may be susceptible to post-synthetic

dimensional reduction. By analyzing the plot shown in Figure 5, researchers may locate structures with low anionic charge and treat them with fluoride to push them toward an unallowed cationic regime, thus forcing dimensional reduction.

The thermal behavior of $[Co(H_2O)_6]_3[U_2O_4F_7]_2$ suggests that we may be able to use low-dimensional pseudo-molecular structures as an intimate mixture of starting elements for the synthesis of desirable oxides. In this case, we have shown that the title compound can be decomposed thermally to produce the antiferromagnetic $CoUO_4$ phase[61]. The idea of using low dimensional crystals as precursors to more condensed oxide materials will continue to be explored in our future work. In order to build a greater library of low-dimensional crystal structures, we will continue to use fluoride ligands to reduce the negative charge felt by metal cations to encourage dimensional reduction to 0D, and 1D materials.

Acknowledgements

References

(1)   Chen, L.; Diwu, J.; Gui, D.; Wang, Y.; Weng, Z.; Chai, Z.; Albrecht-Schmitt, T. E.; Wang, S. *Inorg. Chem.* **2017**, *56*, 6952-6964.

(2)   Dembowski, M.; Colla, C. A.; Yu, P.; Qiu, J.; Szymanowski, J. E. S.; Casey, W. H.; Burns, P. C. *Inorg. Chem.* **2017**, *56*, 9602-9608.

(3)   Klepov, V. V.; Serezhkina, L. B.; Serezhkin, V. N.; Alekseev, E. V. *J. Solid State Chem.* **2016**, *244*, 100-107.

(4)   Morrison, G.; Smith, M. D.; zur Loye, H.-C. *Inorg. Chem.* **2017**, *56*, 1053-1056.

(5)   Prakash, J.; Tarasenko, M. S.; Mesbah, A.; Lebègue, S.; Malliakas, C. D.; Ibers, J. A. *Inorg. Chem.* **2016**, *55*, 7734-7738.

(6)   Burns, P. C. *Rev. in Mineral.* **1999**, *38*, 23-90.

(7)   Mesbah, A.; Prakash, J.; Ibers, J. A. *Dalton Trans.* **2016**, *45*, 16067-16080.

(8)   Tsarev, S.; Waite, T. D.; Collins, R. N. *Environ. Sci. Technol.* **2016**, *50*, 8223-8230.

(9)   Tyumentsev, M. S.; Zubavichus, Y. V.; Shiryaev, A. A.; Anan'ev, A. V. *Radiochemistry* **2014**, *56*, 150-155.

(10) Yeon, J.; Smith, M. D.; Sefat, A. S.; Tran, T. T.; Halasyamani, P. S.; zur Loye, H.-C. *Inorg. Chem.* **2013**, *52*, 8303-8305.

(11) Yeon, J.; Smith, M. D.; Tapp, J.; Möller, A.; zur Loye, H.-C. *J. Am. Chem. Soc.* **2014**, *136*, 3955-3963.

(12) Brusset, H.; Nguyen, Q. D.; Chourou, S. *Acta Cryst.* **1974**, *B30*, 768.

(13) Chen, F.; Wang, C.; Shi, W.; Zhang, M.; Liu, C.; Zhao, Y.; Chai, Z. *CrystEngComm* **2013**, *15*, 8041.

(14) Yeon, J.; Smith, M. D.; Tapp, J.; Möller, A.; zur Loye, H.-C. *Inorg. Chem.* **2014**, *53*, 6289-6298.

(15) Yeon, J.; Smith, M. D.; Tapp, J.; Möller, A.; zur Loye, H.-C. *J. Solid State Chem.* **2016**, *236*, 83-88.

(16) Iwasaki, M.; Ishikawa, N.; Ohwada, K.; Fujino, T. *Inorg. Chim. Acta* **1981**, *54*, L193-L194.

(17) Fleckenstein, J.; Kemmler-Sack, S.; Ruedorff, W. *Z. Naturforsch. B: Chem. Sci.* **1971**, *26*, 1367-1368.

(18) Alekseev, E. V.; Suleĭmanov, E. V.; Chuprunov, E. V.; Marychev, M. O.; Ivanov, V. A.; Fukin, G. K. *Crystallogr. Rep.* **2006**, *51*, 29-33.

(19) Burns, P. C.; Hill, F. C. *Can. Mineral.* **2000**, *38*, 163-173.

(20) Felder, J. B.; Smith, M. D.; zur Loye, H.-C. *CrystEngComm* **2017**, *19*, 3499-3505.

(21) Read, C. M.; Morrison, G.; Yeon, J.; Smith, M. D.; zur Loye, H.-C. *Inorg. Chem.* **2015**, *54*, 6993-6999.

(22) Sykora, R. E.; McDaniel, S. M.; Albrecht-Schmitt, T. E. *J. Solid State Chem.* **2004**, *177*, 1431-1436.

(23) Thuéry, P.; Harrowfield, J. *Cryst. Growth Des.* **2017**, *17*, 2116-2130.

(24) Wylie, E. M.; Burns, P. C. *Can. Mineral.* **2012**, *50*, 147-157.

(25) Alekseev, E. V.; Krivovichev, S. V.; Depmeier, W.; Siidra, O. I.; Knorr, K.; Suleimanov, E. V.; Chuprunov, E. V. *Angew Chem Int Ed Engl* **2006**, *45*, 7233-7235.

(26) Morrison, J. M.; Moore-Shay, L. J.; Burns, P. C. *Inorg. Chem.* **2011**, *50*, 2272-2277.

(27) Read, C. M.; Yeon, J.; Smith, M. D.; zur Loye, H.-C. *CrystEngComm* **2014**, *16*, 7259-7267.

(28) Tecmer, P.; Hong, S. W.; Boguslawski, K. *Phys Chem Chem Phys* **2016**, *18*, 18305-18311.

(29) Volkringer, C.; Henry, N.; Grandjean, S.; Loiseau, T. *J. Am. Chem. Soc.* **2012**, *134*, 1275-1283.

(30) Severance, R. V.; Smith, M. D.; zur Loye, H.-C. *Inorg. Chem.* **2011**, *50*, 7931-7933.

(31) Lychev, A. A.; Mashirov, L. G.; Smolin, Y. I.; Shepelev, V. F. *Radiokhimiya* **1986**, *28*, 682-685.

(32) Nguyen, Q. D.; Chourou, S.; Heckly, J. *J. Inorg. Nucl. Chem.* **1981**, *43*, 1835-1839.

(33) Huang, C. Z.; Liu, B.; Wen, L.; Zhuang, R. C.; Zhao, J. T.; Pan, Y.; Mi, J. X.; Huang, Y. X. *Inorg. Chem.* **2015**, *54*, 6978-6985.

(34) Tulsky, E. G.; Long, J. R. *Chem. Mater.* **2001**, *13*, 1149-1166.

(35) Burns, P. C.; Deely, K. M. *Can. Mineral.* **2001**, *40*, 1579-1586.

(36) Obbade, S.; Renard, C.; Abraham, F. *J. Solid State Chem.* **2009**, *182*, 413-420.

(37) Olds, T. A.; Plasil, J.; Kampf, A. R.; Skoda, R.; Burns, P. C.; Cejka, J.; Bourgoin, V.; Boulliard, J.-C. *Eur. J. Mineral.* **2017**, *29*, 129-141.

(38) Plasil, J.; Skoda, R.; Cejka, J.; Bourgoin, V.; Boulliard, J.-C. *Eur. J. Mineral.* **2016**, *28*, 959-967.

(39) Zhang, Y.; Čejka, J.; Lumpkin, G. R.; Tran, T. T.; Aharonovich, I.; Karatchevtseva, I.; Price, J. R.; Scales, N.; Lu, K. *New J. Chem.* **2016**, *40*, 5357-5363.

(40) Bertolini, J. C. *J. Emerg. Med.* **1992**, *10*, 163.

(41) Peters, D.; Miethchen, R. *J. Fluorine Chem.* **1996**, *79*, 161.

(42) Segal, E. B. *Chem. Health Saf.* **2000**, *7*, 18.

(43) Katz, S. *Toxics* **2014**, *2*, 50-78.

(44) APEX2 Version 2014.9-0, SAINT+ Version 8.34A and SADABS Version 2014/4. Bruker Analytical X-ray Systems Inc, Madison, Wisconsin, USA, 2014.

(45) Sheldrick, G. M. *Acta Cryst.* **2008**, *A64*, 112-122.

(46) Hubschle, C. B.; Sheldrick, G. M.; Bittrich, B. *J. Appl. Cryst.* **2011**, *44*, 1281-1284.

(47) Kubelka, P.; Munk, F. Z. *Tech. Phys.* **1931**, *12*, 593.

(48) Morrison, G.; zur Loye, H.-C. *J. Solid State Chem.* **2015**, *221*, 334-337.

(49) Felder, J.; Yeon, J.; Smith, M.; zur Loye, H.-C. *Inorg. Chem. Front.* **2017**, *4*, 368-377.

(50) Andrews, M. B.; Cahill, C. L. *Chem. Rev.* **2013**, *113*, 1121-1136.

(51) Severance, R. C.; Vaughn, S. A.; Smith, M. D.; zur Loye, H.-C. *Solid State Sci.* **2011**, *13*, 1344-1353.

(52) Severance, R. C.; Smith, M. D.; zur Loye, H.-C. *Inorg. Chem.* **2011**, *50*, 7931-7933.

(53) Bugaris, D. E.; zur Loye, H.-C. *Angew Chem Int Ed Engl* **2012**, *51*, 3780-3811.

(54) Cahill, C. L.; Burns, P. C. *Inorg. Chem.* **2001**, *40*, 1347-1351.

(55) Abeysinghe, D.; Smith, M. D.; Yeon, J.; Morrison, G.; zur Loye, H.-C. *Cryst. Growth Des.* **2014**, *14*, 4749-4758.

(56) Cortese, A.; Wilkins, B.; Smith, M. D.; Yeon, J.; Morrison, G.; Tran, T. T.; Halasyamani, P. S.; zur Loye, H.-C. *Inorg. Chem.* **2015**, *54*, 4011-4020.

(57) Burns, P. C.; Hughes, K.-A. H. *Am. Mineral.* **2003**, *88*, 1165-1168.

(58) Tanabe, Y.; Sugano, S. *J. Phys. Soc. Jpn.* **1956**, *11*, 864-877.

(59) Jorgensen, C. K. *Acta Chem. Scand.* **1954**, *8*, 1495-1501.

(60) Wu, S.; Wang, S.; Polinski, M.; Beermann, O.; Kegler, P.; Malcherek, T.; Holzheid, A.; Depmeier, W.; Bosbach, D.; Albrecht-Schmitt, T. E.; Alekseev, E. V. *Inorg. Chem.* **2013**, *52*, 5110-5118.

(61) Bertaut, E. F.; Delapalme, A.; Forrat, F.; Pauthenet, R. *J. Phys. Rad.* **1962**, *23*, 477.

(62) Udovenko, A. A.; Mikhailov, Y. N.; Davidovich, R. L.; Kuznetsov, V. G. Z. *Neorg. Khimii* **1972**, *17*, 2746-2751.

(63) Miyake, C.; Kondo, T.; Takamiya, T.; Yoneda, Y. *J. Alloys Compd.* **1993**, *193*, 116-118.

(64) Hao, Y.; Kegler, P.; Bosbach, D.; Albrecht-Schmitt, T.; Wang, S.; Alekseev, E. *Cryst. Growth Des.* **2017**, *17,* 5898-5907.

CHAPTER 8:

SUPERCRITICAL SYNTHESIS AND TOPOLOGICAL ANALYSIS OF $K_5U_5O_{17}(OH)$*

Introduction

The synthesis and investigation of uranium containing materials continues to be a vital endeavor in order to understand better the processes by which radioactive waste interacts with the environment, and also for the development of new wasteforms and advanced fuel rod materials[1-5]. While uranium offers rich redox chemistry, displaying oxidation states ranging from +3 to +6, the +6 state is by far the most common, followed by +4. Even though much work has been done on U(VI) containing materials[6-13], there remains a vast phase space yet to be explored.

It is impossible to discuss U(VI) chemistry without discussing the uranyl ion (UO_2^{2+}), which is nearly ubiquitous among U(VI) materials. The uranyl ion is formed by strong bonding of the uranium center to two oxide ligands 180° apart (O=U=O). The uranyl oxygens rarely interact with other cations[14-16], however uranyl centers frequently interact *via* equatorial ligands (oxide, hydroxide, halide, etc.). This equatorial bonding motif leads to uranyl polyhedra that exhibit essentially exclusively bipyramidal coordination environments. This tendency to form bipyramids coupled with the reluctance of the uranyl oxygens to interact leads to coupling between uranyl centers in the equatorial plane, which generally results in uranyl sheet structures[17, 18].

Uranyl sheet-anions are often held together by large alkali/alkaline earth cations, or similar cations for charge balancing. These uranyl sheets can form a large variety of topologies that can be used to compare uranyl compounds. Burns *et al.* developed a method of determining the sheet-anion topology of uranyl sheet compounds, which is often used to classify and group uranyl materials[19]. The continued discovery of new uranyl sheet topologies[20-25] drives further research into uranyl compounds and serves as

evidence to the fact that there is still much work to be done on this diverse class of materials.

The tendency of uranium to oxidize at high temperatures suggests that many U(VI) compounds can be synthesized in a straightforward manner *via* the traditional solid-state ceramic route[26, 27]. It is often desirable, however, to create these compounds in the form of high quality single crystals, which necessitates a different synthetic approach. Among the many advantages of single crystals, not least is the ability to perform highly accurate structure determinations by single crystal diffraction measurements. Uranyl crystals have been synthesized by a wide variety of crystal growth techniques including flux growth[28–34], hydrothermal growth[20, 21], and mild hydrothermal growth[35–37]. Typically there is a large temperature gap between the mild hydrothermal regime (up to ~200° C) and the supercritical regime ($\geq$~500° C). In this work, we begin to explore the intermediate temperature range between these two regimes by operating at just above the critical point of water (374° C).

Herein we report on the supercritical synthesis of $K_5U_5O_{17}(OH)$ at 400 °C resulting in plentiful single crystals. $K_5U_5O_{17}(OH)$ is closely related to the Na analog previously reported by Lii; $Na_5U_5O_{17}(OH)$ [21]. While structurally closely related, $K_5U_5O_{17}(OH)$ crystallizes in a different space group, though the difference is subtle and they are indistinguishable by visual inspection. The uranyl sheet-anions are identical, and we report herein the first topological analysis of this sheet structure to date.

Experimental

Materials and Methods

Caution: Although the uranium oxide used in this experiment contains depleted uranium, standard precautions for handling radioactive materials should be observed. All uranium-containing materials were handled exclusively in labs specially designated for the study of radioactive materials.

Caution: The synthetic strategy employed in this experiment generates high pressures. Extreme caution should be exercised to ensure that the pressure limits of the vessel are not exceeded. High-pressure syntheses were conducted in a specially designated room dedicated to high-pressure synthesis.

The following materials were used as received without further modifications: UO_3 (99%, International Bio-Analytical Laboratories), KOH (ACS Grade, Fisher Scientific), and deionized water. For this synthesis, a stock solution of 5M KOH was prepared.

1 mmol of UO_3 was mixed with 2 mL of 5M KOH solution inside a 5-inch long silver tube that had been welded shut on one end. The tube was immersed in liquid nitrogen to freeze the liquid, and the open end of the tube was then crimped and welded shut using a TIG welder. Once welded, the tube was allowed to return to room temperature. The tube was transferred to a Parr Instrument Company HAST-C pressure vessel rated to 5700 psi at 600° C. Deionized water was added to the pressure vessel to just over the fill level of the silver tube to act as counterpressure.

The pressure vessel was sealed and heated in a programmable furnace to 400° C for 24 hours, then slowly cooled to 350° C, after which point the furnace was shut off and

213

allowed to cool to room temperature. The pressure inside the vessel was estimated to be 5000 psi at the target temperature of 400°. Once cool, the pressure vessel was opened and the silver tube removed. The tube was cut open and the mother liquor was decanted revealing small, high quality, orange plate crystals. The crystals were washed with water and acetone. The product was then allowed to dry under vacuum before being chosen for structure determination. The final product was determined to be present in nearly quantitative yield based on uranium.

Single-Crystal X-ray Diffraction

X-ray intensity data from a yellow triangular plate crystal were collected at 303(2) K using a Bruker D8 QUEST diffractometer equipped with a PHOTON 100 CMOS area detector and an Incoatec microfocus source (Mo K$_\alpha$ radiation, $\lambda = 0.71073$ Å)[38]. The data collection covered 99.8% of reciprocal space to $2\theta_{max} = 70.31°$, with an average reflection redundancy of 8.0 (Laue group 2/m) and $R_{int} = 0.038$ after absorption correction. Though the correct crystal symmetry is primitive monoclinic, indexing of several crystals gave an apparent C-centered orthorhombic unit cell of $a = 8.05$ Å, $b = 11.45$ Å, $c = 20.01$ Å, V = 1844 Å^3. Though metrically consistent with this cell, the higher symmetry is easily dismissed upon examining the R_{int} value of 0.51 for the orthorhombic system. Similar R_{int} statistics were also obtained for various C-centered monoclinic cells. The raw area detector data frames were reduced and corrected for absorption effects using the SAINT+ and SADABS programs[38]. Final unit cell parameters were determined by least-squares refinement of 9824 reflections taken from the data set. An initial structural model was obtained with dual-space direct methods using SHELXT[39]. Subsequent difference

Fourier calculations and full-matrix least-squares refinement against F^2 were performed with SHELXL-2014[39] using the ShelXle interface[40].

The compound crystallizes in the monoclinic system. Systematic absences were consistent with space groups $P2_1$ and $P2_1/m$, the latter of which was confirmed by structure solution. The asymmetric unit consists of three uranium atoms, three potassium atoms, and 11 oxygen atoms. All atoms are located on general positions (site $4f$), except for U(3), K(3) and O(8)–O(10), which are located on mirror planes (site $2e$). O(11) was refined on a general position but is disordered across the inversion center at 0,0,½ (site $2c$), and was refined with half-occupancy. All atoms were refined with anisotropic displacement parameters. In early refinement stages, O(11) was refined on the inversion center of site $2c$. This resulted in an abnormally large prolate anisotropic displacement parameter with U(3)/U(1) = 5.6. Refining O(11) displaced slightly from the inversion center resulted in a normalized ellipsoid (U(3)/U(1) = 2.6) and a stable refinement. The two-fold disorder model for O(11) was therefore retained. After location and anisotropic refinement of all U, K and O atoms, and modeling of the O(11) disorder, the derived crystal composition is $K_5U_5O_{18}$. This generates an average uranium oxidation state of +6.2, which is physically unreasonable. The most reasonable explanation is the presence of a hydroxyl group among the oxide ions. A reliable position for a charge-balancing hydrogen atom could not be located by Fourier difference synthesis. The most likely site is bonded to the disordered oxygen atom O(11). O(11) resides in the most spacious coordination environment of all the oxygen atoms, coordinated to two symmetry-equivalent U(1) centers at U(1)-O(11) = 2.42 and 2.43 Å, and two K atoms at 3.26 and 3.54 Å, leaving ample space for an H atom. O(11) is bounded by eight neighboring

215

oxygen atoms at distances in the range 2.76 - 3.08 Å, all typical hydrogen-bonding distances. A hydroxyl hydrogen bonded to O(11) is therefore potentially disordered over several possible hydrogen-bonding locations. The small hydrogen atom scattering factor, the disorder of the parent oxygen atoms O(11), and the potential disorder of the hydroxyl hydrogen itself, are the reasons this proton could not be located by Fourier difference synthesis. Location of a hydrogen on the half-occupied atom O(11) (i.e. a disordered half-occupied hydroxyl group) gives an electroneutral composition of $K_5U_5O_{17}(OH)$, assuming all U^{6+} ions. Trial refinements of the potassium and uranium site occupancies showed no deviation from unity occupation in all cases. The largest residual electron density peak and hole in the final difference map are +2.62 and -1.46 e-/$Å^3$, located 0.75 Å and 1.14 Å from U(3), respectively. Table 8.1 shows crystallographic and refinement information, and Table 8.2 shows selected bond distances.

The analogous $Na_5U_5O_{17}(OH)$ was previously reported to crystallize in the space group $P2_1/c$ [21]. We have found that atoms U(1), U(2), and O(3) in the potassium structure violate the c-glide plane symmetry operator, which confirms our choice of $P2_1/m$ over $P2_1$/c. We hypothesize that the increased ionic radius of K over Na causes a subtle change in the structure, which results in the shifting of space groups from the Na phase.

Powder X-ray Diffraction

The product single-crystals were ground into polycrystalline powder for PXRD measurements. Powder XRD data were collected on a Rigaku Ultima IV diffractometer using Cu K_α (λ = 1.5418 Å) radiation. Data were collected over the 5° - 65° two-theta range with a step size of 0.02°.

Table 8.1: Crystallographic Data and Refinement Information for $K_5U_5O_{17}(OH)$

Empirical Formula	$H K_5 O_{18} U_5$
Formula Weight (g/mol F. U.)	1674.66
Temperature (K)	303(2)
Wavelength (Å)	0.71073
Crystal System	Monoclinic
Space Group	$P2_1/m$
Unit Cell Parameters:	
a (Å)	6.9926(2)
b (Å)	20.0065(5)
c (Å)	7.0055(2)
β (°)	109.8270(8)
Volume (Å^3)	921.95(4)
Z	2
Density (Mg/m^3)	6.032
Absorption Coefficient (mm^{-1})	44.977
F(000)	1400
Crystal Size (mm)	0.100 x 0.060 x 0.040
Theta Range for Data Collection	3.091 – 35.157
Reflections	33455
Independent Reflections	4195 (R_{int} = 0.0382)
Completeness to theta = 35.155°	99.8%
Data/Restraints/Parameters	4195 / 0 / 140
Goodness of Fit on F^2	1.138
Final R Indices	R_1 = 0.0197 wR_2 = 0.0424
R Indices (all data)	R_1 = 0.0240 wR_2 = 0.0434
Extinction Coefficient	0.00120(3)
Largest Diff. Peak and Hole (e$^-$/Å^3)	2.616 and -1.465

Table 8.2: Selected Interatomic Distances (Å) for K$_5$U$_5$O$_{17}$(OH)

U(1) – O(1)	2.226(2)	K(1) – O(1)	3.266(3)
U(1) – O(2)	2.287(3)	K(1) – O(3)	3.196(3)
U(1) – O(3)	2.412(3)	K(1) – O(4)	2.734(3)
U(1) – O(5)	1.852(3)	K(1) – O(5)	2.615(3)
U(1) – O(7)	1.840(3)	K(1) – O(6)	2.757(3)
U(1) – O(11)	2.42(3)	K(1) – O(7)	2.758(3)
U(2) – O(1)	2.236(2)	K(1) – O(9)	2.782(3)
U(2) – O(2)	2.200(2)	K(1) – O(10)	2.629(3)
U(2) – O(3)	2.237(2)	K(2) – O(2)	3.320(4)
U(2) – O(4)	1.864(3)	K(2) – O(4)	2.770(3)
U(2) – O(6)	1.862(3)	K(2) – O(5)	2.724(3)
U(2) – O(8)	2.1766(13)	K(2) – O(6)	2.643(3)
U(3) – O(1)	2.354(2)	K(2) – O(7)	2.654(3)
U(3) – O(3)	2.281(2)	K(2) – O(11)	3.26(3)
U(3) – O(3)	2.281(2)	K(3) – O(4)	2.771(3)
U(3) – O(8)	2.456(4)	K(3) – O(6)	2.776(3)
U(3) – O(9)	1.839(4)	K(3) – O(8)	3.351(5)
U(3) – O(10)	1.838(4)	K(3) – O(9)	2.656(4)
		K(3) – O(10)	2.755(4)

Optical Spectroscopy

UV-visible spectra were recorded using a Perkin Elmer lambda 35 UV/visible scanning spectrophotometer, used in the diffuse reflectance mode, equipped with an integrating sphere. Spectra were recorded in the range of 200 – 900 nm. The reflectance data were automatically converted to absorbance by the instrument *via* the Kubelka-Munk function[41].

Fluorescence data were collected on a Perkin Elmer LS 55 fluorescence spectrometer. Excitation spectra were recorded from 200 – 450 nm, and emission spectra were recorded from 450 – 900 nm. The sample was excited at the excitation max wavelength of 425 nm. All optical spectroscopy data were collected on polycrystalline powders obtained by finely grinding single crystals.

Infrared spectroscopy was performed on ground single crystals using a PerkinElmer spectrum 100 FT-IR spectrometer. The spectrometer utilizes a diamond-ATR attachment to operate in attenuated total reflectance mode. The IR spectrum was recorded in the spectral range of 4000 cm^{-1} – 650 cm^{-1}.

Energy Dispersive Spectroscopy (EDS)

Energy dispersive spectroscopy was performed directly on product single crystals mounted on an SEM stub with carbon tape. EDS was performed with a Tescan Vega-3 SEM equipped with a Thermo EDS attachment. The SEM was operated in low-vacuum mode with a 30 kV accelerating voltage and 20 second accumulating time.

Results and Discussion

Synthetic Considerations

Hydrothermal crystal growth is a well-established method for crystal growth and phase discovery. There has been much work in both the mild hydrothermal regime ($\leq$ 200°) and supercritical regime (>374° C), especially >450° C. It is suspected that these two temperature regimes are capable of yielding quite different results when used to grow crystals from similar starting materials.

We are interested in exploring the synthetic space of intermediate hydrothermal growth conditions, specifically in the temperature ranges between 300° C and 450° C. The reported syntheses at 400° C show that materials usually grown at much higher temperatures ($\geq$600° C) can be made at more intermediate temperatures, yet still produce different results from the now-common mild hydrothermal methods (<200 °C).

Energy Dispersive Spectroscopy (EDS) and Powder X-ray Diffraction (PXRD)

EDS was used prior to single crystal X-ray diffraction data collection as a non-destructive, qualitative elemental analysis. EDS qualitatively confirmed the presence of K, U, and O in the product single crystals. EDS was performed on several crystals in a batch to confirm that the results are representative of the whole.

The collected powder diffraction pattern was compared to the calculated powder pattern obtained from the crystallographic information file (.cif). The observed pattern matched the calculated pattern with no extra peaks, indicating the sole presence and phase-purity of $K_5U_5O_{17}(OH)$. The PXRD patterns and difference map can be seen in Fig. 8.1.
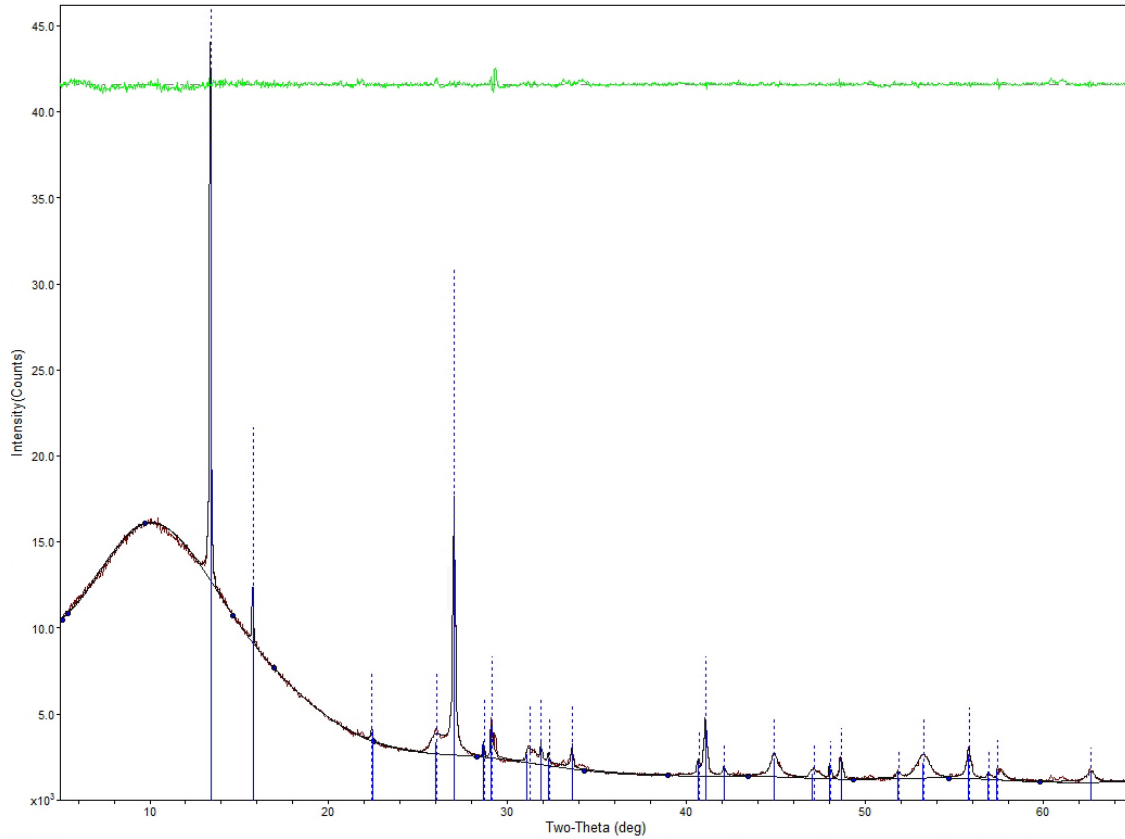
220

Figure 8.1: PXRD Pattern of K₅U₅O₁₇(OH). The powder x-ray diffraction pattern of K₅U₅O₁₇(OH) compared with the calculated pattern derived from the .cif. Observed data is shown in red, and the Le Bail fit is shown in black. Peak positions are marked with blue lines, and the difference map is shown as green.

221

Crystal Structure

K$_5$U$_5$O$_{17}$(OH) adopts a layered three-dimensional structure consisting of two-dimensional uranium-oxide layers separated by potassium ions. The two-dimensional sheets are formed from corner and edge sharing uranyl polyhedra, with the uranyl oxygens extending into the interlayer space, and the equatorial oxygens participating in the 2D sheet connectivity. Figure 8.2 shows a depiction of the overall structure. This type of edge sharing is extremely common among uranyl materials, and gives rise to a large number of uranyl sheet materials [10, 15, 22–24].

The uranyl sheet-anion U$_5$O$_{17}$(OH)$^{5-}$ is built of three unique uranyl coordination environments that are connected via edge and corner sharing, as shown in Figure 8.3. U(1) is coordinated by seven oxide anions, forming a regular uranyl pentagonal bipyramid, where the axial oxide anions are the uranyl oxygens. U(2) is coordinated by six oxide anions forming a highly distorted octahedron, again with the axial oxygens participating in the short uranyl bonds. Finally, U(3) is coordinated by six oxygens and a hydroxyl ion, forming a distorted pentagonal bipyramid.

The U(1) pentagonal bipyramid can be thought of as the central unit in the 2D sheet. It is edge sharing with two U(2) octahedra, and corner sharing with two more. It also is edge sharing with two U(3) pentagonal bipyramids. This arrangement creates triangular voids along the edge formed by the two O(3) ions. The U(2) octahedra share opposite edges with a U(1) and a U(3) pentagonal bipyramid and corner share with one U(1) and two U(3) pentagonal bipyramids as well as one U(2) octahedron. The U(3) pentagonal bipyramids share edges with one each of U(1), U(2), and U(3) polyhedra, as well as corners with two U(2) octahedra. The final vertex of the U(3) pentagonal
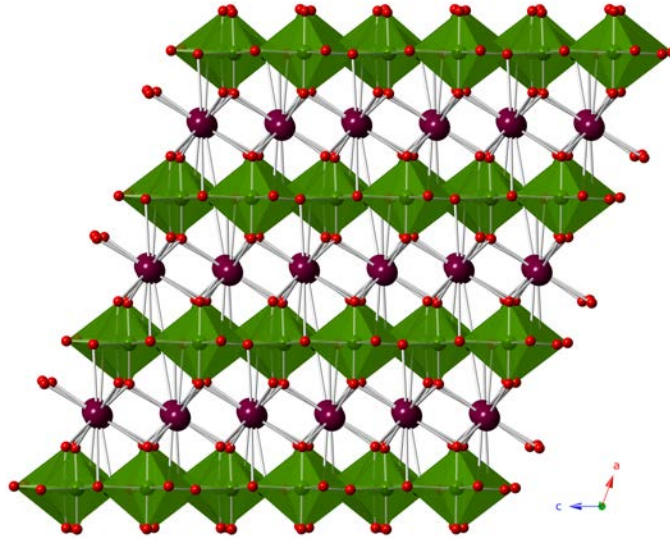
Figure 8.2: The Overall Structure of K₅U₅O₁₇(OH). A polyhedral view of $K_5U_5O_{17}(OH)$. The structure consists of uranyl sheets (green) separated by potassium (maroon) ions. Oxide ions are shown in red. Hydroxyl ions cannot be seen from this view.
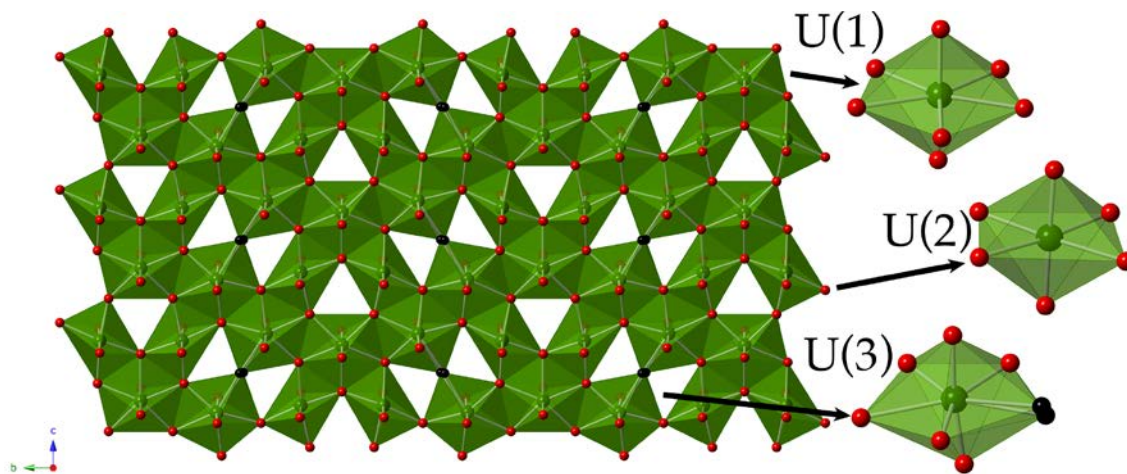
Figure 8.3: Uranyl Sheet and U Local Environments in $K_5U_5O_{17}(OH)$. The uranyl sheet-anion of $K_5U_5O_{17}(OH)$. To the right are shown the local coordination environments of the three unique uranium ions. U(1) forms a regular pentagonal bipyramid, while U(2) and U(3) show distorted coordination environments. Uranium polyhedra are shown in green, oxide ions in red, and hydroxyl ions in black.

bipyramid is formed by the hydroxyl group, which it shares with another U(3) pentagonal bipyramid. Figure 8.3 shows the uranyl oxide sheet along with the local uranium coordination environments.

There are three unique potassium sites, which are identified by their positions between the uranyl sheets. The potassium coordination environments can be viewed in Figure 8.4. K(1) is coordinated by eight oxygens, forming a bicapped octahedron. Looking down the *a* axis, K(1) lies underneath the edges U(1) shares with U(3), and is completely covered by the uranyl sheet. The K(1) ions share an edge to form dimers.

K(2) ions are coordinated by seven oxygens and one hydroxyl group forming bicapped trigonal antiprisms. These antiprisms share edges along the *c* axis forming infinite chains. K(3) ions are coordinated by seven oxygens, forming capped trigonal antiprisms that are isolated from one another. When combined, the three potassium environments fill all space between the uranyl layers.

Bond Valence Sum (BVS) analysis was performed on the structure to confirm the assigned uranium oxidation state of +6. All BVS values fall very close to 6, confirming the 6+ oxidation state of uranium. Table 8.3 compiles the BVS results.

Sheet-Anion Structure and Topology

The structure of the uranyl sheet-anion is a distorted version of the β-U_3O_8 sheet structure and is created by the presence of the hydroxyl ion on the O(3) site. Both α- and β- U_3O_8, along with the sheet-anion of $K_5U_5O_{17}(OH)$, are shown in Figure 8.5. The hydroxyl ion causes an elongation of the U-O bond, which subsequently forces a rotation and distortion of the β-U_3O_8 U(3) octahedron (which is U(2) in $K_5U_5O_{17}(OH)$). This
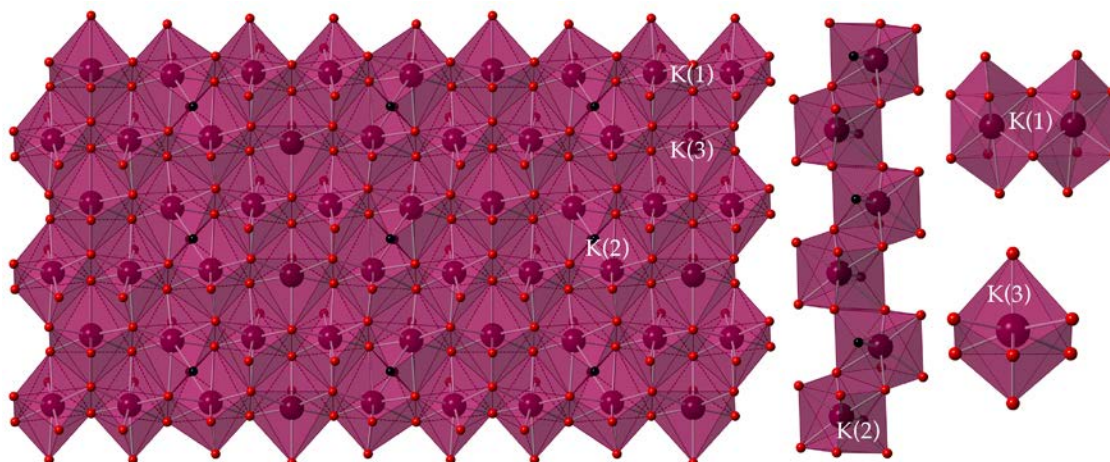
225

Figure 8.4: Potassium Coordination in $K_5U_5O_{17}(OH)$. The potassium layer in $K_5U_5O_{17}(OH)$. K(1) ions form dimers, which serve to connect the K(2) infinite chains. The layer is completed by isolated K(3) polyhedra which fill the voids left by K(1) and K(2). Potassium is shown in maroon, oxygen in red, and hydroxyl ions in black.

Table 8.3: Bond Valence Sum Results for $K_5U_5O_{17}(OH)$.

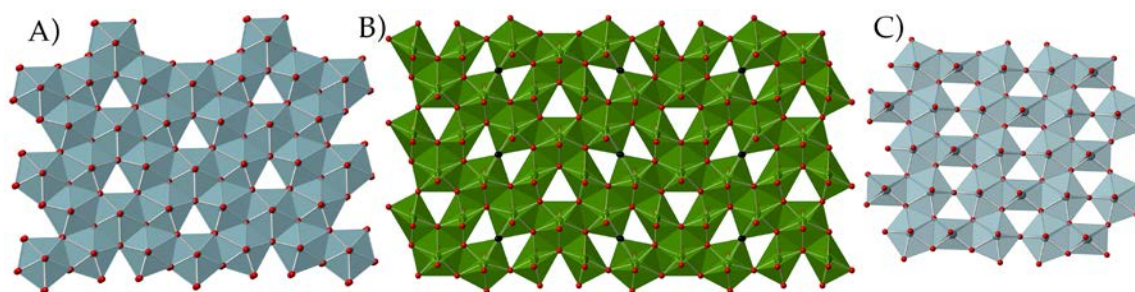| Ion	Bond Valence Sum	Oxidation State
K(1)	1.09	+1
K(2)	0.99	+1
K(3)	0.95	+1
U(1)	5.94	+6
U(2)	5.81	+6
U(3)	5.87	+6

Figure 8.5: Comparison of K$_5$U$_5$O$_{17}$(OH) with U$_3$O$_8$ Structures. The sheet-anion of α-U$_3$O$_8$. **B)** The sheet-anion of K$_5$U$_5$O$_{17}$(OH). **C)** The sheet-anion of β-U$_3$O$_8$. The sheet structure of **B)** is made of a combination of elements from **A)** and **C)**. Oxide ions are shown in red, and hydroxyl ions are in black. Uranium ions in U$_3$O$_8$ are shown in steel blue while uranium ions in K$_5$U$_5$O$_{17}$(OH) are shown in green for contrast.

distortion and rotation creates room for the insertion of an α-U_3O_8 type U(1) (also U(1) in $K_5U_5O_{17}(OH)$) pentagonal bipyramid into the sheet.

As with other uranyl sheet-anions, the topological classification system described by Burns *et al.* can be used to describe the sheet structure [19]. This classification system describes uranyl sheet-anions as being subdivided into one-dimensional chain structures. There are four major one-dimensional units that can be assembled into uranyl sheet structures, specifically P (pentagonal chains), R (rhombus chains), H (hexagonal chains), and U/D (directional variants of the same pentagon + triangular chains; 'arrowhead chains').

The distortion of the β-U_3O_8 sheet and insertion of the α-U_3O_8 structural unit causes $K_5U_5O_{17}(OH)$ to take on a different sheet-anion topology than α- or β- U_3O_8. The obvious place to start assigning a topology to the $K_5U_5O_{17}(OH)$ uranyl sheet is with the regular U(1) pentagonal bipyramid. Upon inspection, it is revealed that this pentagonal unit and neighboring triangular void is the U/D topological unit. In this instance, we begin with the D unit, though both are present and the choice can be made to start with either.

Moving to the $-b$ direction, the next unit encountered is R, followed by distorted U and then D units, followed by an R unit and then a regular U unit. This U unit marks a mirror plane between the topological units, creating mirrored sequences; the cycle repeats at the next uniform D segment. This gives the sequence RUDR**U**RDUR and creates the topology DRUDRRURDUR… Given that the D and U topological units are variants of the same unit, this topology consists of only two types of topological units: D/U and R. To the best of our knowledge, this topology has only been observed once before, in the

Na$_5$U$_5$O$_{17}$(OH) analog, though the topology was not described using these units. Figure 8.6 shows the sheet-anion structure of K$_5$U$_5$O$_{17}$(OH) overlaid with a color mapping of the constituent topological units.

Optical Properties

The UV-visible spectrum of K$_5$U$_5$O$_{17}$(OH) consists of a large absorption band beginning at 550 nm and extending past our instrument's measurement capabilities beyond 200 nm. There are four *f-f* transition bands observed on top of the large absorption feature. The absorption maximum occurs at 388 nm corresponding with one of the *f-f* transitions. The optical band gap was calculated to be 2.25 eV. Figure 8.7 shows the UV-Vis spectrum.

Fluorescence measurements were performed to measure the crystals ability to fluoresce under UV light exposure. The excitation spectrum was recorded from 200 – 450 nm with an absorption maximum at 425 nm. This maximum was chosen to be the excitation wavelength for the emission spectrum, recorded from 450 – 900 nm. The emission spectrum shows a large feature corresponding to the emission maximum of 551 nm. Figure 8.8 shows the fluorescence spectrum for K$_5$U$_5$O$_{17}$(OH).

IR measurements were performed to confirm the presence of hydroxyl ions in the structure. Weak bands corresponding to O-H stretching modes were observed at 3317 and 3256 cm^{-1}. The weakness of the bands can be attributed to the very low concentration of hydroxyl ions per formula unit. The IR spectrum can be seen in Figure 8.9.

Conclusions

A hydrothermal synthesis utilizing the low end of the supercritical temperature regime (400° C) was used to grow single crystals of K$_5$U$_5$O$_{17}$(OH). The as-synthesized
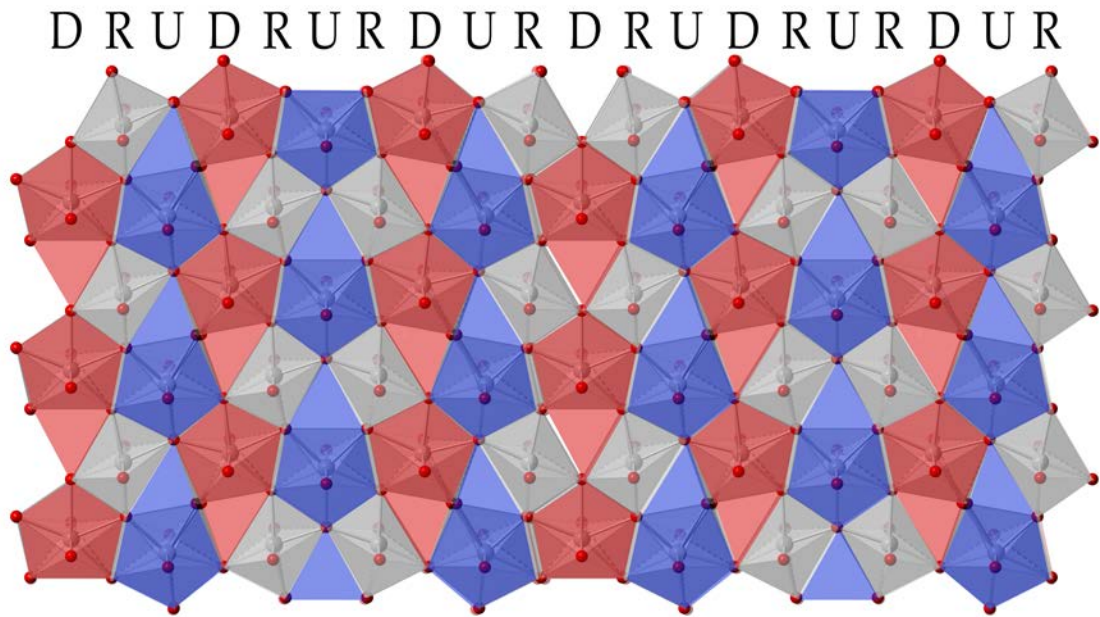
229

Figure 8.6: Sheet-Anion Topology of $K_5U_5O_{17}(OH)$. The sheet-anion topology of $K_5U_5O_{17}(OH)$. D units are shown in red, U units are shown in blue, and R units are in grey. The sheet-anion structure is shown underneath the color map. Two repeating units (from left to right) are shown in this image.
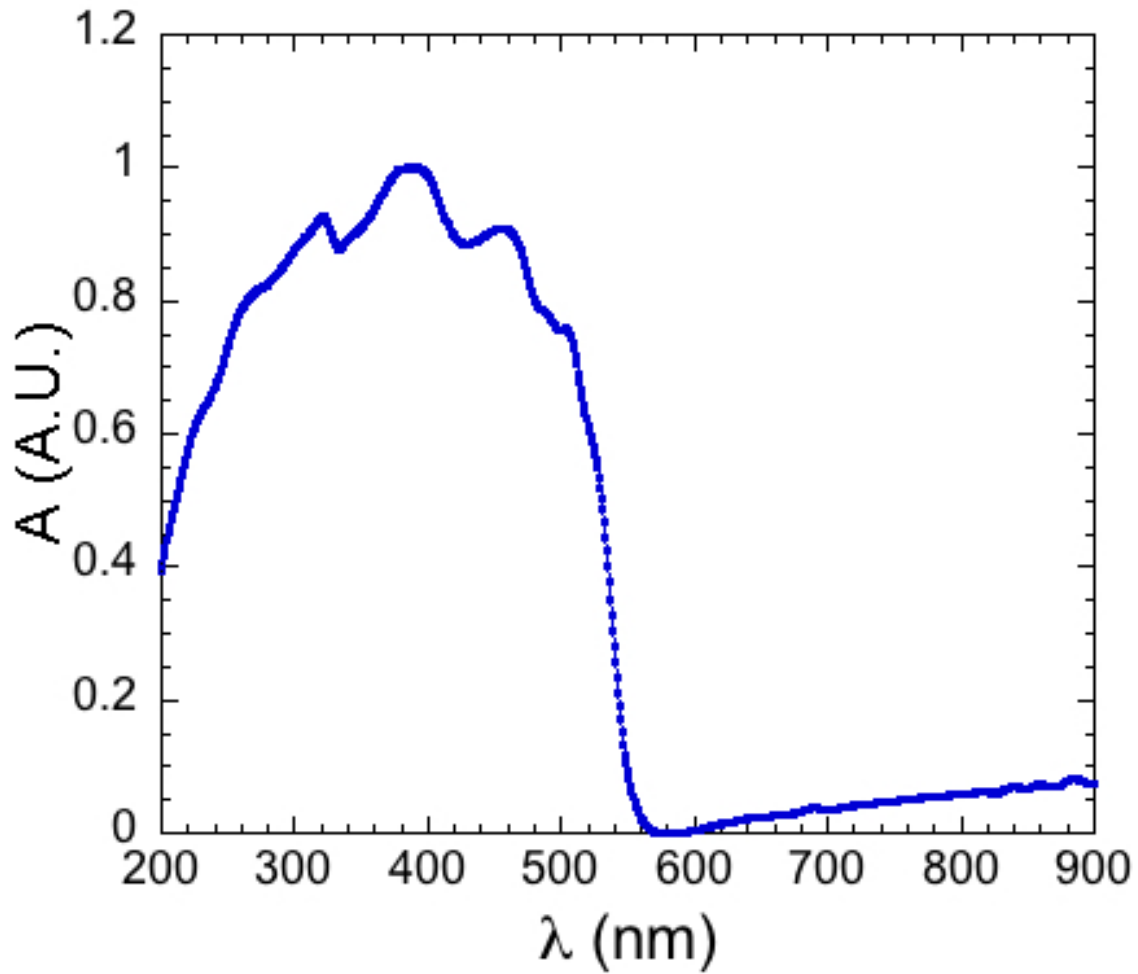
Figure 8.7: UV/Visible Spectrum of $K_5U_5O_{17}(OH)$. The UV-visible absorption spectrum of $K_5U_5O_{17}(OH)$. The spectrum shows a sharp absorption edge at 550 nm and the fine structure corresponding to the U $5f – 5f$ electronic transitions can be seen above the absorption band.
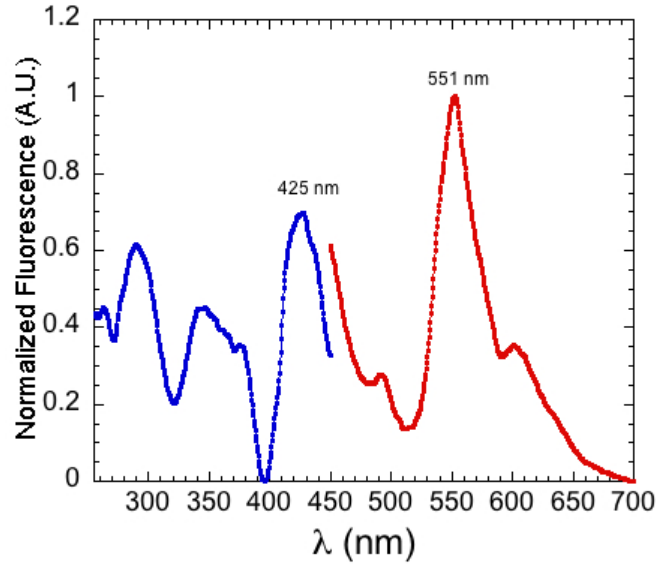
Figure 8.8: Fluorescence Spectrum of K₅U₅O₁₇(OH). The fluorescence spectrum of $K_5U_5O_{17}(OH)$. The excitation spectrum is shown in blue and the emission spectrum is shown in red. The sample was excited at a wavelength of 425 nm, corresponding to the excitation maximum. The emission maximum occurs at 551 nm.
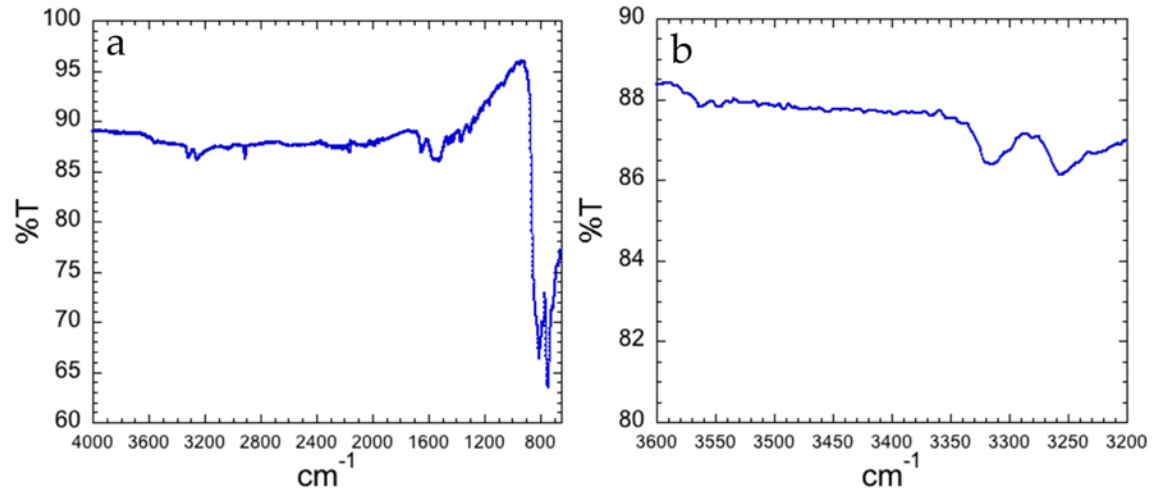
Figure 8.9: IR Spectrum of $K_5U_5O_{17}(OH)$. The IR spectrum of $K_5U_5O_{17}(OH)$. **a)** The full range spectrum from 4000 cm^{-1} to 650 cm^{-1}. **b)** A zoomed-in plot of the IR spectrum from 3600 cm^{-1} to 3200 cm^{-1}. Plot b) highlights the weak O-H stretching bands. The weakness of the bands can be attributed to the low concentration of hydroxyl ions in the structure.

233

crystals were characterized by single crystal and powder X-ray diffraction, and the material was found to be isotypic with $Na_5U_5O_{17}(OH)$. $K_5U_5O_{17}(OH)$ adopts a monoclinic three-dimensional structure consisting of two-dimensional uranyl sheet-anions, whose topology was determined. The sheet-anion topology was found to be the same as the one found in the sodium analog, which had not been observed before in other uranyl materials. This work represents the first full topological analysis of this type of sheet-anion. $K_5U_5O_{17}(OH)$ was characterized using optical spectroscopy, and was found to have a large absorption band beginning at 550 nm. The fluorescence was measured and found to have an emission maximum of 551 nm, which is typical of uranyl materials.

Acknowledgements

References

(1) Burns, P. C.; Olson, R. A.; Finch, R. J.; Hanchar, J. M.; Thibault, Y. *J. Nucl. Mater.* 2000, **278**, 290-300.

(2) Jackson, J. M.; Burns, P. C. *Can. Mineral.* 2001, **39**, 187-195.

(3) Kim, K.-T. *J. Nucl. Mater.* 2010, **404**, 128-137.

(4) Ling, J.; Morrison, J. M.; Ward, M.; Poinsatte-Jones, K.; Burns, P. C. *Inorg. Chem.* 2010, **49**, 7123-7128.

(5) Yamaji, A.; Nakano, Y.; Uchikawa, S.; Tsutomu, O. *Nucl. Technol.* 2012, **179**, 309-322.

(6) Betke, U.; Wickleder, M. S. *Eur. J. Inorg. Chem.* 2012, **2012**, 306-317.

(7) Collomb, A.; Gondrand, M.; Lehmann, M. S.; Capponi, J. J.; Joubert, J. C. *J. Solid State Chem.* 1976, **16**, 41-48.

(8) A., M.; Obbade, S.; Rivenet, M.; Renard, C.; Abraham, F. *J. Solid State Chem.* 2012, **185**, 180-186.

(9) Plasil, J.; Kampf, A. R.; Kasatkin, A. V.; Marty, J.; Skoda, R.; Silva, S.; Cejka, J. *Miner. Magazine* 2013, **77**, 2975-2988.

(10) Read, C. M.; Morrison, G.; Yeon, J.; Smith, M. D.; zur Loye, H.-C. *Inorg. Chem.* 2015, **54**, 6993-6999.

(11) Reynolds, E.; Kennedy, B. J.; Thorogood, G. J.; Gregg, D. J.; Kimpton, J. A. *J. Nucl. Mater.* 2013, **433**, 37-40.

(12) Serezhkina, L. B.; Grigor'ev, M. S.; Makarov, A. S.; Serezhkin, V. N. *Radiochem* 2015, **57**, 20-25.

(13) Wu, S.; Kowalski, P. M.; Yu, N.; Malcherek, T.; Depmeier, W.; Bosbach, D.; Wang, S.; Suleimanov, E. V.; Albrecht-Schmitt, T. E.; Alekseev, E. V. *Inorg. Chem.* 2014, **53**, 7650-7660.

(14) Mougel, V.; Chatelain, J. H.; Caciuffo, R.; Colineau, E.; Tuna, F.; Magnani, N.; Geyer, A. D.; Pecaut, J.; Mazzanti, M. *Angew, Chem. Int. Ed.* 2014, **53**, 819-823.

(15) Read, C. M.; Yeon, J.; Smith, M. D.; zur Loye, H.-C. *CrystEngComm* 2014, **16**, 7259.

235

(16) Volkringer, C.; Henry, N.; Grandjean, S.; Loiseau, T. *J. Am. Chem. Soc.* 2012, **134**, 1275-1283.

(17) Schindler, M.; Mutter, A.; Hawthorne, F. C.; Putnis, A. *Can. Mineral.* 2004, **42**, 1651-1666.

(18) Schindler, M.; Mutter, A.; Hawthorne, F. C.; Putnis, A. *Can. Mineral.* 2004, **42**, 1629-1649.

(19) Miller, M. L.; Finch, R. J.; Burns, P. C.; Ewing, R. C. *J. Mater. Res.* 1996, **11**, 3048-3056.

(20) Liu, H.-K.; Ramachandran, E.; Chen, Y.-H.; Chang, W.-J.; Lii, K.-H. *Inorg. Chem.* 2014, **53**, 9065-9072.

(21) Liu, H.-K.; Lii, K.-H. *Inorg. Chem.* 2013, **52,** 9172-9174.

(22) Obbade, S.; Yagoubi, S.; Dion, C.; Saadi, M.; Abraham, F. *J. Solid State Chem.* 2004, **177**, 1681-1694.

(23) Sykora, R. E.; McDaniel, S. M.; Albrecht-Schmitt, T. E. *J. Solid State Chem.* 2004, **177**, 1431-1436.

(24) Unruh, D. K.; Baranay, M.; Pressprich, L.; Stoffer, M.; Burns, P. C. *J. Solid State Chem.* 2012, **186**, 158-164.

(25) Wylie, E. M.; Burns, P. C. *Can. Miner.* 2012, **50**, 147-157.

(26) Gupta, S. K.; Dhobale, A. R.; Kumar, M.; Godbole, S. V.; Natarajan, V. *J. Mol. Struct.* 2015, **1084**, 89-94.

(27) Keskar, M.; Sali, S. K.; Krishnan, K.; Kannan, S. *J. Nucl. Mater.* 2016, **478**, 245-255.

(28) Babo, J.-M.; Albrecht-Schmitt, T. E. *J. Solid State Chem.* 2013, **206**, 145-150.

(29) Morrison, G.; zur Loye, H.-C. *Cryst. Growth. Des.* 2016, **16**, 1294-1299.

(30) Morrison, G.; Smith, M. D.; zur Loye, H.-C. *J. Am. Chem. Soc.* 2016, **138**, 7121-7129.

(31) Read, C. M.; Smith, M. D.; zur Loye, H.-C. *J. Chem. Crystallogr.* 2014, **44**, 604-608.

(32) Read, C. M.; Smith, M. D.; zur Loye, H.-C. *Solid State Sci.* 2014, **37**, 136-143.

(33) Wu, S.; Kowalski, P. M.; Yu, N.; Malcherek, T.; Depmeier, W.; Bosbach, D.; Wang, S.; Suleimanov, E. V.; Albrecht-Schmitt, T. E.; Alekseev, E. V. *Inorg. Chem.* 2014, **53**, 7650-7660.

(34) Yagoubi, S.; Renard, C.; Abraham, F.; Obbade, S. *J. Solid State Chem.* 2013, **200**, 13-21.

(35) Hao, Y.; Klepov, V. V.; Murphy, G. L.; Modolo, G.; Bosbach, D.; Albrecht-Schmitt, T. E.; Kennedy, B. J.; Wang, S.; Alekseev, E. V. *Cryst. Growth Des.* 2016, **16**, 5923-5931.

(36) Jouffret, L. J.; Hiltbrunner, J.-M.; Rivenet, M.; Sergent, N.; Obbade, S.; Avignant, D.; Dubois, M. *Inorg. Chem.* 2016, **55**, 12185-12192.

(37) Nazarchuk, E. V.; Siidra, O. I.; Kayukov, R. A. *Radiochemistry* 2016, **58**, 571-577.

(38) APEX2 Version 2014.9-0, SAINT+ Version 8.34A, and SADABS Version 2014/4. Bruker Analytical X-ray Systems, Inc, Madison, Wisconsin, USA, 2014.

(39) Sheldrick, G. M. *Acta Cryst.* 2008, **A64**, 112-122.

(40) Hubschle, C. B.; Sheldrick, G. M.; Bittrich, B. *J. Appl. Cryst.* 2011, **44**, 1281-1284.

(41) Kubelka, P.; Munk, F. Z. *Tech. Phys.* 1931, **12**, 593.

237

CHAPTER 9

EVIDENCE FOR A PERSISTENT PARAMAGNETIC GROUND STATE IN STRUCTURALLY RELATED U(IV) PHOSPHATES: SQUID MAGNETOMETRY AND NEUTRON DIFFRACTION*

238

Introduction

The study of uranium containing materials is of great interest to society due to the problem with accumulating radioactive waste. [1–3] This waste is a product of nuclear weapons development as well as nuclear power production. In addition to the large amount of waste being generated by today's nuclear power generation, there is also a substantial amount of legacy waste left over from Cold-War era nuclear weapons projects.

Unfortunately our level of understanding of uranium (the primary constituent of nuclear waste) crystal chemistry is insufficient to be able to design an effective new wasteform capable of safely sequestering nuclear waste for a meaningful amount of time. Therefore, before we can get to work designing new wasteform materials, we must first bolster our understanding of the fundamental chemistry behind uranium's behavior in crystal lattices, as well as the properties of these crystals.

Uranium can exhibit a wide range of oxidation states (from +2 to +6), although only the +4 and +6 oxidation states are readily accessible in solid-state materials. [4] Even though both the IV and VI states are found in nature, by far the majority of the uranium chemistry literature focuses on U(VI) chemistry, which is dominated by the structure directing uranyl ($[O=U=O]^{2+}$) ion. While uranyl chemistry is a rich field that continues to produce interesting new materials [5–7], the U(IV) ion has radically different properties which coupled with the relatively few number of reported materials makes it an attractive system to study.

Whereas the smaller U(VI) ion is fairly soluble, diamagnetic, and often fluorescent due to the uranyl ion, U(IV) is large, insoluble, paramagnetic, and has optical

properties dominated by *f-f* electronic transitions. Out of these properties, the magnetism of U(IV) is by far the most intriguing. U(IV) is a $5f^2$ system whose magnetism arises from a combination of spin-orbit interactions and crystal field effects. [8, 9] These spin-orbit effects are primarily due to low-lying thermal *f* excited states; these states can become depopulated as the temperature decreases. This thermal depopulation leads to formation of a diamagnetic singlet ground state, which is extremely prevalent among reported U(IV) materials. [10–13]

Since the magnetism of U(IV) materials is also dependent on crystal field effects, it should be possible to influence the transition to the singlet state by tuning the crystal electric field. Of course, this is a notoriously difficult proposition, as chemists do not currently possess the ability to tailor coordination environments except in extremely specialized cases. However, herein we report the preparation and magnetic studies of three related uranium(IV) phosphates which have extremely similar structures and coordination environments, which gives us unique insight into the influence of coordination environment on U(IV) magnetism.

Experimental

Materials and Methods

The following materials were used as received with no further modification: $UO_2(CH_3COO)_2$, FeF_3, H_3PO_4, $NH_4H_2PO_4$ and U_3O_8. UO_2 was synthesized by reducing the U_3O_8 under a 4% H_2 atmosphere at 650° C for 18 hours. The UO_2 was confirmed pure by PXRD.

Caution!! Even though the uranium precursors used in these syntheses are depleted, standard precautions and PPE for handling radioactive materials should be followed. All

work involving uranium was performed in labs specially designated for work with radioactive materials.

UFPO$_4$ was synthesized via mild hydrothermal reaction between uranyl acetate and phosphoric acid, with iron(III) fluoride acting as a fluoride source. The uranyl acetate and iron(III) fluoride were mixed with 1 mL of methanol in a 23 mL PTFE liner. 1 mL of concentrated phosphoric acid was added dropwise to the mixture, and the liner was sealed inside a stainless steel autoclave. The sealed autoclave was placed in a programmable oven which was heated to 200° C in one hour, then held for 24 hours. After holding, the oven was slowly cooled at a rate of 0.1°/minute to 40° C, at which point the oven was shut off. After cooling to room temperature, the autoclave was unsealed and the liner opened, revealing emerald-green product crystals and a green mother-liquor. The crystals were isolated by vacuum filtration and were washed thoroughly with water and acetone.

U(UO$_2$)(PO$_4$)$_2$ was synthesized by a flux-assisted solid-state reaction between P$_2$O$_5$ and UO$_2$. The P$_2$O$_5$ was generated *in situ* by decomposing ammonium dihydrogen phosphate at 450° C. Stoichiometric amounts of UO$_2$ and NH$_4$H$_2$PO$_4$ were ground together in an agate mortar, producing an intimate mixture of powders. The powders were loaded into a fused silica tube, which was placed in a box furnace. The furnace was heated to 450° C in 12 hours, and was allowed to dwell for 24 hours. After dwelling the furnace was heated to 800° C in another 12 hours to ensure the slow removal of ammonia gas. The charge was held at 800° C for 24 hours after which point the furnace was shut off. The charge was then heated twice at 850° C with intermittent grinding, resulting in pure U(UO$_2$)(PO$_4$)$_2$. Samples of U$_2$O(PO$_4$)$_2$ were synthesized by reducing U(UO$_2$)$_2$(PO$_4$)$_2$ under hydrogen at 650° C.

241

Single Crystal X-ray Diffraction

A suitable crystal of the green product was selected from the reaction products and X-ray intensity data were collected using a Bruker D8 QUEST diffractometer. The instrument utilizes an incoatec microfocus X-ray source (Mo K_α radiation, $\lambda = 0.71073$ Å) and a PHOTON II CMOS area detector. The detector was operated in shutterless mode, and additional fast scans were collected to account for overtopped pixels during the initial data collection. The final unit cell parameters were determined by least squares refinement of a large set of reflections taken from the raw area detector frames. The data were reduced and corrected for absorption effects using the SAINT+ and SADABS programs. [14] An initial structural model was obtained using SHELXS [15] by direct methods, and subsequent least-squares refinements were performed with SHELXL [15] through the OLEX^2 [16] graphical interface.

The observed lattice parameters were found to be very similar to $NpFPO_4$, which was previously reported by Albrecht-Schmitt. The measured crystal was determined to be isostructural with $NpFPO_4$, crystallizing in the orthorhombic space group *Pnma*. The data refined well to an R_1 value of 1.76%. The largest peak and hole are 2.30 and -1.98 $e^-/Å^3$ respectively. Selected crystallographic and refinement information for $UFPO_4$ can be found in Table 9.1.

Powder X-ray Diffraction

PXRD patterns were collected on a Rigaku Ultima IV diffractometer which utilizes Cu K_α radiation ($\lambda = 1.5418$ Å) and a d/Tex Ultra high speed detector. Patterns were collected in the angular range of 5°-65° 2θ with a step size of 0.02°.

Table 1: Crystallographic and Refinement Data for Compound 9.1

Empirical Formula	F O$_4$ P U
Formula Weight	352.00 g/mol
Temperature	310.52 K
Crystal System	Orthorhombic
Space Group	*Pnma*
a	8.6377(2)
b	6.9826(2)
b	6.3607(2)
Volume	383.637(19) Å^3
Z	4
Density	6.095 g/cm^3
Absorption Coefficient	42.636 mm^{-1}
F(000)	592.0
Crystal Size	0.078 mm x 0.076 mm x 0.022 mm
Wavelength	0.71073 Å
2θ range for data collection	7.958° to 72.624°
Reflections Collected	32820
Independent Reflections	987
Data/Restraints/Parameters	987/0/41
Goodness of Fit on *F*^{2}	1.492
Final R Indices (all data)	R$_1$ = 0.0176; wR$_2$ = 0.0428
Largest Diff. Peak and Hole	2.30/-1.98 *e*$^-$/Å^3

Neutron Powder Diffraction

NPD patterns of $UFPO_4$ and $U(UO_2)(PO_4)_2$ were collected on beamline HB-2A (POWDER) at ORNL's HFIR site. Patterns were collected using a bank of 44 ^{3}He detectors. Data were collected in the 3°-130° 2θ range with a step size of 0.05°. Magnetic contributions were probed using neutrons with a wavelength of 2.41 Å to obtain good resolution at low Q. Data for structural refinements were obtained using a wavelength of 1.54 Å at room temperature from 3° to 160° 2θ.

Thermogravimetric Analysis

Thermal properties were probed using TGA under flowing N_2 or H_2 (5% in 95% N_2;100 mL/minute) from room temperature to 800° C or 900° C. The thermal products were characterized by PXRD and were used to guide the rational syntheses of $U_2O(PO_4)_2$ and $U(UO_2)(PO_4)_2$.

SQUID Magnetometry

Magnetic and inverse magnetic susceptibility data were collected using a Quantum Design MPMS3 SQUID magnetometer. Data were collected under an applied field of 0.1 T in the 2 K – 400 K temperature range. The data were corrected for shape and radial offset effects using previously described methods. [17]

Results and Discussion

Powder X-ray Diffraction

Each of the synthesized compounds were characterized by PXRD for confirmation of purity and identity of the material. PXRD patterns of $UFPO_4$, $U_2O(PO_4)_2$, and $U(UO_2)(PO_4)_2$ are shown in Figure 9.1.
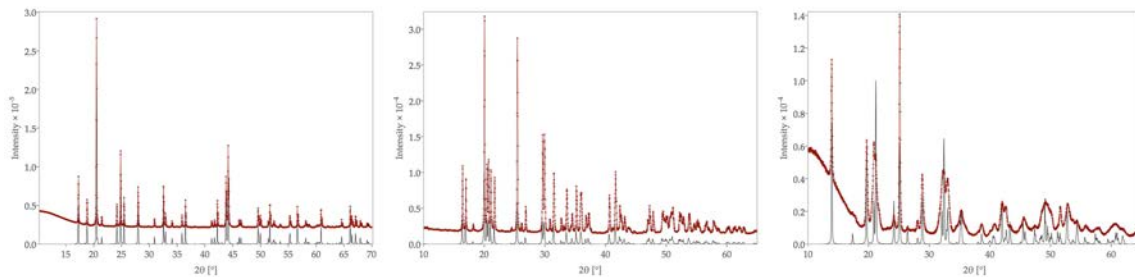
244

Figure 9.1: PXRD Patterns of Materials 9.1-9.3. The PXRD patterns of $UFPO_4$ (*left*), $U(UO_2)(PO_4)_2$ (*middle*), and $U_2O(PO_4)_2$ (*right*). The observed patterns are shown in red, while patterns calculated from the CIF's are shown in black. For UFPO4, the CIF was obtained from the single-crystal structural refinement, while the other CIF's were obtained from the ICSD. In all cases, there is good agreement between the observed and calculated PXRD patterns, indicating a high degree of bulk purity.

Synthesis of UFPO₄

Although the mild hydrothermal method has proven extremely effective at synthesizing new uranium fluorides, the abundance of aqua ligands available in these systems frequently results in hydrated materials, which limit thermal stability and make certain characterization techniques such as neutron diffraction quite difficult. In order to avoid this, a solvothermal approach using a methanol/phosphoric acid solution was employed to limit the amount of water available to the system. In addition, the solubility of many metal species is less in methanol than in water, and so we expect to observe different crystalline products upon switching solvent systems.

Using concentrated HF (48%) would introduce a large amount of water to the system, and so alternate sources of fluorine were used. We investigated the use of alkali and alkaline earth metal fluorides as soluble fluorine sources, however the introduction of these materials resulted consistently in $U_3F_{12} \cdot H_2O$, a previously reported phase. We hypothesize that the reduction of U(VI) to U(IV) happens quickly, and the U(IV) subsequently grabs the available F^- ions and crashes out the stable $U_3F_{12} \cdot H_2O$ phase. By introducing the less soluble (slow-release) FeF_3 as a fluorine source, we ensure that the U(IV) has time to interact with other cations in solution (i.e. phosphorous) before being fluorinated and crystallizing. This method proved successful, and the anhydrous UFPO₄ resulted from these synthetic trials.

Crystal Structure of UFPO₄

UFPO₄ is a three-dimensional structure built of cross-linked uranium oxyfluorides chains. Phosphate groups serve as an additional linkage between the chains. The chains are built primarily of $UO_{6/2}F_{2/2}$ 8-coordinate polyhedra. The local environment of U as

246

well as one chain unit are shown in Figure 9.2. Each uranium ion is coordinated by 6 oxygen and 2 fluorine ions. Four of the oxygen lie in an equatorial plane and form to connect the polyhedra into chains via edge sharing. The remaining two oxygen and two fluorine ligands lie in a perpendicular plane with the fluorine ions arranged roughly *trans* to one another. Each chain is decorated with phosphate tetrahedral such that all oxygen atoms are shared between uranium and phosphorous. Figure 9.3 depicts the phosphate decorated uranium chain, and shows how two chains are bridged by phosphate tetrahedra in the [*c*] direction.

The tetrahedral nature of the phosphate groups mean that the chains shown in Figure 9.3 are connected into sheets that are corrugated. These corrugated sheets are connected in the [*a*] direction by a combination of phosphate and fluoride bridging groups. Figure 9.4 shows the connectivity in the [*a*] direction. Figure 9.5 shows the complete structure viewed down the [*b*] direction in order to visualize the connectivity of uranium chains. Figure 5 shows an alternate complete view of the structure viewed down the [*c*] axis.

Thermal Behavior of UFPO$_4$

The thermal properties of UFPO$_4$ were initially investigated by heating to 800° C under nitrogen flow. The TG curve a smooth weight loss beginning immediately on heating which levels off at 800° C, seen in Figure 9.7. After heating, the resulting powder was analyzed via PXRD and found to consist of a mixture of U$_2$O(PO$_4$)$_2$ and other unidentified phases. The primary phase was U$_2$O(PO$_4$)$_2$, which was found to be closely related to UFPO$_4$ structurally, and so attempts were made to isolate a pure sample of U$_2$O(PO$_4$)$_2$. This was initially attempted by heating the UFPO$_4$ sample to
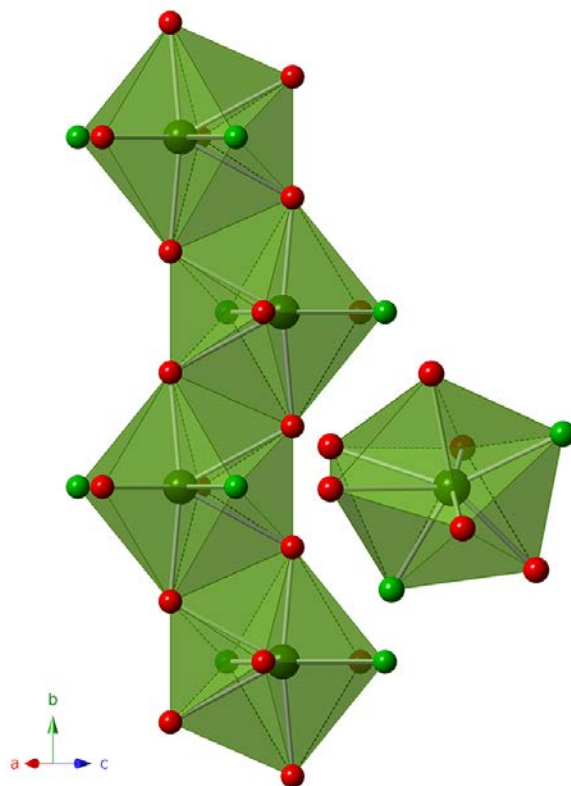
Figure 9.2: Local Environments of U in Compound 9.1. The infinite uranium oxyfluorides chains that make up the structure of $UFPO_4$ (*left*). Each uranium polyhedron (*right*) shares two edges of oxygen ligands to form the infinite chains running along the [*b*] direction. Uranium are shown as green polyhedra, oxygen as red spheres, and fluorine as green spheres.
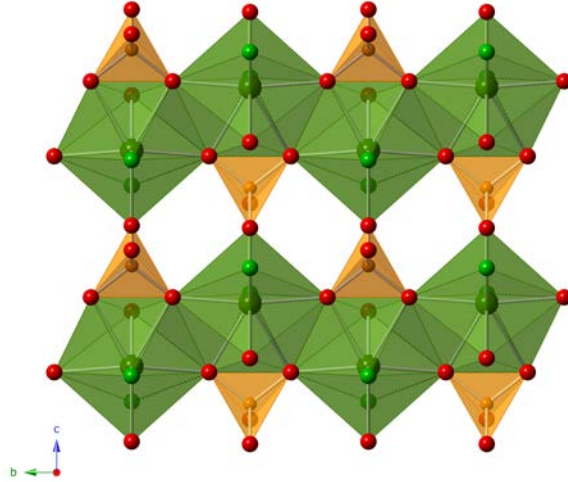
Figure 9.3: Infinite Uranium Chains in Compound 9.1. Edge sharing uranium chains decorated by phosphate tetrahedra. The chains are connected along the [*c*] direction forming 'sheets' of linked chains. The (apparently) unbounded phosphate oxygen shown here will serve to bridge these sheets along the [*a*] direction. Uranium are shown as green polyhedra, phosphorous as orange tetrahedral, oxygen as red spheres, and fluorine as green spheres.
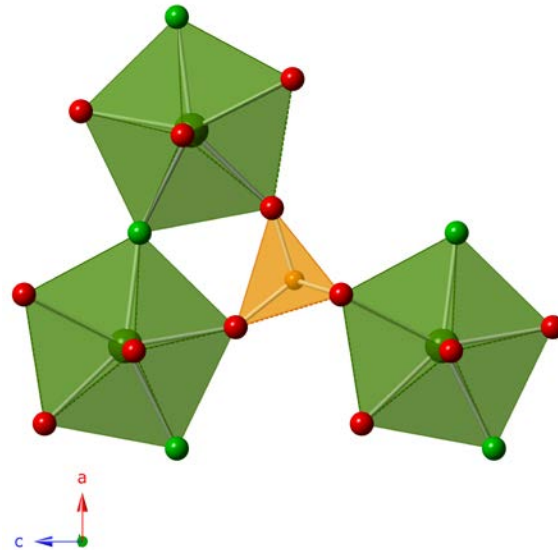

Figure 9.4: Bridging of Chains in Compound 9.1. A tetranuclear cluster of uranium polyhedra bridged by a phosphate tetrahedron. This illustrates how the uranium oxyfluorides chains (running along the [b] direction) are connected in the [*a*] direction by fluoride bridges, and both in the [*a*] and [*c*] directions by phosphate bridges. Uranium are shown as green polyhedra, phosphate as orange polyhedra, oxygen as red spheres, and fluorine as green spheres.
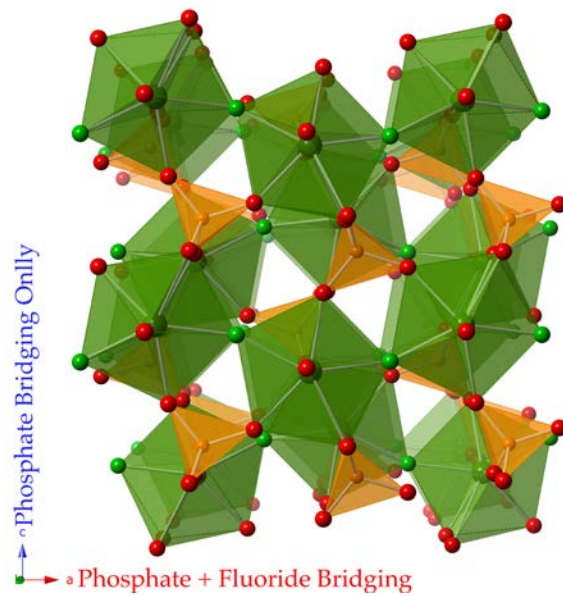
Figure 9.5: [*b*] Axis View of Compound 9.1. The overall structure of UFPO$_4$ as viewed down the [*b*] axis. The uranium chains running along the [*b*] direction are bridged in the [*c*] direction only by phosphate groups, while they are bridged in the [*a*] direction by both phosphate groups and fluoride ligands. Uranium are shown as green polyhedra, phosphorous as orange polyhedra, oxygen as red spheres, and fluorine as green spheres.
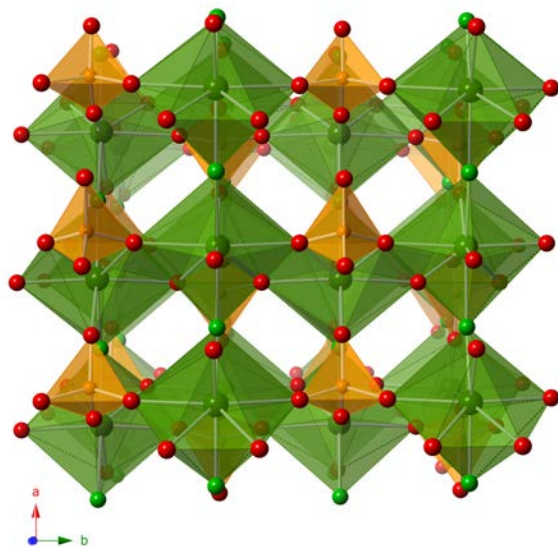
Figure 9.6: Overall View of Compound 9.1. A view of UFPO$_4$ down the [*c*] axis. This view of the structure accentuates the presence of the infinite uranium oxyfluorides chains running parallel to the [*b*] direction. Uranium polyhedra are shown in green, phosphorous in orange, oxygen as red spheres, and fluorine as green spheres.
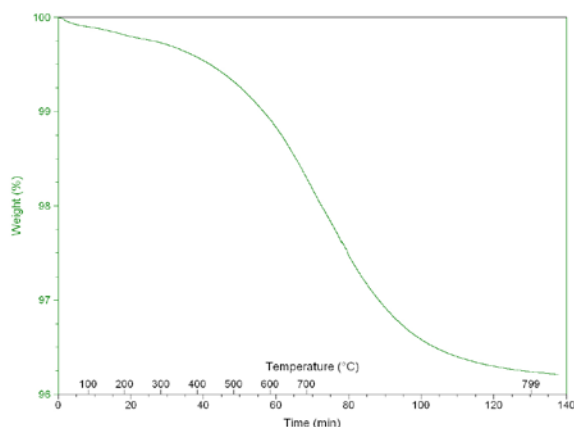

Figure 9.7: TGA to 800° C Under N$_2$ Flow of Compound 9.1. The TG curve of UFPO$_4$ from room temperature to 800° C under a N$_2$ gas flow. UFPO$_4$ loses weight continuously until 800° C at which point it levels out.

251

900° C in the hopes that the higher temperatures would drive the transformation to completion, however this resulted in another structurally related phosphate, $U(UO_2)(PO_4)_2$. The TG curve to 900° C is shown by Figure 7. The second attempt involved heating UFPO$_4$ under a hydrogen atmosphere at 800° C. This TG curve is shown in Figure 9.9, and results in primarily $U_2O(PO_4)_2$, however some small impurity phases remain. Figure 9.10 shows the post-TGA XRD patterns for the three discussed TGA runs. As both $U_2O(PO_4)_2$ and $U(UO_2)(PO_4)_2$ are understudied, we set to developing syntheses for pure samples of both materials.

Synthesis of $U(UO_2)(PO_4)_2$

In order to synthesize the uranium uranyl phosphate material, we made use of a previously reported flux-assisted solid-state synthesis. [18] In this method, stoichiometric amount of UO$_2$ and NH$_4$H$_2$PO$_4$ were combined in a fused silica tube. The charge was heated according to the profile given in the experimental section. This profile first forms P$_2$O$_5$ at 450° C as the ammonia and water vapor are driven off of the phosphate. Finally, the charge is heated to 800° C which renders the P$_2$O$_5$ molten allowing it to react effectively with the uranium. This initial reaction yields unidentified intermediate phases. After the initial heating phase, the intermediate mixture is ground and treated to two heatings at 850° C with an intermediate grinding, which converts the charge to pure $U(UO_2)(PO_4)_2$. The PXRD pattern confirming purity and completeness of the reaction can be reviewed in Figure 9.1.

Synthesis of $U_2O(PO_4)_2$

Since all three reported uranium phosphates are structurally related, it makes sense that interconversion between phases should be possible. $U_2O(PO_4)_2$ contains only
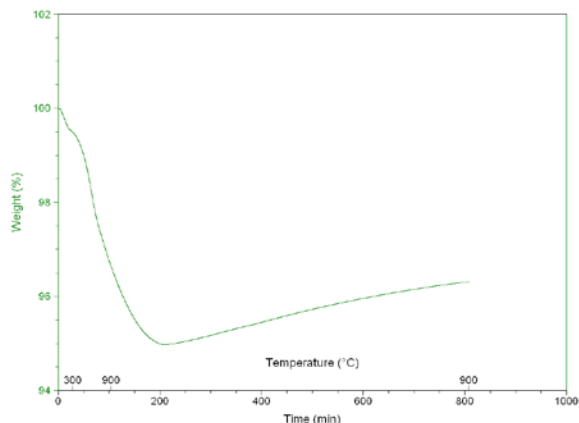
Figure 9.8: TGA to 900° C Under N₂ Flow of Compound 9.1. The TG curve of UFPO₄ up to 900° C under flowing N₂, followed by a 12 hours isothermal hold at 900° C. UFPO₄ loses weight until 900° C, at which it begins to pick up weight presumably corresponding to the oxidation of one U atom from IV to VI.
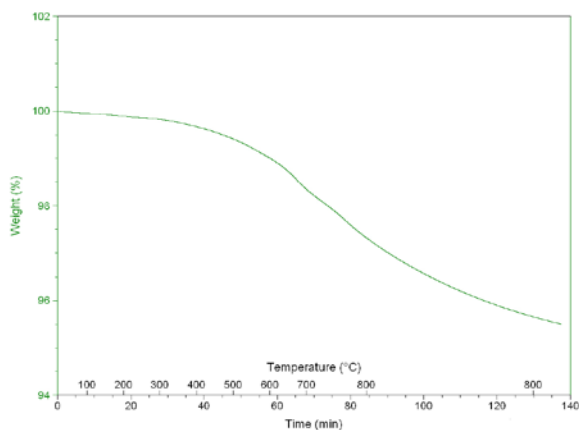

Figure 9.9: TGA to 800° C Under H₂ Flow of Compound 9.1. The TG curve of UFPO₄ from room temperature to 800° C under a 4% H₂ atmosphere. UFPO₄ loses weight again to 800° C at which point it begins to stabilize.
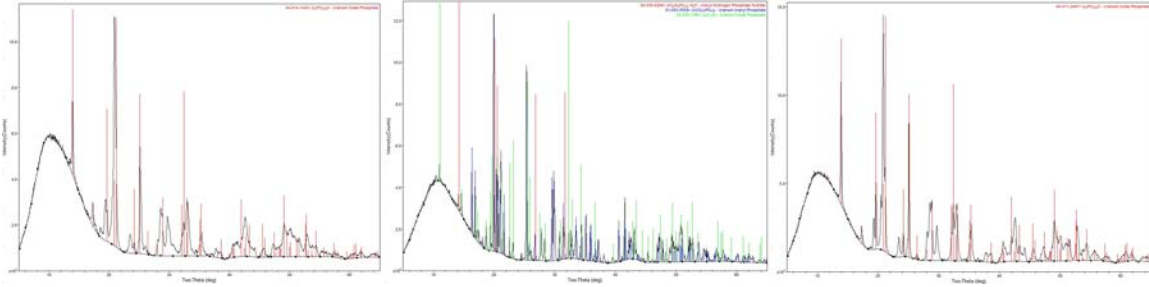
Figure 9.10: Post-TGA PXRD Patterns of Compound 9.1. The post-TGA XRD patterns of $UFPO_4$ after various thermal treatments. The PXRD after heating to 800° C under N_2 (left) shows a transformation to $U_2O(PO_4)_2$ plus unidentified phases. After heating at 900° C for 12 hours under N_2 (middle), the primary products are $U(UO_2)(PO_4)_2$, $U_3P_2O_{12}$, and $UO_2(H_2PO_4)_2 \cdot H_2O$ (which likely formed after picking up water once the furnace was shut off). Finally, heating at 800° C under 4% H_2 (right) formed primarily $U_2O(PO_4)_2$. Judging by the sharper peaks as compared to the left pattern, this sample of $U_2O(PO_4)_2$ is more crystalline.

one less O ion than $U(UO_2)(PO_4)_2$, and so we hypothesized that it should be possible to reduce $U(UO_2)(PO_4)_2$ to form the $U_2O(PO_4)_2$ phase. To test this, freshly made $U(UO_2)(PO_4)_2$ was heated under a 4% H_2 flow at 650° C for 18 hours. This resulted in a pure sample of $U_2O(PO_4)_2$ as evidenced by the PXRD pattern in Figure 9.1.

Structural Comparison of $U_2O(PO_4)_2$ and $U(UO_2)(PO_4)_2$ with UFPO_4

Although the structures of $U_2O(PO_4)_2$ and $U(UO_2)(PO_4)_2$ have been reported elsewhere [18] [19] (ICSD numbers 402120 and 75358 respectively), they will be discussed briefly here in the context of comparing them to $UFPO_4$. $U_2O(PO_4)_2$ is most similar to $UFPO_4$, with a nearly identical structure. Conceptually, doubling the unit cell of $UFPO_4$ in the *c* direction (resulting in $U_2F_2(PO_4)_2$) for charge balancing reasons, then replacing the two fluoride ions with one oxide ion will result in $U_2O(PO_4)_2$. Effectively, this transformation reduces the coordination number of uranium from 8 to 7 and results in a slight rearrangement of the uranium chains from an eclipsed to a staggered arrangement. Figure 9.11 shows the comparison between $UFPO_4$ and $U_2O(PO_4)_2$.

$U(UO_2)(PO_4)_2$ is another related structure whose difference from $UFPO_4$ and $U_2O(PO_4)_2$ is primarily a consequence of the oxidation of half of the U atoms from IV to VI. This half-oxidation of the uranium results in charge-ordering where the uranium atoms are arranged in dimers: alternating U^{4+}-U^{4+}-U^{6+}-U^{6+}-U^{4+}-U^{4+} and so on. All of the U atoms remain in a 7-coordinate environment, however the polyhedron changes from a somewhat irregular UO_7 polyhedron in $U_2O(PO_4)_2$ to a fairly regular pentagonal bipyramid (as would be expected from the uranyl ions) in $U(UO_2)_2(PO_4)_2$. The assignment of U(IV) vs U(VI) can easily be made by finding the uranyl bonds (1.7 Å in this structure) vs the axial bonds of U(IV) (2.1 Å here). Structurally, the oxidation of one
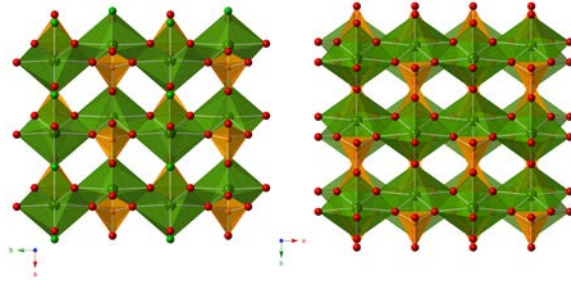
255

Figure 9.11: A side by side comparison of UFPO$_4$ (*left*) with U$_2$O(PO$_4$)$_2$ (*right*). The primary structural consequences of the transformation are the lowering of uraniums coordination number from 8 to 7, and the rearrangement of the uranium chains. This rearrangement is primarily due to the decreased CN which removes half of the interchain U-U bridges (through F in UFPO$_4$, O in U$_2$O(PO$_4$)$_2$). Uranium is shown in green, phosphate in orange, oxygen in red, and fluorine in light green.

of the uranium atoms have fairly major consequence: primarily the loss of U-O-U interchain bonding, which is a result of the now inert uranyl oxygens which cannot form the connection. The phosphate tetrahedra are still present in a more or less unchanged location and still serve to connect the uranium chains. All three reported structures are shown in comparison in Figure 10.

Magnetic Susceptibility of UFPO$_4$, U$_2$O(PO$_4$)$_2$, and U(UO$_2$)(PO$_4$)$_2$

Since U(IV) is a $5f^2$ magnetic ion, we expect both crystal-field and spin-orbit effects to contribute meaningfully to the magnetic moment. This coupled with the close similarity of the three reported structures gives a unique opportunity to probe how small changes in coordination environment effect the magnetism of U(IV). In UFPO$_4$, there are multiple possible magnetic exchange pathways: U-O-U interactions through edge shared members of the uranium chains, U-F-U interaction between chains, and U-O-P-O-U super-superexchange interactions between chains. In U$_2$O(PO$_4$)$_2$ these interactions are slightly simplified as half of the U-F-U interactions (now additional U-O-U) have been removed by the doubling of the *c* axis. Finally, U(UO$_2$)(PO$_4$)$_2$ removes the U-O-U interchain interaction altogether, as well as removes long-range U-O-U intrachain interactions, as the chains are interrupted by diamagnetic uranyl ions. The primary magnetic interactions in this material are U-O-U dimer interactions. These dimers can interact via super-superexchange through phosphate groups along the [*a*] axis.

The magnetic susceptibility of all three materials are shown in Figure 11. All three materials exhibit an increase in susceptibility at low temperatures, to varying degrees. UFPO$_4$ shows the most dramatic increase and is reminiscent of a paramagnet, while the upturns in U$_2$O(PO$_4$)$_2$ and U(UO$_2$)(PO$_4$)$_2$ are more subtle. This behavior is not

257
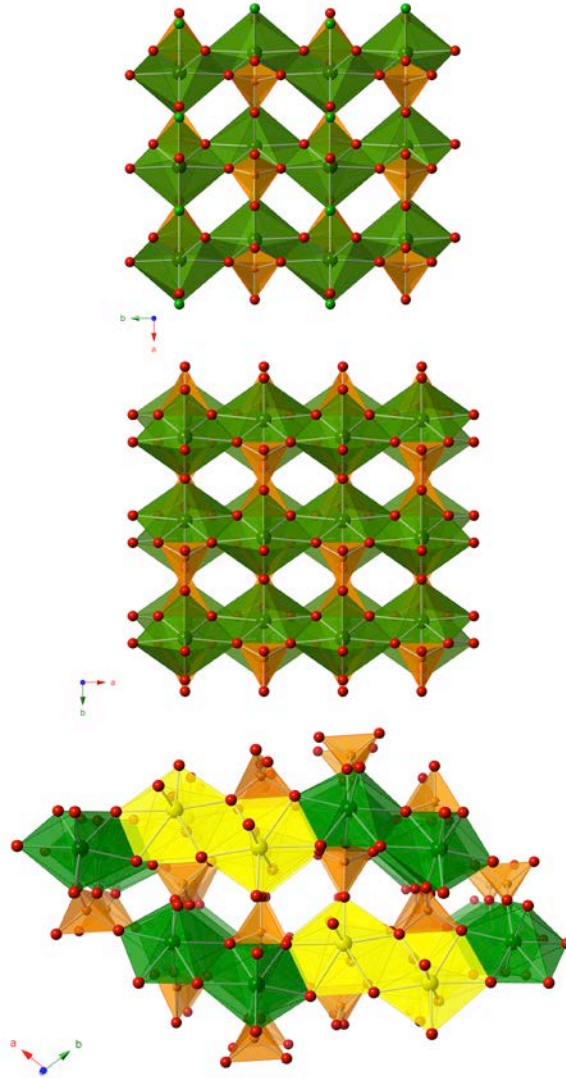
Figure 9.12: Comparison of Structures 9.1-9.3. A comparison of UFPO$_4$ (*top*), U$_2$O(PO$_4$)$_2$ (*middle*), and U(UO$_2$)(PO$_4$)$_2$ (*bottom*). in U(UO$_2$)(PO$_4$)$_2$ there are two uranyl ions which alternate with two U(IV) ions. U(IV) is shown in green, U(VI) in yellow, phosphorous in orange, oxygen in red, and fluorine in light green.
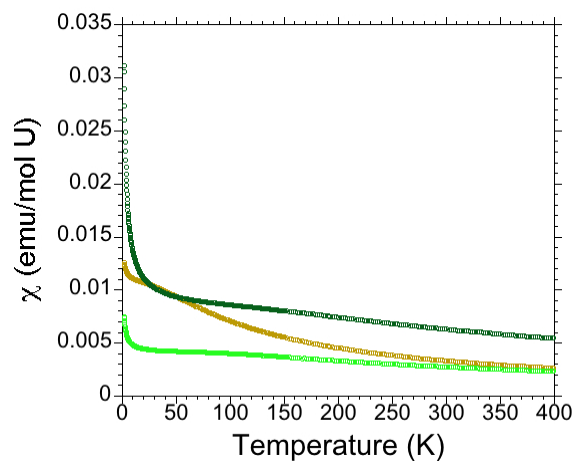
Figure 9.13: Magnetic Susceptibilities of Compounds 9.1-9.3. The magnetic susceptibilities of $UFPO_4$ (dark green), $U_2O(PO_4)_2$ (brown), and $U(UO_2)(PO_4)_2$ (light green). The susceptibilities have been normalized to represent the magnetic susceptibility per U(IV) ion so that values can be directly comparable.

consistent with the singlet ground state that is common among U(IV) materials, although the exact nature of the magnetism is not well understood based off the SQUID data alone. For this reason, neutron diffraction was performed in order to probe the potential for magnetic order.

U(IV) notoriously does not obey the Curie-Weiss law in many cases, which makes obtaining an effective moment somewhat difficult. In order to determine effective high temperature moments, a plot of $2.827(\chi_m \bullet T)^{\frac{1}{2}}$ vs T was generated (Figure 9.14). This plot yields effective moments of 4.2 μ_B/U for $UFPO_4$, 2.9 μ_B/U for $U_2O(PO_4)_2$, and 2.7 μ_B/U for $U(UO_2)(PO_4)_2$. U(IV) typically displays moments of 3.5-3.9 μ_B, meaning these values are slightly outside the reported ranges (although this is not unusual). This exemplifies the great effect that small changes in crystal fields can have on 5f magnetic systems.

Magnetic Neutron Diffraction of UFPO₄ and U(UO₂)(PO₄)₂

The neutron diffraction data has been collected, however is still being analyzed. The diffraction data shows no evidence for long-range magnetic order. Complete analysis of the neutron data will be included in the final version.

Conclusions

Interestingly, the SQUID data seems to indicate that $UFPO_4$, with its higher coordination number and large number of magnetic exchange pathways exhibits a clear retention of a paramagnetic state down to below 2 K. This is coupled with a magnetic moment that is higher than we expect based on previously reported moments for U(IV).

It is difficult to draw any meaningful conclusions from comparing $U_2O(PO_4)_2$ and $U(UO_2)(PO_4)_2$ due to multiple structural differences between the two, however they both
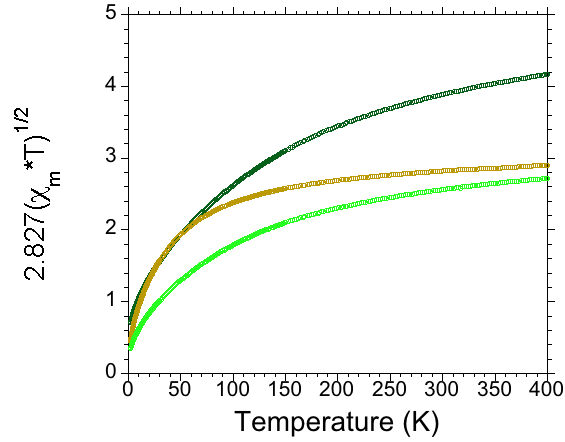
Figure 9.14: Moment vs Temperature Plots of Materials 9.1-9.3. $\chi_m \cdot T$ vs T plots for UFPO$_4$ (dark green), U$_2$O(PO$_4$)$_2$ (brown), and U(UO$_2$)(PO$_4$)$_2$ (light green). The moments decrease with decreasing temperature, consistent with a loss of thermally excited f states, however the moments never reach 0.

clearly exhibit moments almost a full Bohr magneton lower than the expected values. Despite the lack of a clear trends, it is obvious from this study that the coordination environment of uranium plays a clear role in the magnetic behavior of uranium materials.

Acknowledgements

References

(1)   Li, Z.; Li, H.; Guan, X.; Tang, J.; Yusran, Y.; Li, Z.; Xue, M.; Fang, Q.; Yan, Y.; Valtchev, V.; Qiu, S. *J. Am. Chem. Soc.* **2017**, *139*, 17771-17774.

(2)   Meena, A. H.; Arai, Y. *Environ. Chem. Lett.* **2017**, *15*, 241-263.

(3)   Vasconselos, R. G. W.; Beaudoin, N.; Hamilton, A.; Hyatt, N. C.; Provis, J. L.; Corkill, C. L. *Applied Geochemistry* **2018**, *89*, 180-189.

(4)   Zachariasen, W. H. *Actinide Elements* **1954**, 769-796.

(5)   Alekseev, E. V.; Suleimanov, E. V.; Chuprunov, E. V.; Marychev, M. O.; Ivanov, V. A.; Fukin, G. K. *Crystallogr. Rep.* **2006**, *51*, 29-33.

(6)   Read, C. M.; Morrison, G.; Yeon, J.; Smith, M. D.; zur Loye, H. C. *Inorg. Chem.* **2015**, *54*, 6993-6999.

(7)   Wylie, E. M.; Burns, P. C. *Can. Mineral.* **2012**, *50*, 147-157.

(8)   Judd, B. R. *Physical Review B* **1962**, *125*, 613.

(9)   Kindra, D. R.; Evans, W. J. *Chem Rev* **2014**, *114*, 8865-8882.

(10) Boudreaux, E. A.; Mulay, L. N. *Theory and Applications of Molecular Paramagnetism*; Wiley: New York, 1976;

(11) Mortl, K. P.; Sutter, J. P.; Golhen, S.; Ouahab, L.; Kahn, O. *Inorg. Chem.* **2000**, *39*, 1626-1627.

(12) Yeon, J.; Smith, M. D.; Tapp, J.; Moller, A.; zur Loye, H. C. *J. Am. Chem. Soc.* **2014**, *136*, 3955-3963.

(13) Yeon, J.; Smith, M. D.; Tapp, J.; Moller, A.; zur Loye, H. C. *Inorg. Chem.* **2014**, *53*, 6289-6298.

(14) Hubschle, C. B.; Sheldrick, G. M.; Dittrich, B. *J. Appl. Cryst.* **2011**, *44*, 1281-1284.
(15) Sheldrick, G. M. *Acta Cryst.* **2008**, *A64*, 112-122.

(16) Dolomanov, O. V.; Bourhis, L. J.; Gildea, R. J.; Howard, J. A. K.; Puschmann, H. *J. Appl. Cryst.* **2009**, *42*, 339-341.

(17) Morrison, G.; zur Loye, H. C. *J. Solid State Chem.* **2015**, *221*, 334-337.
(18) Benard, P.; Louer, D.; Dacheux, N.; Brandel, V.; Genet, M. *Chem. Mater.* **1994**, *6*, 1049-1058.

(19) Mishra, A. K.; Murli, C.; Singhal, A.; Sharma, S. M. *J. Solid State Chem.* **2008**, *181*, 1240-1248.

CHAPTER 10

BREAKING A PARADIGM: OBSERVATION OF MAGNETIC ORDER IN THE PURPLE
U(IV) PHOSPHITE: U(HPO$_3$)$_2$ *

Introduction

Research into the crystal chemistry of uranium-bearing materials is of great importance due to the large amount of existing radioactive waste that was generated by the United States during the Cold War era, as well as due to the waste that continues to be generated by the United States and other countries involved the production of electricity from nuclear reactions. [1-3] This need for new waste storage materials (as well as new advanced fuel rod materials) drives several research directions [4-10]. In addition, however, uranium-containing materials intrinsically possess fascinating chemistry and, thus, there is also significant interest in examining the fundamental behavior and properties of this and other 5*f* elements. [11-14]

One such fundamental property is magnetism, where the 5*f* elements display unique magnetic behavior due to the extent of their *f* orbitals. [15] In the 3*d* transition metals, strong crystal field effects efficiently quench the orbital angular momentum and the measured magnetic moments reflect the spin-only component. By contrast, in the 4*f* lanthanides with limited 4*f* orbital extent, the crystal field effects are weak and allow for strong spin-orbit coupling. In the actinide elements an intermediate situation is found with spin-orbit coupling effects strong enough to be observed, yet with sufficient orbital extent to make crystal-field effects important. [15]

Uranium can exhibit a wide range of oxidation states (+2 to +6), with all of the oxidation states except +6 showing paramagnetic behavior. All of the possible oxidation states have been observed [16-19], although only the +4 and +6 states are prevalent in extended solid-state materials. The +5 state exists[20], but is rare, as is the +3 state, which is typically not observed in oxide structures. Uranium in the +4 oxidation state is

266

commonly found in large coordination environments (CN > 7) [21, 22] and exhibits paramagnetic behavior due electrons located in low-lying 5f excited states. [15, 23] These excited f orbital states can become thermally depopulated at low temperatures, which leads to a magnetic moment that approaches zero with decreasing temperature as a singlet state is attained. [24–26] This singlet ground state is overwhelmingly prevalent among reported U(IV) materials [25, 27], and cases where paramagnetism persists to low temperatures (< 5 K) are exceedingly rare. [28] Cases where low temperature magnetic behavior is reported in the literature are often convoluted by the presence of multiple magnetic ions [21, 29, 30] (often transition metals) which can obscure the behavior of the uranium. Despite these difficulties it is possible to observe a trend in the magnetic properties of U(IV) containing materials reported in the literature, namely that as the coordination number of the U(IV) ion decreases, the attainment of the non-magnetic singlet state drops to lower temperatures and even goes away. [25, 28]

In a 5f system where both crystal-field and spin-orbit effects are important, it is reasonable to presume that the presence or absence of this singlet state can be influenced by the crystal field experienced by the U(IV) ion. Unfortunately, the ability to "tune" crystal fields by adjusting the crystal structures is notoriously difficult and is limited by our ability (or inability) as chemists to synthesize specific structure types.

It is well known, however, that the anion (ligand) surrounding a metal center strongly influences the crystal field effect, suggesting that by selecting specific anionic species to coordinate to the uranium it is possible to influence the crystal field, and thus the magnetism. A search of the literature reveals this to be the case, as uranium chalcogenides and pnictides have been reported to display magnetic ordering. [31]

267

With the retention of a triplet state down to low temperatures, the potential for long range magnetic ordering arises. Outside the world of intermetallics, there is a dearth of evidence for magnetically ordered extended uranium structures in the literature, and the few reported cases are simple binary or ternary chalcogenides and pnictides such as the ferromagnetic phases UQ, U_3Q_4, and U_2Q_3, U_3Q_5 (Q = S, Se, Te) [30, 31], and the antiferromagnets UN[32], UP[33], and UP_2. [34] Herein, we report the synthesis and characterization of a new uranium phosphite with an unusual purple color that exhibits long-range magnetic interactions at low temperatures.

Experimental

Materials and Methods

The following materials were used as received without further modification: $UO_2(CH_3CO_2)_2$ (ACS Grade, International Bio-Analytical Laboratories, Inc.), $Na_4P_2O_7$ (99+%, Acros Organics), H_3PO_2 (50% in H_2O, Sigma Aldrich), and methanol.

Caution!!! Even though the uranium used in this synthesis is depleted, standard safety precautions for handling radioactive materials should be observed. All work with uranium was performed in labs specifically designated for work with radioactive materials.

The uranyl acetate and sodium pyrophosphate were mixed in a 23 mL PTFE liner with 1 mL of methanol in a 1:1 molar ratio. 1 mL of hypophosphorous acid was added slowly, and then the liner was sealed within a stainless steel autoclave. The autoclave was placed in a programmable oven which was heated to 200° C in one hour, then left at the target temperature for 24 hours. After dwelling, the oven was programmed to cool to 40°

C at a rate of 0.1°/minute. Once at 40° C the oven was shut off and allowed to come to room temperature.

Once cool, the autoclave was opened revealing colorless mother liquor with a suspended blue powder over a denser purple colored powder. The entire charge was decanted into a beaker and mixed with 100 mL of water. The beaker was placed in an ultrasonic bath for 5 minutes, which was sufficient to suspend all of the blue powder. The aqueous blue suspension was decanted off revealing small purple crystals. The crystals were collected by vacuum filtration and were washed thoroughly with water and acetone. The blue suspension was collected by vacuum filtration separately, and was washed with acetone. The yield was found to be approximately 20% purple $U(HPO_3)_2$ and 80% unknown blue phase, based on uranium. Despite the low yield, the materials are easily separable and typically results in ~100 mg of purple $U(HPO_3)_2$ per synthesis.

Single-Crystal X-ray Diffraction

X-ray intensity data were collected from a pale purple-colored plate using a Bruker D8 QUEST diffractometer. The D8 utilizes an Incoatec microfocus source (Mo $K_α$ radiation, $λ = 0.71073$ Å) and a Photon II CMOS area detector. The detector was operated in shutterless mode and additional fast scans were collected to account for overtopped pixels. The raw area detector frames were reduced and corrected for absorption effects using the SAINT+ and SADABS programs. [35] Initial structural models and subsequent least-squares refinements were performed with the SHELX package, through the OLEX[2] GUI. [36, 37]

Crystals of the compound diffracted well to very high resolution, but achieving a correct solution was not straightforward. Examination of the intensity data showed no

systematic absences, leaving 16 possible space groups. R_{int} values did clearly discriminate between likely Laue groups. For structure solution, space group *P*-3 was selected, a solution obtained, and then the ADDSYM program in PLATON was used to search for missed symmetry. This procedure eventually resolved at *P*-3*m*1 (No. 164), a centrosymmetric space group which, after inclusion of a merohedral twin law, yielded excellent refinement statistics and a physically reasonable structure. The dual-space solution program XT returned only space groups *P*3 and *P*-3 using default settings. There are four atomic positions in *P*-3*m*1: U1 (site 1*a*, symmetry -3*m*1), P1 (site 2*d*, symmetry 3*m*.), O1 (site 6*i*, symmetry .*m*.) and H1 (site 2*d*). This model generates a composition of $U(HPO_3)_2$, with ...AB... stacking of PO_3 layers, UO_6 octahedra and two equivalent HPO_3 groups related by a center of symmetry per unit cell. The merohedral twin law [-100 / 0-10 / 001], a two-fold rotation around [001] emulating the higher hexagonal symmetry was applied. This drastically improved the data/model fit, reducing R_1/wR_2 from *ca*. 0.09/0.22 to the values reported. The H atom was located in the difference map, however refining both the H location and the isotropic displacement parameter resulted in an unstable refinement. The P-H bond distance was restrained to be 1.35 Å (based on P-H distances in the ICSD), which allowed the isotropic displacement parameter to be freely refined. The largest residual electron density peak and hole in the final difference map are +1.56 and -0.87 $e^-/Å^3$.

During the several trial solution and refinement attempts, a crystallographically plausible but erroneous solution with reasonable refinement statistics was also obtained in the acentric space group *P*-6*m*2 (No. 182), with major structural consequences. There are three unique atoms in this model (U on site 1*f*, -6*m*2 symmetry; P on 2*h*, 3*m*.

270

symmetry; O on $6n$, $.m.$ symmetry). This solution features ...A... stacking of PO_3 layers, generating UO_6 trigonal prisms and eclipsed P_2O_6 groups with an apparent direct P-P bond (d(P-P) = 2.26(1) Å. The composition is UP_2O_6. The UO_6 prisms and P_2O_6 groups are generated by the action of the -6 rotoinversion axis located at the U atom and at the centroid of the "P-P" bond. This model refined to $R_1 = 0.0240$ / $wR_2 = 0.055$ with difference map extrema of +3.09 / -4.54 $e^-/Å^3$, which are large but not abnormal for an actinide structure. The peaks and holes are located near the U atom and other chemically unremarkable positions. This model generated only three "C-level" alerts in CheckCIF. Interestingly, there is little indication from atomic parameters of the incorrectness of the model; no electron density hole at the phosphorus or oxygen sites or unusually enlarged P or O displacement parameters consistent with excess electron density. The unique P atom refines to 100% occupied within experimental error. Such a pernicious false minimum is primarily the result of the dominance of the uranium scattering factors on the data. Both models have similar $F(000)$ values of 172 or 170 electrons. Of this, the uranium, one P atom, and one oxygen layer (three oxygen atoms), constituting 131 of the 172 total electrons per unit cell (76% of the total scattering) occupy positions common to both models. Only the remaining ~24% of the scattering power of the unit cell differs, and is apparently lost in the background. Table 10.1 lists relevant crystallographic refinement data, and Table 10.2 lists selected interatomic distances.

Powder X-ray Diffraction

Powder X-ray diffraction patterns were collected on a Rigaku Ultima IV diffractometer (Cu K$_\alpha$ radiation, $\lambda = 1.54$ Å) equipped with a D/teX high speed detector. Patterns were collected in the 5° - 65° 2θ angular range with a step size of 0.02°.

Table 10.1: Crystallographic and Refinement Data for U(HPO₃)₂

Empirical Formula	H₂ O₆ P₂ U
Formula Weight (g/mol F. U.)	397.98
Temperature (K)	304(2)
Wavelength (Å)	0.71073
Crystal System	Trigonal
Space Group	*P*-3*m*1
a	5.6825(2)
c	5.6692(2)
Volume (Å³)	158.537(12)
Z	1
Density (kg/m³)	4.168
Absorption Coefficient (mm⁻¹)	26.060
F(000)	172.0
Crystal Size (mm)	0.08 x 0.073 x 0.073
Two-Theta range for data collection	7.224 – 72.502
Reflections	14791
Independent Reflections	321
Completeness	100%
Data/Restraints/Parameters	321/1/15
Goodness-of-Fit on F^2	1.021
Final R Indices	$R_1 = 0.0119$ w$R_2 = 0.0294$
Extinction Coefficient	26.200
Largest Diff. Peak and Hole (e^-/Å³)	1.59/-0.88

Table 10.2: Selected Interatomic Distances (Å) and Angles (°) for U(HPO₃)₂

U(1) – O(1)	2.234(3)
P(1) – O(1)	1.510(3)
P(1) – H(1)	1.347
U(1) – O(1) – P(1)	161.7(2)
U(1) – P(1) – U(1)	100.42

Optical Properties

The optical properties of both the blue phase and the purple $U(HPO_3)_2$ were investigated. UV/Visible absorption measurements were carried out using a PerkinElmer lambda 35 UV/Visible spectrophotometer (used in diffuse reflectance mode) equipped with an integrating sphere. Spectra were recorded in the range of 200 nm – 900 nm. The diffuse reflectance data was converted to absorbance internally by the instrument by use of the Kubelka-Munk function. [38] Infrared spectroscopy was performed using a PerkinElmer spectrum 100 FT-IR spectrometer with a diamond ATR attachment. IR spectra were recorded in the spectral range of 4000 cm^{-1} to 650 cm^{-1}. Final IR spectra consist of 16 total averaged scans.

Magnetic Properties

Magnetic property measurements were carried out using a Quantum Design MPMS3 SQUID magnetometer. Temperature dependent measurements were performed by conducting ZFC and FC temperature sweep from 2 K – 300 K under an applied magnetic field of 0.1 T. Field dependent magnetization measurements were performed at 2 K by sweeping the applied magnetic field from -5 T to 5 T. The data were corrected for radial offset and shape effects by previously described methods. [39] Magnetic property measurements were carried out on both the blue phase and the purple $U(HPO_3)_2$.

Thermogravimetric Analysis

TGA was performed on both samples in order to determine thermal stability. TGA was performed using an SDT Q600 TG-DSC under nitrogen flow (100 mL/min). The samples were loaded in alumina crucibles and heated to 900° C at 10°/minute. The

273

thermal products were analyzed by PXRD, UV/Vis, and IR spectroscopy using the methods and instruments described above.

Results and Discussion

Synthesis.

Single crystals of $U(HPO_3)_2$ were obtained from a hydrothermal reaction involving uranyl acetate, sodium pyrophosphate, methanol and hypophosphorous acid. The purple crystals of $U(HPO_3)_2$, which form together with a secondary blue phase, can readily be isolated in pure form.   This phosphite is related compositionally to $U(HPO_3)_2 \cdot 2H_2O$, first reported by Albrecht-Schmitt [40, 41], however its structure is quite different. An optical photograph of the purple phase can be seen in Figure 10.1 contained in a steel PXRD sample holder.

Crystal Structure

The structural building block of the $U(HPO_3)_2$ structure is the UO_6 octahedron, which is formed by the insertion of U(IV) centers into octahedral holes created by two close-packed oxide layers. Each pair of oxide layers is separated by approximately 3 angstroms, resulting in a van der Waals gap, thereby creating a true layered structure. Figure 10.2 shows a layer of UO_6 octahedra resulting from the close-packed layers (Figure 10.2a), while Figure 10.2b illustrates the fact that the UO_6 octahedra are not directly connected to each other.

The UO_6 units are connected by hydrogen phosphite (HPO_3) units that are located between the UO_6 octahedra such that each HPO_3 tetrahedron bridges three UO_6 octahedra. The phosphite tetrahedra are staggered so that three HPO_3 tetrahedra (per UO_6 unit) are located in one oxide layer, while the other three HPO_3 tetrahedra are located in
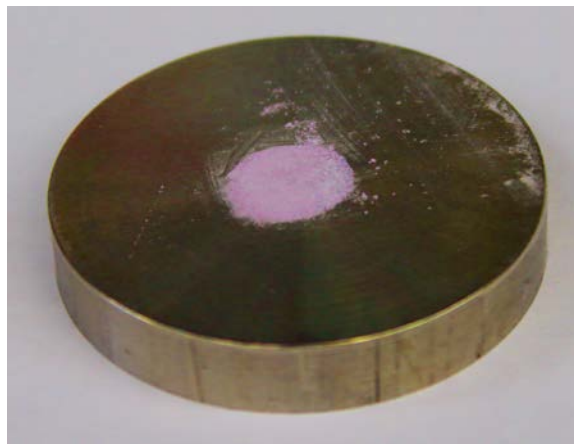
274

Figure 10.1: Purple Color in U(HPO$_3$)$_2$. An optical photograph of U(HPO$_3$)$_2$ showing its unusual purple coloration.
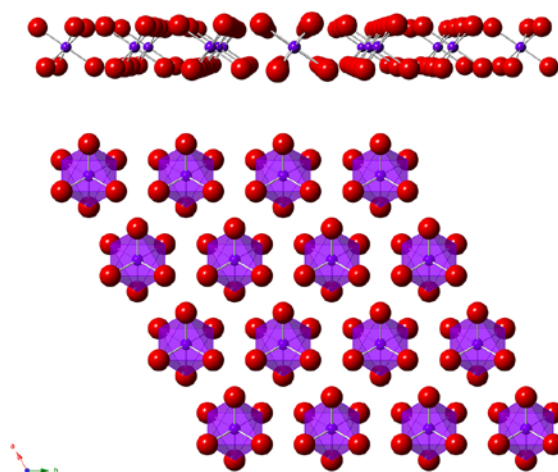

Figure 10.2: Two views of the UO$_6$ layers resulting from oxide close-packing in U(HPO$_3$)$_2$. Uranium is depicted as purple polyhedra, and oxygen as red spheres.

275

the adjacent oxide layer. This causes the phosphite hydrogens to point into the van der Waals gap and to interdigitate with phosphite groups on adjacent layers. Figure 10.3 shows the connectivity of one UO_6 octahedron to six HPO_3 tetrahedra and one complete $U(HPO_3)_2$ sheet.

The H atoms between the close-packed oxide layers are too far apart for strong H-bonding interactions, with the closest H--O distances of ~3.1 angstroms. This suggests that the attractions between the $U(HPO_3)_2$ sheets are dipole-dipole and London dispersion forces. The arrangement of structural units within the $U(HPO_3)_2$ layers is shown in Figure 10.4a and the stacking, interdigitation and the van der Waals gap between the $U(HPO_3)_2$ layers is illustrated in Figure 10.4b.

Optical Properties

The optical properties of $U(HPO_3)_2$ were examined and expected to be quite interesting due to the unusual purple color of the material. The UV/Visible absorption spectrum was found to consist of many weak absorption bands, presumably from *f-f* electronic transitions, however they are noticeably different from the spectra commonly observed in other U(IV) materials. This difference in absorption spectra explains the unusual purple color of the title compound. The UV/Visible spectrum is shown in Figure 10.5. The purple color, while unusual, is not the first report of a purple U(IV) oxide, as green $K_2USi_6O_{15}$ undergoes a structure transition to a low temperature purple phase.

The infrared absorption spectrum, which can be seen in Figure 10.6, contains two prominent features: a broad intense band at 1000 cm^{-1} and a sharp, but weaker band at 2500 cm^{-1}. Both of these bands were assigned by comparison with other phosphite materials in the literature. The strong band at 1000 cm^{-1} is attributed to P – O stretching
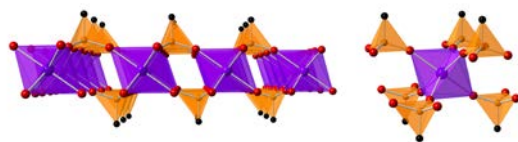
Figure 10.3: U(HPO₃)₂ Layers. Phosphite tetrahedra connect UO_6 octahedra to form a $U(HPO_3)_2$ layer (*left*). The local environment of uranium extended to show bonding interactions with phosphite groups (*right*). Uranium is shown as purple polyhedra, phosphorous as orange polyhedra, oxygen as red spheres, and hydrogen as black spheres.
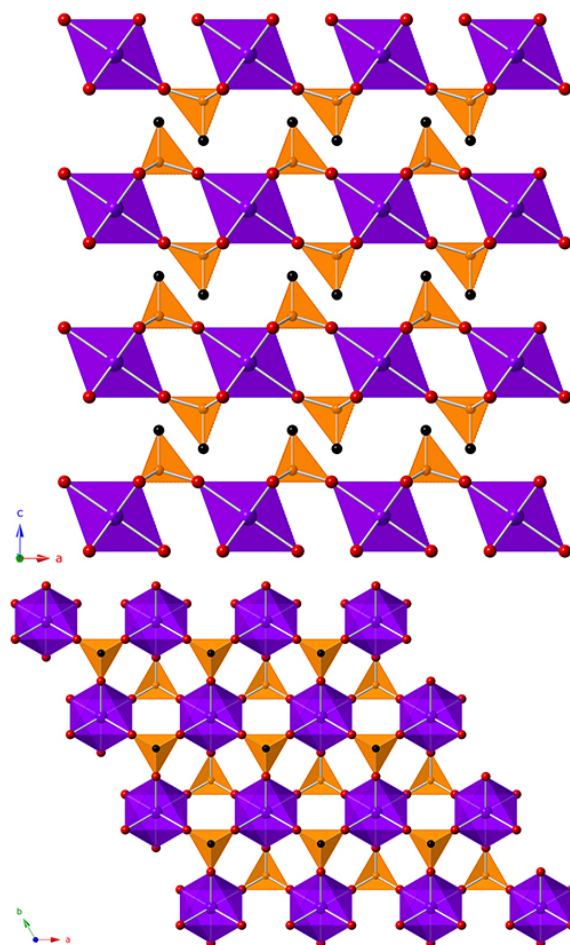
Figure 10.4: Overall structural depiction of U(HPO$_3$)$_2$. View of the [*ab*] plane showing the arrangement of structural units within the U(HPO$_3$)$_2$ layers (*bottom*). View of the [*ac*] plane, showing how the individual layers are stacked and the van der Waals gap between them (*top*). Uranium is shown as purple polyhedra, phosphorous as orange polyhedra, oxygen as red spheres, and hydrogen as black spheres.
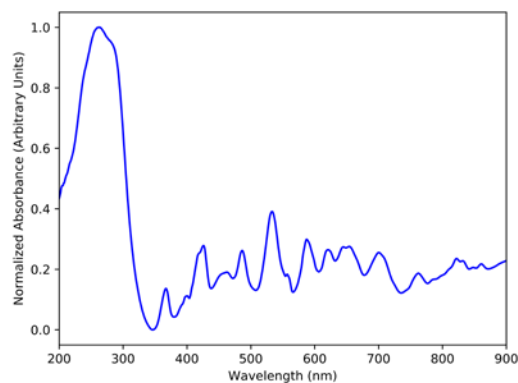
Figure 10.5: The UV/Visible Absorption Spectrum of U(HPO₃)₂. The most prominent features are the multiple *f-f* absorption bands that range from ~350 – 900 nm. The large band below 350 nm represents the onset of the absorption band.
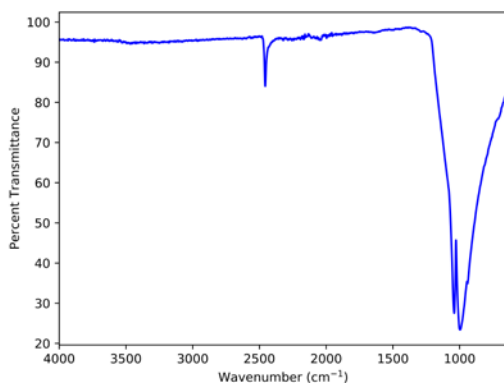

Figure 10.6: The IR Spectrum of U(HPO₃)₂. The sharp band at 2500 cm^{-1} is representative of P – H stretching modes, and the intense bands at 1000 cm^{-1} represent P – O stretching modes.

modes, while the sharp band at 2500 cm $^{-1}$ is attributed to P – H stretching modes, supporting the crystallographic evidence for HPO$_3$ units in the structure.

Powder X-ray Diffraction

The observed PXRD pattern was compared to the calculated pattern generated using the CIF from the single-crystal structural refinement. The observed and calculated patterns agree well, with no detectable extra peaks. (Two small K$_\beta$ peaks can be seen at 14.35° and 21.73° 2θ). The narrow reflections indicate a high degree of crystallinity and the match with the CIF supports a phase-pure bulk sample with no noticeable impurities. The observed and calculated patterns are overlaid in Figure 10.7.

Thermal Properties

It was expected that U(HPO$_3$)$_2$ would not exhibit a high degree of thermal stability, however thermogravimetric analysis in flowing N$_2$ demonstrates that U(HPO$_3$)$_2$ is surprisingly thermally stable up to roughly 500° C; heating the sample beyond 500° C, however, results in a complex sample transformation into the cubic U(IV) pyrophosphate phase, UP$_2$O$_7$. XRD data collected on samples heated to 500° C confirm the absence of a structural change, suggesting that the small, but continuous weight loss to about 400° C is the result of uncoordinated water loss. The TGA curve is displayed in Figure 10.8. The transformation process starting at about 600 °C appears to consist of a weight loss followed immediately by a weight gain, the latter likely from oxygen or water impurities in the nitrogen stream. Interestingly, this uptake of oxygen does not result in the oxidation of uranium from IV to VI, but instead oxidizes the phosphorous, which in this case acts a sacrificial reductant, changing from a formal oxidation state of P(III) in HPO$_3$ to P(V) in P$_2$O$_7$, apparently protecting the +4 oxidation state of uranium. Above 1000° C
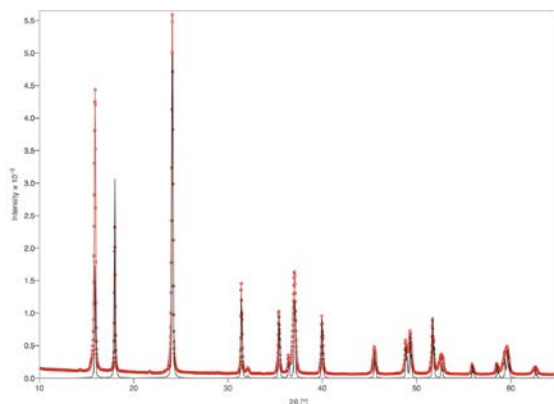
Figure 10.7: The PXRD Pattern of U(HPO₃)₂. The observed (red) and calculated (black) PXRD patterns of U(HPO₃)₂. The calculated pattern was obtained from the CIF generated from the single-crystal XRD refinement. The calculated and observed patterns agree well with no extra peaks.
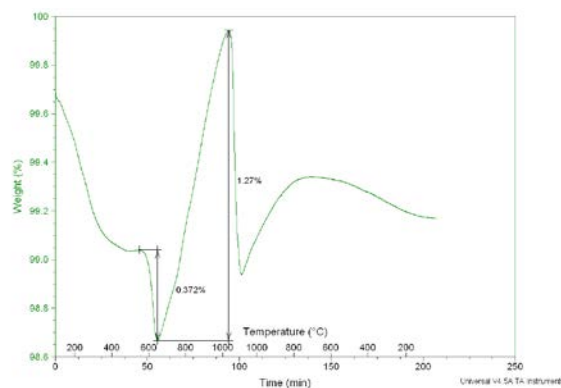

Figure 10.8: TGA of U(HPO₃)₂. The TGA curve from room temperature to $1100°$ C in N_2 for U(HPO₃)₂. The initial weight loss was attributed to surface water, as PXRD revealed no structural change below $600°$ C. The initial weight loss of 0.372% is hypothesized to be from the loss of H from the phosphite groups. The subsequent weight gain of 1.27% is from the uptake of oxygen during the transition to UP_2O_7. The initial weight loss of 0.372% is slightly less than expected from the loss of 2 H atoms, potentially because the material begins picking up oxygen before the loss of H is complete. The weight gain of 1.27% is much less than the expected 8% for the uptake of oxygen, which we attribute to the further transformation of the material before the weight gain can be completed.

281

additional weight losses and gains can be observed and the powder XRD pattern consists of primarily UP_2O_7 alongside a number of additional small reflections that support the formation of one or more additional oxidized phases that could not be identified. Figure 10.9 displays the post TGA XRD patterns.

Magnetic Properties

There is no direct oxide bridge between uranium centers, however, the uranium centers are connected to each other via HPO_3 tetrahedra, thereby forming a hexagonal honeycomb-type lattice, shown in Figure 10.10. In principle, this structure arrangement allows for magnetic uranium centers to couple with each other via super-superexchange interactions mediated by the phosphite groups; such magnetic coupling could potentially result in very weak magnetic interactions. [42, 43] Another consequence of the hexagonal lattice is that although there is only one type of magnetic ion present in $U(HPO_3)_2$ (U^{+4}, $5f^2$), the exchange interactions in such a hexagonal lattice typically result in strong geometric frustration. Geometric frustration can result from a triangular arrangement of spins that attempt to couple antiferromagnetically, a geometrically impossible (frustrating) arrangement.

Given the simplicity of the system (only one type of magnetic ion, and one type of possible exchange interaction), we surmise there are three possible magnetic archetypes that $U(HPO_3)_2$ could belong to. The first type (a) would be a non-magnetically ordered state where the U ions either do not order magnetically (remain paramagnetic) or the U $5f$ electrons pair and the system devolves into a diamagnetic singlet state (a common occurrence among U(IV) systems). The second magnetic archetype (b) would involve a pure ferromagnet, where all of the U spins are aligned. The final archetype (c) is an
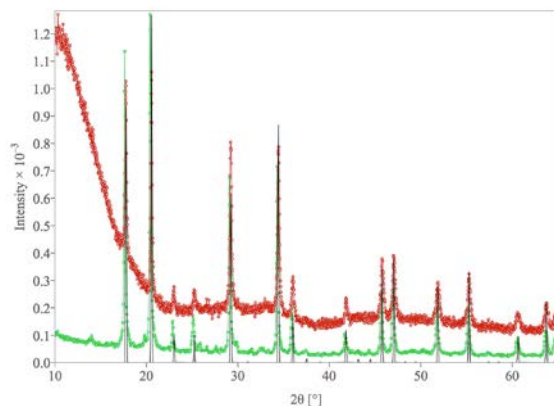
Figure 10.9: Post-TGA PXRD Pattern of U(HPO₃)₂. The post-TGA PXRD plots of the thermal products of $U(HPO_3)_2$. The black plot is the calculated pattern of UP_2O_7, obtained from the ICSD (number 81992). The red pattern is the PXRD taken after heating at 600° C. The large background at low angles is due to Fe fluorescence arising from a stainless steel sample holder. The green pattern is the PXRD pattern taken after heating at 1100° C. The sample is noticeably more crystalline due to the more intense peaks, possible from an annealing effect. The presence of multiple peaks from unidentified phases are present at elevated temperatures.
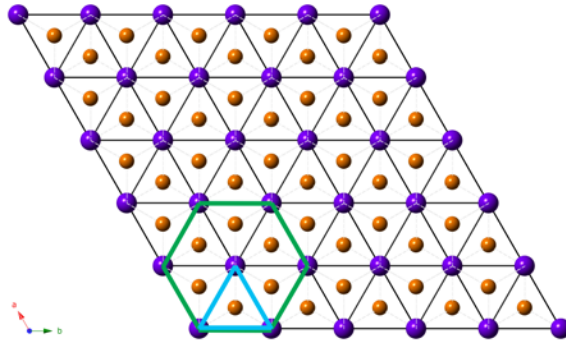
Figure 10.10: Magnetic Lattice of U(HPO₃)₂. Simplified view of the $U(HPO_3)_2$ layers showing magnetic uranium (purple spheres) and super-superexchange mediating phosphorous (orange spheres). Bonding interactions between uranium and phosphorous are shown as light dashed lines (oxide bridges omitted for clarity), and super-superexchange interaction pathways are shown as bold black lines. The magnetic lattice is constructed of triangular units (blue) which form hexagonal tiles (green), building the structure.

antiferromagnetic arrangement which, as discussed for this this system, would be magnetically frustrated. This frustrated magnetic arrangement should result in a small net magnetization caused by the failure of the U atoms to align perfectly antiferromagnetically.

The magnetic susceptibility (Figure 10.11) quickly rules out two of the three possible archetypes. The magnetic susceptibility continues to increase even as the temperature reaches 2K, eliminating possibility (a). The lack of an obvious intense ferromagnetic transition rules out (b). (c) would seem consistent, as at 8 K there is a small jump (a positive deviation) in the ZFC and FC susceptibility data. This is a very weak transition and below the transition the ZFC and FC data no longer overlay, a typical result of magnetic frustration. This leads us to propose that $U(HPO_3)_2$ is a magnetically frustrated system and, since the deviation is positive, likely very slightly canted. This is an intriguing result, as examples of U atoms participating in long-range magnetic order are exceedingly rare in the literature. To further test this hypothesis, the magnetization as a function of field was measured and found to display non-Curie-Weiss behavior and to exhibit a small magnetic hysteresis. The measurements were repeated on several different batches of $U(HPO_3)_2$, consistently yielding the same transition.

$U(HPO_3)_2$ does not exhibit Curie-Weiss paramagnetic behavior, even at high temperatures, preventing the determination of a magnetic moment by fitting the data to the Curie-Weiss Law. This suggests that, as for other U(IV) systems, there is a thermal decrease of f electrons in excited states, however, not enough to prevent magnetic coupling. As is often reported in the literature, a room-temperature paramagnetic moment was obtained by taking the value of $2.827(\chi_m \cdot T)^{\frac{1}{2}}$ at 300 K. This value gives a
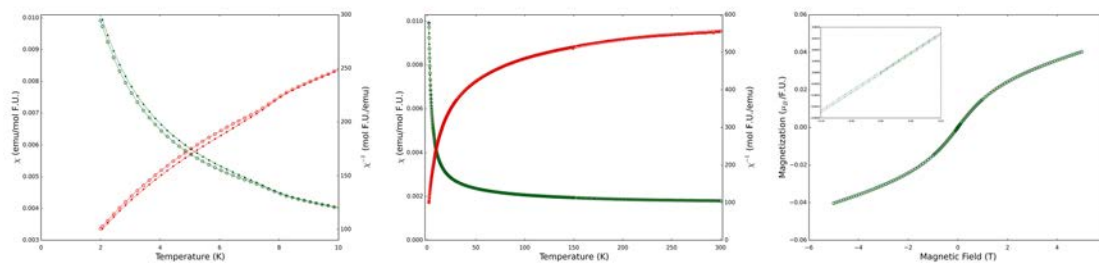
Figure 10.11: Magnetic Measurements of U(HPO₃)₂. (left) The low temperature magnetic susceptibility of $U(HPO_3)_2$ showing the magnetic transition at 8 K. The ZFC (open circles) deviates from the FC (closed points) below the transition. (middle) The full range magnetic susceptibility, highlighting the lack of transition to a singlet state and the non Curie-Weiss behavior of $U(HPO_3)_2$. (right) Magnetization versus Field measurements, the inset shows the low-field region where there is weak field dependence at 2 K. In the susceptibility plots, green data is magnetic susceptibility and red data is the inverse magnetic susceptibility.

moment of ~2.1 μ_B/U, which is significantly lower than magnetic moment values reported for U(IV) (3.58 μ_B) in the literature. Figure 10.12 shows the $\chi_m T$ vs T plot, and the inset confirms the magnetic transition an 8 K. The low observed moment is due to the fact that the uranium moment is not yet saturated, as has been observed in other oxides containing U(IV) in UO_6 coordination environments. [28]

Blue Phase

The blue material that forms during the synthesis of $U(HPO_3)_2$, can easily be separated from $U(HPO_3)_2$, and studied. Unfortunately, no single crystals suitable for diffraction were found in the product, and attempts to recrystallize the blue material failed. The PXRD pattern of the blue phase was found to have a nearly identical PXRD pattern as $U(HPO_3)_2$, with a slight but observable shift in the *c* lattice parameter. The *c* parameter of the blue phase is 0.03 Å smaller ($c_{initial}$ = 5.4467(6) Å and c_{blue} = 5.4156(10) Å [calculated by PXRD]) than the *c* parameter of $U(HPO_3)_2$; the *a* lattice parameters are identical within experimental error. The striking similarity of the patterns suggest that layers similar in structure to those of $U(HPO_3)_2$ are present in the blue phase, however the change in *c* lattice parameter suggests that the layers are slightly closer together. The PXRD pattern of the blue phase is shown for comparison with that of $U(HPO_3)_2$ in Figure 10.13. This is corroborated by the IR spectrum of the blue phase, which shows a slightly broadened and depressed P – H stretching band, suggesting the presence of some H-bonding interactions. Unfortunately, with only laboratory powder X-ray diffraction data and without single-crystal diffraction data it is not possible to determine the origin of such a subtle structural difference. The UV/Vis spectrum is shown with $U(HPO_3)_2$ in Figure 10.14. The difference in the UV/Vis data between the blue and purple
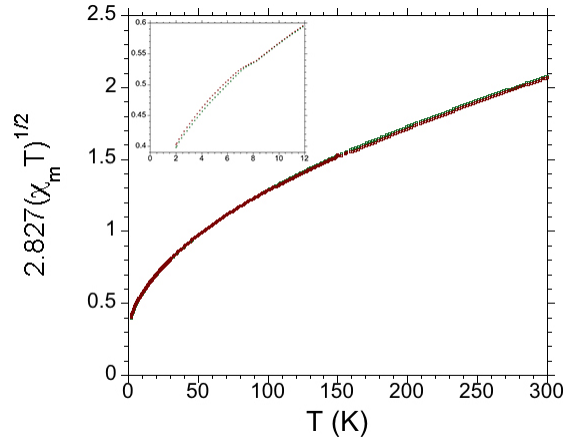
287

Figure 10.12: Moment vs Temperature Plot of U(HPO₃)₂. The $\chi_m T$ vs T plot for U(HPO$_3$)$_2$. ZFC data is shown by green circles, and FC data as red circles. The moment is not yet saturated at 300 K, and gives an observed magnetic moment of 2.1 μ_B. The inset shows the low temperature region, highlighting the magnetic transition.
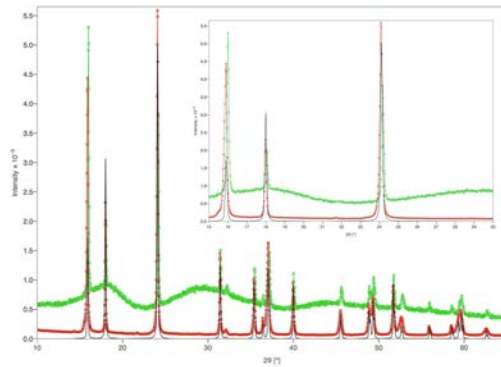

Figure 10.13: PXRD Patterns of U(HPO₃)₂ and the Unknown Blue Phase. The PXRD patterns of U(HPO$_3$)$_2$ (red) and the unknown blue phase (green). The calculated pattern for U(HPO$_3$)$_2$ is shown in black. The blue material has an almost identical powder pattern, however the peaks are shifted slightly (which can be seen in the inset). The two small peaks to the left of the two largest U(HPO$_3$)$_2$ peaks (just under 10 degrees, and over 20 degrees), are peaks resulting from residual Cu K$_\beta$ radiation.
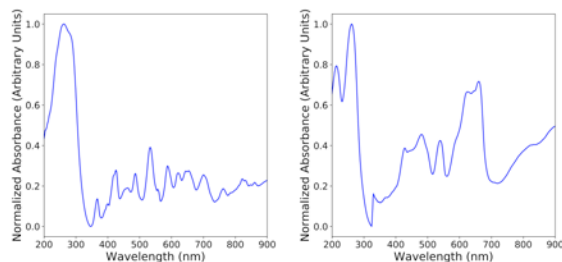
Figure 10.14: Purple and Blue UV/Vis Spectra. The UV/Vis spectra of purple U(HPO$_3$)$_2$ (left) and the blue material (right) shown in comparison. The drastic difference between the two spectra suggests that the coordination environment of the uranium is not identical in the two phases.

phases does, however, indicate that the uranium coordination environments in the two phases are not identical. The IR spectrum is shown in Figure 10.15.

The magnetic susceptibility data of the blue phase indicate that the uranium f-electrons also do not enter a singlet ground state by 2K, however, the magnetic transition exhibited by $U(HPO_3)_2$ is not observed in the blue material. This gives further credence to the fact that the blue material and $U(HPO_3)_2$ are structurally related, however distinctly different materials with different uranium coordination environments. A plot of the magnetic and inverse magnetic susceptibility of the blue material is shown in Figure 10.16, and is shown overlaid with the susceptibility of $U(HPO_3)_2$, in Figure 10.17.

Conclusions

A new purple U(IV) containing phosphite, $U(HPO_3)_2$, was prepared hydrothermally, its crystal structure determined and its physical properties investigated. This layered material consists of a van der Waal gap separated $U(HPO_3)_2$ sheets, exhibits unpaired magnetic electrons down to 2K, and exhibits a weak magnetic transition at 8K. It is hypothesized that the super-superexchange pathway via the linking PO_3H units enables the uranium *f*-electrons to couple weakly and that the presence of the triangular sheet lattice structure leads to magnetic frustration. We surmise that this unusual magnetic behavior arises from a combination of the oxygen coordination environment and the low coordination number of 6 for U(IV).
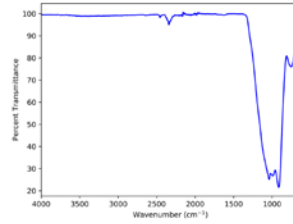
Acknowledgements

Figure 10.15: The IR Spectrum of the Blue Material. The IR spectrum of the blue phase shows intense P-O stretching modes as well as a broadened and depressed P-H stretching mode at 2500 cm^{-1}.
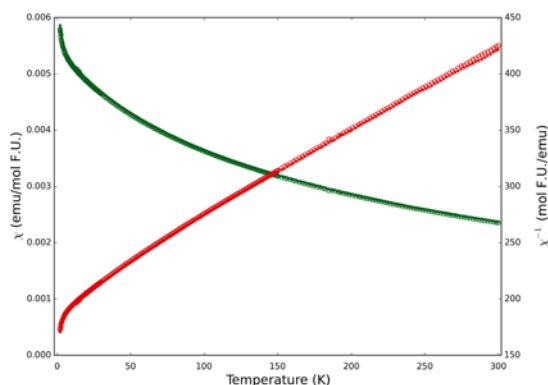
Figure 10.16: Magnetic Susceptibility of the Blue Phase. The magnetic susceptibility (green) and inverse magnetic susceptibility (red) of the unknown blue phase. Although no transition to a magnetically ordered state is observed, this material does appear to remain in a magnetic triplet state through 2 K. No Curie-Weiss fit could be obtained as the formula weight is unknown and so the extracted values would not be a true indication of the properties of the material. ZFC data is shown by open circles, FC data as closed points.
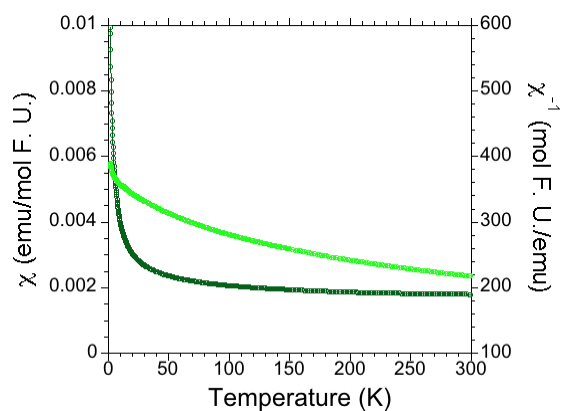
Figure 10.17: Magnetic Susceptibilities of U(HPO₃)₂ and the Blue Material. A comparison between the magnetic susceptibilities of $U(HPO_3)_2$ (dark green) and the unknown blue material (light green). Although the absolute values of the susceptibility of the blue phase are inherently incorrect (by virtue of the fact that the formula weight is unknown), the values were estimated by assuming the formula weight to be 398 g/mol (similar to $U(HPO_3)_2$). The behavior the magnetism is quite different, giving credence to the fact that the materials are distinct.

References

(1) Li, Z.; Li, H.; Guan, X.; Tang, J.; Yusran, Y.; Li, Z.; Xue, M.; Fang, Q.; Yan, Y.; Valtchev, V.; Qiu, S. *J. Am. Chem. Soc.* **2017**, *139*, 17771-17774.

(2) Meena, A. H.; Arai, Y. *Environ Chem Lett* **2017**, *15*, 241-263.

(3) Vasconcelos, R. G. W.; Beaudoin, N.; Hamilton, A.; Hyatt, N. C.; Provis, J. L.; Corkhill, C. L. *Applied Geochemistry* **2018**, *89*, 180-189.

(4) Balboni, E.; Simonetti, A.; Spano, T.; Cook, N. D.; Burns, P. C. *Applied Geochemistry* **2017**, *87*, 84-92.

(5) Dolgopolova, E. A.; Ejegbavwo, O. A.; Martin, C. R.; Smith, M. D.; Setyawan, W.; Karakalos, S. G.; Henager, C. H.; zur Loye, H. -C.; Shustova, N. B. *J. Am. Chem. Soc.* **2017**, *139*, 16852-16861.

(6) Hao, Y.; Murphy, G. L.; Bosbach, D.; Modolo, G.; Albrecht-Schmitt, T. E.; Alekseev, E. V. *Inorg. Chem.* **2017**, *56*, 9311-9320.

(7) Hao, Y.; Klepov, V. V.; Kegler, P.; Modolo, G.; Bosbach, D.; Albrecht-Schmitt, T. E.; Wang, S.; Alekseev, E. V. *Crystal Growth & Design* **2017**, *18*, 498-505.

(8) Morrison, G.; Smith, M. D.; zur Loye, H. -C. *J. Am. Chem. Soc.* **2016**, *138*, 7121-7129.

(9) Zhang, Z. H.; Senchyk, G. A.; Liu, Y.; Spano-Franco, T.; Szymanowski, J. E. S.; Burns, P. C. *Inorg. Chem.* **2017**, *56*, 13249-13256.

(10) Zhu, L.; Sheng, D.; Xu, C.; Dai, X.; Silver, M. A.; Li, J.; Li, P.; Wang, Y.; Wang, Y.; Chen, L.; Xiao, C.; Chen, J.; Zhou, R.; Zhang, C.; Farha, O. K.; Chai, Z.; Albrecht-Schmitt, T. E.; Wang, S. *J. Am. Chem. Soc.* **2017**, *139*, 14873-14876.

(11) Cary, S. K.; Galley, S. S.; Marsh, M. L.; Hobart, D. L.; Baumbach, R. E.; Cross, J. N.; Stritzinger, J. T.; Polinski, M. J.; Maron, L.; Albrecht-Schmitt, T. E. *Nat Chem* **2017**, *9*, 856-861.

(12) Chen, L.; Diwu, J.; Gui, D.; Wang, Y.; Weng, Z.; Chai, Z.; Albrecht-Schmitt, T. E.; Wang, S. *Inorg. Chem.* **2017**, *56*, 6952-6964.

(13) Galley, S. S.; Van Alstine, C. E.; Maron, L.; Albrecht-Schmitt, T. E. *Inorg. Chem.* **2017**, *56*, 12692-12694.

(14) Silver, M. A.; Cary, S. K.; Garza, A. J.; Baumbach, R. E.; Arico, A. A.; Galmin, G. A.; Chen, K. W.; Johnson, J. A.; Wang, J. C.; Clark, R. J.; Chemey, A.; Eaton, T. M.; Marsh, M. L.; Seidler, K.; Galley, S. S.; van de Burgt, L.; Gray, A. L.; Hobart, D. E.; Hanson, K.; Van Cleve, S. M.; Gendron, F.; Autschbach, J.; Scuseria, G. E.; Maron, L.; Speldrich, M.; Kögerler, P.; Celis-Barros, C.; Páez-Hernández, D.; Arratia-Pérez, R.; Ruf, M.; Albrecht-Schmitt, T. E. *J. Am. Chem. Soc.* **2017**, *139*, 13361-13375.

(15) Kindra, D. R.; Evans, W. J. *Chem Rev* **2014**, *114*, 8865-8882.

(16) Biswas, S.; Ma, S.; Nuzzo, S.; Twamley, B.; Russell, A. T.; Platts, J. A.; Hartl, F.; Baker, R. J. *Inorg. Chem.* **2017**, *56*, 14426-14437.

(17) Gong, Y.; Andrews, L. *Inorg. Chem.* **2011**, *50*, 7099-7105.

(18) Read, C. M.; Morrison, G.; Yeon, J.; Smith, M. D.; Zur Loye, H. C. *Inorg. Chem.* **2015**, *54*, 6993-6999.

(19) Tsoureas, N.; Cloke, F. G. N. *J. Organomet. Chem.* **2018**, *857*, 25-33.

(20) Pace, K.; Kocevski, V.; Karakalos, S. G.; Morrison, G.; Besman, T. M.; zur Loye, H.-C. *Inorg. Chem.* **2018**, submitted.

(21) Yeon, J.; Smith, M. D.; Morrison, G.; zur Loye, H. -C. *Inorg. Chem.* **2015**, *54*, 2058-2066.

(22) Yeon, J.; Smith, M. D.; Tapp, J.; Möller, A.; zur Loye, H.-C. *J. Solid State Chem.* **2016**, *236*, 83-88.

(23) Judd, B. R. *Physical Review* **1962**, *125*, 613.

(24) Mörtl, K. P.; Sutter, J.-P.; Golhen, S.; Ouahab, L.; Kahn, O. *Inorg. Chem.* **2000**, *39*, 1626-1627.

(25) Yeon, J.; Smith, M. D.; Tapp, J.; Möller, A.; zur Loye, H. -C. *Inorg. Chem.* **2014**, *53*, 6289-6298.

(26) Boudreaux, E. A.; Mulay, L. N. *Theory and Applications of Molecular Paramagnetism*; Wiley: New York, 1976;

(27) Yeon, J.; Smith, M. D.; Tapp, J.; Möller, A.; zur Loye, H. -C. *J. Am. Chem. Soc.* **2014**, *136*, 3955-3963.

(28) Morrison, G.; Ramanantoanina, H.; Urland, W.; Smith, M. D.; zur Loye, H. -C. *Inorg. Chem.* **2015**, *54*, 5504-5511.

(29) Felder, J.; Yeon, J.; Smith, M.; zur Loye, H.-C. *Inorg. Chem. Front.* **2017**, *4*, 368-377.

(30) Jin, G. B.; Ringe, E.; Long, G. J.; Grandjean, F.; Sougrati, M. T.; Choi, E. S.; Wells, D. M.; Balasubramanian, M.; Ibers, J. A. *Inorg. Chem.* **2010**, *49*, 10455-10467.

(31) Wedgwood, F. A.; Kuznietz, M. *J. Phys. C: Solid State Phys.* **1972**, *5*, 3012.

(32) van Doom, C. F.; du Plessis, P. D. V. *J. Magn. Magn. Mater.* **1977**, *5*, 164-166.

(33) Sidhu, S. S.; Vogelsang, W.; Anderson, K. D. *J. Phys. Chem. Solids* **1966**, *27*, 1197-1200.

(34) Troc, R.; Leciejewicz, J.; Ciszewski, R. *Physica Status Solidi B: Basic Solid State Physics* **1966**, *15*, 515-519.

(35) Hubschle, C. B.; Sheldrick, G. M.; Dittrich, B. *J. Appl. Cryst.* **2011**, *44*, 1281-1284.

(36) Dolomanov, O. V.; Bourhis, L. J.; Gildea, R. J.; Howard, J. A. K.; Puschmann, H. *J. Appl. Cryst.* **2009**, *42*, 339-341.

(37) Sheldrick, G. M. *Acta Cryst.* **2008**, *A64*, 112-122.

(38) Kubelka, P.; Munk, F. Z. *Technol. Phys.* **1931**, *12*, 593.

(39) Morrison, G.; zur Loye, H.-C. *J. Solid State Chem.* **2015**, *221*, 334-337.

(40) Villa, E. M.; Marr, C. J.; Jouffret, L. J.; Alekseev, E. V.; Depmeier, W.; Albrecht-Schmitt, T. E. *Inorg. Chem.* **2012**, *51*, 6548-6558.

(41) Villa, E. M.; Wang, S.; Alekseev, E. V.; Depmeier, W.; Albrecht-Schmitt, T. E. *Eur. J. Inorg. Chem.* **2011**, n/a.

(42) Koo, H.-J. *Bull. Korean Chem. Soc.* **2011**, *32*, 467-471.

(43) Kovrugin, V. M.; Gordon, E. E.; Kasapbasi, E. E.; Whangbo, M.-H.; Colmont, M.; Siidra, O. I.; Colis, S.; Krivovichev, S. V.; Mentré, O. *J. Phys. Chem. C* **2016**, *120*, 1650-1656.

APPENDIX A:

PERMISSION TO REPRODUCE PUBLISHED MATERIALS

American Chemical Society License: Thesis/Dissertation

Chapters 2 and 7

This type of permission/license, instead of the standard Terms and Conditions, is sent to you because no fee is being charged for your order. Please note the following:

- Permission is granted for your request in both print and electronic formats, and translations.
- If figures and/or tables were requested, they may be adapted or used in part.
- Please print this page for your records and send a copy of it to your publisher/graduate school.
- Appropriate credit for the requested materials should be given as follows: "Reprinted (adapted) with permission from (COMPLETE REFERENCE CITATION). Copyright (YEAR) American Chemical Society." Insert appropriate information in place of the capitalized words.
- One-time permission is granted only for the use specified in your request. No additional uses are granted (such as derivative works or other editions). For any other uses, please submit a new request.

Royal Society of Chemistry License: Re-use permission requests

Chapters 4 and 8

Author reusing their own work published by the Royal Society of Chemistry
You do not need to request permission to reuse your own figure, diagrams, etc, that were originally published in a Royal Society of Chemistry publication. However, permission should be requested for use of the whole article or chapter except if reusing it in a thesis. If you are including an article or book chapter published by us in your thesis please ensure that your co-authors are aware of this.

Reuse of material that was published originally by the Royal Society of Chemistry must be accompanied by the appropriate acknowledgement of the publication. The form of the acknowledgement is dependent on the journal in which it was published originally, as detailed in 'Acknowledgements'.

Acknowledgements
The Royal Society of Chemistry publishes some journals in partnership with, or on behalf of, other organisations; these journals require a specific wording of the acknowledgement when work is reproduced from them. The text for the acknowledgement for these journals, and the standard wording to be used by all other journals are given below.

Standard Acknowledgement (Chapter 8)
Reproduced from Ref. XX with permission from the Royal Society of Chemistry.

Reproduction of material from Inorganic Chemistry Frontiers (Chapter 4)
> Reproduced from Ref. XX with permission from the Chinese Chemical Society (CCS), Peking University (PKU), and the Royal Society of Chemistry.

Elsevier License: Personal and Scholarly Purposes

Chapter 5

Authors can use their articles, in full or in part, for a wide range of scholarly, non-commercial purposes as outlined below:

- Share copies of the article and distribute them via email to colleagues for their research use (also known as 'scholarly sharing').
- Share the article for personal use or for the author's own classroom teaching.
- Use the article at a conference, meeting, or for teaching purposes.
- Allow the author's employers to use the article for other internal purposes (such as training).
- Include the article in a printed compilation of the author's works, such as collected writings and lecture notes.
- Include the article in a thesis or dissertation.
- Use the article in full or in part to prepare other derivative works, including expanding the article to book-length form, with each work to include full acknowledgement of the article's original publication.

These rights apply for all Elsevier authors who publish their article as either a subscription article or an open access article. In all cases we require that all Elsevier authors always include a full acknowledgement and, if appropriate, a link to the final published version hosted on Science Direct.